Conformational changes of α-synuclein, ABC and ECF transporters observed by high pressure EPR and DEER

Dissertation

submitted for the degree of

Dr. rer. Nat. (Doctor of Natural Sciences)

in the Department of Physics

University of Osnabrück

by

Michael Sippach, M.Sc.

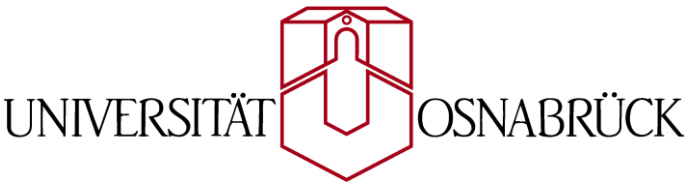

2017

Contents

Abbreviations and Symbols

α-syn	Alpha syunclein
AA	Amino acid
ABC	ATP-binding cassette
AD	Alzheimer´s disease
ADP	Adenosine diphosphate
AMP-PNP	Adenylyl-imidodiphosphate
APS	Ammonium persulfate
ATP	Adenosine triphosphate
BCA	Bicinchoninic acid assay
BSA	Bovine serum albumin
cw	Continuous wave
DEER	Double electron electron resonance
DNA	Deoxyribonucleic acid
DTT	Dithiothreitol
ECF	Energy coupling factor
E. coli	*Escherichia coli*
EDTA	Ethylene diamine tetraacetic acid
ENDOR	Electron nuclear double resonance
EPR	Electron paramagnetic resonance
ESEEM	Electron spin echo envelope modulation
GdnHCl	Guadinine hyrdochloride
HP	High pressure
IAA	4-(2-Iodoacetamido)-2,2,6,6-tetramethyl-1-piperidinyloxy
ID	Inner diameter
IDP	Intrinsically disordered protein
IPTG	Isopropyl-*β*-D-thiogalactopyranoside
LB	Lewy bodies
MMM	Multiscale Modeling of Macromolecules
MOPS	3-(N-morpholino)propanesulfonic acid
MTSSL	(1-oxyl-2,2,5,5-tetramethylpyrroline-3-methyl) methanethiosulfonate spin label

MW	Molecular weight
NAC	Non-Aβ component
NBD	Nucleotide binding domain
NACP	Non-Aβ component precursor
Ni-NTA	Nickel-Nitrilotriacetic acid
NMR	Nuclear magnetic resonance
OD	Optical density
OD	Outer diameter
PCR	Polymerase chain reaction
PD	Parkinson´s disease
PDB	Protein Data Bank
PMSF	Phenylmethylsulfonyl fluoride
PTFE	Polytetrafluoroethylene
SBP	Substrate binding protein
SDS	Sodium dodecyl sulfate
SDSL	Site-directed spin labeling
SL	Spin label
SNARE	Soluble N-ethylmaleimide-sensitive-factor attachment receptor
S. Thyphimurium	*Salmonella enterica* serovar Thyphimurium
OH-Tempo	4-hydroxy-2,2,6,6-tetramethylpiperidine-1-oxyl
TEMED	Tetramethylethylenediamine
ThT	Thioflavin T
TMD	Transmembrane domain
Tris	Trishydroxymethylaminomethane
TTR	Transthyretin
w/v	Weight per volume

1. Preamble

“The most beautiful thing we can experience is the mysterious. It is the source of all true art and science.”

Albert Einstein

Complex, biological macromolecular structures, build from simple elements and compounds, are the foundation of life. Those molecules are differentiated into classes: carbohydrates, lipids, nucleic acids and proteins. Like all biological macromolecules, proteins are essential components of organisms and partake in nearly all processes within biological cells. Therefore, the varied, elaborate structures of proteins facilitate numerous functions in cells like enzymatic activities in metabolic reactions, structural and mechanical functions, the sensory and signaling system, immune responses and cell adhesion. A protein´s function is fundamentally defined by its structure which is obtained by a sophisticated folding pathway originating from an amino acid chain, the gene encoded primary structure, over the secondary to the final tertiary or even quaternary structure.

Because of their essential importance for cellular function, proteins are a major branch of research in the biological sciences and biophysics, respectively. Approximately 134100 macromolecular structures have been deposited in the protein data bank (RCSB PDB) at the time of the creation of this work. The three dimensional structures of proteins are determined mostly by means of X-ray crystallography. Approximately 89.5 % of protein structures were elucidated by this biophysical method. Solution NMR and electron microscopy determined vaguely 8.8 % and 1.3 % respectively of the known protein structures. The remaining 0.4 % of protein structures were solved by techniques like solid-state NMR, electron crystallography and neutron diffraction. However, knowledge about the structural composition of a protein gives only small insight into its dynamics or its conformational equilibrium. The mentioned methods, though powerful techniques, have only limited capability to trace protein dynamics or, in case of solution NMR, are only applicable for a limited range of proteins depending on their molecular weight. On the contrary, the electron paramagnetic resonance (EPR) spectroscopy is well suited for studying the dynamics

of proteins independent of their size and allows in combination high pressure perturbance investigations on conformational equilibria and volumetric properties of proteins. Therefore, this technique represents the methodical backbone of this work. Thus a detailed introduction of the principles of EPR spectroscopy is given in the following chapter and preceds the characterization of the actual studied biological systems in this thesis. The section following the chapter about EPR outlines the biophysical and biochemical materials and methods which were applied in this work. The chapters four and five give introductions to their respective themes and also present and discuss acquired experimental results. The focuses in this thesis are based on two different subjects:

1. Investigations on the conformation equilibria of three different proteins, human α-synuclein, bovine serum albumin and HisJ from *Salmonella enterica serovar* Typhimurium via high pressure EPR. Spin labels (SL) were introduced at specific sites in these proteins by Site-directed spin labeling (SDSL) and their mobilites in dependence of applied pressure were investigated by continuous wave (cw) EPR. The combination of EPR with high pressure is relatively new, thus the questions adressed are whether and how pressure changes the volumetric properties and wheter and which conformational substates of the investigated proteins can be accumulated at high pressure. The goal is to make biological relevant protein intermediates that are otherwise difficult to detect accessible to spectroscopy.

2. Studies on bacterial ABC and ECF transporter systems $HisQMP_2$ from *Salmonella enterica serovar* Typhimurium, BioMNY and CbiMNOQ from *Rhodobacter capsulates* by double electron electron resonance (DEER) spectroscopy and cw EPR. The objective was to shed light on the conformational dynamics of the transport and nucleotide hydrolysis cycles of $HisQMP_2$ and BioMNY. CbiMNOQ was investigated with the question under which conditions the transporter´s substrate binds to the substrate binding unit CbiM.

2. Theory of electron paramagnetic resonance

The principle of the EPR (electron paramagnetic resonance) spectroscopy is based on the electron spin, a quantum mechanical entity. Within an external homogeneous magnetic field the otherwise degenerated spin energy states of free electrons (a paramagnetic centre) are split (Zeeman effect). Microwave radiation (photons) with an equal energy compared to the split energy states is absorbed by the paramagnetic centre. Resulting absorption spectra lead to informations and conclusions about the paramagnetic probe, their environments and interactions.

The *spin Hamiltonian* describes the energy states and time evolution of the investigated spin system on a quantum mechanical basis. Therefore the first part of this chapter describes this quantum mechanical operator, to explain the theoretical principles of EPR. Furthermore the nitroxide spin labels, which carry a paramagnetic centre and are utilized in this work (f.i. methanthiosulfonate spin label - MTSSL), get introduced as well as possible interactions with their environment (*electron Zeeman*, *nuclear Zeeman*, *hyperfine-splitting*, *electron-electron* (dipolar & exchange) interactions). Moreover the EPR methods and applications used to acquire the corresponding particular parameters (cw-EPR, pulse EPR), are described in the following chapters.

2.1 The free electron spin and its magnetic momentum

Electrons are not only characterized by their mass m_e and charge e, but also by their intrinsic angular momentum, the electron spin. The electron spin is an exclusive quantum mechanical property and should not be compared with a rotation of the electron itself. It is described by the spin operator $\hat{S}$ and its components.

$$\hat{S} = (\hat{s}_x, \hat{s}_y, \hat{s}_z) \tag{2.1}$$

Therefore the electron possesses a magnetic momentum $\hat{\mu}$:

$$\hat{\mu} = -g_e \cdot \frac{e\hbar}{2m_e} \cdot \hat{S} \quad (2.2)$$

$$= -g_e \cdot \mu_B \cdot \hat{S} \quad (2.3)$$

Here, the g-factor of the free electron is g_e=2.0023, ħ describes the Planck constant h divided by 2π and m_e=9,109*10^{-31}kg is the mass of the electron. The Bohr magneton is μ_B=9,27400915*10^{-24}JT^{-1}. Within a static homogeneous magnetic field B=(0, 0, B_0), the free electron´s magnetic moment interacts with B. The direction of the magnetic field matches the z-axis of the laboratory coordinate system (lab-frame). This interaction is characterized by the Hamiltonian.

$$\hat{H} = -\hat{\mu} \cdot B \quad (2.4)$$

Together with equation 2.3 $\hat{H}$ results to:

$$\hat{H} = g_e \cdot \mu_B \cdot B \cdot \hat{S} \quad (2.5)$$

$$= g_e \cdot \mu_B \cdot B_0 \cdot \hat{s}_z \quad (2.6)$$

The Schrödinger equation allows the calculation of the corresponding energy Eigenvalue E and the corresponding Eigenvector $|\Psi\rangle$.

$$\hat{H} \mid \Psi\rangle = E \mid \Psi\rangle \quad (2.7)$$

$$E = g_e \cdot \mu_B \cdot B_0 \cdot m_s \quad (2.8)$$

Since the free electrons spin quantum number is S=1/2 the magnetic quantum number resembles only two different values (m_s=±1/2). The electrons two occupied energy states in a magnetic field are therefore given by:

$$E_1 = +\frac{1}{2} g_e \cdot \mu_B \cdot B_0 \quad (2.9)$$

$$E_2 = -\frac{1}{2} g_e \cdot \mu_B \cdot B_0 \quad (2.10)$$

$$\Delta E = E_1 - E_2 = g_e \cdot \mu_B \cdot B_0 \quad (2.11)$$

These two energy states (spin-states) correspond to the z-component of the spin being either parallel (spin down) or anti-parallel (spin-up) to the magnetic field as depicted in figure 2.1. To induce a transition between those states an external energy source in the form of electromagnetic emission (microwaves) is needed. The transition from the energetically lower to the higher spin-state is only possible when the irradiated microwave´s energy corresponds to the energy difference of the two spin-states (see figure 2.1.). The corresponding frequency is given by:

$$\nu = \frac{\Delta E}{h} = \frac{g_e \cdot \mu_B \cdot B_0}{h} \quad (2.12)$$

v is called Larmor frequency and represents the EPR resonance condition which connects the magnetic field strength B_0 with the absorbed microwave frequency. This relation also leads to the fact that a magnetic field of higher magnitude implies microwave radiation of higher energy to reach resonance conditions. Considering the depicted theoretical case of microwave absorption by a free electron (figure 2.1), there would be only one possible resonance position at B_0.

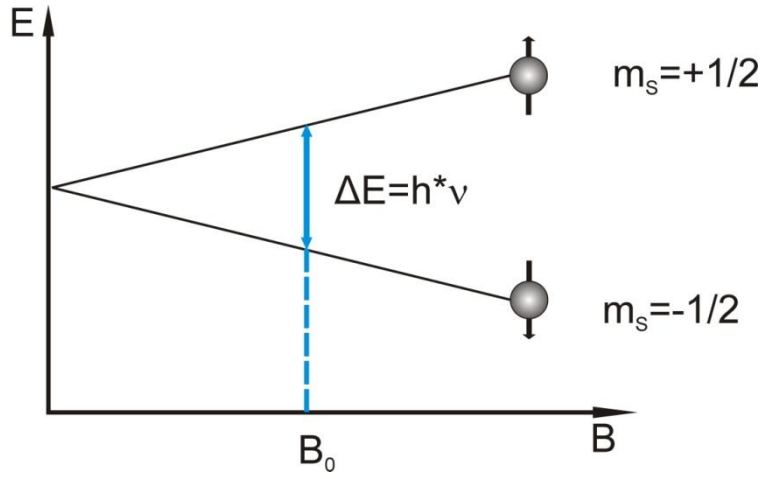

Figure 2.1.: The Zeeman-effect for an electron with spin quantum number s=1/2. The otherwise degenerated energy states of the spin split depend on the magnetic field B.

2.2 The MTSSL and the spin Hamiltonian

2.2.1 The methanethiosulfonate-spin-label

Chapter 2.1 explains the fundamental principle of EPR by the theoretical example of a free electron. But how is EPR applied to a system like a biomacromolecule which lacks a natural free electron or radical. In this case a paramagnetic centre in form of an unpaired electron is introduced to the system via site-directed spin labeling (SDSL) [90] as depicted in figure 2.2. Since those unpaired electrons are compounds of atoms and molecules they cannot be compared to a free electron, as described in chapter 2.1, simply because of their proximity to further electron orbitals or nuclei of adjacent atoms. The molecules which carry the unpaired electron and that were generally used in this work are the (1-oxyl-2,2,5,5-tetramethylpyrroline-3-methyl) methanethiosulfonate (MTSSL) or the 4-(2-Iodoacetamido)-2,2,6,6-tetramethyl-1-piperidinyloxy (IAA) spin label.

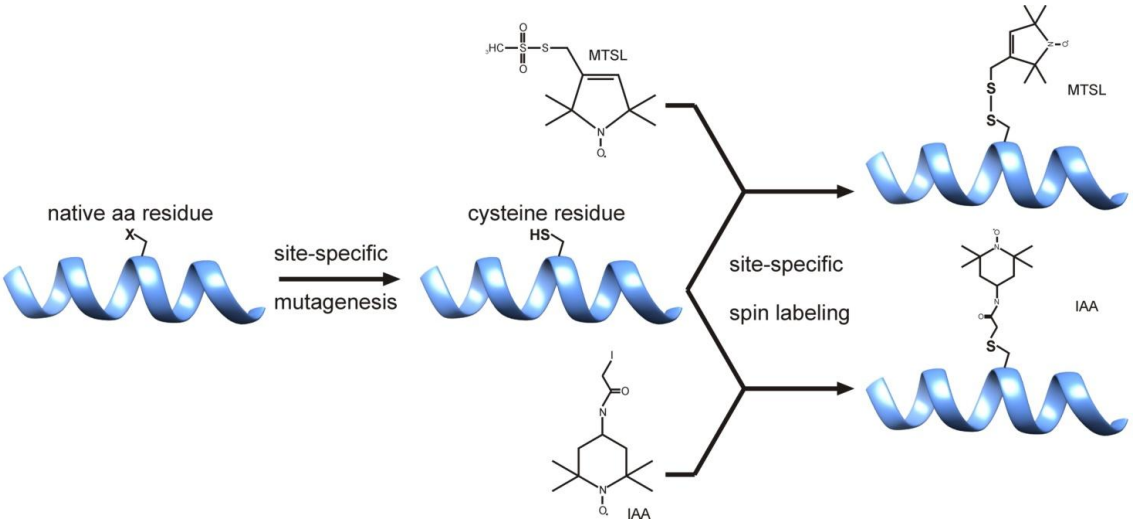

Figure 2.2: Site-directed spin labeling. Substitution of a native amino acid with a cysteine residue establishes site-directed spin labeling. Reaction of a spin label IAA ((4-(2-Iodoacetamido)-2,2,6,6-tetramethyl-1-piperidinyloxy)) or MTSSL ((1-oxyl-2,2,5,5-tetramethylpyrroline-3-methyl) methanethiosulfonate) with the sulfhydryl group of the cysteine residue, generates the spin label side chain.

The chemical structure of a protein-bound MTS spin label is depicted in figure 2.3 a). Its three-dimensional structure (figure 2.3 b) shows the determined molecular frame which simplifies later considerations. The N-O bond of the nitroxide group, which carries the unpaired electron, defines the direction of the x-axis. The z-axis is perpendicular to the plane of the pyrrolyl ring and the y-axis is oriented perpendicularly to the former two axes.

The molecule´s paramagnetic characteristic originates from the nitroxide´s free electron. It is located in the π-orbital arising from $2p_z$ orbitals of the oxygen and nitrogen atom which overlap to some extent. Figure 2.3 c depicts the nitroxide´s schematic electronic structure (density). Due to this context, the unpaired electron already experiences different interactions in the molecule compared to a free electron. Furthermore, the label and therefore the unpaired electron can be subject to other interactions due to atoms and/or molecules in their direct environment that change the MTSSL electron density and consequently the electron spin properties. Those upcoming interactions which affect the EPR spectra and define their characteristic line-shape will be discussed in the chapters ahead.

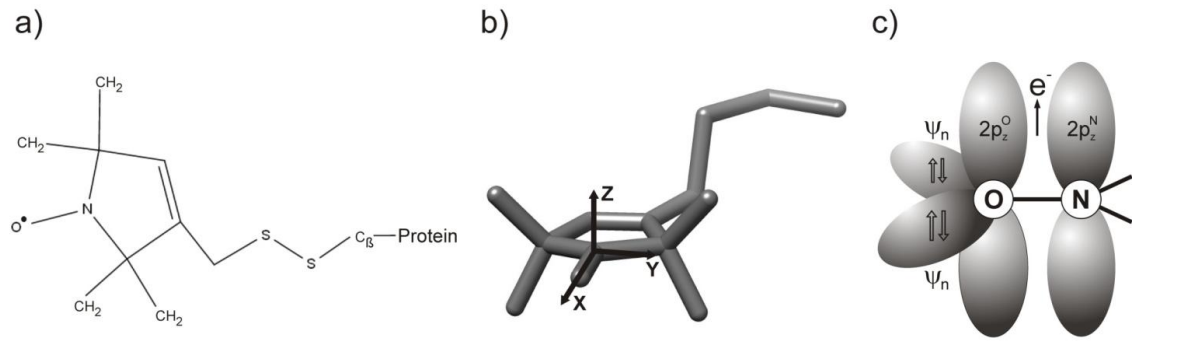

Figure 2.3.: The MTS spin label side chain. a) Chemical structure of the MTS spin label bound to a protein. b) 3D structure of the MTS spin label with the molecular frame axes (x,y,z). c) The electron density at the MTS spin label nitroxide group.

2.2.2 The spin Hamiltonian

The different interactions of the nitroxide´s unpaired electron with its environment and external influences are described by the spin Hamiltonian. This operator displays the quantum mechanical energy conditions and time evolution of the considered spin system. The most prominent interactions in SDSL-EPR are those between the electron spin and an external magnetic field (the electron Zeeman effect: EZ), adjacent nuclear spins (hyperfine interaction: HF) and further electron spins (dipole-dipole and exchange interactions: DD, Ex). The interaction of a nuclear spin with the external magnetic field is described by the nuclear Zeeman effect (NZ). The summed up contributions of the spin Hamiltonian are displayed below:

$$\hat{\mathrm{H}} = \hat{\mathrm{H}}_{\mathrm{EZ}} + \hat{\mathrm{H}}_{\mathrm{NZ}} + \hat{\mathrm{H}}_{\mathrm{HF}} + \hat{\mathrm{H}}_{\mathrm{DD}} + \hat{\mathrm{H}}_{\mathrm{Ex}} \qquad (2.13)$$

The following chapters deal with a look at those different contributions to understand their specific impact on EPR spectra further.

2.2.3 The electron Zeeman interaction $\hat{\mathrm{H}}_{\mathrm{EZ}}$

The electron Zeeman effect describes the interaction between an electron and an external magnetic field. The resulting difference between the split energy states of an

electron was already given for an isotropic coherence of a free electron in equation 2.11 (depicted in figure 2.1.). The molecule-bound electron possesses an orbital momentum $\hat{L}$ which leads to an anisotropic coherence based on the orientation of the electron spin with respect to the molecule or the orientation of the molecule with respect to the external magnetic field direction, respectively.

The magnetic momentum of the electron $\hat{\mu}$ in this case is contributed by the orbital and the spin momentum:

$$\hat{\mu} = -\mu_B \cdot (\hat{L} + g_e \hat{S}) \tag{2.14}$$

Due to the interaction of the orbital momentum $\hat{L}$ with the external magnetic field B and the spin Ŝ the total energy of the system is given by:

$$\hat{H} = \mu_B \cdot B \cdot (\hat{L} + g_e \cdot \hat{S}) + \lambda \cdot \hat{L} \cdot \hat{S} \tag{2.15}$$

The first term describes the interaction of the magnetic field with the orbital and the spin momentum, respectively. The last term characterizes the spin orbit coupling where λ is the spin orbit coupling constant. By applying perturbation theory the Hamiltonian out of equation 2.15 can be derived to [219]:

$$\hat{H}_{EZ} = \mu_B B(g_e 1_3 + 2\lambda\Lambda) \cdot \hat{S} = \mu_B \cdot B \cdot g \cdot \hat{S} \tag{2.16}$$

1_3 is a 3x3 identity matrix. Λ is a symmetric tensor. The g-tensor can be described in a diagonal form within the eigensystem, which is identical to the above mentioned MTSSL frame.

$$g = \begin{bmatrix} g_{xx} & 0 & 0 \\ 0 & g_{yy} & 0 \\ 0 & 0 & g_{zz} \end{bmatrix} \quad (2.17)$$

The contributions of the MTSSL g-tensor can be described as follows [158]:

$$g_{xx} = g_e + \frac{2\lambda(O)\rho_\pi^O c_n^2 y}{\Delta E_{n\to\pi}} \quad (2.18)$$

$$g_{yy} = g_e + \frac{2\lambda(O)\rho_\pi^O c_n^2 x}{\Delta E_{n\to\pi}} \quad (2.19)$$

$$g_{zz} = g_e \quad (2.20)$$

λ(O)=151cm^{-1} describes the spin-orbit coupling parameter of the oxygen atom, ρ_π^O is the spin density on the oxygen 2p$_z$ atomic orbital. $c_n{}^x$ and alternatively $c_n{}^y$ are molecular orbital coefficients of the 2p$_x$ and 2p$_y$ atomic orbitals that contribute to the oxygen lone pair orbital Ψ$_n$. $\Delta E_{n\to\pi}$ is the excitation energy needed for a transition between an orbital of the unbound oxygen electron pairs and the nitroxide bond π-orbital [158].

The relative orientation of the molecule´s eigensystem with respect to the magnetic field is considered by by the polar angles φ and θ of the magnetic field vector:

$$B = B_0 \begin{pmatrix} \sin(\theta)\cos(\phi) \\ \sin(\theta)\sin(\phi) \\ \cos(\phi) \end{pmatrix} \quad (2.21)$$

The electron Zeeman Hamiltonian is therefore described by:

$$\hat{H}_{EZ} = \frac{\mu_B}{\hbar} B_0 \left(\sin(\theta)\cos(\phi) g_{xx}\,\hat{S}_x, \sin(\theta)\sin(\phi) g_{yy}\,\hat{S}_y, \cos(\phi)\, g_{zz} * \hat{S}_z\right) \quad (2.22)$$

With a defined orientation of φ and θ a specific g value can be calculated:

$$g_{spez.} = \sqrt{\sin^2(\theta)\cos^2(\phi)g_{xx}^2 + \sin^2(\theta)\sin^2(\phi)g_{yy}^2 + \cos^2(\phi)\,g_{zz}^2} \qquad (2.23)$$

However, in case of fast molecular motions of MTSSL in aqueous solutions the g-tensor anisotropy averages out. Consequently the EPR spectrum is orientation independent and the averaged isotropic g_{iso} is applied:

$$g_{iso} = \frac{1}{3}(g_{xx} + g_{yy} + g_{zz}) \qquad (2.24)$$

Additionally, magnetic field intensities used in this work (about 300 mT) are not sufficient to resolve g-tensor anisotropy in the EPR spectra. W-band EPR (3 T) must be applied to resolve g-tensor anisotropy.

2.2.4 The nuclear Zeeman interaction $\hat{H}_{NZ}$

Analogous to the electron spin, the splitting of the energy states of the nuclear spin, when exposed to an external magnetic field, is given by the multiplet 2I+1 with the nuclear spin number I. Figure 2.4 depicts schematically the hyperfine interaction of the MTS spin label (S=1/2, $I_{14_N} = 1$).

The nuclear Zeeman interaction describes the interaction of the magnetic momentum of a nuclear spin with an external magnetic field. In most EPR methods this effect can be neglected. Considering different double resonance EPR techniques (DEER, ENDOR) the $\hat{H}_{NZ}$ has to be taken into account. The energy of the nuclear Zeeman is characterized by the Hamiltonian:

$$\hat{H}_{NZ} = \mu_n g_n B \hat{I} \qquad (2.25)$$

The nuclear magneton is defined by μ_n, g_n characterizes the nuclear g-factor and $\hat{I}$ is the nuclear spin operator.

2.2.5 Hyperfine interaction $\hat{H}_{HF}$ and the A-tensor

The hyperfine interaction characterizes the splitting of an electron´s energy state and the EPR resonance line due to a interaction between the electron spin and a nuclear spin. This effect depends on the multiplicity of the nucleus and is described by the Hamiltonian:

$$\hat{H}_{HF} = \hat{H}_{DD} + \hat{H}_{FC} = \hat{S}A_{dip}\hat{I} + a_{iso}\hat{S}\hat{I} = \hat{S}A\hat{I} \tag{2.26}$$

The hyperfine interaction can be subdivided into two specific contributions: the anisotropic dipole-dipole interaction $\hat{H}_{DD}$ between electron and nuclear spin, and the isotropic Fermi contact interaction $\hat{H}_{FC}$. $\hat{S}$ and $\hat{I}$ describe again the electron spin operator and nuclear spin operator, respectively. A is the A-tensor which consists of the terms A_{dip} and a_{iso}.

The isotropic part of the hyperfine interaction is based on the finite probability of presence of the electron at the nucleus and is given by:

$$\hat{H}_{FC} = a_{iso}\hat{S}\hat{I} \tag{2.27}$$

with:

$$a_{iso} = \frac{2\mu_0}{3\hbar} \cdot g_e \cdot \mu_B \cdot g_n \cdot \mu_n |\psi_{r=0}|^2 \tag{2.28}$$

where $|\psi_{r=0}|^2$ is the electron spin density at the nucleus. $\hat{H}_{DD}$ describes the dipolar coupling between the electron spin and the nuclear spin which generates the anisotropy of $\hat{H}_{HF}$. This term is derived from a point dipole approximation and is given by:

$$H_{DD} = -\frac{\mu_0}{4\pi} \cdot g_e \cdot \mu_B \cdot g_n \cdot \mu_n \left(\frac{\hat{S} \cdot \hat{I}}{r^3} - \frac{3(\hat{S} \cdot r)(\hat{I} \cdot r)}{r^5}\right) = \hat{S} A_{dip} \hat{I} \quad (2.29)$$

Herein r is the vector that connects Ŝ and Î. μ_0 is the magnetic field constant, μ_B is the Bohr magneton, μ_n is the nuclear magneton, g_e and g_n are the according g-factors. This interaction depends on the distance between the spins (r^{-3}). Accordingly the A-tensor describes the order of magnitude and the anisotropy of the hyperfine splitting which is independent from the external B-field. In the nitroxide molecular coordinate system has a diagonal form analogous to the g-tensor.

$$A = \begin{pmatrix} A_{xx} & 0 & 0 \\ 0 & A_{yy} & 0 \\ 0 & 0 & A_{zz} \end{pmatrix} \quad (2.30)$$

Analogous to 2.23 the hyperfine constant depends on the orientation of the magnetic field with respect to the molecule as described by:

$$A_{\theta,\phi} = \sqrt{\sin^2(\theta)\cos^2(\phi)A_{xx}^2 + \sin^2(\theta)\sin^2(\phi)A_{yy}^2 + \cos^2(\phi)\, g A_{zz}^2} \quad (2.31)$$

As mentioned before the unpaired electron of the nitroxide-group of the MTSSL spin label interacts with the nuclear spin of the ^{14}N-nitrogen (I=1). Due to the nuclear spin number I=1 the parallel and anti-parallel spin states are split into three different energy levels which results into three resonance positions in the EPR spectrum, respectively. Typical values of contributing elements of the N-O group A-tensor are:

$$A_{xx} \approx 0{,}5mT, \quad (2.32)$$

$$A_{yy} \approx 0{,}5mT, \quad (2.33)$$

$$A_{zz} \approx 3{,}5mT \quad (2.34)$$

The A_{zz} represents a quite important term in interpreting EPR spectra because it is sensitive to the polarity of the spin label´s environment. In polar media, for instance, the electron density of the unpaired electron is shifted in direction of the nitrogen atom which increases the hyperfine interaction. By determining the A_{zz} value it is possible to distinguish between specific sites of proteins which are either located in an aqueous solution, in the protein interior or in the lipid phase of a biological membrane.

2.2.6 Interaction between two electron spins

Former considerations about the contributions of the total Hamiltonian referred to a single unpaired electron only. Furthermore, in the upcoming two chapters a system with two unpaired electrons shall be described by elucidating two contributing elements, which are dependent on the distance between the two investigated spins: The dipole-dipole coupling and the exchange coupling.

Spatial proximity of two magnetic dipoles like two unpaired electrons results in an anisotropic interaction as long as their orbitals are located too far from each other to overlap. The energy of this interaction E can be described classically as:

$$E = -\mu_1 B_2(r_{12}) = -\mu_2 B_1(r_{21}) \tag{2.35}$$

B_1 is the magnetic field induced by spin 1 at the position of spin 2, and vice versa for B_2, respectively. The strength of the magnetic fields is directly related to the distance between the two spins indicated by the vector r. This relation can be described by a Hamiltonian which is derived from the point dipole approximation and by utilization of the correspondence principal:

$$\hat{H}_{dipole-dipole} = \frac{\mu_0}{2h} g_1 g_2 \mu_B^2 \left(\frac{\hat{S}_1 \hat{S}_2}{r^3{}_{12}} - \frac{3(\hat{S}_1 r_{12})(\hat{S}_2 r_{12})}{r^5{}_{12}} \right) \tag{2.36}$$

, where g_1 and g_2 are the g values of the two electron spins, $r_{12}=|r_{12}|$ and $\hat{S}_1$ and $\hat{S}_2$ are the electron spin operators. Considering equation 2.36 the dipole-dipole interaction is inversely proportional to the distance r^3. Therefore by quantifying the dipole-dipole coupling the distance between two spins can be calculated. This in consequence acts as a superb tool to determine inter-spin distances in SDSL EPR.

Introducing the dipole-dipole coupling tensor D and summing up $\hat{S}_1$ and $\hat{S}_2$ to $\hat{S}$ ($\hat{S}=\hat{S}_1+\hat{S}_2$) leads to a simplified Hamiltonian:

$$\hat{H}_{dipole-dipole} = \hat{S}_1 D \hat{S}_2 \tag{2.37}$$

with:

$$D = \frac{\mu_0}{2h}\frac{g_1 g_2 \mu_B^2}{r^3{}_{12}}\begin{pmatrix} -1 & 0 & 0 \\ 0 & -1 & 0 \\ 0 & 0 & -2 \end{pmatrix} \tag{2.38}$$

Utilizing the high-field approximation D can be described in its principal axis system. Introducing the dipolar frequency the Hamiltonian can be described as:

$$\hat{H}_{dipole-dipole} = \omega_{dd}\hat{S}_1\hat{S}_2\hbar \tag{2.39}$$

with:

$$\omega_{dd} = \frac{\mu_0 g_e^2 \mu_B^2}{4\pi\hbar}\left(\frac{1-3cos^2\Theta_{\mathrm{dd}}}{r_{12}^3}\right) \tag{2.40}$$

The dipolar frequency ω_{dd} is directly dependent on the distance between the two spin systems and Θ_{dd}, the angle between the external magnetic field and the vector r_{12} that connects spin 1 and spin 2, called the dipolar vector. Due to the dipolar interaction the resonance lines of + ω_{dd} and - ω_{dd} are split. In case of a frozen solution, a macroscopically disordered sample so to speak, the orientation of the dipolar vector in respect to the external magnetic field is isotropically distributed. This leads to an averaging of equation 2.40 over the angle Θ_{dd} with the weighting factor

$\sin\Theta_{dd}$. As a consequence the so called Pake pattern, the superposition of two distributions of shifted resonance frequencies, can be observed.

Due to the dependence of the Pake Pattern on the dipolar vector r_{12}, interspin distances can be determined. Four pulse DEER spectroscopy allows a direct observation of a Pake Pattern applying a Fourier transform upon the experimental DEER data.

2.2.7 Exchange interactions – Heisenberg spin exchange

Next to the dipole-dipole another electron-electron interaction is the so called Heisenberg spin exchange interaction, or shortly exchange coupling $\widehat{H}_{Ex}$. This phenomenon is observed when the inter-spin distances are so small (≈ 0.8 nm) [166], that electron orbitals partially overlap. This means the two electrons have a non-vanishing probability of presence at the same location which results to a weak binding interaction (anti-parallel spins) according to the Pauli exclusion principle. For the Heisenberg exchange interaction an isotropic contribution exists, which is lacking for the dipole-dipole interaction, and is the most important part of the exchange coupling.

$$\widehat{H}_{Ex}^{0} = -2J_0\hat{S}_1\hat{S}_2 \qquad (2.41)$$

The amplitude of the orbital overlap is described by the isotropic exchange coupling constant J_0. [219]. By determining J information of the distance between the electron spins can be obtained due to the fact that the exchange coupling depends on the inter spin distance.

2.3 Continuous wave EPR

The principle of “continuous wave” (cw) EPR is based on a paramagnetic sample exposed to an external magnetic field of varying strength and microwaves of a fixed frequency. The absorption of the radiated microwave by the paramagnetic centre is

detected in dependence of the applied magnetic field. The resulting EPR spectrum is depicted as first derivative of the absorption due to technical reasons (modulation of the B-field and phase-sensitive detection by a lock-in amplifier). The shape of the spectrum is based on the principles of the spin Hamiltonian, as described in chapter 2.2, which is described in the upcoming chapter with an example. Therefore cw EPR allows the clarification of various parameters of the spin label and its environment. For instance the mobility of the spin label or its accessibility towards specific agents, like paramagnetic quenchers, can be determined. Alongside ordinary measurements at room temperature it is possible to apply cw EPR also at low temperatures (below 200 K). This allows distance measurements between two unpaired electrons in a range of below 2 nm and the polarity of the spin label micro-environment.

The reliance on these parameters and their influence on the spectra shape, their definition and significance are explained afterwards.

2.3.1 Single crystal and powder spectra

As already explained the spin Hamiltonian describes the shape of an EPR spectrum. Herein a corresponding example is given by considering a MTS spin label single crystal. In the single crystal all molecules are oriented consistently and the spin labels unpaired electron interacts with a nitrogen atom (I=1) which results in hyperfine splitting. In this case the corresponding Hamiltonian is represented by:

$$\hat{H} = \hat{H}_{EZ} + \hat{H}_{HF} = \mu_B \cdot B \cdot g \cdot \hat{S} + \hat{S} \cdot A \cdot \hat{I} \qquad (2.42)$$

With a magnetic field B=(0, 0, B) and negligible x and y contributions of $\hat{S}$ and $\hat{I}$, the corresponding eigenvalues are given by:

$$E_{m_S,m_I} = g_{\theta,\phi} \cdot \mu_B \cdot m_S \cdot B + A_{\theta,\phi} m_S m_I \qquad (2.43)$$

The g factor ($g_{\theta,\Phi}$) and hyperfine constant ($A_{\theta,\Phi}$) in equation 2.43 are dependent on the orientation of the B-field with respect to the spin label molecule. m_s is the electron quantum number (m_s=½; -½) and m_I is the nuclear quantum number (m_I=1; 0, -1), respectively. The corresponding magnetic field positions (B_1, B_2, B_3), at which resonance conditions are established, are provided considering the quantum mechanical selection rules (Δm_s=±1; Δm_I=0).

$$B_1 = \frac{\Delta E - A_{\phi,\varphi}}{g_{\phi,\varphi} \cdot \mu_B} \tag{2.44}$$

$$B_2 = \frac{\Delta E}{g_{\phi,\varphi} \cdot \mu_B} \tag{2.45}$$

$$B_3 = \frac{\Delta E + A_{\phi,\varphi}}{g_{\phi,\varphi} \cdot \mu_B} \tag{2.46}$$

As shown in figure 2.4 the resulting nitroxide EPR spectrum consists of three resonance lines which are centered at $g_{\theta,\Phi}$ and separated by $A_{\theta,\Phi}$.

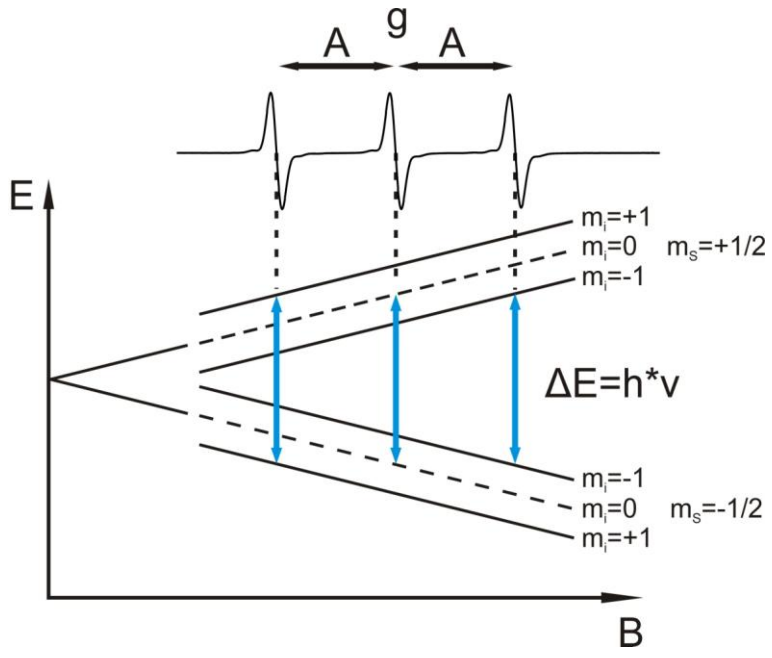

Figure 2.4: Hyperfine coupling. Schematic representation of the energy states of an unpaired electron (s=1/2) hyperfine coupled to a nucleus (I=1) and exhibited to an external magnetic field. The Zeeman interaction leads to a splitting of the otherwise degenerated spin energy states into two

energy states. The hyperfine interaction leads to a further splitting into three different energy states centered at g and separated by A.

Since the g- and A-tensor are anisotropic entities, the EPR-spectrum depends on the orientation of the spin label with respect to the external magnetic field. The first example of a single MTS spin label crystal gives a unified orientation of all molecules. Considering numerous spin labeled proteins in an aqueous solution, this corresponds to an isotropic distribution of the molecules orientation. Next the so called powder spectrum or sample is observed, which requires the sample to be in a frozen state (below 200 K). In this case the spin label orientations are randomly distributed with regard to the B-field. In the extreme cases of the magnetic field orientation, aligned parallel in respect to the spin label molecules x-, y- or z-axis, the resulting spectra are dominated by either A_{xx} and g_{xx}, A_{yy} and g_{yy} or A_{zz} and g_{zz}. For all non-extreme cases of the magnetic field orientation in-between the parallel alignment other g- and A-values arise as described by equations 2.23 and 2.31. All the different possible spectra which correspond to various magnetic field orientations (θ, Φ) can be summed up and result into a so called powder-spectrum.

Additionally the EPR spectra are not only sensitive to the orientation of the spin label but also to the spin label side chain motion. Therefore a time-dependence emerges for the orientations of the spin label, or more specifically, for the effective g- and A-values in respect to a sample in aqueous solution at room temperature. This is resulting in a significant difference of the EPR line shape compared to the powder spectrum because of an averaging of the anisotropic components of the tensors which is based on the nanosecond time scale of the molecular motion during microwave absorption.

The spin label side chain motion plays a significant role in influencing the EPR line shape, like the protein movement, the spin label motional freedom, the viscosity of the solvent or the temperature. Also dipole-dipole interactions can alter the shape of the EPR spectrum by inducing a significant broadening of the line shape depending on the distance between the paramagnetic centers. By analyzing the specific features of an EPR spectrum it is possible to draw conclusions and information about the spin label environment and the protein itself.

2.3.2 Relaxation processes

As described absorption in EPR is based on a paramagnetic system exposed to an external magnetic field B_0 and microwave radiation. A constant uptake of energy by the spin system with opposing emission of smaller magnitude would lead to an equilibration of the population differences (Boltzmann-distribution) and therefore to its complete saturation. Ongoing excitation of energy transitions and the acquisition of an EPR spectrum would consequently not be possible.

However, the thermal equilibrium of an electron spin system is normally re-established by various relaxation processes. Those relaxation effects are responsible for an excited spin system´s emission of energy and return to its ground-state over time and therefore operate against the saturation of a spin system.

It is the spin systems interaction with its surroundings, the so called lattice and adjacent spin-systems, which is essentially responsible for relaxation processes. As introduced shortly in 2.2.2 the longitudinal, or spin-lattice, relaxation time T_1 defines the relaxation governed by the energy transfer between electron spins and their direct environment, the spin-lattice. In consequence the spin-systems net energy changes due to the varying magnetic quantum number m_s. The rate $1/T_1$ gives the velocity measure for a spin systems equilibration dependent on its environment. In solids, the effect originates from lattice vibration and is facilitated by fluctuations of local magnetic fields. In liquid solutions, these fluctuations are contributed by molecular motions, as Brownian diffusion of solutes, or molecular collisions.

In case of a relaxation process based on interacting spin systems it is referred to spin-spin, or transverse relaxation defined by the relaxation time T_2 and the corresponding relaxation rate $1/T_2$. Unlike the longitudinal relaxation the transversal relaxation is an energy conserving mechanism, leaving the net-energy of the spin-system unchanged due to a so called spin flip-flop process between the two corresponding electron spins. However, the process leads to a loss of phase information, basically the phase relation between the interacting spin systems [161].

2.3.3 Line broadenings

The natural linewidth of a EPR spectrums resonance lines are defined by the Heisenberg uncertainty principle $\Delta E \Delta t \geq h/2\pi$. This relation shall be explained

shortly: if the excited state of a molecule or a quantum mechanical entity has a precisely determined life time, its corresponding energy is unknown. For example, when the longitudinal relaxation time of a spin system would be infinitely fast, the uncertainty of the excited states energy would be maximal. This however would lead to a broadening of the EPR resonance lines beyond detection. In other words the line width is inversely proportional to the relaxation time [73].

Regarding a theoretical sample in which all spin systems are completely homogeneous by experiencing the same magnetic field and possess the same spin-Hamiltonian parameters the relaxation processes would lead to homogeneous line broadening and a Lorentzian line shape of the EPR absorption spectrum. Since most samples are not completely homogeneous but come in a distribution of differing orientations of spin ensembles the corresponding spin Hamiltonian parameters differ as well. This leads to the so called inhomogeneous line broadening which exhibits a line shape which is reflected by a Gaussian distribution. The reasons for a inhomogeneous line shape can be different e.g. the distribution of spin orientations in a solid state sample, an inhomogeneous external magnetic field B_0, unresolved hyperfine couplings due to a high amount of nuclei adjacent to the observed spin system or dipolar interactions with other paramagnetic centers can have a broadening effect.

2.3.4 Side chain dynamics and mobility measurements

2.3.4.1 Mobility regimes

EPR spectra acquired at room temperature allow a characterization of the motion and dynamics of the MTS spin label side chain. From this it is possible to draw conclusions about the spin label´s environment and its location. The mobility of the spin label side chain attached to a specific position of a protein structure depends on three different parameters.

1. The mobility or, more specifically, the reorientational freedom of the spin label molecule around the particular bond that connects the label to the protein´s backbone or to an amino acid residue.
2. The motions of segments of the protein´s backbone and secondary structure.

3. The entire protein motion.

To describe the time scale of rotational and transversal motion of a molecule in an aqueous medium by random diffusion, the so called rotation correlation time (τ) is introduced. The rotational correlation time is a measure of the time after the alignment of a molecule is not correlated to its initial orientation anymore. The rotation correlation times of the three above mentioned parameters contribute to the total τ.

For a protein a spherical form can be assumed as approximation and its rotational correlation time can be derived from the Stokes-Einstein relation:

$$\tau = \frac{4\pi\eta a^3}{3k_BT} = V\frac{\eta}{k_BT} \qquad (2.47)$$

The viscosity of the aqueous medium is η, a is the radius of the considered molecule, k_B is the Boltzmann constant and T is the temperature. The molecular volume is depicted by V. Since the rotation correlation time of liposome reconstituted proteins, soluble polypeptides heavier than 200 kDa, or proteins in a medium with a high viscosity is quite large, it is not detectable on the EPR time scale [18]. The rotational correlation time can be determined from the EPR spectral line shape using Redfield theory, utilizing the amplitudes of the spectral high-field line h_{-1}, middle-field line h_0, low-field line h_1 and line width of the middle-field line ΔB, according to

$$\tau = 6.0 * 10^{-6} * \Delta B\left(\sqrt{\frac{h_0}{h_{-1}}} + \sqrt{\frac{h_0}{h_1}} - 2\right) \qquad (2.48)$$

This approximation is valid for rotational correlation times up to ~3 ns. For correlation times exceeding 3 ns or for anisotropic reorientational motion the correlation times can be determined by fitting of simulated spectra to the experimental ones using Freed´s theory [56]. X-Band cw EPR is sensitive in a τ range from 0.1 to 300 ns which matches quite well the rotational correlation times of a protein bound spin

label. This makes the rotational correlation time a versatile tool to investigate and define protein conformational dynamics and conformational changes. Regarding a polypeptide with an attached spin label, the degree of averaging of the anisotropic components of the magnetic tensors depends on the motional freedom of the label bound to a particular site. For instance a spin label attached to a site within a proteins interior is supposed to have lesser motional freedom because of sterical restraints than a spin label bound at the surface of a protein or located at a loop region. This behavior is represented exemplarily in figure 2.5.

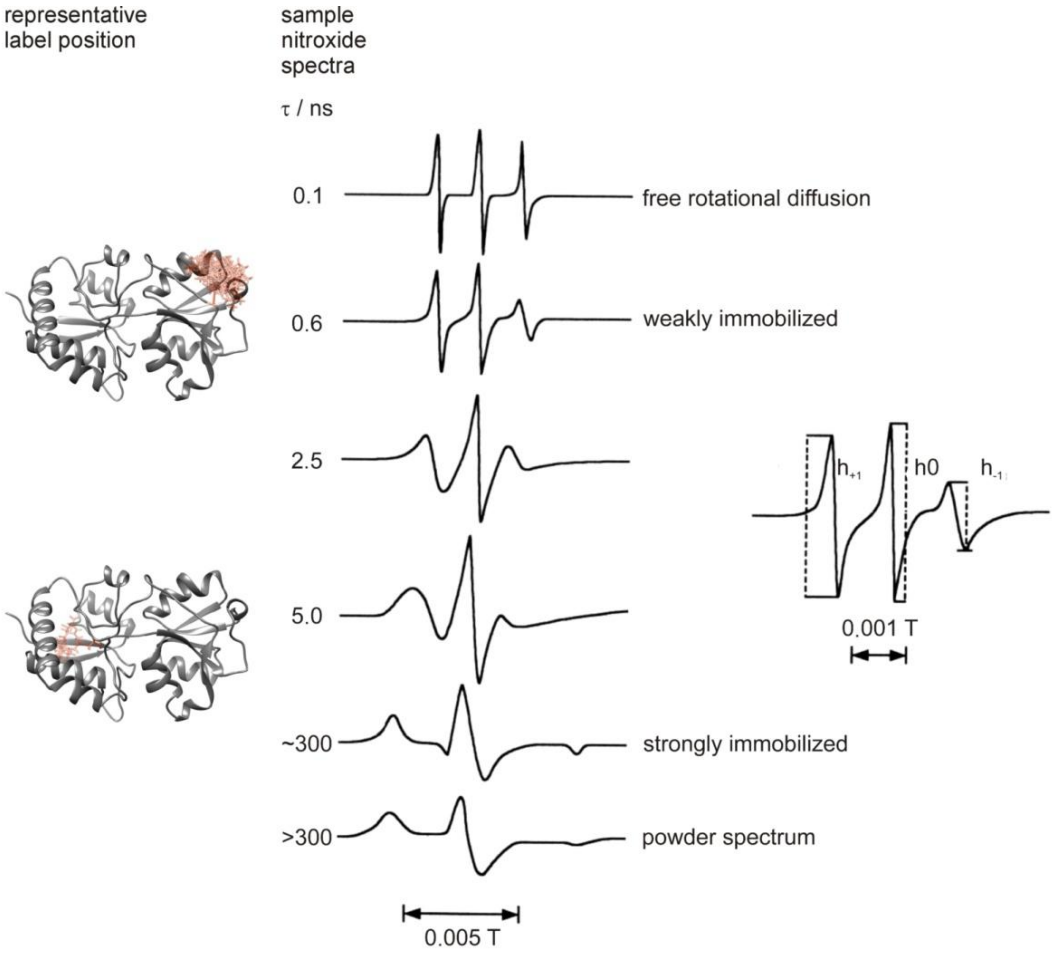

Figure 2.5: Effects of different rotational correlation times on nitroxide cw EPR spectra at X-band frequencies. Two representative examples of labeled positions in a protein are shown to the left. A spin label attached to the proteins surface (top-left) shows a high degree of mobility (probability of orientations is depicted in red) with a small value of τ. In the case of a spin label buried in the protein interior (bottom-left) a larger value of τ is indicated due to its restricted motional freedom (and a smaller distribution of orientations as well). The amplitude heights of the three resonance lines are given by the parameters h_{+1}, h_0 and h_{-1} (right spectrum) [167].

According to the spectral anisotropy Δω, which defines the maximal possible resonance shift induced by anisotropy of the magnetic tensors, the rotational correlation times can be subdivided into four different regimes (figure 2.6). The isotropic limit shows the fastest dynamics with completely averaged anisotropies allowing the exact calculation of the spectral line positions using the isotropic g- and A-values. Analogue to g_{iso} (equation 2.24) A_{iso} is given by:

$$A_{iso} = \frac{1}{3}(A_{xx} + A_{yy} + A_{zz}) \tag{2.49}$$

The line width of an according calculated spectrum is given by the resonance line positions convoluted with a Lorentzian line exhibiting a line width which is proportional to the inverse spin-spin relaxation time $1/T_2$. In the fast-motion regime differing resonance line amplitudes especially at the high field resonance line position are evolving. In this case the spectral line shape is accurately described by Redfield theory [190] and the upcoming broadening of the line width is given by:

$$\frac{1}{T_2} = A_0 + A + Bm_I + Cm_I^2 \tag{2.50}$$

In the fast-motion regime the nuclear quantum number m_I is conditional for the line width. This results, in the case of a nitroxide (m_I= -1, 0, 1), in different line widths at the low and high magnetic field resonance position. Line broadening in response to motional averaging is described by A, B and C while A_0 characterizes parameters like unresolved hyperfine splitting or the natural line width.

To simulate spectra of the slow-motion regime a new formalism is introduced, since the perturbation theory based method is not able to describe the motional averaging properly. Underlying this method is the derivation of the expectation value $\bar{\rho}$ of the time dependent density matrix, which is used for spectra simulations. Solving the stochastic Liouville equation $\bar{\rho}$ can be determined [56].

In case of powder samples or frozen solutions the spin label is completely immobilized, τ>300ns, and the rigid limit is reached which leads to a time independent Hamiltonian. The spectrum is then referred to as powder spectrum which is described in 2.3.1.

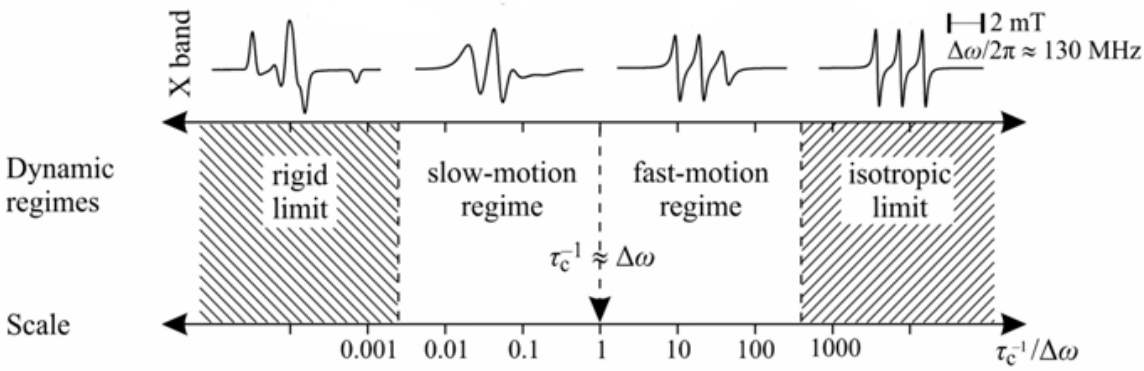

Figure 2.6: Different dynamical regimes of nitroxide cw EPR spectra at X-band frequencies characterized by τ and Δω. The ratio of the rotational correlation time and the spectral anisotropy τ^{-1}/ Δω defines the borders of the different regimes. Considering MTSSL at X-band frequencies Δω is dominated by the hyperfine anisotropy, with Δω/2π=130 MHz. The figure was adopted from [109].

2.3.4.2 Mobility parameters

From the reorientational motion of the spin label the effective correlation time is deduced which is strongly affected by a complex interaction with the secondary, tertiary and quaternary structure of the studied protein. To describe the different dynamic regimes of the MTSSL side chain exactly and in a quantitative manner simulations of EPR spectra are required. Nevertheless, two semi-emperical parameters of specific spectral features can be extracted from experimental acquired EPR spectra which give insight into the spin label side chain mobility. As depicted in figure 2.6 and 2.7 there is a direct relation between the line width of the central resonance line (m_I=0) and the correlation time which is increasing the spectral line width in response of a larger τ. In this context the resonance lines of the m_I= -1, 1 transitions (low and high field) also experience a distinct broadening. As a matter of fact, determination of the inverse line width of the central resonance line ($1/\Delta H_0$), represents a suitable method to gain a measure of spin label mobility [18, 134].

By calculating the spectrums inverse second moment ($1/\langle H^2 \rangle$) the supplementary appearing effect of distinct spectral broadening is taken into account. The inverse second moment is defined as:

$$\langle H^2 \rangle = \frac{\int (B - \langle H \rangle)^2 S(B) dB}{\int S(B) dB} \tag{2.51}$$

$$\langle H \rangle^2 = \frac{\int B S(B) dB}{\int S(B) dB} \tag{2.52}$$

In these equations B is the magnetic field strength and S(B) is the EPR absorption. Since the inverse line width overestimates mobile components in an EPR spectrum and the inverse second moment shows a similar issue considering immobile components these dimensions are at least questionable in their application on two component spectra. Therefore their utilization is recommended for single component spectra only.

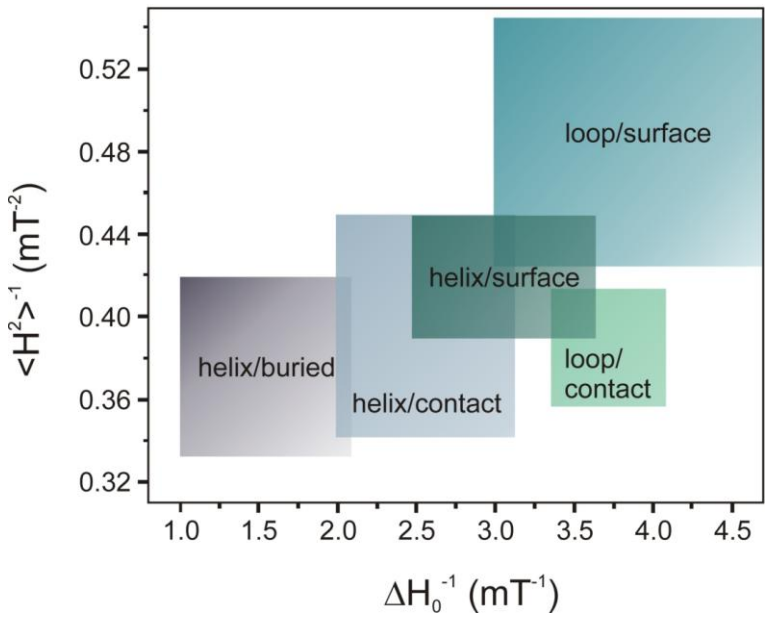

Figure 2.7: Classified side chain locations in reference to the protein structure. The inverse spectral second moment ($1/\langle H^2 \rangle$) is plotted versus the inverse central line width ($1/\Delta H_0$). The semi empirical parameters are calculated from cw X-band EPR spectra at room temperature. The picture was adapted from [18].

2.3.5 Cw EPR measurements at low temperature

Cw EPR measurements of frozen solutions at low temperatures (below 200 K) yield so called powder spectra (see 2.3.1 & 2.3.4.1) due to completely immobilized macromolecules and spin labels and their randomly distributed orientation in respect to the external magnetic field. The spectral shape based on such an experimental approach is especially governed, among other parameters, by dipole-dipole interactions between spin pairs. For instance distances between nitroxides below 2 nm result in a dipolar splitting which leads to a distance dependent line broadening (the dipole-dipole interaction is inversely proportional to the distance to the power of three, r^3) . Low temperature measurements also enable polarity measurements by observing the hyperfine splitting. This allows discrimination between spin labels in environments with polar or apolar character, for example spin labeled domains of proteins that are located in aqueous solution or in a lipid phase.

Very important parameters that depend on temperature are the longitudinal and transversal relaxation times. Since relaxation times decrease with increasing temperatures (see figure 2.8) it is only possible to study paramagnetic centers directly with very short spin-lattice relaxation times, e.g. some metal ions in metalloproteins like Co^{2+} (T_1~100 ps at 160 K), at very low temperatures. Otherwise a resulting EPR spectrum would be broadend until it would not be detectable anymore.

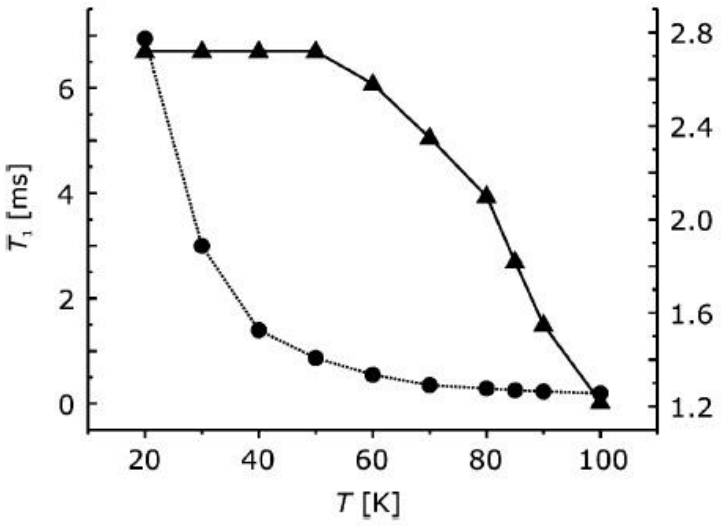

Figure 2.8: Temperature dependence of relaxation times for a sample of spin labeled plant light harvesting complex IIb. Longitudinal relaxation time T1 - left scale, dotted line, circles; transversal relaxation time T2 - right scale, solid line, triangles. The figure was adapted from [97].

2.3.6 Pulse EPR measurements

Apart from the variety of information that cw EPR provides, pulse EPR greatly increases the range of application for EPR spectroscopy. In contrast to cw EPR in pulse EPR experiments short microwave pulses (nano-second time scale) are applied on a sample within a constant external magnetic field. Various approaches of pulse EPR experiments (ENDOR, ESEEM, DEER, HYSCORE, etc.) enhanced the informative content that can be extracted out of a spin system [212]. Amidst the variety of pulse EPR techniques this work focuses on double electron-electron resonance (DEER) spectroscopy which yields distance distributions between dipolar coupled paramagnetic centers in a range of 2-8 nm. Especially for studying biological macromolecular systems this strategy is quiet convenient and yields information which helps to elucidate structure and conformational dynamics as well. The following chapter introduces shortly the DEER spectroscopy.

2.3.7 Double electron-electron spectroscopy

The origins of this pulse EPR spectroscopy were established with a 3-pulse-sequence (ELDOR-ESE – electron-electron double resonance – electron spin echo) by Milov and coworkers [135]. The DEER (double electron-electron spectroscopy) experiment which is based on a 4-pulse sequence was developed by Pannier et al. in 2000 and facilitates the determination of dipolar coupling frequencies of dipolar coupled spins, yielding information about the inter spin distance [153].

The principle behind this method is the selective excitation of two separated spin populations (spin A and spin B) with microwave pulses of different frequency. These distinct frequencies are labeled observer-frequency (v_o) and pump-frequency (v_p). The observer-frequency, corresponding the resonance frequency of spin A, is used to investigate the characteristics of this very spin population which depends on the polarization change of electron spin B induced by the pump-frequency. The effects of the dipolar coupling strength between the electron spin pair A and B are therefore observed by the characteristics of spin population A. The magnitude of the dipole-dipole interaction facilitates furthermore the determination of the distance between the electron spins. The separation of frequencies v_o and v_p is essential for a DEER experiment since applying a microwave pulse of finite length always develops a bandwidth of microwaves which induce energetic transitions. This bandwidth of exciting microwaves can be approximated by the inverse time interval $1/t_{pulse}$ of the

pump pulse. Accordingly the bandwidth of exciting frequencies increases with decreasing t_{pulse}. As a direct consequence the pulse duration and frequency offset $\Delta\nu=\nu_p-\nu_o$ must be organized in such a way that the electron spins A and B are specifically excited by the according resonance frequencies ν_o and ν_p. This requires the excitation of as much spins as possible simultaneously to optimize the signal intensity and increase the amount of excited coupled spins. The pump frequency ν_p is chosen from the EPR absorption spectrums maximum and the corresponding pump pulse is usually given a length of t_p=12 ns. For a nitroxide spin label in X-band observer pulses are set with a frequency offset of $\Delta\nu=\nu_p-\nu_o$=+65 MHz which typically corresponds to the low field maximum. The length of the observer pulse is normally put to t_o=32 ns. In Q-band measurements the pump pulse is also put on the nitroxide absorption maximum but the observer pulse is set with an offset of $\Delta\nu$ ranging from 80 MHz to 120 MHz in relation to the pump pulse (figure 2.9).

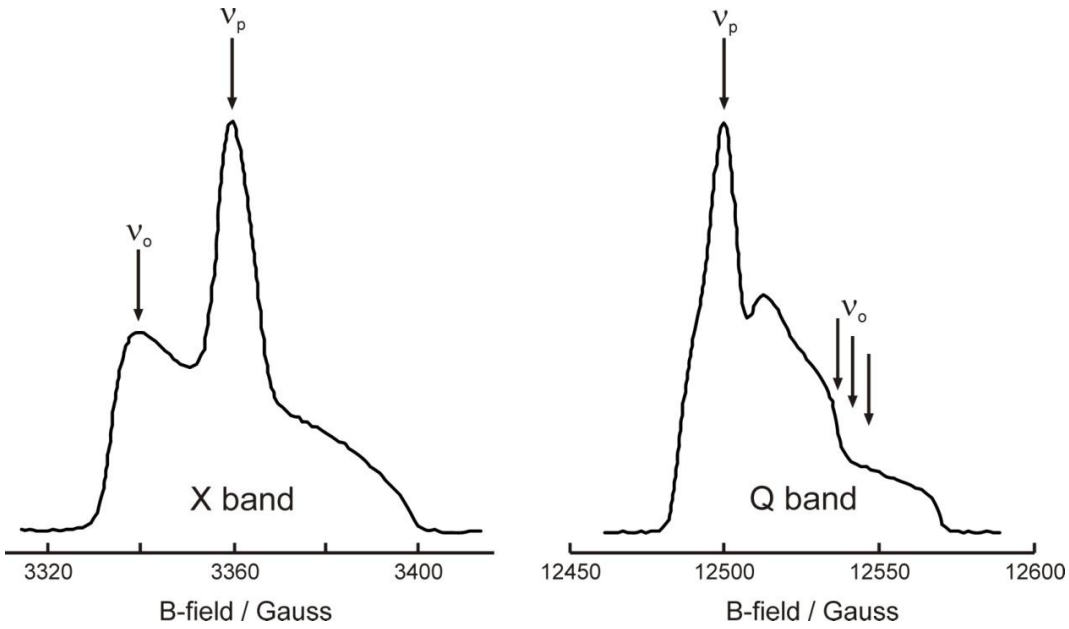

Figure 2.9: Excitation conditions for DEER of nitroxide spin pairs in X- and Q-band. The observer frequency ν_o and pump frequency ν_p positions are shown in the EPR absorption spectra (black trace) in X-and Q-band DEER. The π pulse lengths are typically t_o=32 ns for the observer pulse and t_p=12 ns for the pump pulse. The resonance condition (3.12) gives the relation between the magnetic field strength and the corresponding frequency. The figure was adapted from Polyhach and coworkers [160].

In the following the 4-pulse sequence of the DEER experiment is going to be explained (figure 2.10) which is advantageous in contrast to the 3-pulse sequence

because it is excluding a distinct dead-time. The first two pulses, π/2 and π, with the observer frequency v_o are separated by the delay time T_1. After the two pulses and the interval $2T_1$ a spin echo emerges, the so called Hahn-echo. Following the interval T_2 another π pulse with the frequency v_o is applied with the result that the echo of the spin population A, exhibiting the resonance frequency v_o, is refocused and detectable at time $2(T_1+T_2)$. Essential for the 4-pulse DEER sequence is the application of an additional π pulse at time t after the Hahn echo, the so called pump pulse. This pulse changes the polarization of spin population B by excitation with the microwave frequency v_p.

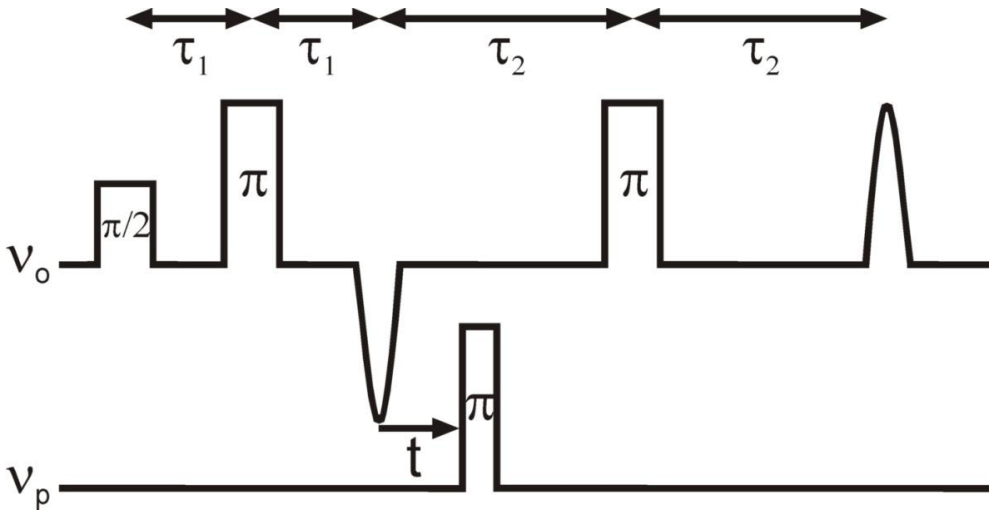

Figure 2.10: 4-pulse DEER spectroscopy. See text for details. The figure was adapted from Martin et al. [130].

A direct result of the pump pulse and the excitation of spin population B is a shift of the resonance frequency of spin population A that is dipolar coupled to population B. This shift adds up to ± $2\omega_{dipole\text{-}dipole}$, the dipolar frequency. Consequently, the amplitude of the echo at $2(\tau_1+\tau_2)$ is modulated as a function of the pump pulse position and the interval t, and yields the DEER signal V(t). This signal consists of the intra-molecular contribution $V^i(t)$, also called dipolar evolution function or form-factor F(t) which is modulated by ω_{dd}, and an un-modulated background contribution $V^b(t)$ (see figure 2.11).

$$\mathbf{V(t) = V^i(t)\, V^b(t) = F(t)\, V^b(t)} \qquad (2.53)$$

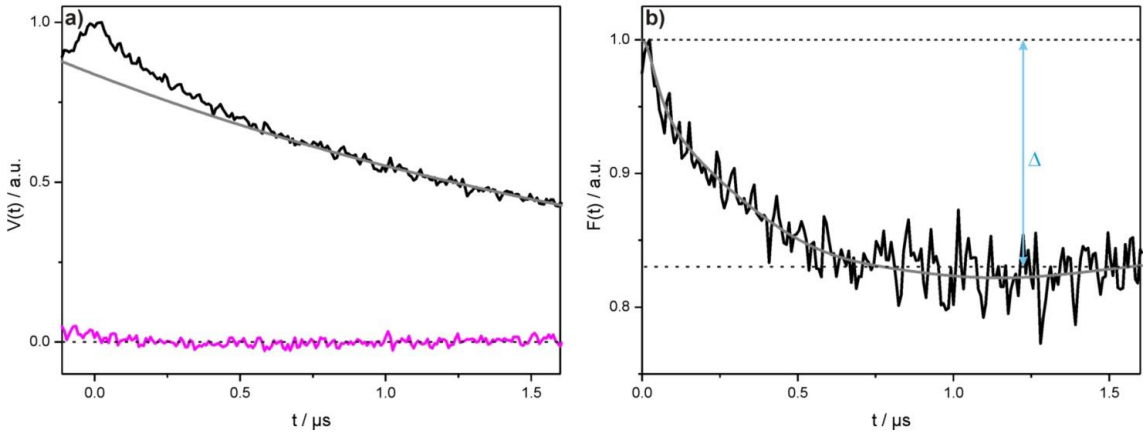

Figure 2.11: Processing DEER data. a) An experimental DEER spectrum (black line) consists of the intra-molecular contribution $V^i(t)$ and a background contribution $V^b(t)$. The simulated background contribution is depicted as gray line. The DEER experiment´s corresponding phase is highlighted as a magenta line. b) After background correction of the DEER signal the dipolar evolution function ($V^i(t)$) or form factor (F(t)) is obtained (black line). A simulated fit is indicated as gray line and the modulation depth Δ is depicted as blue line.

The background contribution originates from homogeneous distributed molecules featuring statistical inter spin distances r between each other. The $\omega_{dd}(r)$ which arise from these distances can be interpreted as a superposition which represents the background contribution and can be described in the form of an exponential decay:

$$V^b(t) = e^{-k^* t^{D/3}} \tag{2.54}$$

where k is given by:

$$k = \frac{8\pi^2 \mu_B^2 g_A g_B}{9\sqrt{3}\hbar} C\lambda \tag{2.55}$$

In this formula the spin concentration is given by C. λ is the percentage of spins excited by the pump pulse. The g factors of spin population A and B are given by g_a and g_b, respectively. D is the background dimensionality.

For calculation of the distance distribution from the intra-molecular contribution $V^i(t)$, the experimental DEER spectrum is first background-corrected by dividing it by the background contribution $V^b(t)$. The intensity of $V^i(t)$ is calculated by:

$$V^i(t) = 1 - \lambda(1 - \bar{V}^i(t)) \tag{2.56}$$

with

$$\bar{V}^i(t) = \cos(\omega_{dd} t) \tag{2.57}$$

$V^i(t)$ or F(t) is oscillating with ω_{dd}. The dipolar frequency ω_{dd} and the percentage of spins excited by the pump frequency ν_p affect the magnitude of the signals modulation depth Δ (see figure 2.11b).

$$\Delta = 1 - (1 - \lambda)^{N-1} \tag{2.58}$$

with N as number of interacting spins [98]. When the dipolar evolution function is processed further by a Fourier transformation the so called Pake pattern (see 2.2.6) is obtained, which allows the calculation of inter spin distances in terms of a distance distribution [129]. For analysis of DEER data the so called Tikhonov regularization is a generally used approach which is also utilized in the software DEER Analysis by Jeschke et al. and is applied in this work [96]. The Tikhonov regularization is based on a minimization of the function:

$$G_\alpha(P) = \|S(t) - D(t)\|^2 + \alpha \left\| \frac{d^2}{dr^2} P(r) \right\|^2 \tag{2.59}$$

The root mean square deviation of the simulated spectrum S(t) and the background corrected experimental DEER data D(t) is described by the first addend of equation 2.59. The second addend represents the square norm of the second derivative of P(r) weighted by the regularization parameter α. The smoothness of the distance distribution is determined by this second term. The simulated spectrum is calculated as followed:

$$S(t) = \int K(t,r)P(r)dr \tag{2.61}$$

All functions K(t,r), which oscillate with the dipolar frequency ω_{dd} influenced by the respective inter spin distances r, are superimposed and form S(t). K(t,r) is called Kernel-function and is described as:

$$K(t,r) = \int_0^{\pi/2} \cos(\omega_{dd}(\Theta_{\mathrm{dd}})\mathrm{t})\, \mathrm{d}\Theta_{\mathrm{dd}} \tag{2.62}$$

Since the dipolar frequency ω_{dd} is conditional on the dipolar angle Θ_{dd} all angles 0 to π/2 are integrated to include randomly distributed molecules. Moreover the pump efficiency λ also depends on the ω_{dd} and the excitation bandwith σ_{exc} of the entire DEER experiment. At distances below 2 nm equation 2.62 has to be expanded,

$$K(t,r) = \int_0^{\pi/2} \exp\left(-\frac{\omega_{dd}^2}{\sigma_{\mathrm{exc}}^2}\right) \cos(\omega_{dd}(\Theta_{\mathrm{dd}})\mathrm{t})\, \mathrm{d}\Theta_{\mathrm{dd}} \tag{2.63}$$

This is a consequence of the phenomenon that an inversion of spin B changes the resonance frequency of spin A by $2\omega_{dd}$. Therefore the following echo only occurs if both fractions of the dipolar coupled spin populations are affected within the excitation range of the refocusing pulse. As a consequence the detection of smaller distances requires a larger bandwidth.

Tikhonov regularization accomplishes a compromise between smoothness and the resolution of the distance distribution P(r) by computing the regularization parameter α. An appropriate regularization parameter can be identified from the so called L-curve. The L-curve is a plot of $\|S(t) - D(t)\|^2$ versus $\left\|\frac{d^2}{dr^2}P(r)\right\|^2$ giving the most suitable value for α at the knee of the curve which is consistent with the compromise between smoothness and resolution [96].

3. Materials and Methods

3.1 Sample preparations and biochemical procedures

3.1.1 Characterized variants of bovine serum albumin

Bovine serum albumin (BSA) samples investigated in this study were spin labeled at the protein´s single native cysteine residue at position 34 in accordance to the method described in the section below.

3.1.1.1 Spin labeling of BSA

BSA solution (100 µM) was prepared from lyophilized protein powder (Sigma-Aldrich) solubilised in Tris/HCl buffer (10 mM, pH 6.8). Spin labelling was accomplished by incubating the protein solution for 48 h at 37°C with a 10-fold molar excess of IAA spin label. Unbound IAA was removed by repeated dilution steps with Tris/HCL buffer (10 mM, pH6.8) utilizing Amicon® ultra centrifugal filters with MWCO 30K (Merck Millipore). In this last step spin labeled protein was concentrated as well. Protein concentration was determined by UV-Vis spectroscopy (ε_{BSA} = 43824 $M^{-1}cm^{-1}$ at 280 nm).

Labeling efficiency (IAA spin label concentration per protein concentration) for each sample was determined by comparison with a reference spin probe (OH-TEMPO, 100 µM).

3.1.2 Characterized variants of the histidine ABC-type transporter $HisQMP_2$ and the substrate binding protein HisJ

Studied spin labeled variants of the histidine ABC-type transporter $HisQMP_2$ and the substrate binding protein HisJ were purified and prepared by the workgroup of Professor Dr. Erwin Schneider (Humboldt-University of Berlin, Germany) in accordance to methods described in the literature [189].

3.1.3 Characterized variants of the biotin ECF-type transporter BioMNY

Studied spin labeled variants of the biotin ECF-type transporter BioMNY were purified and prepared by the workgroup of Professor Dr. Thomas Eitinger (Humboldt-

University of Berlin, Germany) in accordance to methods described in the literature [51].

3.1.4 Characterized variants of the cobalt ECF-type transporter CbiMNQO

Studied spin labeled variants of the cobalt ECF-type transporter CbiMNQO were purified and prepared by the workgroup of Professor Dr. Thomas Eitinger (Humboldt-University of Berlin, Germany).

3.1.5 Characterized variants of α-synuclein

The mutants of α-synuclein (α-syn) prepared and tested in this study were made available in *Escherichia coli* BL21(DE3) strains. The wild type human α-syn gene, extended with a N-terminal histidine-tag (10 histidine residues) and a factor Xa restriction site in between the tag and the gene, was cloned into the pET28a plasmid and is regulated by a T7 promoter. The according plasmid, its respective map is depicted in figure 3.1, was prepared and purchased from life technologies™.

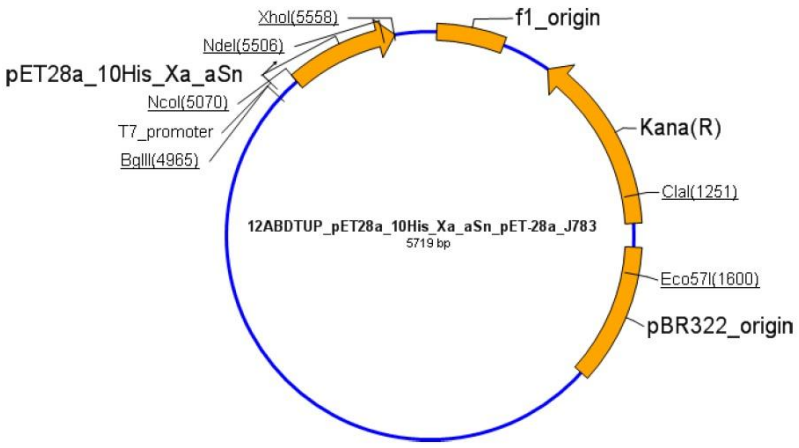

Figure 3.1: Plasmid map of of the α-syn expression plasmid. The vector pET28a_10His_Xa_aSn has a size of 5719 base pairs. The incorporated recombinant α-syn gene including a N-terminal histidine tag has size of 494 base pairs.

A specific single mutant at position V74, a cysteine substitution, was incorporated into the gene sequence by site-directed mutagenesis. The corresponding expression plasmids were present in $_{dd}H_2O$ or Tris/HCl buffer(10 mM, pH 7.0) or in the according bacterial strain *E. coli* BL21(DE3) in a glycerol culture (87%), which were stored at -

80 °C. Table 3.1 lists the bacterial strains, table 3.2 lists the plasmids and table 3.3 lists the primers utilized in this study.

Table 3.1: Utilized *E. coli* strains.

Bacterial strain	Genotype	Reference of source
E. coli BL21(DE3)	*fhuA2 [lon] ompT gal (λ DE3) [dcm] ΔhsdS λ DE3=λ sBamHIo ΔEcoRI-B int::(lacI::PlacUV5::T7 gene1) i21 Δnin5*	*New England Biolabs®*

Table 3.2: Utilized plasmids.

Name	Function	Reference of source
pET28a_10His_Xa_aSn	Expression plasmid Ka^R	life technologies™
pET28a_10His_Xa_aSn V74C	Expression plasmid Ka^R	this study

3.1.5.1 Site-directed mutagenesis

Site-directed mutagenesis on the expression plasmid pET28a_10His_Xa_aSn encoding for histidine tagged α-ysn (see table 3.2) was accomplished by utilizing the Phusion site-directed mutagenesis kit (Thermo Fisher Scientific). Forward and reverse primers to insert a cysteine point mutation in α-syn at position 74 are listed in table 3.3. Polymerase chain reaction (PCR) was performed in a PCR Sprint Thermal Cycler (Thermo Fisher Scientific). The according PCR sequence is listed in table 3.4. PCR products are ligated by utilizing the ligation protocol of the Phusion site-directed mutagenesis kit (Thermo Fisher Scientific). PCR products were detected by gel electrophoresis and compared to a 1 kb DNA ladder standard (New England BioLabs® Inc.) in a 1% agarose gel (figure 3.2). Modified

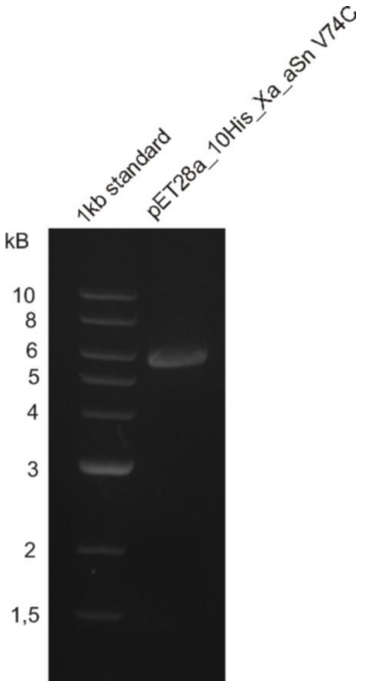

Figure 3.2: Gel electrophoresis of PCR product α-syn expression plasmid. 1kB DNA standard (left row) in comparison to the PCr product of pET28a_10His_Xa_aSN V74C (right row) loaded on a 1% agarose gel.

plasmids were transformed into *E. coli* Bl21(DE3) in accordance to the method described in section 3.1.7. Transformed cells were checked via selection plates with kanamycin (0.05 mg/ml). Successfully transformed cell colonies were used for plasmid isolation as described in the according section below. Isolated plasmids were sequenced (Seqlab) to verify the validity of the site-directed mutagenesis/amino acid substitution.

Table 3.3: Utilized primers for cysteine substitution in α-syn.

Name	Function	Sequence 5'-3'	Length / aa	Temperature	Reference of source
V74C_Forward	V74C point mutation	GCA GTT GTT ACC GGT TGT ACC GCA GTT GCA C	31	65.7°C	eurofins
V74C_Reverse	V74C point mutation	ACC ACC AAC ATT GGT AAC CTG TTC TTT GGT TTT CTC GGC	39	66.6°C	eurofins

Table 3.4: PCR sequence for site-directed mutagenisis of α-syn V74C.

Step	Function	Temperature	Time	Cycles
1	initial denaturation	98°C	30 sec	1
2	denaturation	98°C	10 sec	25
	annealing	65.7°C	30 sec	
	extension	72°C	170 sec	
3	final extension	72°C	10 min	1

3.1.5.2 Transformation of *E. coli* BL21(DE3) with pet28a_10His_Xa_aSn, growth conditions and purification of α-syn

3.1.5.2.1 Tranformation

For the transformation of competent cells, 100 µl of *E. coli* Bl21(DE3) were admixed with 1 µl of plasmid DNA. After 30-60 min of incubation at 4°C., a heat shock occurred at 37°C for 30 s. After further 10-20 min incubation at 4 C., 900 µl of LB medium (table 3.5) were added to the cells and incubated for 60 min at 37°C. and 750 rpm in a thermocycler. 100 µl of the mixture are plated on a selection plate with kanamycin (0.05 mg/ml) and incubated at 37°C overnight.

Table 3.5: LB medium

LB medium	mass per 1000 ml
tryptone	10 g
yeast extract	5 g
NaCl	10 g

3.1.5.2.2 Plasmid DNA isolation

For isolation of plasmids out of bacterial cells, 5 ml of *E. coli* overnight cultures, grown in LB medium with kanamycin (0.1 mg/ml), and the QIAprep® Spin Miniprep Kit (Qiagen, Hilden) were used. Plasmid isolation was carried out according to the manufacturer's instructions. The plasmid DNA was eluted with 30 µl of sterile $_{dd}H_2O$ or Tris/HCl buffer (10 mM, pH 7).

3.1.5.2.3 Cultivation of transformed *E. coli* cells

For the cultivation of the transformed *E. coli* cells a pre-culture is prepared in advance. The *E. coli* cultures transformed with the corresponding vectors were incubated in 100-200 ml of LB medium with kanamycin (0.1 mg/ml) at 37 °C and 155 rpm overnight. To store a culture 85 µl of sterile glycerin were added to 15 µl of bacterial cell culture, frozen in liquid nitrogen and stored at -80 °C. 1 l LB medium containing kanamycin (0.1 mg/ml) is seeded with the pre-culture to an optical density of OD_{600}=0.1 and incubated at 37 °C and 155 rpm. The culture is incubated for 4 h or until the optical density reaches OD_{600}=0.5-0.7.

3.1.5.2.4 Induction

At an optical density of OD_{600}=0.5-0.7 α-syn expression was induced with IPTG (0.238 mg/ml). For the highest possible protein expression, the induced bacterial culture was incubated for 4 h at 37 °C and 155 rpm.

3.1.5.2.5 Cell harvesting, cell disrpution and extraction of the protein fraction

Cell harvesting is carried out by centrifugation for 20 min at 4 °C and 5000 rpm (SLA 3000 rotor, Sorvall). The cell pellet is either stored at -20 °C or directly resuspended in buffer (10 mM Tris/HCl, 1 mM EDTA, 1mM PMSF, pH8). Resuspended cells are

disrupted by sonification (Sonifier: 20% power, output 20%, duty cycle 20-30%, micro tip limit 7). The resulting cell suspension is heated to 80 C for 10-20 min to denature and precipitate cellular proteins other then the IDP α-syn. Cell debris is removed by centrifugation for 20 min at 4 °C and 13500 rpm (SS34 rotor, Sorvall). Further purification of the supernatant is done by Ni-NTA affinity chromatography.

3.1.5.2.6 Ni-NTA affinity chromatography

For purification of the histidine-tagged α-syn Ni-NTA affinity chromatography was executed utilizing HisTrap FF columns (GE Healthcare Life Sciences). The pump system is pre-washed with 50-100 ml $_{dd}H_2O$ (flowrate 4-5 ml/min) and connected air-free to the Ni-NTA column. The column is washed (flowrate 1-5 ml/min) with a fivefold excess $_{dd}H_2O$ of the column´s volume and equilibrated (flowrate 1-5 ml/min) afterwards with a fivefold excess of washing buffer (10 mM Tris/HCl, 10 mM imidazol, 0.5 mM PMSF). The sample is loaded onto the column (flowrate 1 ml/min) and the flowthrough is collected for SDS-PAGE. The column is then washed with a tenfold excess of the column volume with washing buffer and the flowthrough (wash fraction) is collected for SDS-PAGE. The protein is eluted with increasing concentrations (4%, 10%, 50%, 100%) of imidazol elution buffer (10 mM Tris/HCl, 250 mM imidazol, 0.5 mM PMSF; 250 mM imidazol corresponds to 100% elution buffer). Fractions of protein eluted with 4% and 10% elution buffer were collected to 10 ml each. Fractions of protein eluted with 50% and 100% elution buffer were collected to 1 ml each. Protein is detected by SDS-PAGE, as depicted in figure 3.3, and the according fractions are pooled. Imidazol is washed out via Amicon® ultra centrifugal filters (MWCO 3K; Merck Millipore) with repeated steps of buffer exchange (20 mM Tris/HCL, 150 mM NaCl, pH 6.8). The protein concentration is determined with UV/VIS-spectroscopy at 214 nm. α-syn is then directly labeled with MTSSL or stored at -80 C.

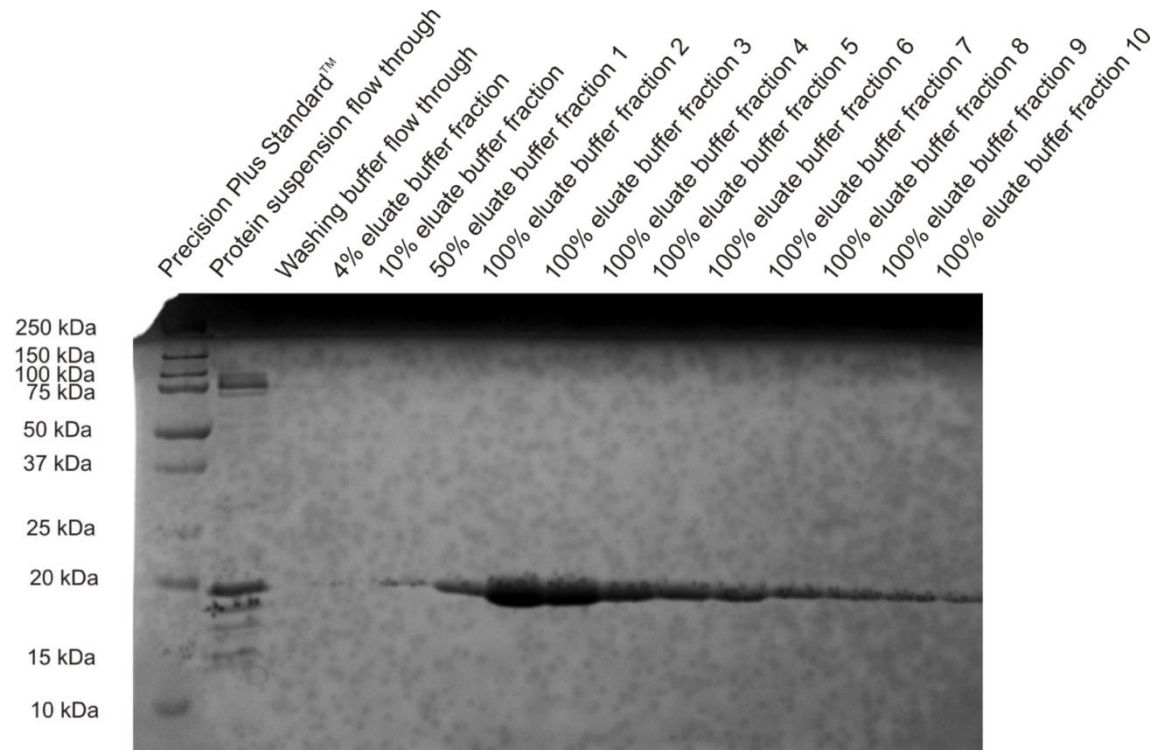

Figure 3.3: SDS PAGE of the elution profile of the expression of histidine tagged α-syn wild type. Fractions of eluted α-syn from Ni-NTA affinity chromatography. From left to right: 1. MW standard (Precision Plus Standard™), 2. protein suspension flow through, 3. Washing buffer flow through, 4. 4% eluate buffer fraction of Ni-NTA, 5. 10% eluate buffer fraction of Ni-NTA, 6. 50% eluate buffer fraction of Ni-NTA, 7-15. 100% eluate buffer fraction of Ni-NTA.

3.1.5.2.7 Spin labeling of α-syn and exclusion of aggregates

The specific cysteine residue which has been inserted into α-syn are labeled with a methanethiosulfonate spin label. Eluted fractions from the Ni-NTA affinity chromatography were pooled. DTT was added to the batch at a final concentration of 10 mM and incubated for about 1 h at 4°C. DTT was washed out via Zeba™ Spin desalting columns (MWCO 7K; Thermo Fisher Scientific) and buffer exchange (20 mM Tris/HCL, 150 mM NaCl, pH 6.8). 1 mM of MTSSL was added to the protein solution and incubated at 4°C for 4 h. The unbound free spin label was washed out via Zeba™ Spin desalting columns (MWCO 7K; Thermo Fisher Scientific) and buffer exchange (20 mM Tris/HCL, 150 mM NaCl, pH 6.8). Aggregated α-syn multimers were excluded from the monomeric α-syn fraction of the protein solution via Amicon® ultra centrifugal filters (MWCO 30K; Merck Millipore). Monomeric spin labeled α-syn was collected in the flow through fraction and the concentrated multimeric α-syn aggregate fraction was discarded. The monomeric α-syn fraction was concentrated

via Amicon® ultra centrifugal filters (MWCO 3K; Merck Millipore). Protein concentration was determined by UV-Vis spectroscopy ($\varepsilon_{\alpha\text{-synuclein}}$ = 238662 $M^{-1}cm^{-1}$ at 214 nm). Labeling efficiency (IAA spin label concentration per protein concentration) for each sample was determined by comparison with a reference spin probe (OH-TEMPO, 100 µM).

3.1.5.2.8 α-syn fibrillation protocol and "seeding" of spin labeled α-syn

Fibril growth of wild type α-syn was established under specific conditions. Protein solution was diluted to a final concentration of 150 µM. 500 µl were incubated at 37 C under constant agitation (stirring at >700 rpm) for 120 h. After α-syn aggregation the solution was centrifuged for 30 min at 4 C and 106000 g (SS0AT3 rotor, Sorvall). The gel-like pellet was washed/resuspended with buffer (20 mM Tris/HCL, 150 mM NaCl, pH 6.8) and centrifuged again 30 min at 4 °C at 106000 g. The supernatant was discarded. The pellet was resuspended in Tris/HCl buffer (20 mM Tris/HCL, 150 mM NaCl, pH 6.8).

Fibril growth and preparation of spin labeled α-syn was established equally but required an initial nucleation step which was induced by adding 5 µl of wild type α-syn fibril seed solution to the sample. Fibril seeds of wild type α-syn were prepared by disrupting respective fibrils by shear forces. This is accomplished by ultra sonification the α-syn fibril solution for 5 min.

3.1.6 SDS gel electrophoresis (SDS-PAGE)

Proteins were separated by means of SDS-polyacrylamide gels by the method of Schägger and Jagow. For SDS gel electrophoresis, 12% separating gels were used and 4% collecting gels (table 3.6). 10 µl of sample are mixed with 10 µl of 2xSDS sample buffer (table 3.7) and loaded onto the gel. In 1x SDS running buffer a voltage of 100 V is applied to the stacking gel and a voltage of 180 V is applied to the separating gel. As a protein standard the Precision Plus Protein™ standard (Biorad) was loaded onto the gel. A coomassie staining was used for the visualization and fixation of the protein bands in the SDS gel. The gels were incubated for 5 min in heated coomassie staining solution (table 3.8) and afterwards swayed in coomassie

destaining solution (table 3.8) until the gel background was almost completely decolorized.

Table 3.6: SDS gel composition

Reagents	4% collecting gel (~9 ml)	12% separating gel (~24 ml)
$_{dd}H_2O$	5.31 ml	6.36 ml
gel buffer (collecting gel: 4x Tris/HCl buffer pH 6.8; running buffer: 4x Tris/HCl buffer pH 8.8)	2.2 ml	6.6 ml
acrylamide (30%)	1.3 ml	10.6 ml
SDS (10%)	90 µl	0.24 ml
APS (10%)	60 µl	80 µl
TEMED	20 µl	20 µl

Table 3.7: 2x SDS sample buffer

2x SDS sample buffer
6% SDS
35% glycerol
120 mM Tris/HCl
0.41 M monothiolglycerol
0.05% bromphenol blue

Table 3.8: Coomassie staining and destaining solution

Coomassie staining solution	Coomassie destaining solution
0.1% coomassie R250	10% acetic acid ($C_2H_4O_2$)
10% acetic acid ($C_2H_4O_2$)	5% ethanol (C_2H_5O)
50% ethanol (C_2H_5O)	---

3.1.7 Protein concentration determination

Determination of protein concentration in this work was executed with UV/VIS-spectroscopy or with a BCA assay.

3.1.7.1 Fotometric protein concentration determination

In general the basis for the photometric determination of the concentration is the absorption of photons by proteins at a wavelength of 280 nm, since the aromatic amino acids tryptophan, tyrosine and slightly phenylalanine absorb light of this wavelength. The extinction coefficient is calculated by ProtParam (ExPASy) from the primary structure of the protein. Furthermore, the protein concentration of the samples is determined from the absorption A_{280} and the extinction coefficient ε by means of Lambert-Beers law (equation 3.1).

$$A_{280} = \varepsilon_{280} * c * d \qquad (3.1)$$

A_{280} is the absorption of the sample at 280 nm, ε_{280} is the molar extinction coefficient at 280 nm, c stands for the concentration and d for the layer thickness of the measuring cuvette. The extinction coefficient of BSA calculated by ProtParam is ε_{280}=43824 $M^{-1}cm^{-1}$. The absorption spectra of BSA were recorded in a wavelength range of 250-320 nm.

Since α-syn does not possess any aromatic amino acids like tryptophane the fotometric determination of the protein concentration was obtained by measuring at a wavelength of 214 nm. The molar extinction coefficient of the protein at 214 nm has to be calculated as described in the literature [110]. The extinction coefficient of α-syn at 214 nm is ε_{214}~238662 $M^{-1}cm^{-1}$. The absorption spectra of α-syn were recorded in a wavelength range of 200-300 nm.

The measurements were carried out in a photometer (UV-2450 UV-Vis spectrophotometer, Shimadzu) with quartz glass cuvettes (0.1 cm, Hellma®Analytics).

3.1.7.2 BCA assay

Protein determination by means of BCA assays were carried out in this work with the ROTI®Quant Universal BCA test (Roth). Bovine serum albumin was selected as the reference for this analysis. By using different concentrations of the reference, a calibration series (1-2000 µg/ml) was prepared. The result of the BCA assay of the sample was compared to the reference to determine its corresponding protein concentration. The BCA assay was carried out according to the manufacturer's

instructions. Photometric measurements were made at 562 nm in a photometer (UV-2450 UV-VIS spectrophotometer, Shimadzu).

3.1.8 Thioflavin T assay

Amyloid fibril assembly was attested by the Thioflavin T assay. A Thioflavin T (ThT; Sigma-Aldrich) stock solution was prepared by adding 8 mg ThT to 10 mL Tris/HCl buffer (20 mM Tris/HCL, 150 mM NaCl, pH 6.8) and filtering through a 0.22 µm syringe filter (Roth). The stock solution was diluted with the Tris/HCl buffer (1 mL ThT stock solution to 50 mL buffer). Fluorescence spectra of ThT samples were measured in a LS55 fluorescence spectrometer (Perkin Elmer). As reference the fluorescence intensity of 1mL working solution was measured (excitation at 440 nm, slitwidth 5 nm; emission at 482 nm, slitwidth 10 nm; averaging over 60 s). As a control sample an aliquot of monomeric protein solution (5–10 µL) was added to the reference, stirred for 1 min, and the fluorescence intensity was measured over 60 s. These steps are repeated with 5–10 µL of the aggregated protein solution. A measured intensity above the control sample is indicative of amyloid fibrils.

3.2 Biophysical methods

3.2.1 EPR studies

3.2.1.1 Buffers for EPR studies

Buffer conditions for EPR studies on spin labeled protein variants are listed in table 3.9.

Table 3.9: Buffer conditions for EPR studies on different spin labeled protein variants.

Protein	Buffer
α-synuclein	20 mM Tris/HCL, 150 mM NaCl, pH 6.8
BSA	10 mM Tris/HCL, pH6.8
BioMNY	20 mM Tris/HCL, 100 mM NaCl, pH 7.4
CbiMN	100 mM Tris/HCl, 300 mM NaCl, 0.05 % Dodecyl-x,D-Maltopyranosid, pH 8.0
$HisQMP_2$ / HisJ	50 mM MOPS/KOH, pH 7.5

3.2.1.2 Cw EPR spectroscopy at room temperature

The cw EPR spectra were recorded with a Varian spectrometer (Standard E-109, X-band) utilizing the dielectric resonator ER 4118X-MD5(-W1) (Bruker Biospin). A microwave power of 0.5 mW and a B-field modulation amplitude of 0.15 mT were used for the measurements. Samples (volume 20 µl) were transferred into EPR glass capillaries (0.9 mm inner diameter). The efficiency of spin labeling was derived from the recorded spectra and the determined protein concentration. For this purpose the concentration of the spin-labeled proteins was derived from double integration the spectra and comparison with that of a standard. The label efficiency a is calculated as

$$a = \frac{c_{spin\ labeled\ protein}}{c_{protein\ total}} \tag{3.2}$$

3.2.1.3 Cw EPR spectroscopy at low temperature

3.2.1.3.1 Cw measurements at 160 K

Inter-spin distances within 0.8-2 nm were determined using a cw-EPR spectrometer. The spectrometer has a rectangular resonator (AEG H103, AEG, Berlin, Germany) as well as a RMN 2 B-field meter (Drusch, Québec, France) for measuring the magnetic field. In order to ensure a constant temperature of 160 K of the sample, a temperature control unit (ITC 4; Oxford Instruments) with a cryostat Oxford ESR900 (Oxford Instruments, Oxfordshire, UK) is used. A microwave power of 0.2 mW and a magnetic field modulation of 0.25 mT were used for the measurements. The sample volume of 40 µl was applied for measurement in an EPR quartz capillary (3 mm inner diameter). Fitting of simulated EPR spectra to the experimental ones recorded at 160 K was performed in the Dipfit program [195].

3.2.1.3.2 Cw measurements at 10 K

Cw measurements at a constant temperature of 10 K at X band frequency were accomplished with a Bruker Elexsys 580 spectrometer. The ER 4118X-MD5 (-W1) resonator (Bruker, Rheinstetten, Germany) was used as resonator. An Oxford

temperature control unit ITC 503S controls a continuous helium flow through a cryostat ESR900 (Oxford Instruments). A microwave power of 0.007 mW and a magnetic field modulation of 0.5 mT was used for the measurement. The sample volume of 40 µl was applied for measurement in an EPR quartz capillary (3 mm inner diameter). Simulation and respective fitting of the EPR powder spectra recorded at 10 K was performed with the Easyspin toolbox [196].

3.2.1.4 Cw EPR spectroscopy at high pressure conditions

3.2.1.4.1 The high-pressure resisting sample cell

To establish a combination of variable hydrostatic pressure and SDSL-EPR the typical setup of cw EPR experiments has to be expanded by pressure resistant sample capillaries and a high pressure generating unit. Two different types of high-pressure sample cells were developed for SDSL-EPR purposes. The first approach requires the self-fabrication of the cell from PTFE-coated silica capillary tubing, with an appropriate ratio of inner to outer diameter to resist high pressure (1ID:3OD). This strategy was described by McCoy and Hubble for EPR measurements [133] and previously by Pfund and co-workers for NMR spectroscopy [157]. Due to the small sample volume within the unprepared capillary, which is not sufficient for detection in X-band EPR, it must be shaped into a bundle of several repeating loops that adds up to a total inner volume of 12-16 µl of the capillary (including the connection to high pressure generating system, which can vary in length). Because this

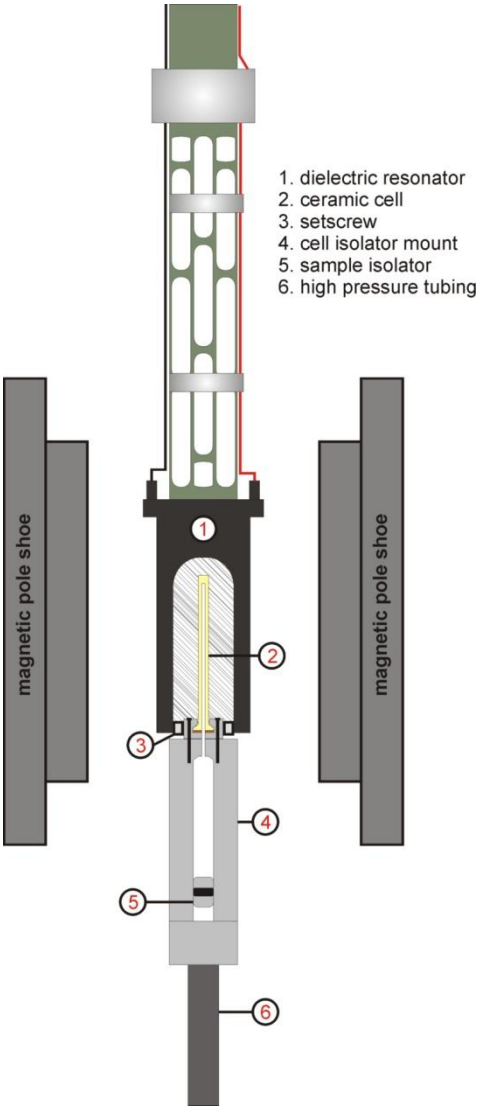

Figure 3.4: The ceramic pressure cell and the dielectric resonator. Schematic representation of the assembly/introduction of the high-pressure resistant sample cell within the EPR spectrometer resonator.

technique still provides only a small sample volume (<2 µl) in the resonator´s sensitive area a relative high sample concentration (~500 µM) is a necessity. Utilizing micro-resonators could be a promising approach to simplify this method. The pressure maximum that can be reached with this kind of folded silica capillary is approximately at 4 kbar. Since this strategy is not applied in this work it will not be considered in further detail. The high-pressure cell of choice within this work is the yttria-stabilized zirconia ceramic cell (HUB440-Cer) developed for X-band SDSL-EPR by Pressure BioSciences, Inc. [116]. The dielectric resonator ER 4118X-MD5 (-W1) (Bruker Biospin) is customized with a setscrew to support the requirements of the HUB440-Cer ceramic cell. Figure 3.4 depicts the experimental setup of the high-pressure ceramic cell introduced in the dielectric resonator. The ceramic cell´s setup is depicted in figure 3.5a and 3.5b.

The ceramic pressure cell provides a total sample volume of 19 µl with approximately 5 µl in the resonator´s sensitive area, which requires again a relative high sample concentration (>200 µM) for a sufficient sample-to-noise ratio. The pressure maximum that is accomplishable with this cell is 2.4 kbar. A metal cell isolator mount serves as base for attachment of the ceramic cell with a polyimide disc as gasket at the mount/cell-interface. The cell isolator mount is used moreover to connect the ceramic cell with the pressure generating unit. To separate the sample from the pressurization fluid within the generating unit a small isolator device is introduced into the metal mount (figure 3.5b). As depicted in figure 3.5c the ceramic cell exhibits a broad EPR signal in the same magnetic field region like nitroxide signals. The pressure independent signal of the cell, which originates from paramagnetic inclusions [191], is subtracted after data recording.

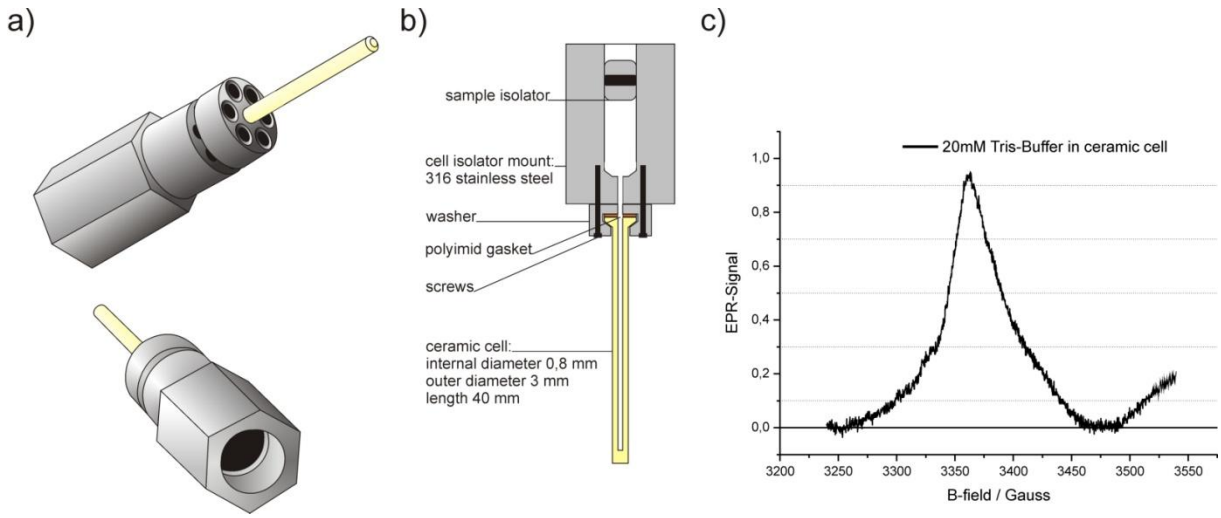

Figure 3.5: Pressure resistant cell for cw EPR purposes. a) Schematic depiction of the Yttria-stabilized zirconia ceramic cell (HUB440-Cer) and attachment to the metal cell isolator mount. **b)** Side view on the ceramic cell assembly. c) EPR spectrum of 20 mM Tris/HCl buffer in ceramic cell at atmospheric pressure. The ceramic cell´s EPR signal gives a g factor of ~1.994 corresponding to the signal maximum.

3.2.1.4.2 The pressure generating unit

Various pressure generating systems suiting the needs for bio-macromolecular studies are available commercially and can be categorized into syringe-like pump systems, which transmit pressure changes through uncompressible high-pressure fluids, and air-operated pressure intensifiers. In this work a hand pump with spindle drive from NOVA SWISS®, suited for smaller high-pressure applications and independent of a compressed air or electrical power supply, is utilized and schematically depicted in figure 3.6. Static pressure can be adjusted precisely up to a maximum of 4000 bar with the systems fine-thread, non-rotating spindle. Operation of the pump is facilitated by three propelling levers. The pressure detection unit is located directly after the spindle utilizing a gauge pressure sensor (Burster® tip sensor) that converts pressure values into voltage which are readout accordingly by an electronic manometer (Newport® manometer). A high quality hydraulic oil (LiquiMoly® ATF TopTec 1100) is used as high-pressure fluid. A separator is introduced between the pressurization fluid and the sample as mentioned in the description of the ceramic sample cell to eliminate diffusion between the two media. High-pressure tubing and fittings (NOVA SWISS® CRS-70-4E for 7000 bar) connect the pump system with the metal mount of the pressure resistant ceramic cell.

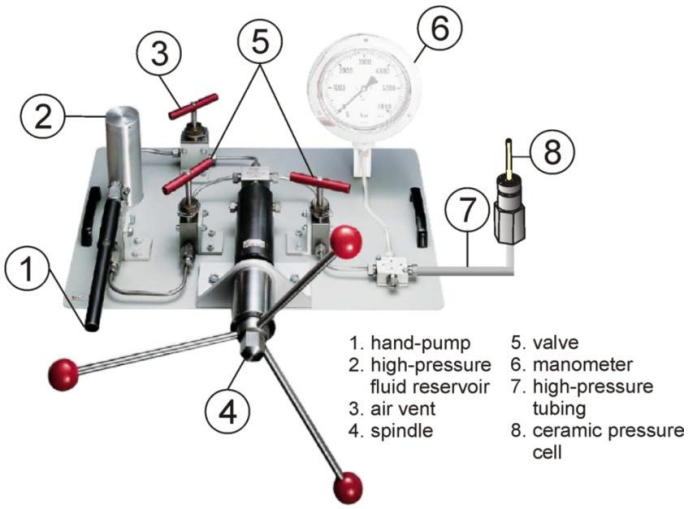

Figure 3.6: A pressure generating system for static high-pressure EPR experiments. Schematic of the pressure pump connected to the pressure resistant ceramic cell.

3.2.2 Double electron electron resonance (DEER) spectroscopy

The double electron-electron resonance (DEER) spectroscopy experiments were carried out in the X-band (9.3-9.4 GHz) or in the Q-band frequency (33-50 GHz) range with a Bruker Elexsys 580 spectrometer. A Bruker Flexline split ring ER 4118X-MS3 resonator was used. An Oxford temperature control unit ITC 503S controlled a continuous helium flow over a cryostat ESR900 (Oxford Instruments). The four pulse DEER sequences formed the basis for the measurements: $\pi/2(\nu_{obs})$-π_1-$\pi(\nu_{obs})$-t'-$\pi(\nu_{pump})$-(τ_1+τ_2-t') τ_2-echo. The <x> channels were used for the DEER pulses at the observer frequency, with a two-stage "phase-cycling" (+<x>; -<x>) being performed with respect to $\pi/2(\nu_{obs})$. The time t' was varied, while τ_1 and τ_2 were kept constant. The dipolar development time (dipolar evolution time) resulted from t = t'-τ_1 and was evaluated only for the case t>0. The resonator was overcoupled with Q<100. The pump frequency ν_{pump} was adjusted to the frequency of the center of the resonant dips and matched with the maximum of the nitroxide EPR spectrum according to the respective frequency regime, X- or Q-band.

All measurements were carried out at a constant temperature of 50 K. The length of the observer pulses for $\pi/2$ was 16 ns and for π 32 ns, the length of the pump pulse was 12 ns at X-band and 16 ns at Q-band frequency. Proton modulations were averaged by increasing the τ_1 value starting at $\tau_{1,0}$=200 ns (X-band) or $\tau_{1,0}$=320 ns (Q-band) with a difference of 8 ns each eight times. The spectra were recorded with

one data point per 8 ns, the measurement time per sample being 24-48 h. The raw data were evaluated using the DEERAnalysis 2013 program [96].

3.2.3 Computational methods

3.2.3.1 Fitting of simulated continuous wave low temperature EPR spectra

Experimental dipolar broadened EPR powder spectra recorded at 160 K were simulated and fitted according to the method described by Steinhoff et al. [195]. It is assumed that the nitroxide orientation is randomly distributed, due to the flexibility of the spin label residue, with respect to the interspin distance. A Gaussian distribution of interspin distances is therefore applied to take the range of distances into account that arise from the various spin label orientations.
Within the fitting process, the g-tensor values (g_{xx}=2.0082, g_{yy}=2.0062, g_{zz}=2.0023), the A-tensor values of A_{xx} and A_{yy} (A_{xx}=0.52 mT, A_{yy}=0.45 mT), and the line width parameters were fixed with respect to values yielded from analysis of MTS spin labeld samples without indication of dipolar broadening. The A-tensor component A_{zz} was varied to comprehend different polarities of the nitroxide environment. The distance distribution was fixed to 0.5 nm. The average interspin distance and A_{zz} were permitted to vary with respect to the differing dipolar broadening of the respective protein variants and the different states.

3.2.3.2 EPR spectra analysis by Easy spin

Cw EPR spectra of Co^{2+} ions obtained at 10 K were computed by the MATLAB toolbox EasySpin [196] and its implemented function ‘pepper‘ for calculation of field – swept solid state cw EPR spectra for powders, frozen solutions and crystals. Simulations were carried out assuming a low spin configuration (S=1/2) for the Co^{2+} ions and a ^{59}Co nucleus with a nuclear spin of I=7/2.

3.2.3.3 Rotamer library analysis

The rotamer library analysis approach allows attachment of a conformational distribution of the nitroxide residues at any chosen site in a protein´s three dimensional structure. This application is facilitated by a library of pre-calculated

rotamer ensembles. The respective position in the protein´s structure is superimposed with the spin label backbone atoms. This provides the nitroxide side chain orientation in dependence of the protein structure and yields the energy of the nitroxide-protein interaction calculated from Lennard Jones potential. Boltzmann weighting and normalization by the partition function provides the probability for each rotamer. Subsequently this probability is multiplied by the probability of the nitroxide side chain to occupy each conformation which results in the distribution of rotamer probability at the position of choice. By attaching such rotamer probability ensembles at two sites in the protein a respective distance distribution covering the possible inter spin distances between the ensembles is calculated weighted by the product of their according probabilities. The rotamer library analysis was executed with the software package MMM (Multiscale Modeling of Macromolecules, version 2013) [159].

3.2.3.4 Fitting of simulated high pressure continuous wave EPR spectra

Fitting of simulated multicomponent cw EPR spectra to the experimental ones recorded at room temperature was performed with the MultiComponent simulation and fitting tool for nitroxide cw EPR line shapes provided by Christian Altenbach. Within the fitting process, the g-tensor values (g_{xx}=2.0099, g_{yy}=2.0063, g_{zz}=2.0025), and two of the A-tensor values (A_{xx}=0.73 mT, A_{yy}=0.60 mT) of both components were fixed with respect to values yielded from analysis of nitroxide spin labeled samples [13]. The A-tensor component A_{zz} was varied to comprehend different polarities of the nitroxide environment. The rate R of the spectral mobile component was simulated with an isotropic model while the immobile component was fitted assuming axially symmetric.

4. The influence of hydrostatic pressure on macromolecular entities

4.1 Introduction

The condensation of a polypeptide chain from its primary to the tertiary structure is a process of high complexity. In nature a natively folded protein can consist of many symmetrical structural elements while its initial point, a sequence of amino acids, seems to have a random character. Arrays of amino acids within the sequence have the tendency to self-organize into sequence-specific secondary structures. Further intra-molecular interactions and an entropic driving force, the so called hydrophobic effect, lead to the composition of the protein´s tertiary structure. Moreover, there are proteins that are distributed in many different species and which are almost non-distinguishable in structure and function, but they can vary to a high extent in their sequence. How do these sequences which seem to be apparently random form up to highly functional structures and how is this process regulated? Levinthal theorized that a protein is not able to reach its native conformation by searching randomly the huge variety of possible conformations. He therefore postulated that there must be a kinetically controlled distinct path of folding which directs the protein to its functional native state [118]. The studies of Affinsen contradicted this theory by stating that there is no folding-route controlled by kinetics. The protein´s native state corresponds to its global minimum of free energy, where the folded state is thermodynamically most favored. This is the so called thermodynamic hypothesis of protein folding [10]. Various scientists contributed with their work to this two contradicting viewpoints until Onuchic, Wolynes, Dill and co-workers postulated the existence of a funnel-like model in which the proteins condensation is guided to the native state and does not depend on a specific pathway. The idea of a “folding funnel” is the current acknowledged model and was elaborately enhanced till today [115]. To understand the pathway and the folding process of a polypeptide a comprehensive knowledge about the protein´s energy surface is a necessity. A respective statistical energy landscape gives insight in the organization of ensembles of structural intermediates, which are occupied until the protein gains its native conformation. The energetics of the multiple folding pathways is summarized in the folding-funnel with the proteins low-energy native state at the bottom. The energy-funnel exhibits also additional local energy-minima, in which intermediate states of the protein can reside. According to

this a protein in the process of folding can follow several different routes down the funnel toward the native structure while it is trapped transiently in local energy minima on its way. Exactly the local minima which are only slightly higher in terms of free energy compared to the native state and that correspond to the intermediate states, seem to be essential for the understanding of the functional principle of proteins, no matter if those intermediates are on or off the pathway of folding. The protein´s function is often regulated by a minor change of its conformation which can be induced by chemical or physical triggers. A particular notion explains this mechanism as a result of an equilibrium of structural states which are differently populated dependent on their relative energies [126]. This chapter shall give a basic understanding how pressure as a thermodynamic entity can be used to investigate the structural folding and the equilibrium of conformational substates of proteins and multimeric protein compounds in connection with their volumetric properties [21, 70, 149]. Various authors have contributed to this theme by investigating a variety of polypeptide systems with high pressure which is known to perturb the conformational stability and equilibrium of proteins by disrupting hydrophobic interactions and elimination of water-excluded cavities [5, 187]. In this context it was postulated that pressure decreases the partial molar volume of a protein parallel to the decrease of its conformational order, exemplified by high pressure NMR experiments on ubiquitin and hen lysozyme [5]. In combination with EPR it was shown based on spin labeled T4 lysozyme that high pressure experiments can be utilized to demonstrate the equilibrium between spectrally resolved states, assigning these states to a conformational exchange or a rotameric exchange of the spin label, and to determine the partial molar volume and the isothermal compressibility of conformational substates from their equilibrium constant in the dependence of pressure [133]. In addition to studies on soluble monomeric proteins it was shown that protein aggregates, associated to neurodegenerative diseases, like amyloid fibrils of α-synuclein (α-syn) or transthyretin can be reversibly dissociated by high pressure [54]. Further, the mechanism which is responsible for the dissociation of α-syn fibrils into the protein´s monomeric form was elucidated, revealing that pressure forces water molecules into the hydrophobic core of the fibril and thereby releasing α-syn monomers [237].

4.1.1 The motivation and purpose of this of this work: High-pressure cw EPR on different soluble proteins and protein aggregates

Hydrostatic pressure perturbance has proven to be a versatile tool to investigate volumetric properties of proteins as well as their conformational equilibria and energy landscape of folding. However, a variety of strategies and questions can still be addressed in context of this technique and/or in connection with EPR spectroscopy. For instance, pressure could provide a possibility to study of spin label internal motion by determining the activation volume of side chains [133]. Furthermore, the difference between rotamer and conformational exchanges is difficult to determine and only distinguishable in favorable cases [133]. With this work we want to expand the understanding of the impact of pressure on protein complexes by investigations on three different soluble proteins as described below.

In order to establish hydrostatic high pressure experiments in combination with EPR spectroscopy, nitroxide spin label in aqueous solution was investigated to understand the influence of pressure on the corresponding spectrum. In this regard appropriate experimental conditions for studies on spin labeled polypeptides have been verified. In this work three different biological macromolecular systems are studied under high pressure conditions to elucidate the effects of pressure on protein folding, structure and flexibility. First, investigations on bovine serum albumin (BSA) and the histidine binding protein HisJ were done to demonstrate the EPR analysis and interpretation of the influence of variable hydrostatic pressure on proteins. Furthermore, we gained insight into the volumetric properties and into the conformational equilibria of these proteins. To our knowledge, no investigations of these proteins were done likewise to date. Second, the behavior of protein aggregates, amyloid fibrils of α-syn, under hydrostatic pressure was investigated to elucidate the wide spectrum of possible applications of the experimental approach in respect of not just soluble monomeric proteins but larger protein compounds, which are hardly examinable in a conventional way. It was demonstrated that polymeric protein structures, like amyloid fibrils produced from α-syn, can be resolved by hydrostatic high pressure [54, 237]. In this study we address the question how the conformational equilibrium between fibril formation and monomer changes in dependence of pressure and which volumetric changes result correspondingly. Further, we want to find out if high pressure has an impact not only on the amyloid fibrils but also on the soluble monomer of α-syn.

For the elucidation of structural changes of the above mentioned model systems upon pressurization, X-band EPR methods were applied that are explained in the materials and methods chapter. The upcoming paragraphs cover state of the art methods and knowledge as well as the utilized model systems.

4.1.2 Pressure in thermodynamics

In classical mechanics pressure is defined as the ratio of a force per surface unit which is applied perpendicular to a surface. It can also be described as a measure of a substance´s resistance against the decrease of the available volume. Pressure (p) in terms of a fundamental thermodynamic parameter has potential to perform work on a system and is conjugate to volume. Therefore, pressure can be understood as a measure of potential energy stored per unit volume, or as the ratio of the internal energy (U) with respect to the volume.

$$p = -\frac{dU}{dV} \tag{4.1}$$

Pressure is an integral component of different thermodynamic energy potentials as, e.g., the internal energy of a System (U), Enthalpy (H) or Gibbs free energy (G):

$$U = TdS - pV + \sum_i \mu_i N_i \tag{4.2}$$

$$H = U + pV \tag{4.3}$$

$$G = U + pV - TS \tag{4.4}$$

In the upper equations T corresponds to temperature, S is the entropy, V is the volume and N_i is the amount of particle i with the according chemical potential μ_i.

4.1.3 Pressure as a tool to investigate protein folding, structure and dynamics

Since a protein´s function is directly correlated to its structure and to its structural dynamics the respective information is increasingly valuable in structural genomics and of high interest. This includes not only the overall conformation and topology of a protein and its conformational sub-states but also its folding pathway, the connected changes in its energy-landscape and furthermore possible disorders in the condensation process. The investigation of these properties, especially the functionally relevant conformational sub-states, however, is quiet challenging. This is due to the fact that these conformational sub-states only make a minor, spectroscopically undetectable fraction in the overall ensemble of conformational states a protein exists at thermodynamic equilibrium. It appeared that hydrostatic pressure represents a feasible and unique tool to exploit the different conformational states and local energetic minima of a protein by shifting the equilibria. This is based on the phenomenon that high pressure perturbs macromolecules in solution such as proteins by a change of volume only [220]. Other methods which are used to probe intermediates between the fully folded and the fully unfolded structure and which perturb their tertiary structure like high temperature, pH or denaturing agents, are based on various changes within a sample and are therefore less reversible. High temperature for instance affects both the energy of the studied system and its volume. The effect of denaturing agents such as urea on the other hand is based on its binding characteristics. There is also no guarantee that the intermediate states stabilized under the influence of these methods match those which transiently develop in the process of folding in native environment. Consequently, emerging intermediates can match also those which are off the folding pathway but still hold an important functional role. The advantage of pressure perturbation above the other approaches is simply that it reverses the folding process without disturbing the system chemically. As a matter of fact, pressure perturbance can still be combined with other denaturing approaches, since for some proteins pressure alone is not sufficient to induce conformational sub-states or denaturation, due to only minor volume changes or a low compressibility of the protein [83, 186]. For example, high pressure is used for cold denaturation studies below a temperature of 0°C because pressure decreases the freezing point of water (-20°C at 2000 bar) [53].

Proteins in solution consist of an ensemble of fluctuating structural intermediate states, or simply conformers, that differ in volume and in their degree of organization

which are distributed over the entire energy-landscape. Pressurizing a polypeptide allows the trapping of these sub-ensembles by shifting of the equilibrium between the intermediate- and native conformation in favor of the former state (figure 4.1a). The increased level of the intermediate population makes spectroscopic detection often possible in the first place.

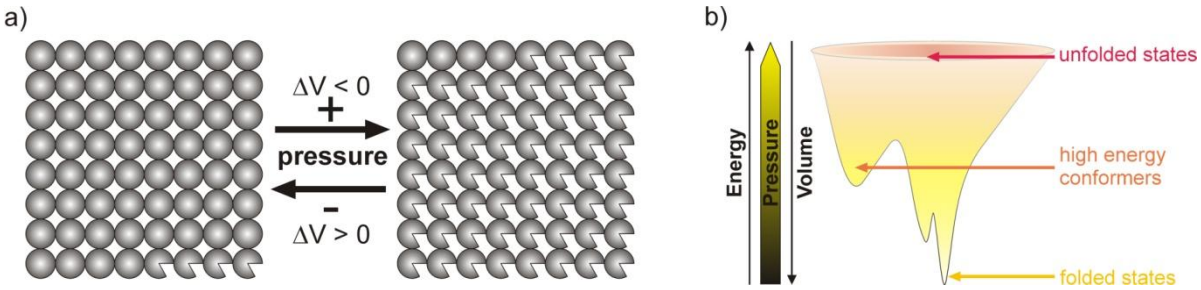

Figure 4.1:Schematical depiction of the influence of pressure on the energy landscape and the conformational equilibrium of proteins. a) Schematic representation of a shift in a proteins conformational equilibrium. The native state (N) changes upon pressurization in favor of a lower volume intermediate state (I). The figure was adapted and modified from [4]. b) Energy-Pressure-Volume relation in context of a proteins energy landscape. The proteins way of folding is associated to intermediate states of distinct energy and conformational order. Hydrostatic pressure can shift the equilibrium of conformational states towards higher energy conformers specifically [5].

At the same time a change of the Gibbs free energy emerges which corresponds the shift of the protein specific volume. Hence pressure perturbance can cause a shift in the population of conformational states in favor of states with a lower degree of order ranging from energetically higher lying conformers to a partially unfolded molten-globule state or even a completely unfolded state. The polypeptide´s energy landscape is determined by the vertical axis of the solvent-averaged conformational energy and the horizontal axis which parallels the conformational entropy (see figure 4.1b). Generally, the change of volume accounts only to a small percentage of a protein´s total specific volume (≤1.0%) upon complete unfolding [176]. In case of occupying an intermediate state the according change of volume tends to be even lower. A detailed consideration reveals that the fluctuation of a protein´s specific volume and the denaturation based on pressure perturbance depends on several effects [4, 5]. Hydration of hidden cavities in the protein interior is caused by the disruption of salt bridges and the loss of cavities always contributes negatively to the volume. Moreover polar and non-polar amino acid residues, which were formally

inaccessible, are subject to hydration. In terms of volume and hydration this pressure induced behavior contradicts the hydrophobic effect which normally drives the proteins way of folding. In this context the presence of water seems to play a crucial role in decreasing the stability of a protein, since pressure denaturation is not effective in the absence of water and several pressure induced conformers of varying proteins bind increasingly water [54, 55, 148]. This mechanism is schematically depicted in figure 4.2 and can be applied to soluble monomeric proteins, oligomeric protein compounds and protein aggregates like amyloid fibril structures [54, 187].

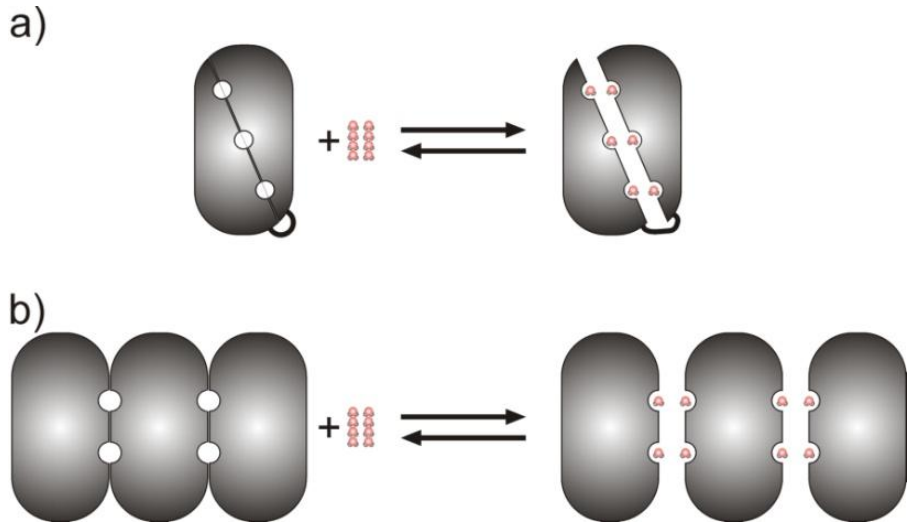

Figure 4.2: Effects of hydrostatic pressure on proteins in an aqueous environment. a) Pressurization can have a denaturing effect on proteins, due to the disruption of intra-molecular interactions, followed by the hydration of former hidden and now exposed cavities b) Dissociation of oligomeric protein structures. Water molecules are represented as red and gray spheres. The representation was adapted and modified from [187].

Additionally, packing defects within the natively folded structure can decrease the free volume due to compression of hydrogen bonds within secondary structures for instance. To determine these respective individual contributions to the volume changes in the conformational equilibrium of proteins in terms of quantity remains a challenge and needs further investigation [75]. A schematic example of the pressure effect is depicted in figure 4.3. Apomyoglobin is subject to a conformational shift originating from the protein´s native state and ranging from an intermediate-state over the molten-globule state to the unfolded state. The partial molar volume of a

protein decreases in parallel with its conformational order while pressure increases and it goes higher up the folding funnel [4].

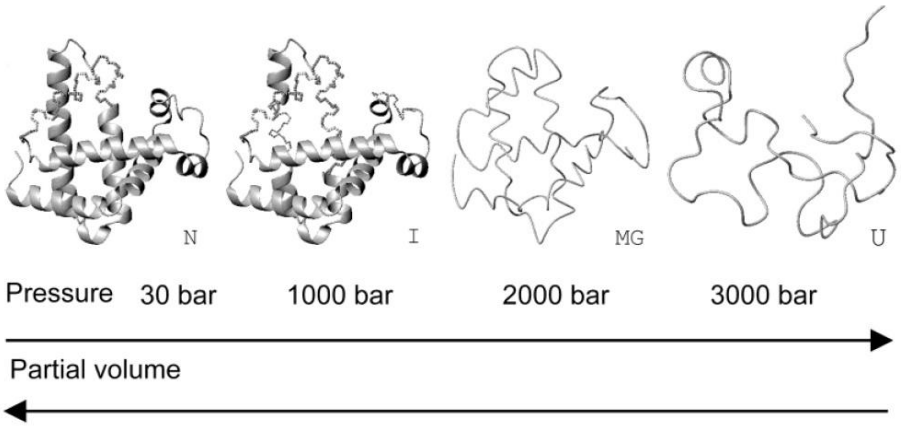

Figure 4.3: Major conformational subensembles found in apomyoglobin. N is the native state, I the locally unfolded, MG the molten globule, and U the fully unfolded subensemble. Qualitative structures of N and I are based on the structure of holomyoglobin with iron removed. Thin lines represent loop and disordered segments. Note that the conformational order and the order of volume are parallel to each other. The figure was adapted by Akasaka [4].

4.1.4 Thermodynamic effects of hydrostatic pressure on proteins

Focusing on volume changes for the population of intermediate states within a single sub-ensemble of conformers the protein´s volume is reduced by compression only. This effect is ruled by the isothermal compressibility coefficient $\beta_T=-(dV/dp)_T$, which is protein and furthermore conformer specific. Mean squared volume-fluctuation of a particle which is solvent-impenetrable is related to the compressibility [38]. Thus, a conformer´s volume fluctuation ∂V_{rms} is related to the compressibility as follows:

$$\partial V_{rms}^2 = \beta_T kT \qquad (4.5)$$

In this equation V defines the volume of the system, k is the Boltzmann´s constant and T is the absolute temperature. Hence, determination of β can also improve the information content about the overall structural dynamics of a macromolecule.

As already mentioned a protein in solution exists in an equilibrium mixture of sub-ensembles which differ in the thermodynamic energy state, partial molar volume and

degree of order. Therefore compression is accompanied by a shift in the equilibrium of differing conformers, depicted in figure 4.1a. The ratio between the intermediate state (I) and the native state (N) in dependence of pressure is given by the equilibrium constant K which is given by:

$$K = \frac{I}{N} = e^{(-\frac{\Delta G}{RT})} \tag{4.6}$$

with

$$\Delta G = G(I) - G(N) = \Delta G_0 + p\Delta V \tag{4.7}$$

with

$$p\Delta V = \Delta V_0(P - P_0) - \frac{1}{2}\Delta\beta_T V_0(P - P_0)^2 \tag{4.8}$$

The change of the Gibbs energy between N and I is given by ΔG and ΔG_0 with respect to the applied gauge pressure P and the atmospheric pressure P_0. The change of the partial molar volume is given by ΔV_0, which is either due to solvent entry into cavity volumes of one conformer but not the other [171], or an alternative packing of one conformer that occupies cavities with amino acid side chains [116]. $\Delta\beta_T$ is the change of the compressibility coefficient which becomes important at high pressure values due to the quadratic dependence of pressure in the second term. R is the gas constant while the absolute temperature is given by T. At ambient pressure and physiological conditions the native conformer N is normally more stable than the intermediate state ($\Delta G_0 > 0$). On the contrary and interestingly the term $p\Delta V$ is negative in most situations due to a negative ΔV for the majority of proteins under physiological conditions. This implies that the unfolded or intermediate states of a protein have a smaller partial molar volume in comparison to the completely folded state [176]. Hydrostatic pressure allows a reversible change of the equilibrium of sub-ensembles towards a population with a lesser degree of order or partial molar volume, respectively. By applying pressure the term $p\Delta V_0$, see equation (4.7), acts contrary the positive term ΔG_0 and may even compensate it, resulting in the reversal of the folding reaction. Analogous to that the Gibbs energy G_0 changes accordingly,

accompanied by a change in the equilibrium constant K, which results in a pressure-stabilized intermediate sub-ensemble.

Following equations 4.6-4.8), for the equilibrium between two states of a system, the ratio of the pressure-dependent equilibrium constant K(P) to that at atmospheric pressure K(0), is given to second order in pressure by [133]:

$$ln\frac{K(P)}{K(0)} = -\frac{\Delta V_0}{RT}(P) + \frac{\Delta\beta_T}{RT}(P)^2 \qquad (4.9)$$

with

$$\beta_T = -\left(\frac{\partial V}{\partial P}\right)_T \qquad (4.10)$$

Here the differences in partial molar volume and partial molar isothermal compressibility of the two states are given by ΔV_0 and $\Delta\beta_T$.

4.1.5 A combination of two powerful techniques: hydrostatic high pressure EPR and site-directed spin labeling

Over the years site-directed spin labeling (SDSL)-EPR has evolved to a powerful spectroscopic method which provides both detailed information of bio-molecular structures and dynamics in vitro and also in vivo. A variety of techniques are available, for instance with continuous wave (cw) spectral analysis leading the way and pulse-saturation recovery (sr) of site-specific incorporated spin-labels. In addition, interspin distance measurements between a pair of nitroxides in frozen state (at 50-150 K), for example by cw EPR or by the time resolved double electron-electron resonance (DEER) spectroscopy, allow further investigation and modeling of structural features and conformational dynamics. Up to the present day and next to NMR [5] and circular dichroism (CD)-spectroscopy [116], two EPR-methods, cw spectral analysis and DEER, have been combined with high pressure applications to monitor the influence of high pressure on spin labeled protein structure and dynamics [117].

The dynamics and the order of freedom of spin-labels introduced into a protein are encoded in the shape of the EPR spectrum with contributions from the proteins rotary

diffusion, side chain motions and backbone fluctuations. In X-band EPR spectroscopy (~9,5 GHz) the rotational correlation time (τ_R) of a nitroxide spin-label is reflected directly in the spectral lineshape additionally to lifetimes which determine the exchange between different states (τ_{ex}), which reside in the nano-second timescale (~1-100 ns). This range spans the time window in which protein motion can be investigated by cw EPR. It is most beneficial that fast backbone motions of proteins proceed in the nano-second regime which gives the opportunity to map the relative amplitude and rate of these dynamics by using sequence-dependent variations in the lineshape of the spin-label´s cw EPR spectra [33].

A nitroxide residue R1 located on the proteins surface or any other solvent accessible site, showing no interaction with its immediate macromolecular periphery, exhibits a single spectral component displaying its anisotropic movement with contributions from side chain and backbone fluctuations.

Induced by pressure a change in the label´s mobility may occur, which is reflected in a change of the rotational correlation time. To quantify the relationship between pressure and the spin label´s mobility two different models were established. The more simply approach considers the spin label side chain and the connected polypeptide area as one kinetic unit [133]. A more sophisticated model defines the R1 side chain movement and protein motions separately and is composed as follows in context of non-interacting helix surface sites which would result in a single component cw spectrum [117]. Rocking motions in a helical protein segment influence directly an attached nitroxide residue and, together with internal fluctuations of the label, the total reorientational correlation time (τ_t) is given by the correlation times τ_i (internal-motions) and τ_p (protein-motions):

$$\frac{1}{\tau_t} = \frac{1}{\tau_i} + \frac{1}{\tau_p} \tag{4.11}$$

McCoy and Hubbell [133] stated that the rates of the reorientational correlation times and pressure are correlated by the activation volume $\Delta V^{\ddagger}$ which determines the volume increase of a solvent cage that is needed to allow rotational motion of the nitroxide spin label [41].

$$ln\frac{\tau(p)}{\tau(0)} = \frac{\Delta V^{\ddagger}}{RT} * P \tag{4.12}$$

McCoy and Hubble [133] also stated that $\Delta V_i^{\ddagger}$, the activation volume of spin label side chain movement, depends on fluctuations of the label´s surrounding solvent cage and is most likely independent of its site. Therefore deviations of the slope in a plot of $\ln 1/\tau_p$ versus P for different sites originates from varying values of $\Delta V_p^{\ddagger}$, which in this case is associated to fluctuating local volumes and the compressibility, see equation 4.5. According to this the activation volumes of solvent-accessible helical sites at various pressure values give furthermore the possibility to map the different regions of a protein site-specifically in context of their relative compressibility [117].

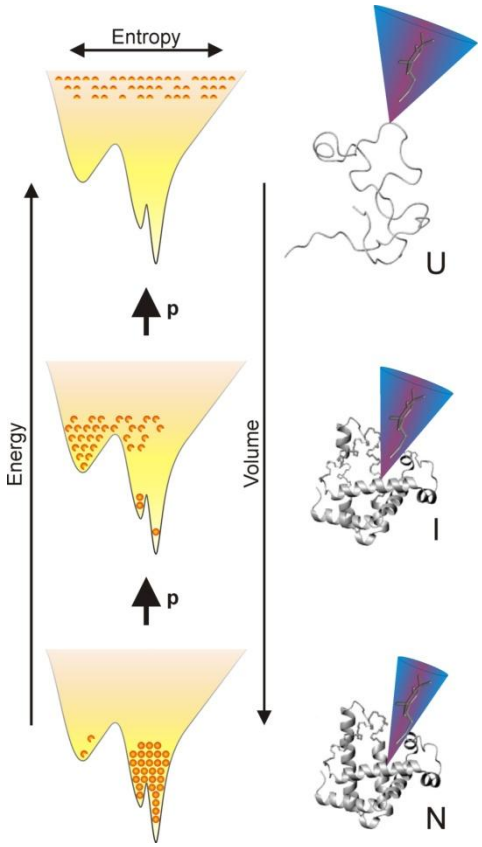

Figure 4.4: Schematic representation of pressure (p) dependent changes in a population distribution of conformers. Apomyoglobins energy landscape of folding is depicted with the vertical axis representing the conformational order (right axis) and the proteins internal energy plus the hydration free energy (left axis). The horizontal axis determines the proteins conformational entropy. The (ribbon models, gray) different conformational states (native – N; intermediate – I; unfolded – U) are arranged in order of decreasing conformational order and volume (N > I > U). According to the changing conformational order an attached spin label (blue cone) experiences a change in mobility (represented by the cones change in width).

Exchange of differing conformational states does not produce a direct impact in the spectral line-shape because the corresponding τ_{ex} exists in the µs to ms regime. The cw EPR spectrum still allows detection of a proteins conformational equilibrium by showing multiple spectral components. In the case of an EPR spectrum with more than one resolved component the spin label residue is located at a site in or on the protein where it experiences different modulation due to different interactions with its macromolecular environment.

Such multi-component spectra can originate from a conformational exchange. Although such spectra point towards the existence of a conformational exchange they give no information about the time constant τ_{ex} [123]. The components

in a multi-component EPR spectrum are differently weighted due to the extent of the populations of the conformational states. Conveniently, these dynamical components resolved in EPR spectra are pressure sensitive and encode the desired information the combination of high pressure with SDSL-EPR yields.

The reception of pressure may trigger, as discussed before, the change in the equilibrium of conformers (see equation 4.9). This can imply a change in the ratio of components in the EPR spectrum. By unraveling the components from the spectrum, using computer simulations, the respective equilibrium constant between the two states can be derived and thermodynamic parameters that are connected to conformational exchange can be defined. Figure 4.4 depicts a schematic representation of pressure dependent changes in a population distribution of conformers in conjunction with changing mobility of a protein associated spin label.

As explained above, due to the EPR timescale a significant difference evolves between the “slow” exchange of distinguishable conformational states or multiple sub-states of equal energy in one distinct conformer ($<10^7$ s^{-1}), which are the origin for multiple components in cw EPR spectra, and “fast” backbone fluctuations ($>10^7$ s^{-1}) that directly influence the spectral line-shape and average distinct states. Considering the case of multiple components it is of importance to distinguish exactly between differing resolved conformational states and the exchange of diverging sub-states in a consistent conformation. Resolving this difference is hard if not impossible to establish by a single multi-component cw EPR spectrum alone, but the latter provides hints that are beneficial for distinguishing between the two phenomena. For instance it can be assumed that exchanges between sub-states feature spectral alteration of smaller amplitude than those of conformational exchange. High pressure double electron-electron resonance (DEER) spectroscopy studies give an additional tool to discriminate between the two options since it provides the measurement of conformational transitions and their magnitude in terms of inter-residue distance changes dependent on the applied pressure [117].

4.1.6 Establishing variable-pressure experiments for cw EPR

4.1.6.1 The high-pressure resistent sample cell

The high-pressure cell of choice within this work is the yttria-stabilized zirconia ceramic cell (HUB440-Cer) developed for X-band SDSL-EPR by Pressure BioSciences, Inc. [116]. The utilized setup for combining cw EPR with the pressure resisting cell is described further in the materials and methods section (3.2.1.4).

4.1.6.2 Considerations about buffer conditions and compressibility of aqueous solutions

Pressurizing aqueous biological samples requires considerations about solvent conditions, because the pressure induced compression of an aqueous solution leads to electrostriction of water molecules. Volume changes accompanied by buffer ionization and varying pH are the consequence. The buffer ionization volume may contribute to the overall volume change of bio-macromolecules in solution due to the transition between different conformational states or denaturation, associated with protonation or deprotonation of tritatable groups [113]. Therefore, for high-pressure experiments, buffers are desired that exhibit only small ionization volumes and marginal pH changes upon pressurization. Suitable buffers for use under high pressure were presented by Samaranayake and Sastry among others [177] and are specified in excerpts in table 4.1.

Tabelle 4.1: Suitable buffer agents for high-pressure experiments [177].

Buffer	pH range	ΔV° ionization (ml/mol)	ΔpH/Δp (kbar^{-1})
Tris; 2-Amino-2-(hydroxymethyl)propan-1,3-diol	7.0-9.0	4.3	-0.03
MES; 2-(*N*-Morpholino) ethanesulfonic acid	5.5-6.7	3.9	-0.06

Moreover, the compressibility of water has to be taken into account when combining high-pressure and EPR techniques. Firstly, water compression causes accumulation of the effective spin concentration in the sample. Secondly, the compressibility of

water under the influence of pressure (at 4 kbar water is compressed by ~12% [27]. leads to an increased amount of water, or more precise, an increased dielectric permittivity in the active region of an EPR resonator. In this regard the increased dielectric constant of water causes a shift in the resonant frequency and a decrease in the resonator quality factor.

4.1.7 Introduction to the investigated protein systems

The following sections introduces into the structure and fuction of the proteins and their spin labeled variants examined in this work.

4.1.7.1 Bovine serum albumin

BSA is an intensively investigated and well characterized protein with an established threedimensional structure which finds many uses in biochemistry and biophysics [9, 128,156]. Therefore, the protein is a suitable model system for the purpose to elucidate pressure induced unfolding and shifting conformational equilibria by HP-EPR as a proof of principle. As an albumin-class protein BSA (from *Bos Taurus*) is a globular polypeptide of 583 amino acids (AA) (66.463 kDa) that is most abundant in blood plasma making approximately 60% of its protein content. It is a multifunctional protein with a significant ligand binding capacity, making it a versatile transporter-system for diverse metabolites and nutrients [128]. It also has an essential function as regulator of colloid osmotic pressure in blood vessels and an important role in reducing inflammatory responses on the contact-site of blood and body tissues [197, 198].

In figure 4.8 the dimeric form of BSA is depicted (pdb 3V03) [128]. The exceptional structural stability of the protein is achieved by a high amount of 35 cysteine residues. 34 of these cysteine residues are oxidized to 17 disulfide bridges in the polypeptide core [156]. The only cysteine residue that is not involved in a disulfide bond is located at position 34 and contains the only free thiol group in the protein which is therefore the site of interest that was labelled in this work with iodoacetamideproxyl (IAA) spin label (4-(2-Iodoacetamido)-2,2,6,6-tetramethyl-1-piperidinyloxy). Previous investigations on the same position of BSA with cw EPR

resulted in a two-state model for the spin label side-chain. According to this model the nitroxide-group is either located in the solvent with a high degree of reorientational freedom or it is closely bound to the local protein backbone in a more immobile state. The interactions that are responsible for the nitroxide immobilization either evolve from formation of hydrogen bonds between the spin label side-chain of IAA and adjacent amino acid residues or from the location of cysteine residue 34 within a hydrophobic recess of 9.5-10 Å depth [7, 9, 40, 142].

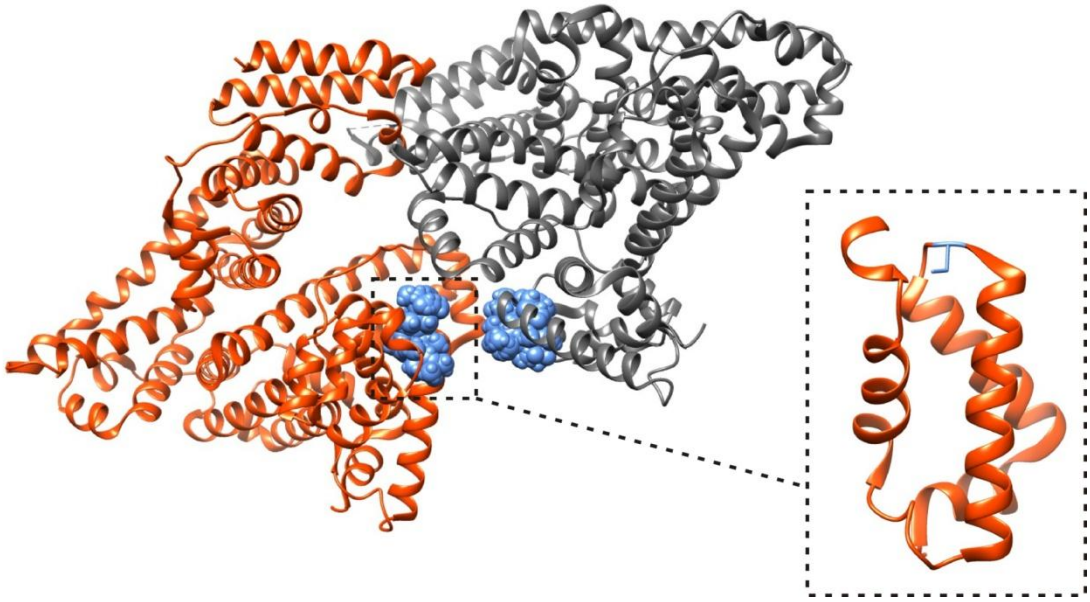

Figure 4.8: X-ray structure of the BSA dimer (3V03.pdb) witch attached rotamers of an IAA spin label. The two domains of the homo-dimer [128] are colored in orange and gray, respectively. Rotamer library analysis predicted 9 possible rotamers of the IAA spin label at position 34 at 298 K. Spatial rotamer populations are colored in blue. The cut-out zooms into the recess in which position 34, colored in blue, is located.

4.1.7.2 The substrate binding protein HisJ

The substrate-specific binding protein (SBP) HisJ from *Salmonella enterica serovar Typhimurium*, consists of 238 AA (26.156 kDa) and is an essential factor in the function of the prokaryotic ABC-binding cassette transporter system $HisQMP_2$. The transporter´s substrate is bound by HisJ in the periplasm and is transported to the transmembrane translocation complex. The tertiary structure of HisJ resembles two globular domains connected with a flexible linker region, acting as a hinge. Each domain consists of a centre of β-sheets and surrounding α-helices. Upon substrate

binding, which is localized in a binding-pocket within the cleft between the two domains, the SBPs mode of operation simulates a venus flytrap resulting in the closed conformation of the protein. Without substrate the protein HisJ exists predominantely in its open conformation. HisJ itself and its corresponding transport system are discussed in greater detail in section 5.1.5. For studies on HisJ under high pressure conditions in its substrate-free and substrate–bound state, three different residues were spin labeled. The crystal structure of histidine-bound HisJ with attached spatial rotamer populations of an MTS spin label located at positions G24 (loop-region), C45 (interface between loop-region and β-strand) and T151 (α-helix) is depicted in figure 4.9.

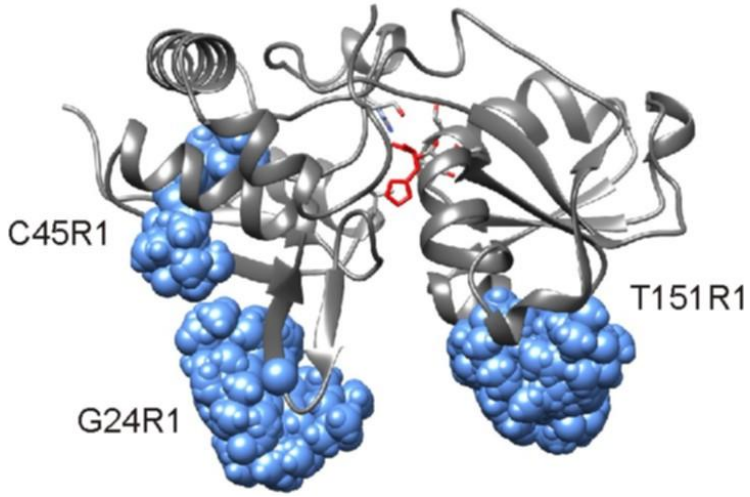

Figure 4.9: Structure of the substrate binding protein HisJ (1HPB.pdb) with rotamers of MTSSL. HisJ (colored in gray) consists of two lobe-like domains that enclose the substrate histidine (colored in red) upon binding. Amino acid residues that coordinate the substrate are depicted in stick representation. Rotamer populations of MTSSL at positions G24, C45 and T151 are depicted in blue.

4.1.7.3 The intrinsically disordered and amyloid fibril forming protein α-synuclein

α-synuclein (α-syn) is a model system, that is representative for investigations on intrinsically disordered proteins (IDP) in general and which is an important protein in a whole variety of neurodegenerative diseases based on protein-misfolding and aggregation. In this context the following paragraphs introduce the typically unfolded

(or intrinsically disordered) protein α-syn in detail, considering its biological structure, function and interactions with regard to the appeal for variable-pressure cw EPR.

The cellular and molecular mechanisms of many neurodegenerative diseases like Alzheimer´s disease (AD), Parkinson´s disease (PD) and amyotrophic lateral sclerosis (ALS) share common features as they all exhibit irregularities including protein accumulation and the formation of inclusion bodies. Accumulation is caused by aggregation of misfolded proteins that form insoluble fibers with high β-sheet content, characterized as amyloid fibrils derived from amyloidosis. In the particular case of PD, a prevalent neurodegenerative movement disorder, serious damage is inflicted to dopaminergic neurons in a region of the midbrain (mesencephalon), the substantia nigra pars compacta, by toxic protein-aggregates. It appeared that the IDP α-syn, which is abundant in all tissues, with highest concentrations in presynaptic areas of neuronal cells, especially in the neocortex, hippocampus, substantia nigra, thalamus and cerebellum, takes a main role in the pathology of PD. Its aggregated fibril form is a key component of Lewy bodies (LB) together with ubiquitin and neurofillaments. These intraneuronal inclusion bodies are found in high amounts in the substantia nigra, which develop in PD and comparable neurodegenerative disorders. It was suggested that neuro-cellular dysfunction could be caused by a conformational change and the connected fibril formation of α-syn [44, 112]. On the contrary other studies interpret α-syn oligomers as crucial factor in cellular toxicity [25].

Belonging to the protein family of synucleins human α-syn is localized in the cytosol of neurons and represents 1% of the protein-mass in brain cells [92]. The full-length protein consists of 140 amino acids which is the prevalent form. However, shorter isoforms have also been detected. Isoforms which are truncated at the C-terminus for instance show a tendency of accelerated aggregation, suggesting a direct coherence with the development of PD [215]. Similar effects were also obtained with particular point mutations of the full-length protein.

4.1.7.4 Identification of the intrinsically disordered protein α-synuclein

In studies of amyloid proteins from plaques of AD neuronal cells, besides beta-amyloid (Aβ), two other peptides were identified. It was proposed at first that due to their high hydrophobicity and the tendency to form β-sheet rich structures, those two

peptides would induce accumulation of Aβ. Therefore, these proteins were characterized as non-Aβ components (NAC) of AD amyloid. It was found that both peptides were fragments of a larger NAC precursor (NACP) which was identified later as a 140-AA protein that is expressed ubiquitously, with highest concentrations in brain tissue [202]. Later, additional two proteins were found highly concentrated in human brain tissue. After purifying and sequencing it was proven that the 140-AA peptide was equivalent to NACP. It also exhibited high homology to synucleins from the pacific electric ray (*torpedo californica*) and rats (rattus). Another purified and sequenced protein of 134-AA, that was also found in high amounts in human brain tissue, showed a homology of 61% with the 140-AA protein. The 140-AA and 143-AA peptide were then named α-syn and β-syn, respectively, which build the foundation for a new family of human brain proteins. Both α-syn and β-syn which are mainly expressed in the brain are predominately concentrated in neuronal presynaptic terminals [93].

4.1.7.5 α-synuclein functions

The functional mechanisms of α-syn are not entirely clarified, but some verified activities of the protein give evidence about its functional principles. α-syn has the ability to decrease the expression level of protein kinase C (PKCδ) in dopaminergic neurons and therefore suppress apoptotic cell death [99].

The calcium-modulated protein calmodulin (CaM) interacts with α-syn under the influence of Ca^{2+} ions. This interaction induces fibril formation of α-syn. In turn α-syn suppresses the inhibitory effect of CaM on the G-protein-coupled receptor kinase 5 (GRK5). Therefore, the IDP converts CaM from an inhibitor to an activator [131]. The oligomeric form of α-syn, an intermediate product in the formation of fibrils, has a damaging effect by binding to the N-terminal domain of synaptobrevin-2, a SNARE (N-ethylmalmeimide-sensitive factor attachment protein receptor) protein, and thereby inhibits the assembly of SNARE complexes [30]. Filaments of aggregated α-syn can interfere with the homeostasis of the cell and disrupt cellular topography and physiology by provoking dysfunction of several essential cell compartments, like the endoplasmatic reticulum (ER) or mitochondria [89, 193].

The assumed function of α-syn as a molecular chaperone refers to amino acid sequences that are homologous with 14-3-3 proteins which belong to a family of

cytoplasmic chaperons. 14-3-3 proteins bind to a variety of interaction partners and studies yielded that α-syn can interact with the ligands of 14-3-3 proteins as well. α-syns activity as a chaperone is based on its N- and C-terminal domains, where the N-terminal region interacts with the target protein and the C-terminal region establishes the solubilization of the complex of chaperone and substrate protein [154]. Other studies have shown that α-syn is involved in complex building with the heat shock proteins (HSP) Hsc70/Hsp70 and two additional chaperone proteins that mediate neurotransmitter release [223]. The function of α-syn as a molecular chaperone and its relationship to heat shock proteins is also recognized in experiments with CSPα (cysteine string protein) knock-out mice. CSPα works as a chaperone HSP and is involved in neurotransmitter release as well. Deletion of CSPα leads to a reduction of α-syn levels in the cell and lethal degeneration of neurons. This lethal CSPα deletion in mice can be prevented by an overexpression of human wildtype α-syn, showing the IDP can compensate for the chaperone activity [26]. As mentioned before α-syn interacts with 14-3-3 proteins and also with its targets as for instance the kinase repressor of Ras. In this respect α-syn is included in a variety of cellular mechanisms that depend on the activation of Ras [58]. Another cellular function α-syn is involved in is the regulation of dopamine synthesis due its indirect down-regulating activity on tyrosine hydroxylase dependent on the interaction with protein phosphatase 2A. Therefore, a decrease of cellular level of α-syn would increase the concentration of dopamine and the oxidative stress due to the dopamine metabolism as well [155]. Though α-syn is mainly present in the cytosolic fractions, the proteins lipid-membrane associated form has essential functions. An important function in the mechanisms of neurotransmitter release which is acquired by α-syn´s chaperone activity is involved in the maintenance of SNARE structures and complexes. Monomers of α-syn bind to presynaptic membranes and form homomer complexes of the α-helical folded α-syn, which work as chaperones for SNARE complexes, which mediate presynaptic vesicle docking [24]. The assembly and disassembly of SNARE complexes are consecutive processes in the release of neurotransmitters. A deficiency and accumulation of α-syn diminish the assembly of functional SNARE complexes and lead to dysfunction in neurotransmitter release [23]. The formation of synaptic vesicles is organized in a pathway which starts with inducing curvature of the membrane and initiating the budding process utilizing scaffold proteins like clathrin. Synaptic vesicles are directed then to a specific localization where secretion is accomplished with the help of

SNARE proteins. The curved membranes of the vesicles are targeted selectively by α-syn which regulates thereby the presynaptic vesicle dynamics [163]. The regulating function of vesicle traffic is based on α-syn´s N-terminal structure that can take membrane-binding α-helical conformation upon lipid recognition. The α-helical structure consists of two helices connected by a random coil region [213]. In this context there is indication that α-syn interacts predominately with lipid membranes with high curvature, unsaturated acyl chains and small anionic hear groups [217]. The vesicle size, the composition of phospholipids and the protein to lipid ratio determins the degree of interaction between the membrane vesicles and α-syn. In vitro experiments have shown that the strongest interactions and formation on helical structure arise between α-syn and vesicles comprised of phosphatidic acid, phosphotidylcholine and phosphatidylglycerol [233]. There is also evidence that α-syn is important for neuronal/synaptic homeostasis due to a reducing effect on the speed and quantity of vesicle recycling from synapses to the presynatic region [182].

4.1.7.6 α-synuclein: a model for intrinsically disordered proteins and amyloid fibril formation

In the cell, the small α-syn (14.5 kDa) is localized in the cytosol and exists in an intrinsically disordered (natively unfolded) conformation. Dependent on its environment the protein can experience distinct structural changes. In association with phospholipid bilayers or micelles α-syn can adopt a horseshoe-shaped α-helical structure [206]. The corresponding crystal structure of micelle-bound α-syn is depicted in figure 4.10. The sequence of α-syn can be subdivided into three domains, which show different function and influence on the protein´s properties. The N-terminal domain (AA 1-87) is mainly positively charged, containing seven repeating amino acid sequences of 11 residues length each, which encode for amphipatic helices. The repeats include the conserved hexameric motif KTKEGV which can also be found in apolipoprotein α-helical domains and is important for the ability of phospholipid-binding [194]. Specific point

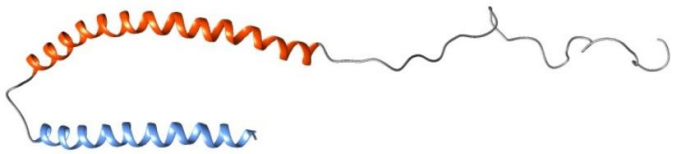

Figure 4.10: X-ray structure of micelle-bound human α-synuclein (1XQ8.pdb). α-helical structures are colored in blue and orange, respectively. Random coil segments are depicted in gray [206].

mutations in the N-terminal domain, like A30P, A53T and E46K are directly related to early onset forms of inherited PD. Two of these mutations, A30P and A53T, seem to self-associate more rapidly than the wild type and therefore show an increased fibril growth-rate [35, 120].

Substitutions at position A53 facilitate especially the protein´s tendency of aggregation and accumulation [36, 62, 63].

Point mutations A30P and E46K have also direct influence on the proteins binding affinity to lipids and its lipid-associated conformation. The substitution A30P decreases the affinity strength of α-syn to the membrane, while E46K seems to have a promoting effect on the interaction between protein and phospholipids [57].

The central domain (AA 61-95) is mostly relevant in composing the amyloid fibril formation. The ability of the core region (NAC) to form β-sheets is essential for fibrilization and aggregation [175]. The C-terminal domain (AA 96-140) is the protein´s tail region including ten glutamate and five aspartate residues making 34% of the domain acidic [1]. The high negative charge and the low hydrophobicity of this domain are responsible for its random coil structure. It is hypothesized that the C-terminal domain inhibits fibril forming by interacting with the core (NAC) region. Several modifications of the C-terminal domain have influence on the conformational transition to the ß-sheet rich state that induces aggregation. By reducing the negative charges of the tail region due to an increasing pH the aggregation process of the protein can be facilitated as *in vitro* experiments have shown [87]. A similar effect can be achieved by exposing α-syn to Al^{3+} ions which shield the negatively charged residues of the tail region and therefore prevent the domain´s inhibitory effect on aggregation into multimers [125]. Other polyvalent metal ions like Cu^{2+}, Fe^{3+} and Pb^{2+} show similar effects [204, 226].

A truncation of the protein´s tail region by deleting a sequence of the C-terminals acidic residues leads to a propagated aggregation of the protein as well [88]. Besides sequence truncations and environmental conditions like the pH and salt concentration, a variety of interactions with other proteins like Tau protein of FK506-binding proteins can catalyze the misfolding and accumulation of α-syn [211]. Fibril aggregation of α-syn is also accelerated due to the proteins strong affinity to polyamines like spermine and histones. Depending on the length, concentration and type of polymer the intensity of the aggregation process is varied. Similar to metal

cations, polyamines have an electrostatic effect on α-syn and neutralize the negative charges of the protein´s C-terminus [11, 67].
Paradoxically the high flexibility of α-syn also potentially increases its propensity to misfold, oligomerize and to aggregate. Various *in vitro* studies have yielded different morphological aggregates, including amorphous aggregated compounds, protofibrill structures, oligomeric intermediate states, and amyloid fibrils of course [68, 211].
In this respect it was shown that oligomeric species of α-syn could have a more toxic effect than fibril aggregates. For instance, the IDP can build oligomeric pore-like structures which can permeabilize lipid membranes and are therefore capable of inflicting serious damage on the cell [111]. As already indicated α-syn can adopt several different stable conformations, pointing towards the fact that its energy landscape is quit complex. In this respect studies on α-syn in different alcohol solvents of different concentration revealed different stable conformations and corroborate this theory [137]. The next paragraph will give an overview of the formation of different conformational species of α-syn with a particular focus on the fibril state of the protein and the conditions that induce aggregation.

4.1.7.7 Formation of α-synuclein fibrillic aggregates

Exposing monomeric α-syn to specific environments will induce a condition-dependent fibrilization. For instance, incubation at 37°C and pH 7.4 is sufficient to start the aggregation process which is accelerated particularly by agitation. Different solution condition can furthermore affect the growth-rate and morphology of α-syn fibrils and will be discussed later [22, 206].
Aggregation of α-syn is based on a mechanism similar to crystallization, a nucleated polymerization. Fibril aggregation is characterized by a slow processing lag phase, in which the formation of an oligomeric fibril-nucleus takes place and other transient soluble oligomeric species emerge that are off the pathway to fibrils but in equilibrium with the monomer [103, 111].
The lag phase is followed by an accelerated assembly of fibril aggregates in an exponential growth phase which reaches a final plateau. The fibril growth-rate increases in parallel with increasing concentrations of the monomeric entity [224]. Several studies of *in vitro* cultivated α-syn aggregates showed that emerging fibrils vary in length ranging from 500 nm up to 3 µm. Atomic force microscopy (AFM) and

electron microscopy (EM) have both shown that appearing fibril species come in three different flavors, which can be distinguished by their height: protofilaments (3.8±0.6 nm), protofibrils (6.5±0.6 nm) and the mature fibrils (9.8±1.2 nm) [172].

Regarding its molecular mechanism and structure the fibrillation process depends initially and critically on the formation of a partially folded intermediate species of the α-syn monomer [205, 210].

The fibrillation process can be considerably accelerated or otherwise decelerated and even inhibited by various factors. In this matter factors that shift the equilibrium between the unfolded monomeric state and the intermediate species in favor of the latter, like the ionic strength, facilitate and accelerate the fibrillation process [138]. In this respect decelerating and inhibiting factors promote the monomeric state or oligomers that are off the fibril- pathway. The effectors that accelerate the fibrillation of α-syn include specific metals [207], polycations [11], pesticides [204], glycosaminoglycans (f.i. heparin and other sulfated polymers) [31], lipids and molecular crowding.

On the contrary inhibiting effectors of fibrillation exist as well. A covalent modification of α-syn´s tyrosine residues by nitration leads to an inhibition of fibril formation due to the development of soluble non-fibrilogenic oligomers [227]. Other members of the syn family fibrilize much slower (γ-syn) or do not even form fibrils at all (β-syn) under the known *in vitro* or *in vivo* conditions that lead to α-syn fibril formation. In the presence of stoichiometric concentrations (4:1 excess) of β- and γ-syn the fibrillation of α-syn is also inhibited [208].

The fold of α-syn fibrils was studied with several biophysical approaches with the result that the monomer develops a cross β-sheet structure which represents the fibril core unit. In this conformation the β-sheets are orientated perpendicularly to the fibril axis with spacing of 4.7-4.8 Å along the fibril axis and 10-11 Å perpendicular to the axis.The C-terminal end and partially the N-terminus of the protein are excluded of the tightly structured fibril core and stay in a mobile conformation and lack a defined secondary structure [37, 184, 210].

Various EPR and NMR studies [29, 45, 77, 162]. and proteolysis experiments located the fibril core largely in the hydrophobic NAC region, extending towards the N-terminal region. Combining the experimental findings it can be assumed that the fibril core comprises of five possible β-strands. The assigned location of the β-strand

regions varies in different studies but is always located between residues 35-97 as depicted in figure 4.11.

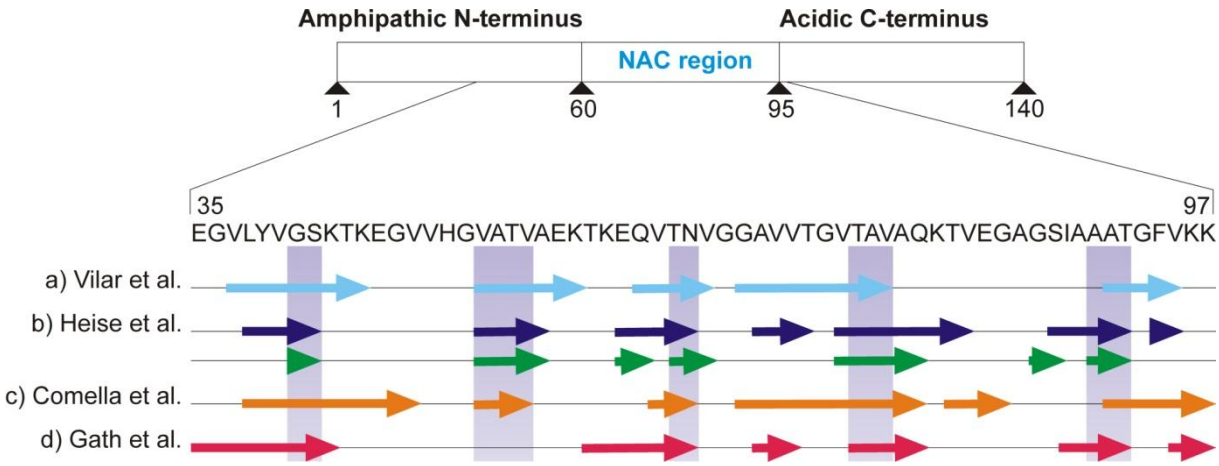

Figure 4.11: Amino acid sequence and β strand locations of human α-synuclein´s NAC region. Top: Breakdown of α-syn into the N-terminal, NAC and C-terminal region with additional representation of the amino acid sequence of residue 35-97. Bottom: Representation of β-strand regions (arrows) as identified by solid state NMR spectroscopy in the according references. a) ^{13}Cα–^{13}Cβ chemical shift data (light blue) from [216]. b) β-strand regions for two different types of fibril forms (form A in blue and form B in green) [77] c) structured regions of α-syn fibrils (orange) [34] d) Solid-state NMR sequential assignments of α-syn (red) [61]. Bars denote conserved β-strands. The graphic was adapted from Pornsuwan et al. [162].

These studies suggest that adjacent β-strand interact with each other, taking a sandwich-like formation with a repeating β-sheet loop sequence in which β-strand 1 interacts with β-strand 2, β-strand 2 with β-strand 3, β-strand 3 with β-strand 4 and β-strand 4 with β-strand 5. Incorporated into a protofibrillar or mature fibrillar structure an arrangement of parallel in-register β-sheets layers develops. It was also suggested that fibrils can assemble to “super”-fibrillic structures by aligning straight to each other or twisting around each other [216].

A simple model of the upcoming steps in fibrillation is depicted in figure 4.12, suggesting the conversion of the single α-syn molecule into the partially folded, β-sheet rich intermediate as starting point of the aggregation pathway, with subsequent association of further monomeric intermediates into a nucleus and fibrils. Along with different fibril species other off-pathway products may arise, for instance the already mentioned oligomeric species, or insoluble amorphous aggregates indicating the existence of particular aggregation pathways depending on the environmental conditions.

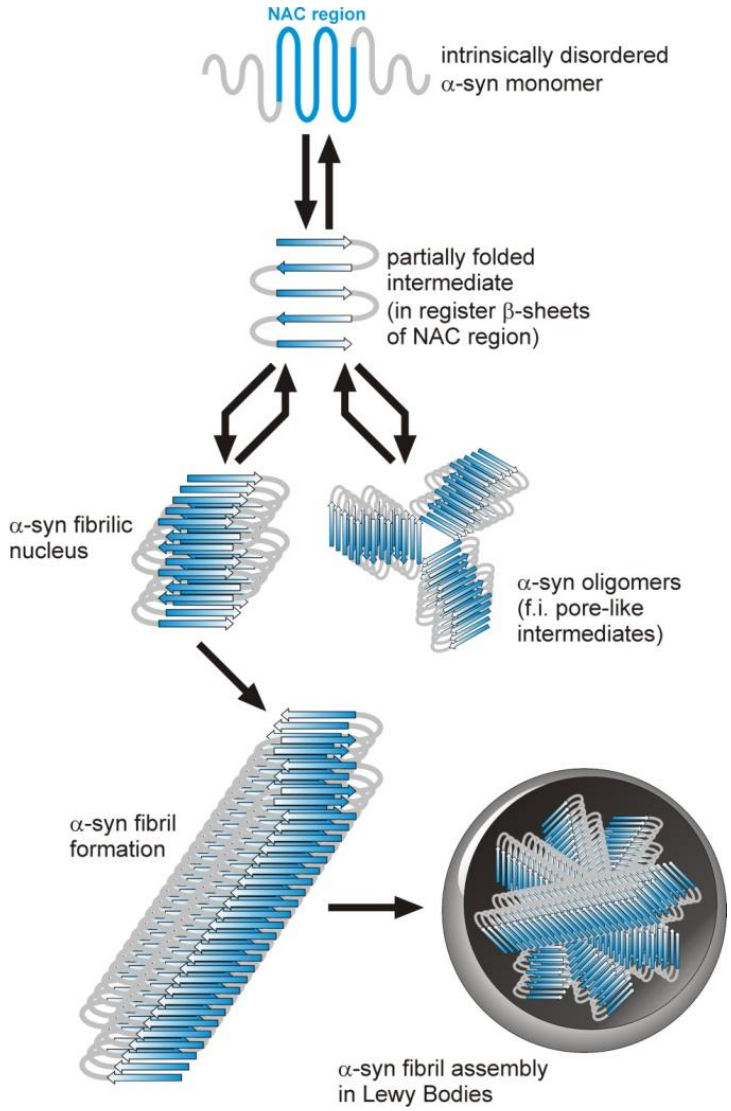

Figure 4.12: Aggregation of alpha synuclein into fibril formation and oligomeric states. The natively unfolded α-syn is able to adopt a five in-register β-sheet formation due to the influence of several different effectors. The β-sheet rich monomer has the propensity to form oligomeric (protofibrillar) intermediates and fibrillic aggregates. Some oligomeric species can show a toxic or even lethal effect on the cell, like pore forming intermediates that disrupt the integrity of cellular membranes. Furthermore, α-syn fibrillize and accumulate into Lewy bodies. Diverse factors, including overexpression of the protein, environmental stress, single point-mutations like A53T or A30P facilitate the development of α-syn oligomers and fibrils.

As depicted in figure 4.12 oligomeric species that turn up during the lag phase and are off the fibril-pathway are in equilibrium with the monomeric partially folded α-syn. It is still a matter of debate if these oligomers directly add to fibril formation or if an additional dissociation step produces the monomeric form that adds to the growing fibrils [36, 47, 103].

4.1.7.8 Oligomeric structures of α-synuclein

A variety of studies on the transient oligomer types that are present in the lag phase have been done to elucidate this state. Dynamic light scattering (DLS) experiments and Fourier transformed infra-red spectroscopy (FTIR) show that oligomer formation reaches a maximum near the end of the lag phase and begins to decrease followed by an immediate acceleration of fibril formation [103]. In addition, studies using fluorescence resonance energy transfer (FRET) supported these findings [103].
Furthermore, fluorescence spectroscopy showed that two different types of oligomeric intermediates are produced predominantly at different time points in aggregation, during the lag phase and the conclusion of fibrillation, respectively. [47].
It was hypothesized that amyloid fibrils of α-syn form efficiently by association of oligomers to the fibril termini. [64, 183].
Investigations on the emerging oligomers with atomic force microscopy (AFM) suggested two intermediate populations during the lag phase of which the population of oligomers that are formed at the end of the lag phase decrease in concentration at the same rate that fibril growth increases. This strengthens the notion that fibril formation could be accomplished by longitudinal association of full grown oligomers [103].
In contrast to this hypothesis, kinetic data suggests that amyloid fibrils grow by monomer and not oligomer addition to the fibril ends and are subject to higher-order assembly [22, 32].

Stable oligomeric structures can be induced by modifying the α-syn monomer. Those modifications range from oxidation of the methionine residues to methionine sulfoxide [65, 209] over the interaction with polyphenols [121, 234] to covalent binding of specific chemical agents like 4-hydroxynonenal [164]. Emerging oligomers are very stable and show a very slow dissociation rate. Because usually oligomer formation occurs more rapidly than fibril formation, modified α-syn only shows marginal fibrillation. It seems plausible that the difference between the stable and the transient oligomers originates from structural differences between their subunits suggesting the structure of the stable populations must be considerably more compact.

4.1.7.9 The effect of hydrostatic pressure on amyloid fibrils

It was already indicated that hydrostatic pressure which affects the energy and conformational landscape of a protein in solution also destabilizes oligomeric compounds and protein aggregates. In this context studies have been made with amyloid fibrils prepared from α-syn and transthyretin (TTR), showing the corresponding aggregates are highly sensitive to high hydrostatic pressure and dissociate due to packing defects or hydration of cavities in the fibril core [54]. It was also ascertained that point mutations in the studied proteins change the sensitivity to hydrostatic pressure of the respective amyloid fibrils in comparison to aggregates generated from wildtype protein. The integrity of wildtype α-syn fibrils in this context is less vulnerable to pressure than fibril types that emerge from mutated α-syn which are connected to early onset forms of Parkinson´s disease like A53T or A30P [54]. Studies on recombinant hamster prion protein, that undergoes temperature-dependent aggregation and an associated change in its secondary structure from α-helical to β-sheet rich, demonstrated also pressure induced subunit dissociation of protein polymers [201].

Another study on α-syn in cultured neuronal cells leads to contrary conclusions considering the effect of pressure. It was shown that hydrostatic pressure can promote the aggregation of monomeric α-syn to higher order structures [69]. Additional findings of the study implied that the loss of α-syn´s binding partners or release of α-syn from bound protein partners due to high pressure is responsible for increased aggregation as was indicated in other studies [69].

A closer look at the effect of hydrostatic pressure on the α-syn fibrils, is supposed to determine to what extent these can be dissociated into the monomeric form and if a re-fibrillation occurs after de-pressurization. In this context volumetric parameters and the monomer-fibril conformational equilibria of α-syn are identified within this work. These properties could indicate whether hydrophobic cavities in the aggregate interior or packing defects, imperfect contacts between the amino acid side chains in the fibril core, are responsible for susceptibility against pressure. Besides, the soluble monomeric protein is studied accordingly to determine what effect pressure has on the IDP´s conformational equilibrium and if pressure can drive an accumulation of α-syn into ordered complexes or armorphous aggregates.

4.2 Results of hydrostatic high pressure EPR studies on soluble proteins and amyloid aggregates

4.2.1 EPR experiments on free nitroxide spin-label under high pressure conditions

The studies presented in this chapter were accomplished to examine the influence of variable hydrostatic pressure on free nitroxide spin label motion in aqueous buffer solution and an organic solvent, respectively. In solution the rotational diffusion of the molecules is approximately isotropic. If the molecules rotational correlation time is smaller than the absorption process of microwaves, the anisotropy of the g- and A-tensor are averaged out and the spectral line shape becomes independent of the orientation to the external magnetic field B_0 with respect to the nitroxide molecule resulting in three equally sharp resonance lines. Because a molecule´s rotational correlation time is correlated to the viscosity of its surrounding medium the results of this experiment admit to draw conclusions about changes of the solvents viscosity due to compression by pressure and possible differences between aqueous solutions and organic solvents in viscosity and compressibility will be reflected in the EPR line shape. Acquired cw-EPR spectra of OH-TEMPO (4-Hydroxy-2,2,6,6-tetramethylpiperidinyloxyl) dissolved in either 20 mM Tris/HCl buffer or in 1-hexanol, pressurized from atmospheric conditions up to 2000 bar are depicted in figure 4.13. Corresponding rotational correlation times of the free radical molecule in both solvents are depicted in figure 4.14 and were calculated by employing Redfield theory (see 2.3.5.1).

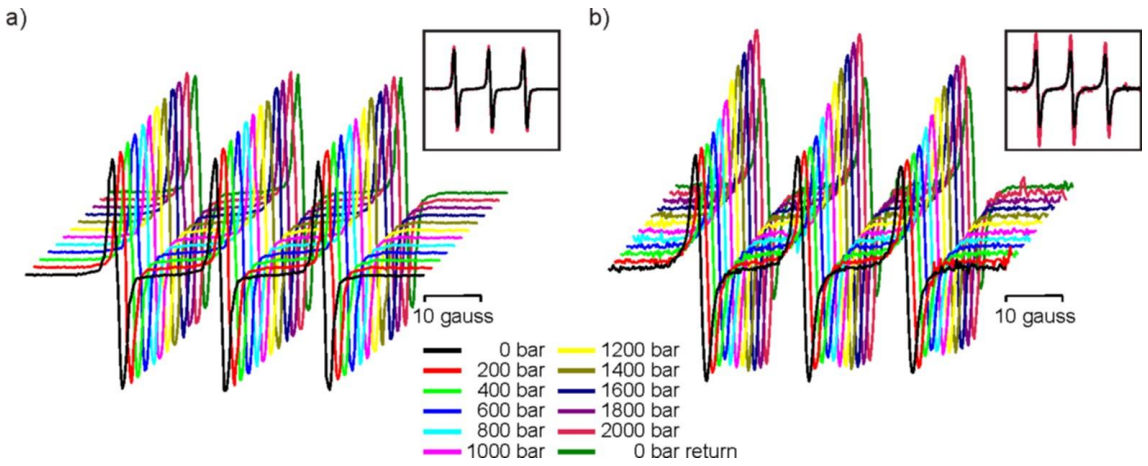

Figure 4.13: High-pressure cw-EPR spectra of hydroxy-TEMPO in Tris/HCl buffer or in 1-hexanol. EPR spectra were acquired at X-band frequency. Pressure was applied ranging from atmospheric conditions to 2000 bar in steps of 200 bar at room temperature. a) 100 µM OH-TEMPO in 20 mM Tris/HCl buffer (pH 7). Inset: comparison of spectra at atmospheric pressure (black line) and 2000 bar (red line). b) 100 µM OH-TEMPO in 1-hexanol. Inset: comparison of spectra at atmospheric pressure (black line) and 2000 bar (red line).

The change in the effective rotational correlation time (figure 4.14a) and spectral line shape of OH-Tempo in Tris/HCl buffer shows only a marginal dependence on increasing pressure. A plot of $\ln[\tau/\tau_0]$ versus pressure, shown in 4.14b, exhibits a linear correlation of OH-Tempo in Tris/HCl buffer giving a activation volume of $\Delta V^{\ddagger}$=4.6±3.8 ml/mol according to equation 4.12. This behavior is addressed to the low compressibility of the aqueous solution and a slightly decreasing viscosity at room temperature induced by low pressure (≤1 kbar) [16, 178].

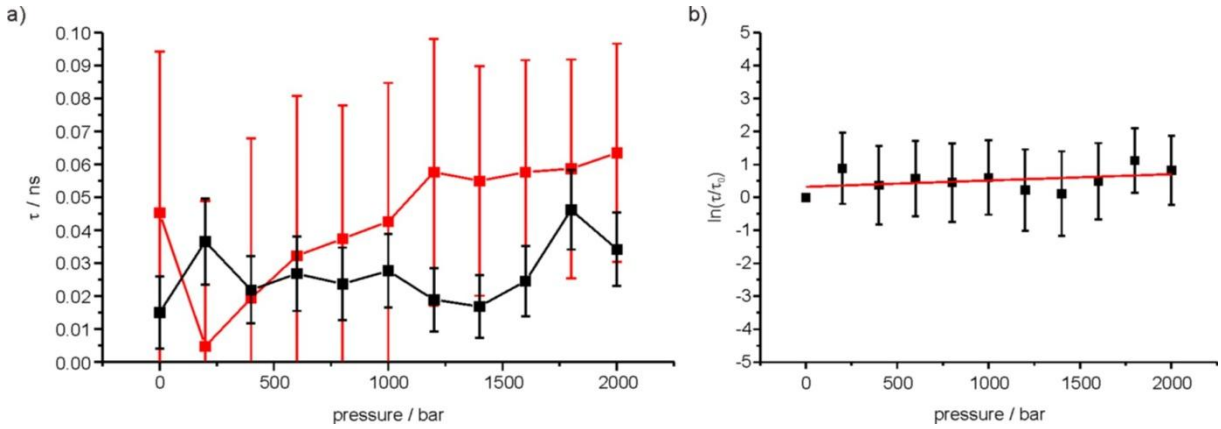

Figure 4.14: High-pressure dependence of rotational correlation times of OH-Tempo in different solvents. a) Process of τ of OH-TEMPO (100 µM) over pressure in 20 mM Tris/HCl buffer (pH 7) (black squares) and 1-hexanol (red squares). b) Values for $\ln(\tau/\tau_0)$ plotted versus pressure (black squares) of OH-TEMPO (100 µM). A linear fit is depicted as solid red line.

The only noticeable variation is the increased concentration of spin label, indicated by higher signal intensity, see inset in figure 4.13 a. Likewise the ratio of resonance lines, the line widths and the resulting rotational correlation times of the spin label dissolved in 1-hexanol exhibits small changes due to the samples exposure to pressure. The pressure induced change of the hexanol viscosity seems to have an effect on the radical molecules rotational correlation time, since τ decreases upon pressurization and increases furtheron with increasing pressure (figure 4.14). However, the course of the change in τ within the error limits is not significant. The viscosity of 1-hexanol at 298.15 K and atmospheric pressure, 1 bar, amounts to 4.51 mPa s and only increases slightly with pressure [132]. Nevertheless, a recognizable change in the ratio of the EPR spectral peak to peak-amplitudes, the line widths and the according rotational correlation time of OH-Tempo at room temperature would occur at higher viscosities (≥109 mPa s), see figure 4.15. Therefore, it can be concluded that the pressure induced change of the viscosity of 1-hexanol is too small within the range of the experimentally applied pressures and temperatures to have a significant effect on the spectral line shape.

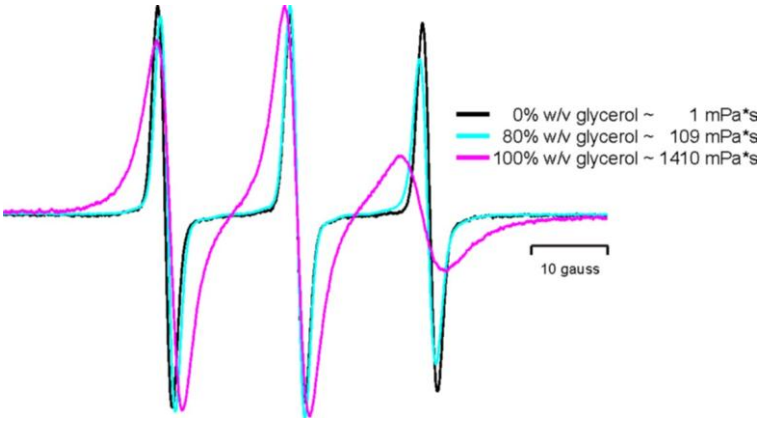

Figure 4.15: Nitroxide spin label in environments of different viscosity. EPR spectra (normalized by maximum) of 100 µM OH-tempo in mixtures of 20 mM Tris/HCl (pH7) and glycerol (w/v) with different values of viscosity. 0% w/v glycerol ~ 0.89 mPa*s – black line, 80% w/v glycerol ~ 109 mPa*s – cyan line, 100% w/v glycerol ~ 1410 mPa*s – pink line.

However, on the contrary the spectral amplitudes of OH-Tempo in 1-hexanol show an unambiguous dependence on pressure increase which is reflected by equally increasing amplitudes of all three resonance lines depicted in the inset of figure 4.13 b. This effect is explainable by the increased concentration of spin label molecules in the resonator cavity due to compression of the solvent. The signal intensities of the

alkanol and the Tris/HCl buffer samples increases by ~7% and ~4% at 2000 bar, respectively, see insets in figure 4.13 a & b. For further experiments it was therefore important to use only uncompressible solvents, like aqueous buffer solutions, as described in chapter 4.1.6.2, in order to eliminate unwanted influences of pressure perturbation like increasing viscosity of the solvent medium or spin concentration changes due to compression.

4.2.2 Hydrostatic pressure EPR experiments on bovine serum albumin

Pressure perturbation experiments on spin labeled proteins were accomplished by investigating bovine serum albumin (BSA) as model system because of its high availability and easy way of preparation. The only free, accessible thiol-group of BSA at position C34 was chosen to investigate the influence of pressure on the conformational landscape of the protein and was labeled with IAA spin label (I1), see figure 4.16b. EPR experiments on pressurized spin labeled BSA were accomplished starting at atmospheric conditions (1 bar) and reaching up to 2000 bar in steps of 200 bar. The EPR spectrum of BSA labeled at position C34 shows contributions of two states, an immobile (~85% amount of population) and a mobile component (~15% amount of population). The attached spin label is either located in a solvent exposed orientation or in close contact with the local protein backbone. As indicated before in chapter 4.1.7.1 the immobilization of the spin label is either affiliated by the formation of hydrogen bonds between the IAA spin label side chain and adjacent amino acid residues or due to the location of cysteine residue 34 within a hydrophobic recess of 9.5-10 Å depth at the protein surface. A change of the spectral lineshape over pressure is noticeable which is reflected especially in the variation of the equilibrium of the mobile and immobile population, figure 4.16 a and c. The effect of pressure is completely reversible after returning to atmospheric conditions, see figure 4.16 d. Pressure-dependent dynamic parameters as the reorientational correlation time τ and the rate tensor R were obtained from fits of the acquired EPR spectra. The populations and the equilibrium constants K of the two components as function of pressure were determined from the fits as well. All simulations were accomplished by utilizing the EPR analysis program MultiComponent as described in the materials and methods section (chapter 3.2.3.4). The according fits are depicted in the appendix, figure 7.1.

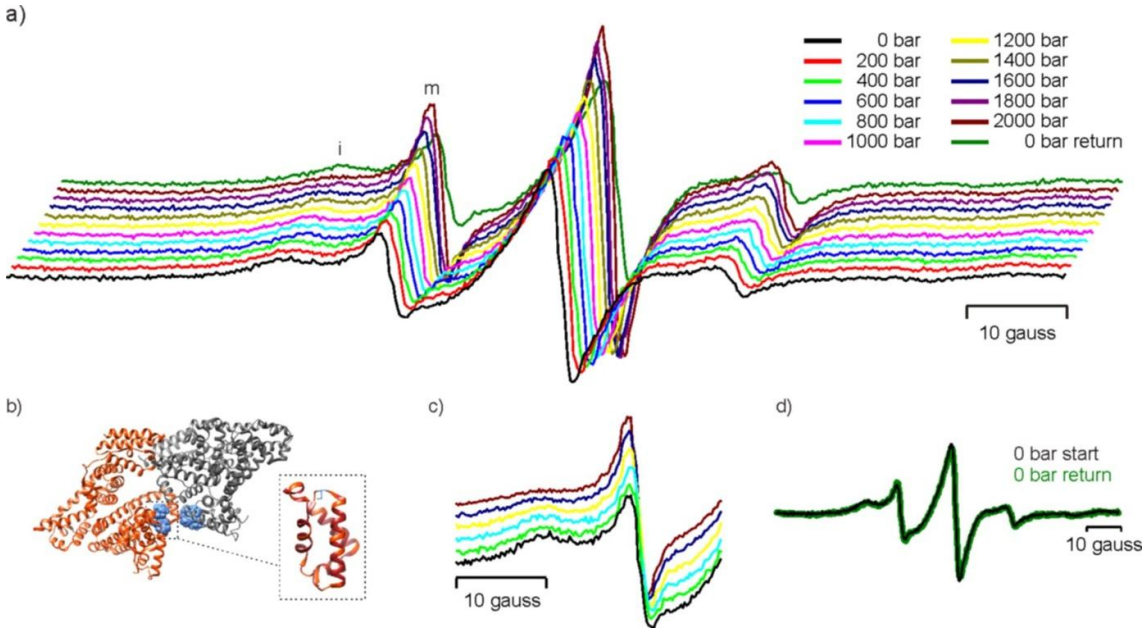

Figure 4.16: EPR experiments on pressurized bovine serum albumin. a) Pressure dependence of BSA studied by cw-EPR spectroscopy. High pressure measurements were induced in steps of 200 bar starting at atmospheric pressure (1 bar) rising up to 2000 bar in total. b) Model of the BSA dimer with rotamer populations of IAA spin label (4-(2-Iodoacetamido)-2,2,6,6-tetramethyl-1-piperidinyloxy - blue spheres) located at position C34 based on the homo-dimeric crystal structure (3V03.pdb). The close-up view depicts the spin labeled cysteine residue (blue). c) Extract of the EPR spectra depicting the change of the low-field resonance lines over pressure d) EPR spectra of spin labeled BSA at atmospheric pressure (1 bar) before and after inducing pressure of 2000 bar.

The reorientation rate, R, which is directly connected to the reorientational correlation time τ, of both the mobile and immobile component were obtained from the simulations of the spectra of BSA C34I1 and plotted versus pressure to give a first impression on the relationship of pressure and the spin label mobility (figure 4.17). The rates of the spectral mobile and immobile component were simulated with an isotropic model. The contributions of both the mobile and immobile components experience a rate growth over the applied pressure. A linear fit to the logarithm of the rates versus pressure of the mobile component, predicted by equation 4.12 (chapter 4.1.5), results in a slope of $4.2*10^{-5}$ bar^{-1} (figure 4.17a). The change of the immobile component´s rate, log R, over pressure is simulated with a linear fit as well, giving a result of $1.5*10^{-5}$ bar^{-1}. Due to the correlation between the rates and the rotational correlation time (isotropic correlation: $\tau=(6R)^{-1}$) [13], a linear correlation between log τ and pressure ,similarly described by equation 12 (chapter 4.15), is discussed further on.

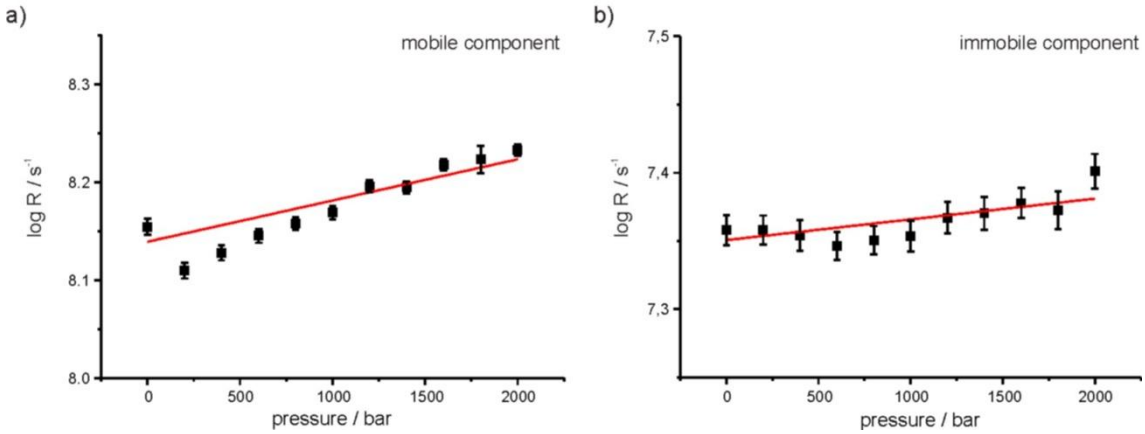

Figure 4.17: Pressure-dependent reorientation rates of I1 in spin labeled BSA. The reorientation rates, R, determined from simulated fits to the spectra of BSA C34I1 (shown in the appendices) plotted versus pressure (black squares). The mobile and immobile components were simulated with a model for isotropic motion. a) The logarithm of the rate, logR, plotted versus pressure of the spectrums mobile component. An according fit of the data is indicated as solid red line. b) The logarithm of the rate, logR, plotted versus pressure of the immobile component. An according fit of the data is indicated as solid red line.

The rotational correlation times τ for the spin labeled site C34 decrease for both the mobile and the immobile component with increasing pressure. This effect is not attributable to changes in the viscosity or the compression of the bulk solvent surrounding the spin label since the applied pressure should compress and change the aqueous media´s viscosity only marginally. According to equation 4.12 (chapter 4.1.5) the rotational correlation time of a nitroxide can be correlated to hydrostatic pressure. The equation enables the calculation of the activation volume $\Delta V^{\ddagger}$, which characterizes the change of a solvent cage`s volume that permits rotational diffusion of a spin label.

For the mobile component a plot of $\ln[\tau/\tau_0]$ versus pressure exhibits a linear correlation (figure 4.18 a). The slope results in a value of $\Delta V^{\ddagger}$=-3.3±0.4 ml/mol at room temperature. In similar studies the analysis for the immobilized state was not given because the motion of this state gains significant contributions from protein rotary diffusion [133]. In this study the rotary diffusion of the protein in solution does not significantly contribute to τ of the immobile component. This is because the rotational correlation time of bovine serum albumin is in the range of 78-125 ns [94]

that is clearly out of the regime of the experimental data ($\tau_{immobile}$~6.5-7.5 ns) presented in this study. For the immobile component a plot of $\ln[\tau/\tau_0]$ versus pressure shows linear behavior as well (figure 4.18 b).In this case the slope results in a value of -1.0±0.3 ml/mol for $\Delta V^{\ddagger}$ at room temperature. The obtained activation volumes for the spin labeled position 34 are interpreted in the discussion.

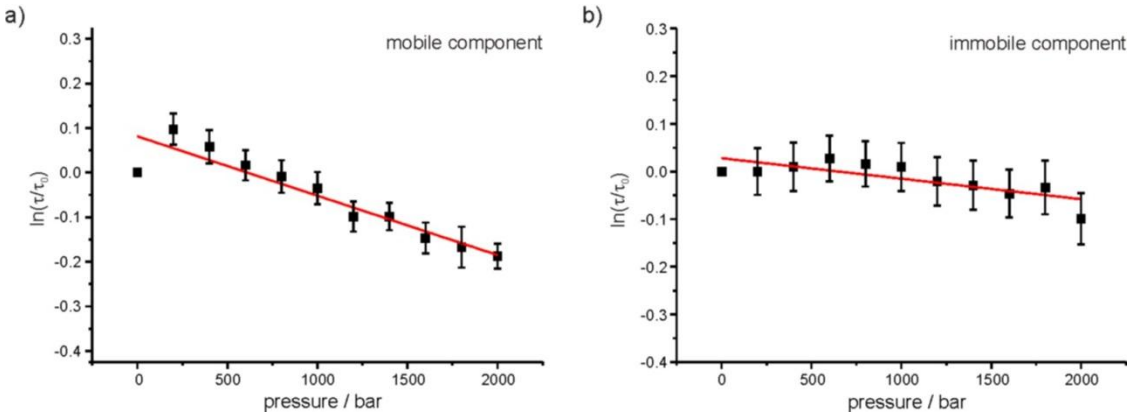

Figure 4.18: Pressure dependent reorientational correlation times of BSA C34. Values for τ determined from simulated fits to the spectra of BSA C34I1 (shown in the appendices) plotted versus pressure (black squares). a) Plot of the reorientational correlation times of the mobile component vs. pressure. A linear fit is depicted as solid red line. b) Plot of the reorientational correlation times of the immobile component vs. pressure with a linear fit depicted as solid red line.

As already mentioned the effect of pressure on the BSA C34I1 spectrum is visible notably in the shift of the two relative rotamer populations, the mobile and the immobile component. With increasing pressure the ratio of the spectral amplitudes of the mobile component m to the immobile component i shifts in favor of the mobile state (figure 4.16 a & c). From simulated fits of the corresponding spectra the relative populations were obtained and the respective pressure-dependent ratios of equilibrium constants k/k_0 were calculated. The experimental results yield a plot of $\ln(k/k_0)$ versus pressure as depicted in figure 4.19. Considering the characteristics of the plot it is noticeable that there is a linear relation in the range from 0 to 2000 bar. Since the shifts in the rotameric equilibria of a nitroxide result in a linear relation between $\ln(k/k_0)$ and pressure, the partial molar isothermal compressibility can be assumed to be $\Delta\beta_T \approx 0$ [133]. Along with equation 4.9 from chapter 4.1.4 the

experimental data yield the values for the differences in partial molar volume ΔV^0=-6.0±0.4 ml/mol and the partial molar isothermal compressibility $\Delta\beta_T$=0.

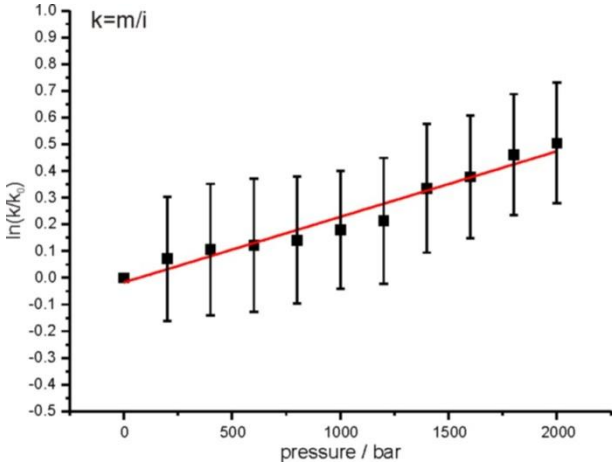

Figure 4.19: Pressure dependent equilibrium constants of BSA C34I1. Equilibrium constants determined from simulated fits to the spectra of BSA C34I1 (shown in the appendices) plotted versus pressure (black dots) with a linear fit (solid red line).

4.2.2.1 EPR experiments on bovine serum albumin subject to pressure perturbation and guadinine hydrochloride.

Similar experiments with BSA C34I1 were accomplished under the same conditions but in addition to a chaotropic medium, guanidine hydrochloride (GdnHCl), a strong denaturant used particularly in studies on protein folding. Here it is evaluated whether destabilization of BSA by GdnHCl induces conformational equilibria which can be explored by pressure dependent EPR.

EPR spectra of BSA C34I1 with increasing concentrations of GdnHCl were obtained to determine the maximal amount of applied denaturant which does not alter the spectral line-shape at ambient pressure but was likely to have a destabilizing impact, see figure 4.20 a. The according fits are depicted in the appendix, figure 7.2. From the sigmoidal plot of the equilibrium constant (mobile/immobile component) versus concentration (inset in figure 4.20 a) a concentration of c_{GdnHCl}=200 mM was chosen. Investigations on BSA in the presence of this concentration of GdnHCl exhibit a stronger alteration of the EPR spectra with increasing pressure compared to the influence of pressure alone, depicted in figure 4.20 b. The respective fits are shown

in the appendix, figure 7.3. In this case the GdnHCl based effect is recognizable in an additional change of the equilibrium constant of the mobile and immobile component showing a more prominent shift to the mobile population of rotamers.

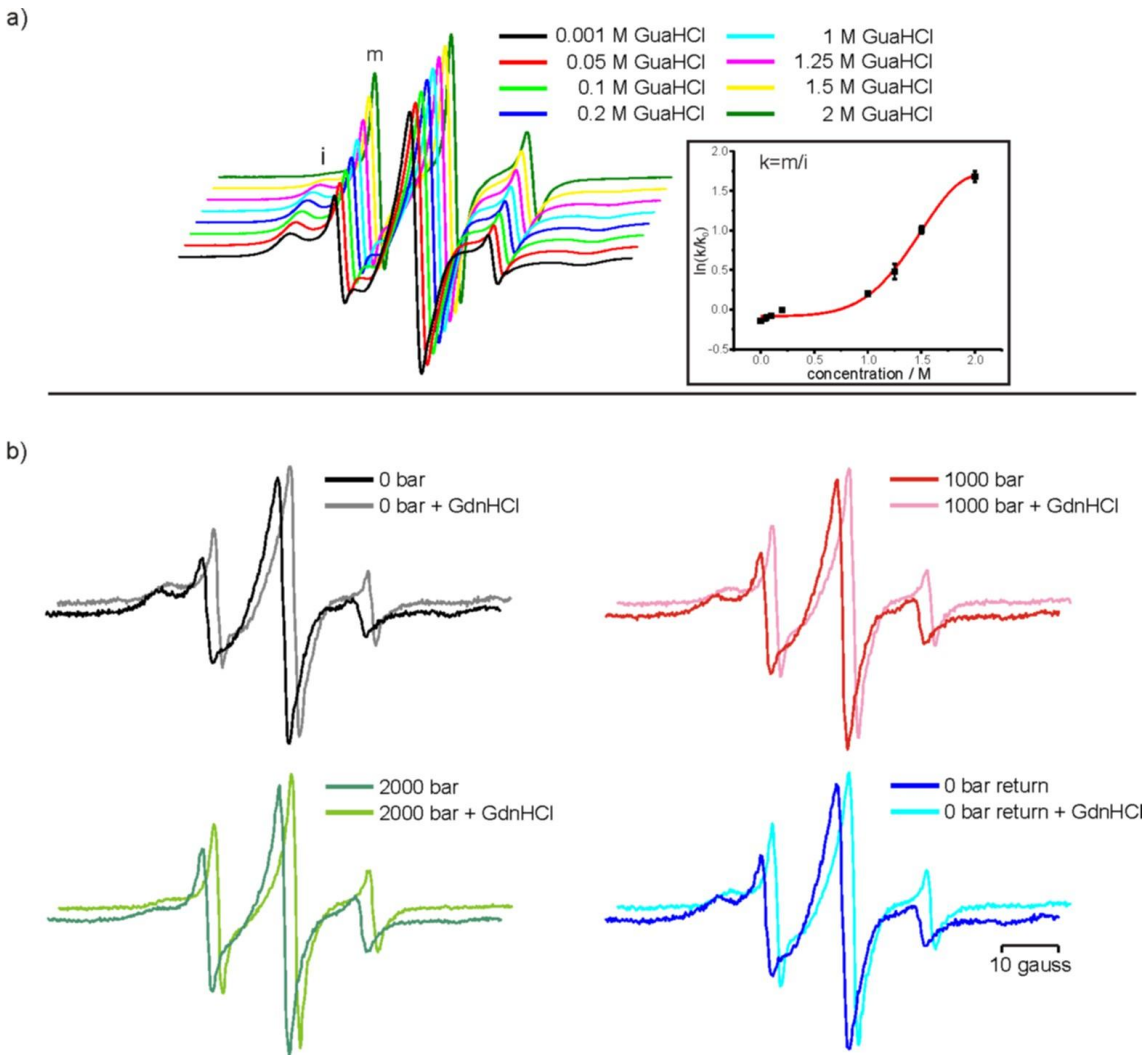

Figure 4.20: EPR experiments on pressurized BSA in presence of guanidine hydrochloride. a) EPR spectra of BSA C34I1 upon addition of guanidine hydrochloride of various concentrations. Inset: GdnHCl concentration dependent equilibrium constants (black squares) with a sigmoidal fit to the equilibrium constants vs. concentration of GdnHCl (solid red line). b) Changes in EPR spectra upon addition of 200 mM guanidine hydrochloride at different pressures.

Similar to the experiments with BSA in the absence of guadinine hydrochloride the reorientation rates, R, of the spectral mobile and immobile components were simulated with an isotropic model (figure 4.21 a & b). The rates of both, of the mobile

and the immobile states, increase in dependence of the applied pressure. The logarithm of the rate of the mobile components varies linearly with pressure. The according fit results in a slope of $2.4*10^{-5}$ bar^{-1}. The pressure-dependent change of the logarithm of the immobile component rate is linear as well, giving a slope of $3.5*10^{-5}$ bar^{-1}.

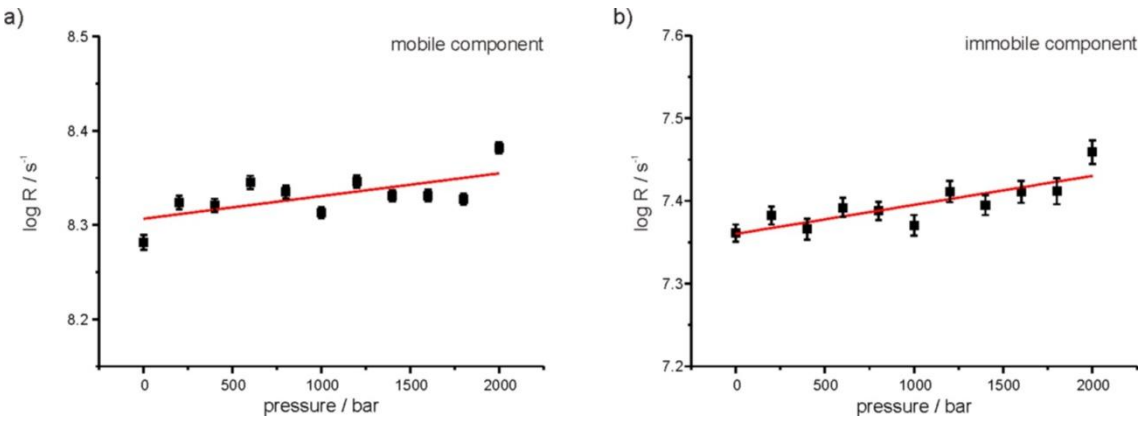

Figure 4.21 : Pressure dependent rates of the spin label reorientational motion of BSA C34I1 in presence to guanidine hydrochloride. Rates determined from simulated fits to the spectra of BSA C34I1 in presence of 200 mM GdnHCl (shown in the appendices) plotted versus pressure (black squares). a) Mobile component. An according linear fit of the data is indicated as solid red line. b) Immobile component. An according fit of the data is indicated as solid red line.

The respective value, $\ln(\tau/\tau_0)$, of the mobile and immobile components from the I1 spectra are both linear in pressure (figure 4.22). An activation volume of $\Delta V^{\ddagger}$=-1.4±0.5 ml/mol at room temperature can be calculated for the mobile component. The immobile component gives a value of $\Delta V^{\ddagger}$=-2.1±0.4 ml/mol under the same conditions.

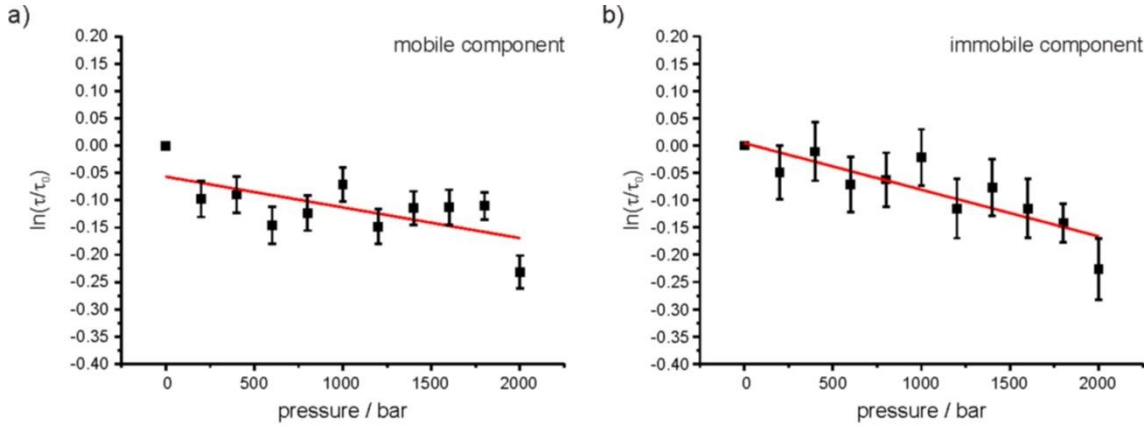

Figure 4.22: Pressure dependent reorientational times of BSA C34I1 albumin in presence of guanidine hydrochloride. Reorientation correlation times determined from simulated fits to the spectra of BSA C34I1 in presence of 200 mM GdnHCl (shown in the appendices) plotted versus pressure (black squares). a) Mobile component. A linear fit to the plot is depicted as solid red line. b) Immobile component. A linear fit to the plot is depicted as solid red line.

The experimental data of BSA C34I1 in presence to guanidine hydrochloride yields a linear plot of $\ln(k/k_0)$ versus pressure in the range from 200 to 2000 bar as depicted in figure 4.23. The plot gives the values for the pressure-dependent difference in partial molar volume $\Delta \boldsymbol{V^0}$=-6.6±0.9 ml/mol at C34I1. Due to linearity of the plot the partial molar isothermal compressibility is again assumed to be $\Delta \boldsymbol{\beta_T}$=0. At pressure values between 0 and 200 bar a decrease in the ratio k/k_0 is noticeable that could point to a non-linear behavior at low pressure. However, due to the error of $\ln(k/k_0)$ at 200 bar and above and due to lacking experimental data between 0 and 200 bar the emerging non-linear behavior is neglected in the quantification of the results and is supposed to be insignificant.

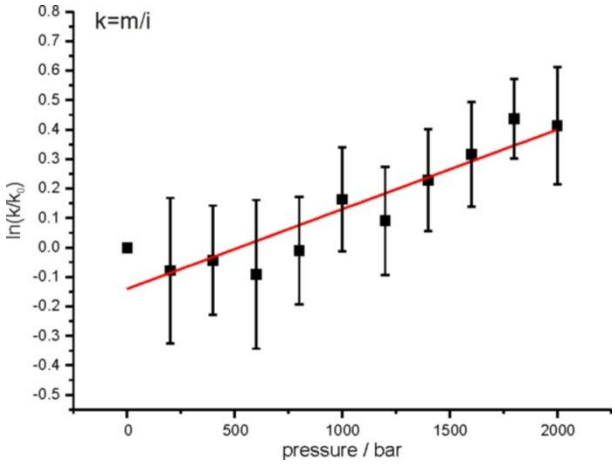

Figure 4.23: Pressure dependent equilibrium constants of BSA C34 upon addition of guanidine hydrochloride. Equilibrium constants determined from simulated fits to the spectra of BSA C34I1 in presence of 200 mM GdnHCl (shown in the appendices) plotted versus pressure (black dots). A linear fit to the equilibrium constants vs. pressure is depicted as solid red line.

4.2.3 Pressure perturbation of the histidine binding protein HisJ investigated with EPR

Experiments on the substrate binding protein HisJ from *Salmonella enterica serovar Typhimurium* were done to investigate the influence of pressure perturbance on a protein in its substrate-free compared to its substrate-bound state in order to understand if substrate-binding has an increasing or decreasing effect on the protein´s conformational stability. HisJ, a substrate delivery system for the membrane-bound histidine translocator $HisQMP_2$, exists in the absence of a ligand in a loose, open conformation of two globular domains connected by a hinge region. Upon substrate recognition, the binding of the ligand induces a change into the closed conformation with the two global domains approaching each other, resembling in function a venus fly trap.

For this purpose three different variants of HisJ labeled with MTSSL, in lobe 1 at positions G24 (located in a loop-region) and C45 (located at a junction between a loop and a β-sheet) and in lobe 2 at position T151 (located in an α-helix) (see figure 4.24 a), were studied either in the absence or in the presence of 1 mM histidine as substrate. According to the crystal structure (1HPB.pdb) all investigated sites are exposed on the protein surface with only the residue at position C45 into the protein interior. It must be indicated that only HisJG24 was purified in the absence of histidine whereas HisJ C45 and T151 were purified in the presence of the substrate.

Therefore, it must be considered that the spectra of HisJ C45R1 apo and T151R1 apo could represent a mixture of contributions of the substrate-free and the substrate-bound form of the protein. Thus an addition of substrate to those particular samples is still responsible for spectral changes as described further in the text. In all cases EPR spectra were obtained that show only a single component spin-label population (figure 4.24 b). Position G24R1 is obviously the most mobile of the variants ($\tau_{HisJ\ G24R1}$= 2.0 ns), with128 predicted rotamers, which correlates with its location in a surface exposed loop region. HisJ C45R1 exhibits spectral features that indicate a restricted degree of mobility ($\tau_{HisJ\ C45R1}$= 6.2 ns) which agrees with the R1 orientation facing the protein interior with only few rotamers (3) predicted by the rotamer library analysis. Site T151R1 is located in an α-helix with 59 predicted rotamers exposed on the protein surface suggesting high motional freedom. However, the assumption of a highly mobile spin label based on the rotamer library approach is not reflected in the according EPR spectrum which exhibits motional restriction of R1 ($\tau_{HisJ\ T151R1}$= 5.7 ns) similar to position C45.

Due to a pressure dependent diminishing of the EPR signal, which applies to all investigated variants of HisJ to the same degree, measurements were accomplished only up to a maximum of 200 bar in steps of 20 bar. A quantitative analysis of the spectra was only taken in consideration up to 100 bar (figure 4.24 a,b,c), because of the extreme spectral broadening that already occurred at small pressure values and which did not allow a reasonable simulation of the acquired data over the whole range of applied pressures. Accordingly, a mainly qualitative analysis of the obtained results is given as follows.

In all cases the substrate bound variant shows a reduced signal compared to the substrate-free form. Both the substrate-free and the substrate-bound sample were produced utilizing the same respective HisJ stock solutions. A dilution of the sample by adding 1 mM of histidine (dilution factor of 0.01) cannot be responsible for the lower signal intensity. A mechanical issue in the course of loading the EPR sample cell or inefficient tuning of the EPR spectrometer could be responsible in this context. However, this divergence does not influence the interpretation of the altering protein- and according spin label-properties induced by pressure.

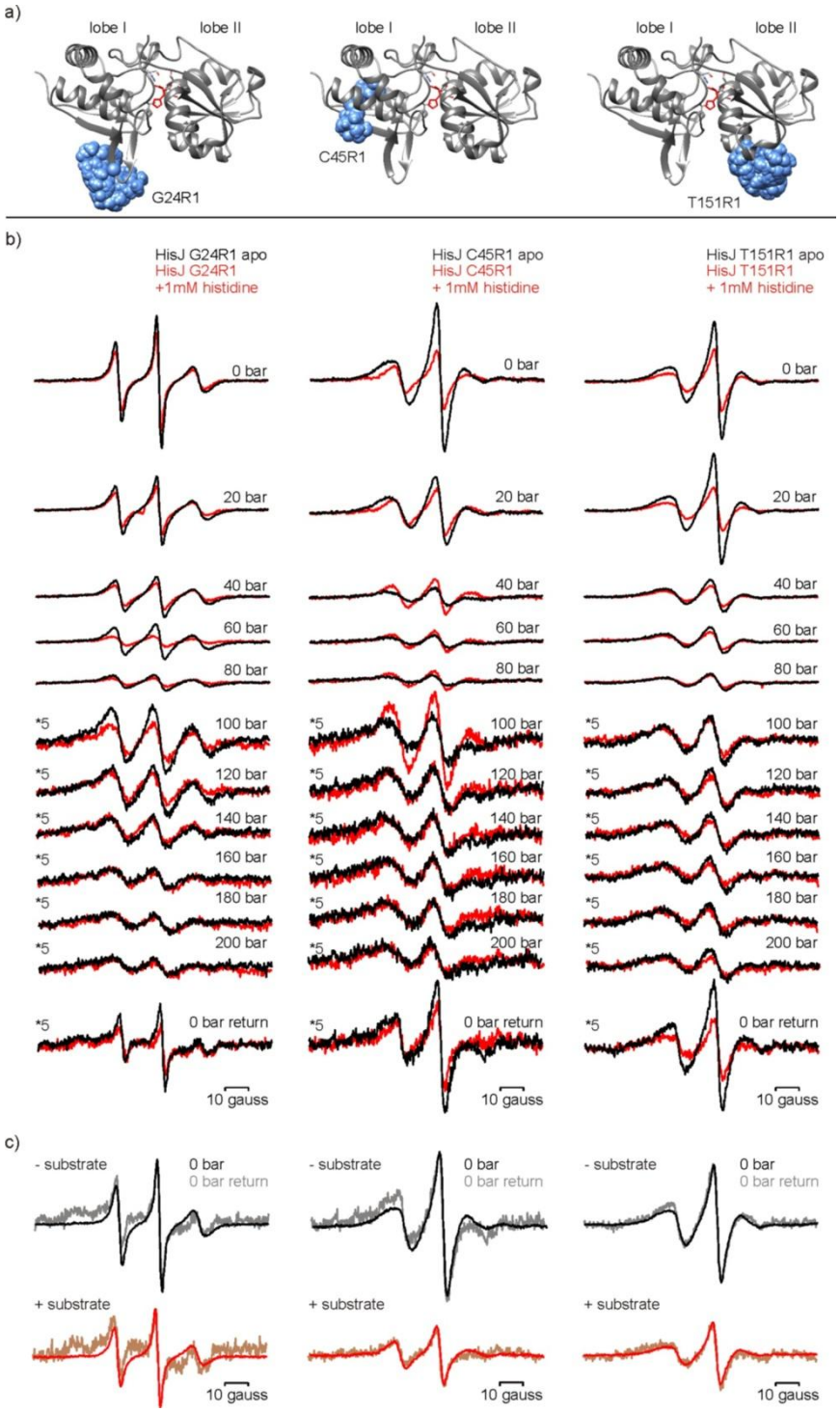

Figure 4.24: High pressure dependence of HisJ G24R1, C45R1 and T151R1 in absence and presence of histidine. a) Crystal structure of HisJ with histidine (red) (1HPB.pdb) withl MTS-spin label distribution (blue sphere) at positions G24, C45 and T151. b) HP-EPR spectra of 300µM HisJ G24R1 (left row), 300µM HisJ C45R1 (middle row) and HisJ T151R1 (right row) in the absence (apo – black line) or presence (1 mM histidine – red line) of substrate. High pressure was induced in steps of 20 bar starting at atmospheric pressure rising up to 200 bar in total. Spectra denoted with *5 were multiplied with a factor of 5 for better presentation. c) EPR spectra at atmospheric pressure (black line – without substrate; red line – with substrate) and after de-pressurization (gray line – without substrate; brown line – with substrate) normalized to maximum.

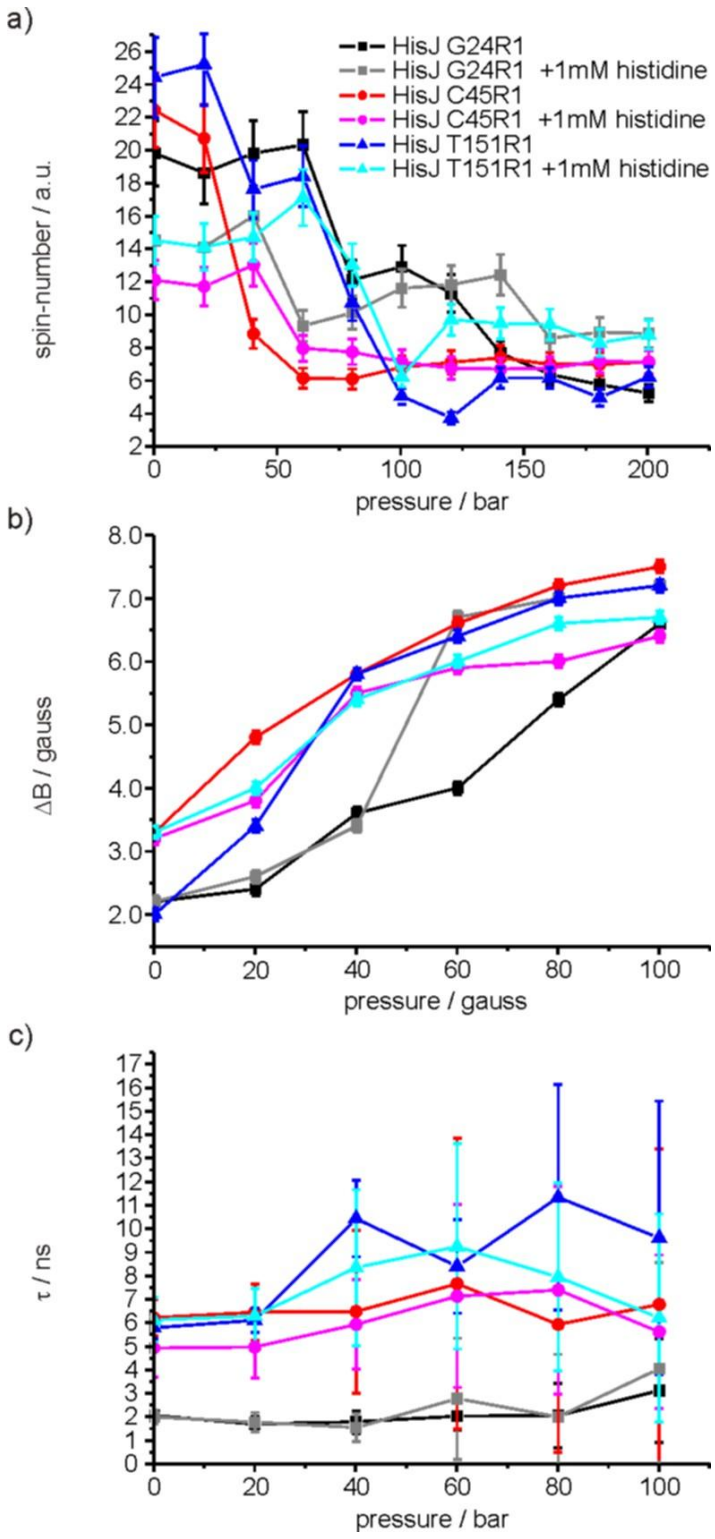

Figure 4.25: Pressure-dependent changes on different parameters of spin labeled variants of HisJ. Spin-number (a), spectral linewidth (b) and rotational correlation (c) of 300µM HisJ G24R1, C45R1, T151R1 in presence and absence of substrate (1mM histidine) in dependence of pressure perturbance.

The influence of hydrostatic pressure on all studied HisJ variants is already observed at an initial pressure value of 20 bar. A change in the shape of the EPR spectrum occurs that is characterized by increased broadening of the linewidth and decreasing resonance line amplitudes which can be associated to varying rotational correlation times and/or spin-spin coupling, and/or precipitation (see figure 4.24b and 4.25b & c) revealing a pressure dependent perturbance and altering of the protein conformational order.

Figure 4.25a depicts the decrease of the measured spin-numbers of the HisJ variants over pressure. The reduction of signal intensity is possibly due to precipitation of the aggregated sample. Due to the according difficulty to determine the line-width change ΔB of the middle resonance line (M = 0) the progression of ΔB over pressure is depicted in figure 4.25b beginning at atmospheric conditions and rising to 100 bar only. The linewidth increases more than twice which must be explained by increasing spin-spin interaction because the rotational correlation time (4.25 c) does not display such a distinct

change over pressure. This could point towards a pressure induced oligomerization of the protein. All studied samples do not exhibit significant changes of τ over the range of applied pressure. The progression of τ, however, should be interpreted carefully because the spectra´s signal-to-noise ratio decreases with increasing pressure and therefore the error of τ increases correspondingly.

The return to atmospheric pressure (~1 bar) drives a change of the EPR spectra back to narrow linewidths and increased amplitudes (figure 4.24). Accordingly, this indicates a recovery of the protein, which remained in the resonator, back to its native monomeric state.

The comparison of the histidine-free and the histidine-bound form of HisJ shows a difference in pressure dependence. The signal intensity of all histidine-bound variants is reduced to smaller degree with increasing pressure compared to the samples without the substrate (figure 4.25a). This is giving evidence that the binding of histidine leads to a higher resistance against the pressure induced precipitation for all studied variants. Figure 4.24b and 4.25 b show that the addition of histidine implicates spectral changes for C45R1 and T151R1 at atmospheric pressure already, with most prominent changes of the spectrum of HisJ C45R1. C45R1 responds with a minor reduced ΔB upon substrate binding. On the contrary, the linewidth ΔB of T151R1 increases upon substrate binding at atmospheric pressure. It occurs that the spectral line shapes of substrate-bound HisJ G24R1 shows a stronger broadening, based on larger spin-spin interactions, than the substrate-free form above 40 bar (figure 4.25b) until the spectra of substrate-free and –bound forms are broadened to an almost equal extent. The opposite effect emerges for the substrate-bound form of HisJ T151R1 and HisJ C45R1. Though increasing, the spectral broadening of T151R1 with histidine is smaller over pressure compared to the substrate-free variant. In the case of C45R1 the substrate-free form of the protein shows a stronger spectral broadening caused by pressure than the substrate-bound form. Similar to the substrate-free forms, the substrate-bound variants exhibit no significant changes of τ over the range of applied pressure.

4.2.4 Hydrostatic pressure effects on monomeric α-synuclein and its amyloid fibril formation.

4.2.4.1 Aggregation of the α-synuclein monomer into its amyloid fibril formation

The intrinsically disordered protein (IDP) α-syn, more specifically its aggregated amyloid fibril form, which is associated to Parkinson´s disease (PD), represents a very attractive model for pressure perturbance experiments. Since other studies have already shown that the highly organized structure of α-syn fibrils and other amyloidic aggregates are sensitive to hydrostatic pressure [54, 55] further analysis in this direction, in order to elucidate the mechanisms of amyloid fibril association and dissociation, was realized in this study with the established HP-EPR setup which was not accomplished to our knowledge in other studies by now. In this context HP-EPR is able to trace volumetric changes between the fibril to the monomer form.

In this study the investigated IDP is the human α-syn, modified with a N-terminal His-tag for purification purposes. The investigated site at position V74 was chosen with regard to its proposed location in a β-strand rich sequence, see chapter 4.1.7.7 figure 4.11, that is located within the second half of the fibril core region. Due to the compact packing of the fibril core it can be estimated as a rigid environment which would clearly confine the attached spin label´s degree of motional freedom, see inset in figure 4.26 a. This behavior was already verified in previous EPR experiments that display an immobilization of the spin-labeled sites in the fibril core in comparison with the high degree of mobility in the monomeric random coil structure [29, 45]. Similar results were obtained in this study as depicted in figure 4.26 a. Exposing a spin labeled α-syn sample to the defined conditions for fibrillation, alters the according EPR spectrum of monomeric α-syn, which shows very mobile features, into a spectrum showing mainly the broadened features of the aggregated formation with only small contributions of the mobile monomer. The reason behind the spectral broadening resulting in a single line is strong Heisenberg exchange and dipolar interactions due to overlapping orbitals of several spin labels within the tight packed core formation. As a result of this, contributions to the spectrum that arise alone from the overall conformational change of the protein monomer to the fibril form are impossible to distinguish from the contributions of the exchange interactions. This issue made it also particularly difficult to simulate the obtained spectra to calculate

characteristic parameters. Simulations of the spectra were therefore renounced. This problem could be solved in further studies by introducing spin diluted protein samples into the fibrillation process.

Since the fibrillation process is an equilibrium reaction a respective EPR spectrum always comprises of both the monomer and the aggregate contributions shifted in ratio depending on conditions like temperature, salt concentration and incubation time. It is possible that a very small fraction of the aggregate is formed under conditions in which the conformational equilibrium is predominately shifted to the monomer. Therefore, the aggregated form can contribute to the spectrum of the monomer stock solution but is barely traceable due to the much higher signal of the monomer in the sample.

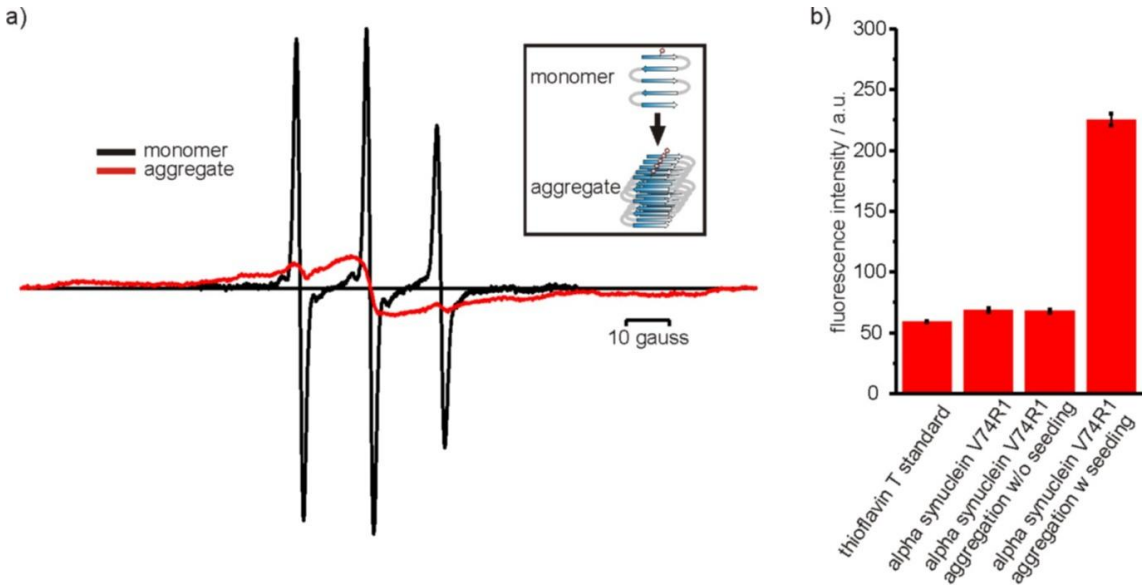

Figure 4.26: Aggregation of α-synuclein into amyloid fibrils. a) cw-EPR spectra of the α-syn V74R1 monomer (black line) and the aggregated α-syn V74R1 fibril form (red line). Inset: schematic of spin labeled α-syn aggregation from the β-sheet rich monomer to the aggregated fibril form. b) Histogram of amyloid-structure specific thioflavin T assay on the α-syn V74R1 monomer and on α–syn V74R1 aggregation stocks after 48 h under fibrillation conditions in absence and presence of wild type fibril seeds.

To facilitate the fibrillation process of spin labeled α-syn it was necessary to add a small amount of prepared disrupted fibrils produced from the α-syn wildtype to the spin labeled protein monomer solution as a nucleation seed [22]. Previous attempts to generate fibril growth from spin labeled protein alone failed and did not result in

enhanced fibril formation. As shown in figure 4.26 b a notable increase of β-sheet rich aggregate, verified by an amyloid specific thioflavin T binding assay [104], occurred only in presence of wild type fibril-seeds, otherwise progresses only on a very long timescale. Still a small fraction of fibrillated α-syn V74R1 was detectable in the non-incubated stock solution and the aggregation mix without nucleation seeds. This contributes to the notion that fibrillation of the spin labeled α-syn can occur independently from a nucleation seed, as assumed from EPR data, but only on a very long time scale. It is also important to mention that the N-terminal His-tag did not interfere with the formation of fibril aggregates although the primary sequence influences the fibril stability and growth as was shown in earlier studies [36]. The α-syn V74R1 monomer and the obtained amyloid fibrils were investigated by means of time resolved high pressure EPR, as described in the following paragraphs.

4.2.4.2 Pressure can trigger the oligomerization of the α-synuclein monomer

In order to understand the impact of pressure on the intrinsically unfolded monomer three different concentrations of the α-syn V74R1 sample were examined.

Figure 4.27 elucidates the pressure dependence of two α-syn V74R1 monomer samples of varying concentration (100 µM and 460 µM) and time resolved spectral changes of the higher concentrated sample as well. The pressure-dependent measurements of α-syn V74R1 (100µM), depicted in figure 4.27 a, show no spectral change over a range of 2000 bar, as indicated by the normalized spectra. Also the rotational correlation time is not effected significantely by pressure, as depicted in figure 4.28. A linear plot to ln(τ/τ0) yields an activation volume close to zero ($\Delta V^{\ddagger}$=-0.19±0.04 ml/mol). This gives reason to assume that pressure does not influence the conformational state of the monomer. The return to ambient pressure, however, leads to signal decrease maybe due to a displacement of the sample in the ceramic pressure cell upon pressure release. Investigations on an α-syn V74R1 sample of higher concentration (460 µM) under equal experimental conditions are depicted in figure 4.27 b and show a similar behavior. Again an alteration of the spectral line shape is not evident over the whole range of applied pressures, as evident of the normalized spectra, which indicates that in this experiment the protein stays in its soluble monomeric state as well. However, a reduction of signal intensity occurs at

400 bar and proceeds until 1000 bar where the signal intensity reaches approximately 40% of the starting signal intensity at ambient pressure. Again this effect is probably due to a displacement of the sample or its dilution in the ceramic pressure cell, triggered by increasing pressure. After returning to atmospheric pressure the sample did not show any spectral changes within 48 h (see figure 4.27 c). There is no indication in this experimental approach for an effect on the monomeric conformational state based on pressure.

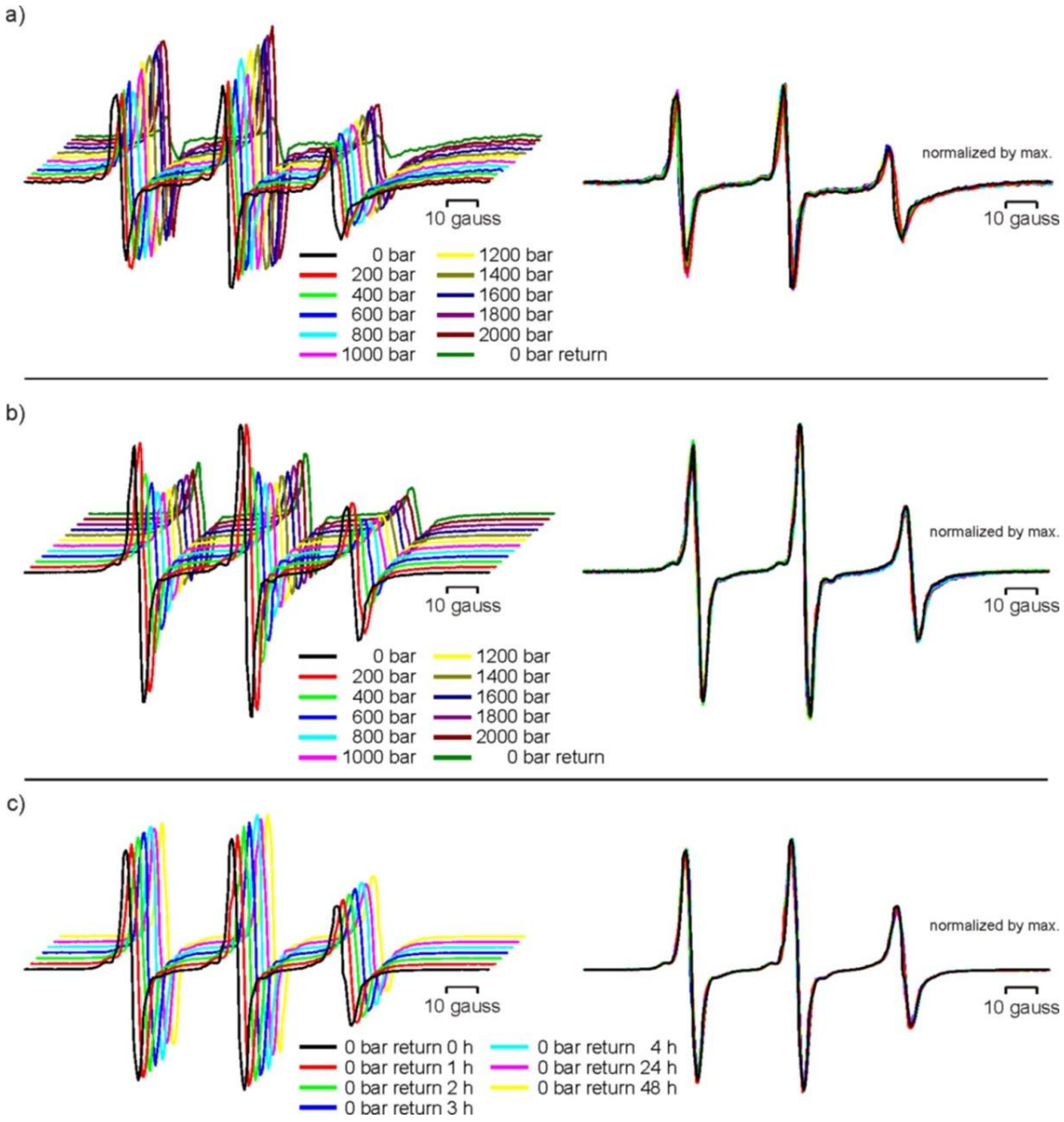

Figure 4.27: Pressure and time dependencies of monomer α-synuclein at a concentration of 100 and 460 µM. a) EPR spectra of α-syn V74R1 (100 µM) monomer under pressure perturbance ranging from atmospheric conditions (1 bar) up to 2000 bar in steps of 200 bar (left). Overlay of the EPR spectra normalized by their maximum (right). b) EPR spectra of α-syn V74R1 (460 µM) monomer

under pressure perturbance ranging from atmospheric conditions (1 bar) up to 2000 bar in steps of 200 bar. Overlay of the EPR spectra normalized by their maximum (right). c) EPR spectra of α-syn V74R1 (460 µM) monomer at atmospheric pressure in dependence to time. Overlay of the EPR spectra normalized by their maximum (right).

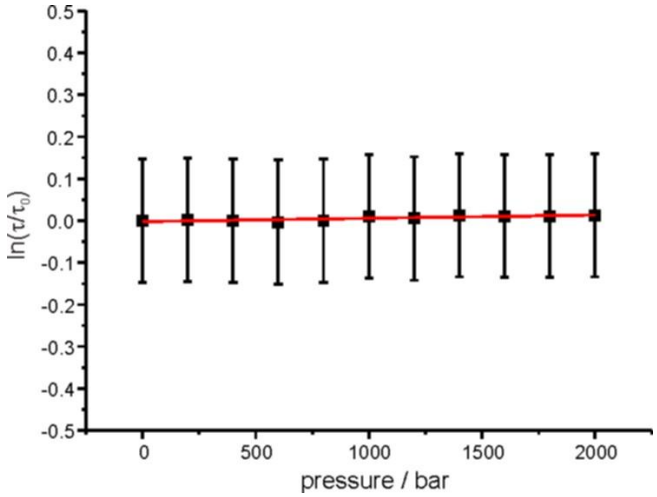

Figure 4.28.: Pressure dependent reorientational correlation times of the α-synuclein V74R1 monomer. Values for $\ln(\tau/\tau_0)$ plotted versus pressure (black squares) of the α-syn V74R1 (460 µM) monomer. A linear fit is depicted as solid red line.

Figure 4.29 elucidates the pressure dependence of high concentrated (1.4 mM) α-syn V74R1 in solution. Increasing the pressure from atmospheric conditions to 200 bar leads to a change of the spectral line shape that is characterized by line broadening typical for spin-spin interaction as evident from the normalized spectra (for 200 and 400 bar) shown in the inset of figure 4.29. As shown later these spectral line shapes do not coincide with those of the fibril form or the artificially precipitated protein (figure 4.31) and therefore point to an unspecific oligomeric form induced by pressure. At 1200 bar and beyond the characteristic resonance lines of the nitroxide spectrum become almost completely unrecognizable due to line broadening as a result of spin-spin interaction and decreasing signal intensity. This effect could result from an unspecific aggregation process. The return to ambient pressure is accompanied by decreasing of the spectral line width close to the starting condition before pressurization (see inset figure 4.29) indicating dissolving of the aggregated state. The decreased signal intensity during the experiment is probably caused by

precipitation of aggregated protein followed by sedimentation out of the sensitive volume of the resonator.

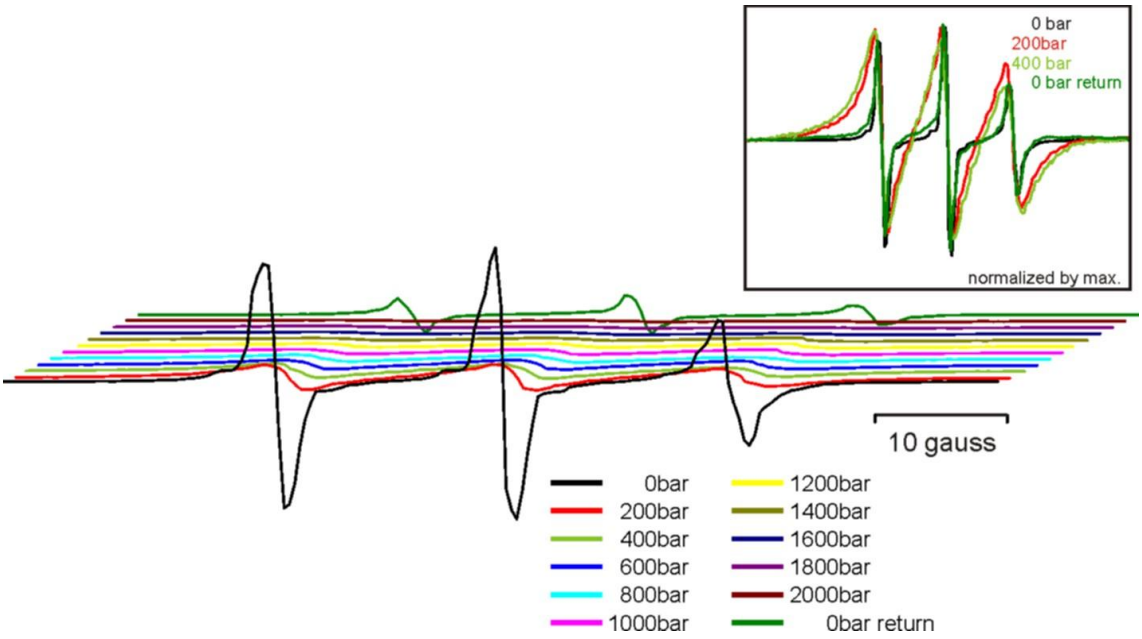

Figure 4.29: Hydrostatic pressure dependence of high concentrated monomer α-synuclein. EPR spectra of α-syn V74R1 (1.4 mM) monomer under pressure perturbance ranging from atmospheric conditions (1 bar) up to 2000 bar in steps of 200 bar. Inset: comparison of the EPR spectra (normalized by maximum) at ambient pressure conditions (black line), at 200 bar (red line), at 400 bar (light green line) and after returning to atmospheric pressure (dark green line).

Further investigations on the pressure-dependent aggregation of α-syn were accomplished with a smaller sample concentration. Two different experimental approaches are shown. Figure 4.30 a and b depict pressure-dependent experiments with a lead incubation time of 48 h at room temperature within the sample cell before pressurization. Figure 4.30 a depicts investigations on 100 µM α-syn V74R1. In this particular experiment a time dependent spectral change occurs within 24 h of incubation. Both spectra at 24 and 48 h show the line broadened contributions of an aggregated entity and of the mobile monomer. In this case it is likely that some artifact in the sample cell facilitated the aggregation of the protein and served as nucleation seed. Presumably, amyloid fibrils have formed in the sample cell which is indicated by comparison of the spectrum recorded after 24 h with the spectrum of α-syn V74R1fibrils, see figure 4.31. Inducing 200 bar after 48 h leads to an additional

broadening of the spectral line shape and to disappearance of the monomer signal contribution. This effect is also observed upon pressurization of the amyloid fibrils of α-syn (figure 4.32 a). In contrast, further increase of pressure does not result in complete dissolving of the aggregate at maximal pressure (2000 bar) as it would be expected from experiments on amyloid fibrils (see below). The spectrum at 2000 bar does not resemble the line shape of the monomeric α-syn spectrum at atmospheric pressure though the signal intensity is increasing and line widths are decreasing due to pressurization. Actually the respective spectral line shapes point toward an oligomeric entity similar to the experiments on highly concentrated α-syn. Returning to ambient pressure implies a converging of the spin labels and therefore an immediate fibril re-aggregation indicated by de novo line width broadening. A comparison of the most important spectral changes in this experiment is given in the inset of figure 4.30 a. However, the lead incubation time can also induce a different pressure dependence of the α-syn monomer as long as no time-dependent fibrillation has taken place before pressurization as depicted in figure 4.30 b. An aggregation process of the protein within the pressure cell does not take place within the lead incubation time of 48 h, most likely to a missing nucleation seed. Instead, aggregation is induced upon pressurization of the sample with 200 bar pointed out again by converging spin labels and associated dipolar coupling. Line broadening increases further with pressure until 600 bar and maintains the resulting spectral line shape up to 2000 bar. Once more the respective spectral line shape points towards an aggregated species that differs from the amyloid fibril form. De-pressurization drives the opposite effect of line width reduction although the broadening effect is not completely reversible, see inset in figure 4.30 b.

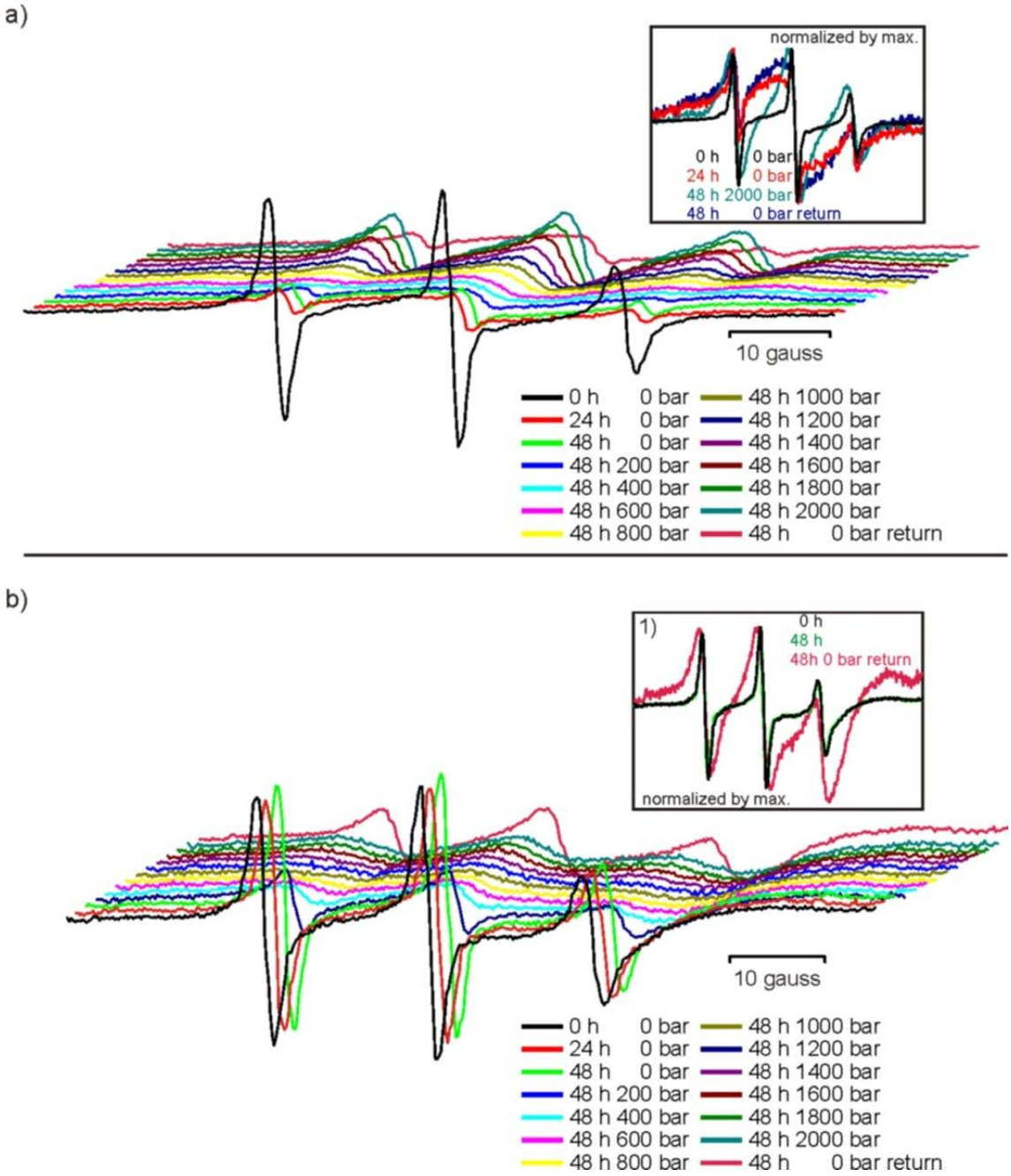

Figure 4.30: Differing aggregation pathways of monomeric α-synuclein (100 µM) in dependence of lead incubation time and pressure. a) EPR spectra of α-syn V74R1 monomer (100 µM) after 48 h incubation at room temperature in the EPR sample cell and under pressure perturbance up to 2000 bar in steps of 200 bar . Inset: comparison of the EPR spectra (normalized by maximum) at ambient pressure (black line), after 24 h (red line), after 48 at 2000 bar (cyan line) and after 48 h returning to ambient pressure (dark blue line). b) EPR spectra of α-syn V74R1 (100 µM) monomer after 48 h incubation at room temperature in the EPR sample cell and under pressure perturbance up to 2000 bar in steps of 200 bar. Inset: comparison of the EPR spectra (normalized by maximum) at ambient pressure (black line), after 24 h (red line), after 48 at 2000 bar (cyan line) and after 48 h returning to ambient pressure (dark blue line).

Figure 4.31 depicts EPR spectra of α-syn V74R1 that indicate an unspecific aggregation process, with respect to different conditions of incubation time and applied pressure, in comparison to the spectra of amyloid fibrils produced from α-syn V74R1 and of α-syn V74R1 artificially precipitated with acetone. It appears that the spectrum of time dependent aggregation resembles the spectrum of the amyloid fibrils. In this case it can be hypothesized that incubation over time promoted amyloid fibril growth through an unspecified seeding or nucleation event since for spin labeled α-syn a seeding nucleus is necessary to grow fibril form aggregates due. Spectra that depict an aggregation based change of the spectral features due to hydrostatic pressure show a different behavior in comparison to time based aggregation and artificially sedimented protein precipitated with acetone.

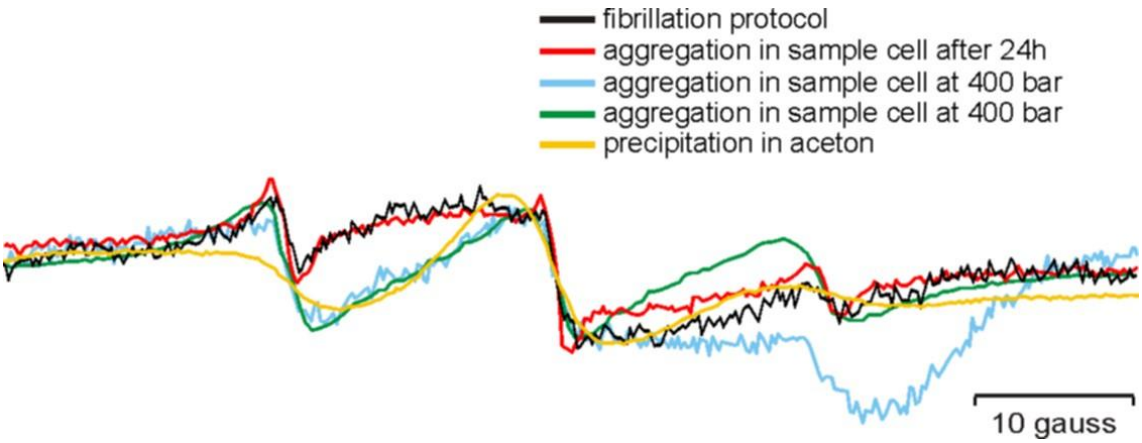

Figure 4.31: Comparison of α-synuclein aggregates. Normalized spectra of α-syn V74R1 amyloid fibril form (black line), α-synuclein V74R1 (100 µM) incubated 24 h in EPR pressure cell at room temperature without agitation (red line), α-syn V74R1 (100 µM) at 400 bar (cyan line), α-syn V74R1 (1,4 mM) at 400 bar (green line), α-syn V74R1 (100 mM) in acetone (yellow line).

The difference is recognizable especially in the discrete line broadening that occurs between the low- and middle-field resonance-line. This indicates a more relaxed conformational packing in the pressure-dependent aggregate with bigger distances between spin-labels compared to the amyloid fibril formation. This correlation verifies a pressure dependent form of aggregation that differs from the time based fibrillation process. On the other hand, the differences between spectral line shapes of the precipitate in aceton and the non-amyloid aggregates indicate that pressure does not only triggers precipitation and sedimentation of the monomeric protein but induces

the formation of an unspecific oligomeric species. This pressure-dependent aggregation pathway of the α-syn monomer is further debated in the discussion.

4.2.4.3 Dissolving amyloid fibril formation by hydrostatic pressure

The influence of pressure on amyloid fibrils grown from α-syn V74R1 is depicted in figure 4.32 a.

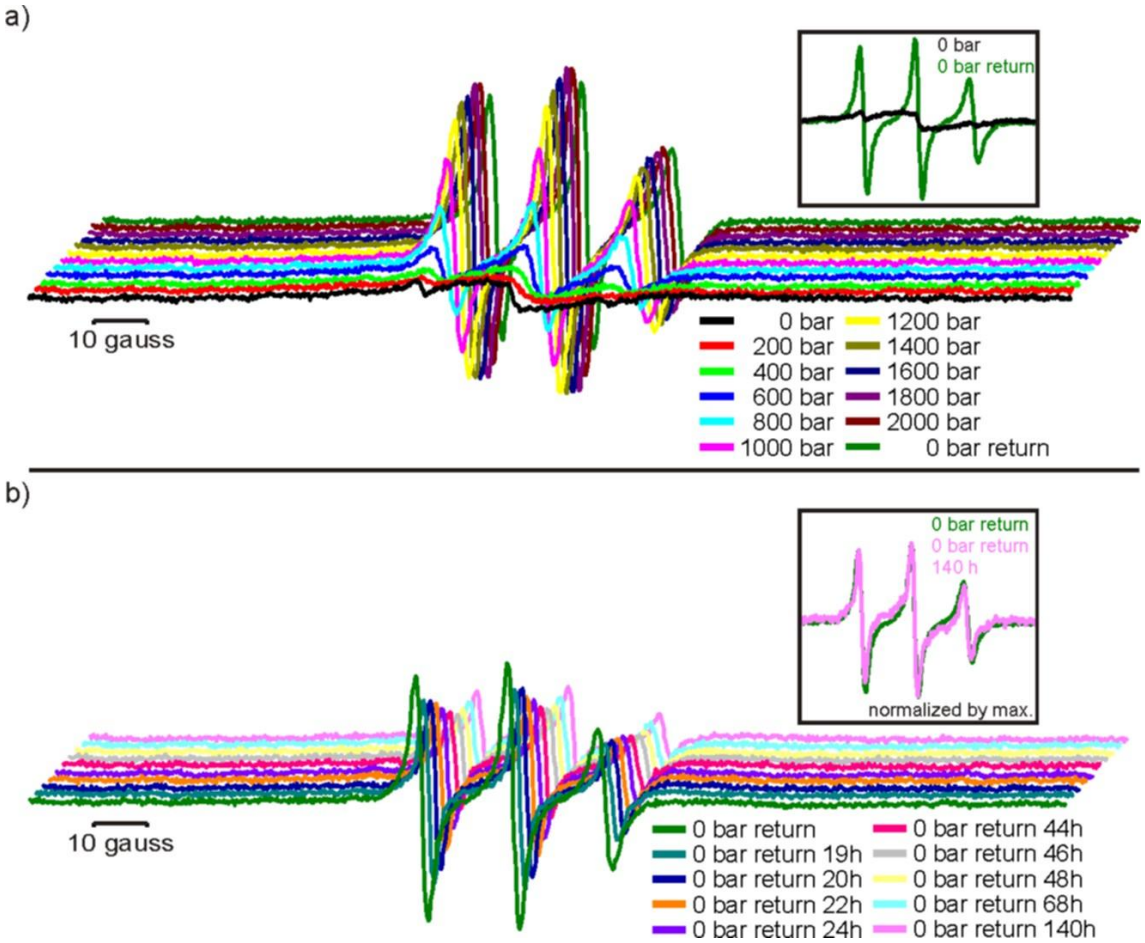

Figure 4.32: Hydrostatic pressure dependence of α-synuclein aggregate and time dependent behavior of monomeric α-synuclein dissolved by pressure. a) EPR spectra of α-syn V74R1 fibrils under pressure ranging from atmospheric pressure (1 bar) up to 2000 bar in steps of 200 bar. Inset: comparison of the EPR spectrum at atmospheric pressure (black line) and upon return to atmospheric pressure after applying 2000 bar (green line). b) EPR spectra of α-syn V74R1 monomer from dissolved fibrils at atmospheric pressure as function of time. Inset: comparison of the EPR spectra (normalized by maximum) directly after de-pressurization (green line) and after 140 h (pink line) at atmospheric pressure.

As before, investigations were accomplished utilizing the EPR pressure cell described above at pressures up to 2000 bar in steps of 200 bar. An increase of pressure from atmospheric conditions to 200 bar leads first to further broadening of the EPR spectrum, indicated by almost complete vanishing of the small contributions from the mobile α-syn monomer at ambient pressure. This is a hint on an aggregating effect induced by low pressure (<200 bar) on the α-syn monomer in the presence of fibrils. Further progression of pressure results in a conformational transition, starting between 400-600 bar, from the aggregated form to the monomer until the fibril formation is dissolved completely at 1800 bar. This correlation is visible in the changes of the spectral lineshape over pressure namely, the increasing amplitudes of the re-appearing three nitroxide resonance lines, the decreasing line widths and the disappearing exchange interactions. Figure 4.33a depicts the increase of the middle field resonance line amplitude indicating a shift from the fibril form to the monomer. Two different fitting approaches, a linear and a quadratic fit, were applied on the plot because a linear relationship can be assumed in the range from 0-1400 bar but ln(k/k0) versus pressure shows a non-linear behavior between 1600-2000 bar. In the case of a non-linear relation between $\ln(k/k_0)$ and pressure, which points towards a conformational equilibrium, the isothermal compressibility can be assumed to be $\Delta\boldsymbol{\beta_T} \neq 0$ [133]. The linear fit to the experimental data yields the values for the differences in partial molar volume $\Delta\boldsymbol{V^0}$=-60.7±4.0 ml/mol and the isothermal compressibility $\Delta\boldsymbol{\beta_T}$=0. The quadratic fit in contrast yields a change in both the partial molar volume $\Delta\boldsymbol{V^0}$=-85.3±12.9.0 ml/mol and the partial molar isothermal compressibility $\Delta\boldsymbol{\beta_T}$=-0.025±0.012 ml/mol bar.

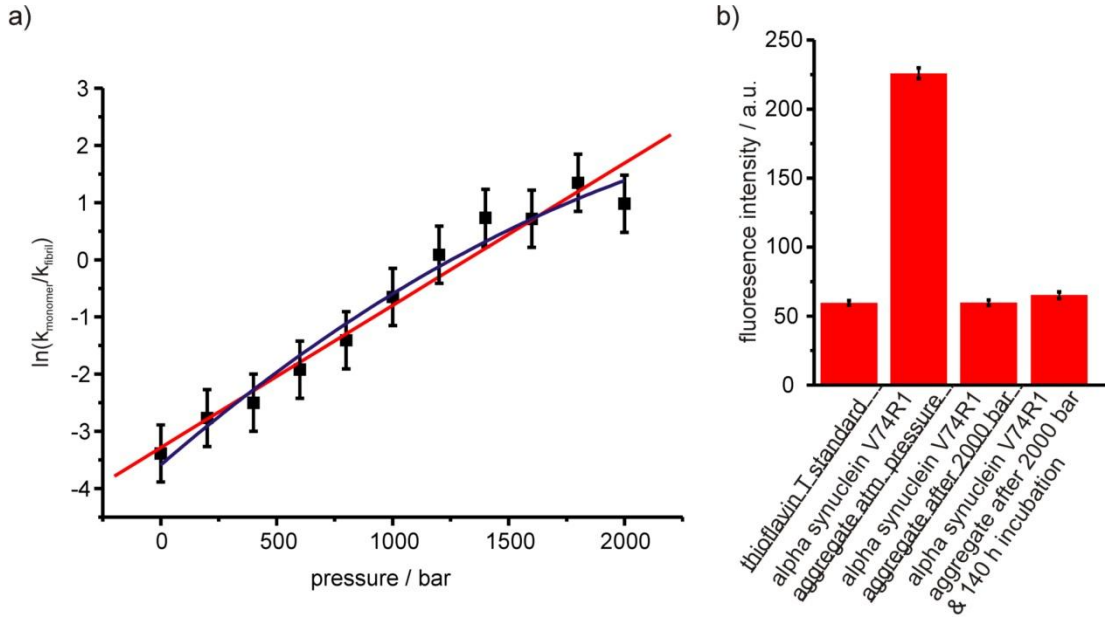

Figure 4.33: Progression of dissolving α-synuclein V74R1 fibrils by high hydrostatic pressure. a) Plot of α-syn V74R1 amyloid fibril´s middle field resonance line amplitude Δh_0 taken from the according EPR spectra versus the applied pressure. A linear fit to the equilibrium constants vs. pressure is depicted as red line. A quadratic fit (2nd order polynomial) to the equilibrium constants vs. pressure is depicted as blue line. b) Histogram of amyloid-structure specific thioflavin T assay on the α-syn V74R1 aggregate before pressurization (atmospheric conditions) , after pressurization (2000 bar) returning to atmospheric conditions and after pressurization (2000 bar) returning to atmospheric conditions in addition to 140 h incubation within the high pressure sample cell at room temperature.

This notion is supported by comparison of the amount of β-sheet rich amyloid structures in the samples of the aggregated α-syn V74R1 before and after pressurization (figure 4.33b). At de-pressurization from 2000 bar to ambient pressure conditions the signal amplitude decreases probably because of displacement of the sample within the EPR pressure cell as there is no indication for immediate re-aggregation of the protein. Time-dependent changes of the same sample after returning to atmospheric pressure are depicted in figure 4.32b. Over 140 h the signal intensity decreases by approximately ~57%. This may be due to slow diffusion and therefore decreasing concentration of the sample in the sensitive volume of the EPR pressure cell. In addition, an emerging broadening of the spectral line shape as obvious after 140 h (inset of figure 4.32b), especially at the middle field resonance line, could indicate a slow re-fibrillation process. Comparison of the fluorescence intensities obtained from a Thioflavin T assay support the assumption of a slow re-fibrillation process due to increasing intensity after incubation for 140 h, as depicted in figure 4.33b.

4.3 Discussion on HP-EPR studies on soluble proteins and amyloid aggregates

4.3.1 Viscosity change and compression of an aqueous solution and an organic solvent as a result of applied pressure

Variable pressure has influence on fluid´s viscosity and its amount of compression such as an aqueous solution. In this context clarification of the pressure induced effects on free spin label in solution is a prerequisite for further investigations on spin labeled proteins. The results of this work indicate that the influence of variable pressure on the viscosity of an aqueous solution can be neglected for investigations on soluble spin labels or spin labeled proteins since the detected changes of the EPR line shape of a nitroxide in aqueous solution is marginal over the range of applied pressure. This is supported by the fact that the viscosity of water declines faintly at room temperature with increasing pressure and is set around <0.9 mPa*s in the range of 1-1000 bar at 293.15 K [178]. Therefore an impact on the spectral line shape due to pressure induced increasing viscosity cannot be expected in measurements of free spin label in solution and soluble spin labeled proteins.

However, a verifiable effect that is based on the compressibility of the solvent, which is a function of pressure and temperature, leads to an increased content of solute in the EPR resonator and an increase of the effective spin label concentration in the sample which results in a higher signal intensity but not in line shape alteration. That is the case for the investigated samples of spin label in aqueous Tris buffer (4% increase of signal intensity at 2000 bar) and 1-hexanol (7% increase of signal intensity at 2000 bar). Studies state that the alkanol is compressed by ~3% at 400 bar and 298.15 K [132] and is much more affected by this behavior than the aqueous solution. A reference quotes a compression of water by only 12% at 4 kbar [27]. Therefore the described effect can be thought of as a minor impact for an aqueous buffer solution and for the range of applied pressures utilized in this thesis.

4.3.2 Pressure perturbation alters the structural integrity of bovine serum albumin.

First investigations on the perturbance of the conformational equilibria of a protein utilizing high hydrostatic pressure were accomplished with spin labeled bovine serum albumin. From high pressure EPR data the dependence of the spin labels rotational correlation time τ on the applied pressure was demonstrated. Derived from the pressure-dependent changes of τ the activation volume for rotational diffusion of the spin label ,$\Delta V^{\ddagger}$, was determined which gives information about the change of the volumetric properties of the solvent cage surrounding the spin label necessary for steps of rotational diffusion. Thus the parameter is one qualitative indicator for the site-dependent internal dynamics of the nitroxide label [133]. $\Delta V^{\ddagger}$ for C34I1 are consistently negative for the mobile ($\Delta V^{\ddagger}_{mobile}$ = -3.3±0.4 ml/mol) as well as for the immobile ($\Delta V^{\ddagger}_{immobile}$ = -1.0±0.3 ml/mol) component of BSA C34I1.

The negative $\Delta V^{\ddagger}$ values support the notion that the spin label side chain is in a high volume state, probably due to interaction with neighboring protein side chain or backbone atoms, and suggest that the transition state of spin label reorientation involves a hydration-mediated activated state of smaller volume. In contrast, for completely solvent-exposed non-interacting nitroxides, the R1 side chain at position V74 of the α-syn monomer, the activation volume is close to zero (this work). Positive activation volumes were found for unbound spin labels in solution ($\Delta V^{\ddagger}_{OH\text{-}Tempo}$=4.6±3.8 ml/mol, this work) and spin labeled sites in T4 lysozyme ($\Delta V^{\ddagger}_{80R1}$=2.3±0.4 ml/mol; $\Delta V^{\ddagger}_{82R1}$=1.2±0.5 ml/mol) which is explained by contributions of backbone motions to the kinetic unit [133].

The presence of GdnHCl has a supporting impact on the pressure-dependent denaturing effect on BSA C34I1. The activation volumes for both the mobile and immobile spectral component are also negative, $\Delta Vm^{\ddagger}_{mobile}$ = -1.4±0.5 ml/mol and $\Delta V^{\ddagger}_{immobile}$ = -2.1±0.4 ml/mol, similar to BSA C34I1 in absence of the chaotropic agent. Because the presence of guadinine hydrochloride denaturates the native structure of the protein, interactions of C34I1 with backbone and side chain atoms may change and the additional pressurization of the sample implicates a higher $\Delta V^{\ddagger}$ of the mobile component compared to the C34I1 in the absence of the denaturating agent. On the other hand, $\Delta V^{\ddagger}$ of the immobile component decreases in the presence of GdnHCl indicating that the volume for a rotational diffusive step gets smaller than in the absence of GdnHCl. The largest $\Delta V^{\ddagger}$ (4.2 ml/mol) in the studies on T4

lysozyme was detected for site 118R1 in the presence of a denturating agent (urea) [133]. 118R1 is similarly buried in a crevice on the protein´s surface like C34I1 in BSA, and reveals an interaction of the spin label side chain with a segment of the protein backbone in the activation state, therefore increasing the volume of the kinetic unit [133].

The most obvious impact of high pressure on the side chain dynamics of IAA connected to the backbone of BSA at position C34 is visible in the reversible shifts of the mobile and immobile components representing the equilibrium between the two states. The equilibrium of the spectral components originates either from slow exchange between the two rotamer populations of I1 or an exchange between two conformational substates of the protein [20]. In both cases the respective equilibrium constant K is directly dependent to pressure and is therefore defined by equation 4.9 from chapter 4.1.4. Earlier studies have already shown that the two spectral components of site C34I1 are based on the equilibrium of rotamers that are either solvent exposed or constrained in a crevice, in close proximity to the local backbone [9, 40].

Consequently; it can be figured that the recess on the protein surface harboring position C34 is structurally perturbed or gets more accessible and solvent-exposed by hydration. This observation would correlate with the assumption of a rotameric equilibrium. This interpretation is also supported by McCoy and Hubbell who state that a linear relationship of $\ln(k/k_0)$ versus pressure is representative for a rotameric equilibrium, which is theorized in other high pressure EPR-studies on T4-lysozyme [133]. On the contrary, a non-linear relationship would be exemplary for a conformational equilibrium. Therefore, high pressure EPR establishes a criterion for distinguishing rotameric from conformational equilibria [133]. The linear dependence of $\ln(k/k_0)$ gives also evidence that the compressibility does only change marginally ($\Delta\beta_T \approx 0$) between the mobile and the immobile state. Though, there is evidence of non-zero changes of the compressibility relating to a non-linear dependence of lnK versus pressure the influence of pressure perturbance on the compressibility of proteins remains a matter of debate [176]. The pressure induced change in the partial molar volume at site C34I1 amounts to ΔV^0 = -6.0±0.4 ml/mol representing the reversible shift to lesser conformational order according to the volume theorem [4]. A similar linear progression of $\ln(k/k_0)$ versus pressure was found for the T4 lysozyme

variant 44R1 giving ΔV^0 = -9.4±2.2 ml/mol and $\Delta\beta_T \approx 0$ [133]. The additional disordering effect of GdnHCl on the protein´s conformational integrity becomes noticeable in particular in the change of the partial molar volume that increases to ΔV^0 = -6.6±0.9 ml/mol in comparison to the probe without GdnHCl. Again a change of the isothermal compressibility can be ruled out in this case due to a linearity of lnK versus pressure.

4.3.3 Low pressure triggers precipitation and oligomerization of the substrate binding protein HisJ

The substrate-binding protein HisJ from *Salmonella enterica* serovar Typhimurium was chosen as another model protein for high hydrostatic pressure experiments especially with regard to its two substrate-dependent conformations. In this context the leading question is if a difference in pressure-dependence emerges between the substrate-bound and the substrate-free form of the protein. Surprisingly all studied variants of the substrate binding protein HisJ are characterized by spectral broadening, decreasing amplitudes and EPR signal loss based on an intense response to low hydrostatic pressure (<200 bar). This effect is not inflicted by pressure-dependent changes to the properties of the solvent and shows the same degree of magnitude for all investigated surface exposed sites. However, the sites differ in their affiliation to a secondary structure element and the orientation of the residue, facing inside or outside the protein interior. Accordingly, the influence of pressure on residues G24 and T151, which face the aqueous phase, is similar to the effect on residue C45, which is also located at the protein surface but is oriented into the protein interior.

The mobility of all labeled sites of the substrate-free form exhibits no evidence of restriction over the applied range of pressure since there is no significant variation of τ which indicates that the conformational structure at the investigated sites is not destabilized. However, the increasing spectral linewidths indicate that pressure perturbance triggers an increase of spin-spin interaction which can be interpreted as an oligomerization of the protein. This effect is accompanied by precipitation of the protein indicated by the loss of signal. Since the pressure resistant sample cell is inserted into the spectrometer from below, the sedimentation of the precipitated protein would be responsible for its decrement in the sensitive volume of the

resonator. The reason for the oligomerization could be attributable to the structure of HisJ. The protein consists of two globular domains connected by a hinge-region resembling in function and shape a venus fly trap, binding its substrate. Binding is coordinated by several charged amino acids within the binding pocket formed by the two lobe-like domains. As stated, there is no indication for an unfolding of the lobe-like domains due to pressure. However, the flexible structure of the substrate-free protein in respect of the hinge-region could be responsible for oligomerization of the protein. For instance, a higher accessibility for water molecules at the interface between the two globule domains induced by pressure could lead to an exposure of hydrophobic amino acid residues and thereby facilitate an entropically favored oligomerization.

Upon binding of the substrate a conformational transition occurs that decreases the distance between the two approaching globular domains, lobe 1 and 2, of HisJ. A direct structural effect or change on the studied sites upon substrate recognition and binding is not known and unfortunately only the crystal structure of the histidine bound HisJ was elucidated until now [144] which renders an interpretation relating to differing pressure-dependencies difficult. The binding of the substrate to HisJ alters the proteins response to pressure perturbance. It can be assessed that the binding of substrate decreases the water-accessible protein surface for all studied variants which could be related to the decrease of relative signal loss over pressure. It was already theorized that the oligomerization of the substrate-free protein could be due to a higher accessibility of the interface between the lobe-like domains to water molecules. Furthermore, it can be observed that the substrate-bound variants of the studied HisJ variants increase in ΔB similarly to the substrate-free variants in dependence of pressure. This points towards an oligomerization effect for the substrate-bound form of HisJ as well. Therefore, it seems likely that substrate binding does not prevent a pressure induced oligomerization of HisJ but reduces the effect of precipitation of the protein. This behavior could be attributable to substrate which remains in its binding pocket during pressurization, stabilizing the closed conformation and reducing the exposition of hydrophobic residues.
Further investigations on HisJ utilizing the high pressure approach must be scheduled at a low pressure maximum (<20 bar) because of the high susceptibility of the protein to pressure. This would allow to bypass the high signal-loss due to

precipitation of the protein and would give more accurate insight in the proteins pressure dependence in its substrate-free and substrate-bound condition.

4.3.4 Hydrostatic pressure dissociates amyloid fibrils but can also drive an unspecific aggregation of IDP monomers

As considered before amyloid fibrils are most important factors in many neurodegenerative diseases and therefore of high interest in studies about highly organized misfolding of proteins. So is α-syn, a soluble unfolded polypeptide, the hallmark protein of Parkinson´s disease (PD), aggregating into amyloid fibrils that are the main component in PD characteristic cell inclusions called Lewy bodies. In the present work *in vitro* aggregated amyloid fibrils of α-syn V74R1 were investigated to gain information about their stability against high hydrostatic pressure and to determine volumetric properties based on the conformational equilibrium of the monomeric and the fibril form. First the studies of this work approved the tight structural packing in the core region of α-syn amyloid fibrils. The highly immobilized character and emerging exchange interactions [124] in the obtained EPR data suggested not only a decreased degree of motional freedom at the investigated site but also a close contact between the spin labels. In this case the converging electron oribtals of the nitroxide spin labels, which are stacked on top of each other, have resulted in an averaging of the hyperfine interaction. Another case in which such an exchange-narrowing occurs is in crystals of spin labels, where the nitroxides are stacked in highest periodicity [13].
These results correlate with the findings of Chen et al. who also investigated the α-syn fibril structure by site-directed spin labeling and suggested a distance of 4.7-4.8 Å between the parallel aligned β-strands of single polypeptides in the fibril core, schematically depicted in figure 4.34 [2].

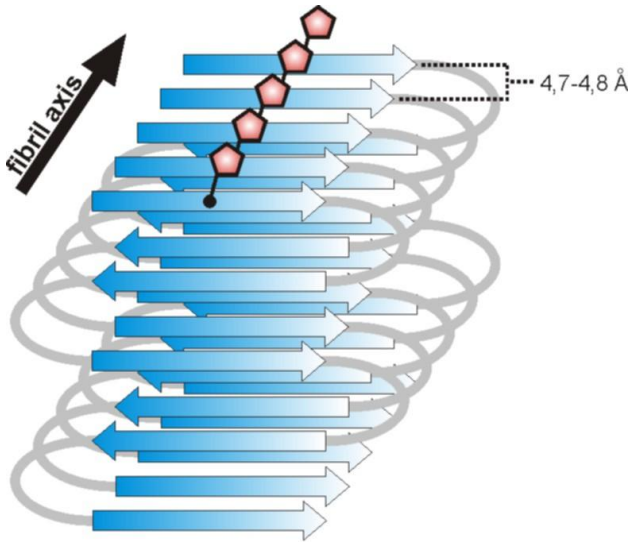

Figure 4.34: In-register arrangement of β-strands as suggested for α-synuclein amyloid fibrils. A parallel alignment of β-strands, represented by blue arrows, runs perpendicular to the fibril axis (β-strands are 4.7-4.8 Å apart). Each layer belongs to a single molecule. Spin labels, introduced at specific equivalent sites within the β-sheet rich core region (represented by red pentagons), are stacked on top of each other and are set in close proximity due to the contact between the same residues in neighboring polypeptides.

Besides the fibril formation assembly of α-syn, the results of this work also imply a different aggregation pathway of monomeric α-syn that is not only based on incubation time and protein concentration but can be induced by hydrostatic pressure. This pressure-dependent aggregate must clearly differ from the structural composition of the in-register β-sheet formation of amyloid fibrils. A looser and different kind of packing can be assumed for the non-amyloid aggregate since the obtained data of the present work suggests a larger distance between the investigated sites of the pressure dependent-aggregate in comparison to the amyloid fibril formation. An averaging of the hyperfine splitting that results in a single line as noted in the amyloid fibril spectra of α-syn does not emerge but increasing spin-spin coupling proofs the convergence of the spin label. Although the obtained data does not permit a conclusion in regard to the aggregated form, a small oligomeric species could have possibly formed. The spectral characteristics of acetone-precipitated amorphous aggregates of α-syn does not resemble the yielded data of pressure-induced aggregates. These results sharply contrast the notion of the denaturating effect of pressure on proteins especially considering the fact that the protein of interest, α-syn, is already natively unfolded as a monomer at atmospheric conditions

in solution. An unspecific pressure induced aggregation of single α-syn is not reported within the literature to date.
Studies on α-syn in cultured neuronal cells have shown that hydrostatic pressure is associated with the transition from the monomer to unspecific higher order aggregates [69]. However, this study links the aggregation process with the pressure-induced damage on α-syn binding partners like phospholipase Cβ and the dissociation of α-syn-protein heterodimers and does not indicate a pressure-dependent association of aggregates of single α-syn by itself.

Different sources in literature already stated that high hydrostatic pressure destabilizes the formation of amyloid fibrils for instance transthretin fibrils as well as α-syn-fibrils [39, 54, 237] or fibrils from an artificial intrinsically disordered protein, a disulfide-deficient mutant of hen lysozyme [141]. The findings of this work correlate with the results of Foguel and co-workers [54] and confirm the hypothesis that amyloid fibrils are sensitive to hydrostatic pressure and dissolve, in the case of the investigated histidine-tagged, spin labeled α-syn, completely within ambient conditions up to 2000 bar. Interestingly, the results of this study differ from those made in the references in terms of the pressure-dependent course of dissociation of the α-syn fibrils, implying a different unfolding kinetic. The fast disaggregation recognized in this work, which advances most prominently in the range of 600-1200 bar, is confronted by the results for fibrils obtained from wildtype α-syn made by Foguel et al. (utilizing light scattering experiments) indicating a much slower fibril disassembly starting at 1250 bar and even exceeding 2500 bar [54]. This difference is most likely based on modifying the primary sequence of the protein with the MTS-spin label which makes the fibril formation more susceptible to pressure than the regular non-modified form. Most probably, the label´s additional volume prevents the tight packing of the unmodified fibril form and could be responsible for additional internal cavities or easy hydratable residues in the hydrophobic fibril core. Interestingly, the pressure titration induced dissociation process of fibrils produced from α-syn A53T and A30P [54], point mutations that make the according aggregate more susceptible to hydrostatic pressure, resembles the pressure-dependent behavior of the spin labeled α-syn fibrils rather than the course of dissolving of the wildtype formation. Both point mutated fibril types begin to disaggregate at much lower pressures than the wild type (A53T at 200 bar; A30P at 600 bar) and continue

to dissociate much faster with increasing pressure. It can be theorized that substitutions at positions A53 and A30 with threonine or prolin respectively, both residues are bulkier than the alanine residue, are responsible for packing defects and/or cavities of higher water-accessibility in the aggregated fibril similar to the investigated spin labeled variant in this work.

There is also no indication within the literature that low pressure (<200 bar) could promote aggregation of the remaining monomer molecules in the sample before unfolding of the fibrils starts at higher pressures, as suggested by the EPR data of this work. This correlation gives a hint for another pressure-dependent effect that can be regarded as a non-amyloid aggregation of the α-syn monomer. The results made in this work also correlate with the already described model [170] of the α-syn amyloid fibrils which define the fibril core, or more precisely the β-sheet region, as free of water molecules, while the loop-regions, which connect the single β-strands, are hydrated. Correspondingly, it can be theorized that hydrostatic pressure dissolves the fibril aggregates by hydration of water free cavities or protruding amino acid residues, schematically depicted in figure 4.35 [188]. The difference of the partial molar volume between the fibril conformation and the monomer amounts to ΔV^0=-60.7±4.0 ml/mol in case of a linear fit to the course of the equilibrium constant versus pressure with an isothermal compressibility of $\Delta\beta_T$=0. However, since a conformational equilibrium between the fibril conformation and the monomer can be assumed, a non-linear bevavior may apply [133]. A non-linear quadratic fit to the plot of the equilibrium constant versus pressure yields ΔV^0=-85.3±12.9 ml/mol and $\Delta\beta_T$=-0.025±0.012 ml/mol bar, representing the shift to a lesser conformational order according to the volume theorem and quantifying the volumetric change during dissolving the amyloid fibril into the monomer form. Values for ΔV^0 and $\Delta\beta_T$ in this case agree with those found in the literature for T4 lysozyme variant 118R1 upon addition of urea (ΔV^0 =-51.4±1.7 ml/mol and $\Delta\beta_T$=-0,017±0.001 ml/mol bar) [133]. In that case the the native structure of T4 lysozyme is completely unfolded by pressure induced dissociation.

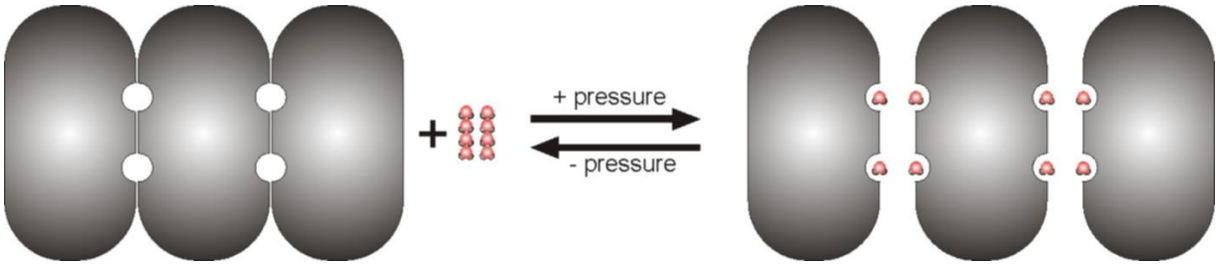

Figure 4.35: Hydrostatic pressure hydrates water free cavities in amyloid fibrils. Dissociation of aggregated protein (amyloid fibril core region) structures, represented as gray bulk. Water molecules are represented as small red and gray spheres. Water free cavities in the core region of the fibrils are prone to hydration by pressure perturbance. Applied pressure shifts the equilibrium in favor of the natively unfolded monomer. The representation was adapted and modified from [187].

The time dependent re-fibrillation after pressure-dependent dissolving of the amyloid aggregates could be utilized in further studies to gain knowledge about the kinetics and organization of the folding process as indicated by the results obtained in this work. Further studies by high hydrostatic pressure EPR on different sites in the fibril core and on additional point mutations promoting or demoting fibrillation together with additional structural elucidation by ssNMR or cryo-EM could provide a sophisticated model of the amyloid fibril assembly.

5. Investigations on ABC and ECF transporters

5.1 Introduction

All biological cells are separated from their surrounding environment by at least one lipid membrane just as the different organelles in the cell interior are demarcated from the intercellular medium. Since the metabolism of a cell depends on the exchange of substances with its environment and the uptake of extracellular nutrients, a transport across the cell membrane is essential. This transport is facilitated either passively through diffusion and membrane-channels or coupled to a source of energy like metabolic energy (primary transport) or to an electro-chemical gradient (secondary transport). The so called ATP-binding cassette (ABC) transporters belong to the primary active transport systems and promote the translocation across the membrane by hydrolysis of ATP. A subgroup of the ABC transporters are the so called energy-coupling-factor (ECF) transporters. The investigation of the conformational dynamics of a canonical ABC-type transporter and two ECF-type transporters the object of this work.

For type I ABC importers a transport mechanism, the ‘alternate access’ model, was postulated based on the well understood maltose transporter $MalFGK_2$. To figure out whether this transport model is applicable in general for type I importers the dynamics of the histidine transporter $HisQMP_2$ from *Salmonella enteric* serovar Typhimurium is investigated in this work with regard to its transport cycle. Furthermore, it is known that so called substrate binding proteins work as a substrate delivery system for the membrane-bound complexes of canonical ABC transporters. Therefore it is an aim of this work to clarify the conformational changes of the substrate binding protein upon substrate recognition, as well as the dynamics of the transfer of the substrate from the substrate binding protein to the transmembrane domains of the transporter. Accordingly, the substrate binding protein of $HisQMP_2$, HisJ, is studied in this work representatively.

Furthermore, the subgroup I ECF-type transporter for biotin from the purple bacterium *Rhodobacter capsulatus*, BioMNY, is subject to this work. Here, it was attempted to gain experimental insight into the conformational dynamics of the nucleotide binding domains of the transporter during the nucleotide hydrolysis cycle. Also, the reorientation of the substrate binding domain of BioMNY during substrate translocation is object of the investigations in this work to find experimental evidence

for the postulated ‘toppling over’ transport mechanism. As a second experimentally investigated ECF transporter model the cobalt transporter CbiMNOQ also from the purple bacterium *Rhodobacter capsulatus* was chosen. In general, substrate binding to vitamin-specific single substrate binding domains of ECF transporters is independent of the complex assembly with the corresponding transmembrane domains. This correlation is not verified for the purified metal ion specific substrate binding unit, CbiM, of CbiMNQO. In here it is analyzed if Cbi(MN), the enzymatic inactive variant Cbi(M_{H2D}N) and CbiM are able to bind cobalt ions.

5.1.1 ABC transporters

ABC transporters belong to a large family of membrane proteins that facilitate actively the transport of specific substrates across cell membranes by hydrolysis of ATP [43]. This particular transporter type exists in eukaryotes, bacteria and archaea with diverse distribution that varies from organism to organism [85]. For instance the human genome contains 49 genes encoding for ABC transporters [214] while the K-12 strain of *Escherichia coli* is assumed to encode for 71 ABC transporters [136]. Plant genomes also encode for a high number of ABC transporters like *Oryza sativa* or *Arabidopsis thaliana* containing more than 120 genes [168]. Considering the relation between the complete size of the genome and the amount of ABC-transporter encoding genes, bacteria occupy the highest number of ABC transporter systems [43]. The first complete sequence of an ABC transporter system, the histidine transporter HisQMP$_2$ from *Salmonella enterica* serovar Typhimurium (*S*. Typhimurium), was published in 1982 [84]. A variety of substrates, sugars, peptides, amino acids, vitamins, metal ions, hormones, antimicrobial drugs, are subjected to the transport by ABC transporter systems associating the latter to all kinds of cellular functions.

The structural organization of canonical ABC transporters is modular, comprising two transmembrane domains (TMDs), homo- or hetreodimers, through which translocation occurs, and two cytoplasmic nucleotide-binding domains (NBDs) that mediate binding and hydrolyzing ATP as energy source.

Based on the transporter´s function and sequence comparison a classification of four different ABC transporter classes was established. Class 1 consists of exporters which are involved in secretion of various agents. Those transporters comprise of

fused TMDs and NBDs as depicted schematically in figure 5.1 a-c. Class 2 type transporters include cytoplasmic ABC systems which lack the transmembrane domains and do not act as transporters but have distinct function in regulatory processes like DNA repair or mRNA translation [43]. Class 3 describes the importer systems which mainly exist in bacteria, though there is evidence for an importer system in eukaryotes, the acyl-Coa-fatty acid transporter from *Arabidopsis thaliana* [101]. The structure of the transporters of this class mainly consists of NBDs and TMDs formed by separate polypeptides as depicted in figure 5.1 d-h. Class 3 can also be subdivided into the importer I and importer II types. This distinction is based on the amount of transmembrane helices the TMDs consist of. The TMDs of subclass I comprise 10-14 transmembrane helices, while the TMDs of subclass II comprise up to 20 transmembrane helices [48]. Furthermore, prokaryotic importers are characterized by a highly specific substrate binding protein (SPB), which acts as a periplasmic substrate delivery system for the translocation through the TMDs (figure 5.1 d-h).

The fourth class of ABC transporters, the so called energy-coupling-factor (ECF) transporter systems, is described in the following paragraph.

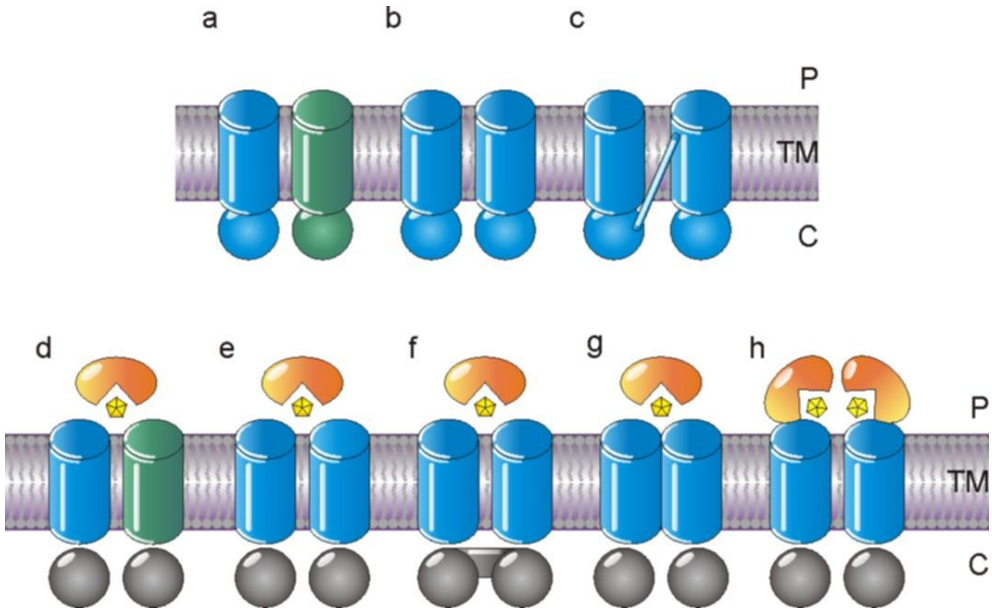

Figure 5.1: Diversity in the structural organization of ABC transporters. Schematically illustrated export systems are depicted from a-c. a) The heterodimeric TAP (Transporter associated with antigen processing-system). b) The homodimeric Sav1866 from *Staphylococcus aureus*. c) The human, full-size transporter P-glycoprotein. Schematics from d-g depict import systems with mainly separated TMDs and NBDs. d) The heterodimeric histidine transporter from *S*. Typhimurium e) The homodimeric maltose transporter from enterobacteria. f) *E. coli* K12 ribose transporter with fused NBDs. g) Fused

TMDs, from the iron-hydroxamate transporter of *E. coli* K12. h) Fused SBPs and TMDs of the glycine betaine transporter from *Lactococcus lactis*. P: Periplasma, TM: Transmembrane Region, C: Cytosol.

5.1.2 ECF transporters

The ECF-transporters build the youngest class of ABC transporters (class 4 or importer type III). ECF transporters exist in bacteria and archaea and are importer systems that translocate vitamins and vitamin-precursors, amino acids and metal ions [48, 174]. The term energy-coupling-factor goes back to the 1970s and was applied for an unknown component that promoted substrate transport together with a substrate-binding protein. Back then it was theorized that ECF facilitates transport by means of ATP hydrolysis. [78, 79, 80, 81]. This transporter class was assigned to the ABC systems because its structural organization consists of a NBD dimer next to the TMDs as was discovered from bioinformatic analysis of ~400 microbial genomes [173]. ECF transporters are furthermore divided into two subclasses which are depicted in figure 5.2 exemplary.

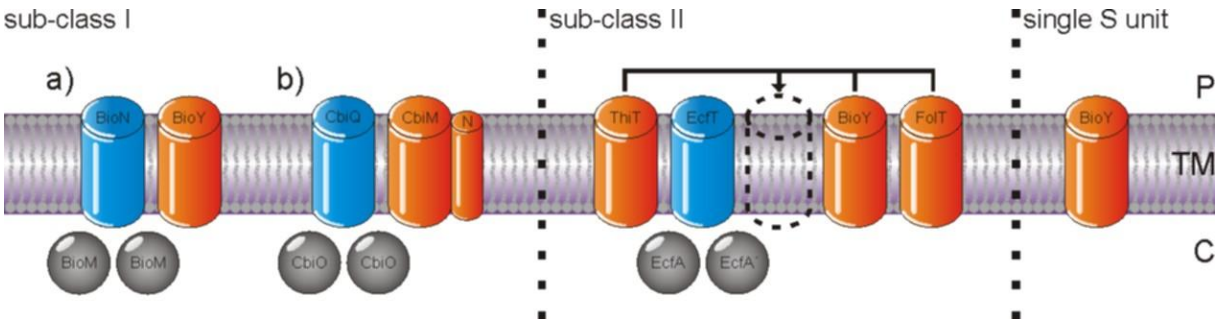

Figure 5.2: Modular organization of ECF transporter systems. Sub-class I and II transporters show a similar modular setup consisting of two cytoplasmic A-units and the transmembrane T-unit and S-unit. The cytoplasmic ABC-ATPase domain consists of two identical (BioM, CbiO), homologuos (EcfA/A´) or fused (not shown) A-units (gray). The two transmembrane domains consist of the T-unit (BioN, CbiQ, EcfT; blue) and the S-unit (BioY, ThiT, FolT; orange). The combined T- and A-units form the so called ECF module or energizing module. For some cases the S-unit, which is responsible for substrate uptake, can be subdivided into several sub-units (CbiM+CbiN). Sub-class I transporters harbor for each S-unit a specific energizing module. For sub-class II transporters several unspecific S-units can form along with an energizing (EcfAA´T) module a functional transporter system. As an exception of sub-class I & II, in some organisms the single S-unit BioY was found uncomplexed with an energizing module.

The first subclass comprises transporters which components, the S-, T- and A-units, are encoded by genes that are located in one operon. The second subclass consists of transporters which consist of one module of AA´T-units which can be associated to various S-units of different substrate specifity. The corresponding compound of AA´T-units is encoded in one operon and the according genes for the S-units are distributed through the genome of the organism [48]. Some organisms contain multiple S-units of different substrate specifity, which all associate to a distinct ECF module [199]. Various organisms utilize transporters of both subclasses [174].
The ECFs organization consists of two structural and functional asymmetric TMDs, a membrane-integral substrate-binding domain (S-unit), a conserved transmembrane domain (T-unit) and a pair of cytoplasmic NBDs (A-units). The S-unit mediates substrate-binding while the T-unit in association with the A-units represents the energizing module, the energy-coupling-factor, which facilitates substrate-transport by ATP-hydrolysis and a not fully understood conformational transition across the TMDs [192, 200]. The stoichiometry of these different components is still a matter of debate and oligomerization of the TMDs is a highly discussed notion. [15, 105, 174].

5.1.3 Nucleotide-binding domains – the ATPases

The ATP-binding cassette of the NBD is characteristic and eponymous for ABC transporter systems. Of all domains in ABC transporters the NBD has the highest amount of highly conserved sequences typical for ATP-binding and a conserved tertiary structure. They are coupled to the cytoplasmic face of the TMDs and facilitate the substrate-transport across the membrane by nucleotide-hydrolysis. The NBD consists of a catalytic RecA-like subdomain which is connected to a smaller α-helical subdomain via two flexible loops [152]. In addition few canonical ABC transporters also possess a third, C-terminal subdomain in their NBDs, which has regulatory function [200]. The NBD MalK of the maltose/maltodextrin transporter $MalFGK_2$ from *E.coli* comprises a C-terminal subdomain (figure 5.3) [19]. From X-ray crystallography it was revealed that the NBDs of ECF transporters also include a C-terminal domain. It was shown that the C-terminal domain is responsible for the assembly of NBD homo- and heterodimers in ECF- and canonical ABC-transporters as well [102]. The RecA-like subdomian consists typically of two β-strands and six α-helices, where by contrast the α-helical domain comprises four α-helices[43]. Both subdomains

comprise highly conserved motifs that are essential for dimerization of the NBDs and the associated ATP-hydrolysis. The NBDs structural organization of two canonical ABC transporters, $HisQMP_2$ and $MalFGK_2$, with highlighted motifs, essential for ATP-binding and hydrolysis, is depicted in figure 5.3. Through dimerization of the NBDs two ATP molecules can be coordinated by the binding-motifs. In the RecA-like subdomain, the Walker A-motif (GXXGXGKS/T, X: random amino acid) is localized, which interacts with the β- and γ-phosphate of ATP by forming hydrogen-bonds. Also localized in the RecA-like subdomain is the β-strand-rich Walker B-motif (ϕϕϕϕD, ϕ: hydrophobic amino acid). Its terminal aspartate residue is necessary for coordination of Mg^{2+}, which is essential for the hydrolysis of ATP. Two loop motifs, the H-loop and the D-loop, reside also in the RecA-like domain. While the H-loop´s conserved histidine residue is involved in coordinating the γ-phosphate of the ATP molecule [28], the loop motif also interacts indirectly with the ATP that is coordinated by the opposite NBD with the aid of a conserved aspartate residue of the D-loop [229]. The conserved LSGGQ-motif, localized in the α-helical subdomain, interacts with the γ-phosphate of the nucleotide and is involved in its hydrolysis as well. This motif is unique to the NBDs of ABC systems and is therefore entitled as signature motif [46, 179]. A further conserved amino acid, which is involved in coordinating the nucleotides β- and γ-phosphates, is the glutamine residue located in the Q-loop. The flexible Q-loop consists of about 8 amino acid residues and connects the RecA-like and the α-helical subdomain [100]. One ATP molecule is then coordinated by the LSGGQ-signature motif and the D-loop of one NBD and the Walker A-motif, the Walker B-motif, the H-, and Q-loop of the opposite NBD [200, 236].

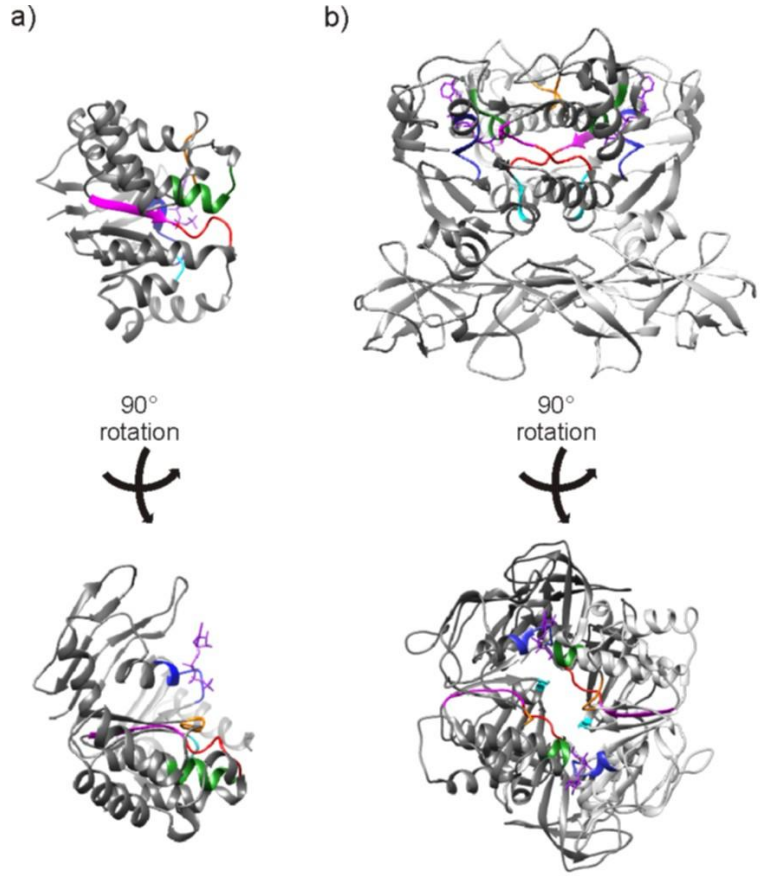

Figure 5.3: Organization of nucleotide binding domains of ABC-transporters. a) Crystal structure of a HisP monomer from *S.* Thyphimurium (PDB:1B0U). Conserved sequences are emphasized in color: Walker A motif (blue), Walker B motif (magenta), LSGGQ motif (green), Q-loop (orange), D-loop (red), H-Loop (cyan). ATP is indicated in purple. b) Crystal structure of the MalK dimer from *E.Coli* (PDB:1Q12). The color code corresponds to a). The figure was adapted from Licht & Schneider [122].

Within the Q-loop of ECF transporter ATPases alone, a helical motif emerges, that is called Q-helix (XPD/EXQϕ, ϕ: hydrophobic amino acid), according to its location. Binding of ATP drives a conformational transition in the NBDs that triggers the dimerization of the domains and the transition from the open to the closed conformation. Also the RecA-like subdomain and the α-helical subdomain approach each other upon ATP-binding and exhibit an opposite motion upon ATP-hydrolysis by what the position of the Q-loop is altered. The Q-loop has therefore a transmitting function, transferring the NBD´s conformational change to the TMDs and facilitating substrate-transport [200]. It was shown for homologs of the LivFGMH transporter from E.coli that dimerization of the NBDs occurs only upon binding of one ATP molecule to each NBD. On the contrary hydrolysis of only one bound ATP is sufficient to facilitate reopening of the ATPase dimer [235, 236].

5.1.4 Transmembrane domains, their coupling to the NBDs and postulated transport mechanisms of ABC and ECF type transporters

ABC exporter and importer systems comprise two homo-dimeric or hetero-dimeric, in the latter case structure-symmetric, TMDs which are coupled to the highly conserved NBDs. The TMDs reveal a high diversity due to various specificities for different substrates and exhibit different numbers of transmembrane helices accordingly. Exporter systems feature six transmembrane helices while the TMDs of importer class I consist of five to six helices. Importer class II systems exhibit up to ten helices per TMD. The TMDs of importer class I and II form a translocation pore for the substrate as revealed from crystal structures of several transporters. It is assumed that substrate-transport of exporters is organized equally by providing a pore-like pathway through the interface of the TMDs [200]. Crystal structures of two importer type I transporters are depicted in figure 5.4 a and b. The molybdate/wolfram transporter ModBC (figure 5.4 a) comprises six helices per TMD while each TMD of the arginine transporter ArtQN consists of five helices (figure 5.4 b). Both structures reveal a translocation pathway closed at the periplasmic side and opened at the cytoplasmic side of the complexes. Cytoplasmic coupling helices, localized in the last intracellular loop of the TMDs, are associated to the NBDs and transmit conformational transitions of the nucleotide hydrolysis cycle. Nucleotide-binding induces a cytoplasmic closed conformation while nucleotide-hydrolysis drives a transition into the periplasmic closed conformation as revealed by the crystal structures of the importer I class maltose/maltodextrin transporter $MalFGK_2$ from *E.coli*.

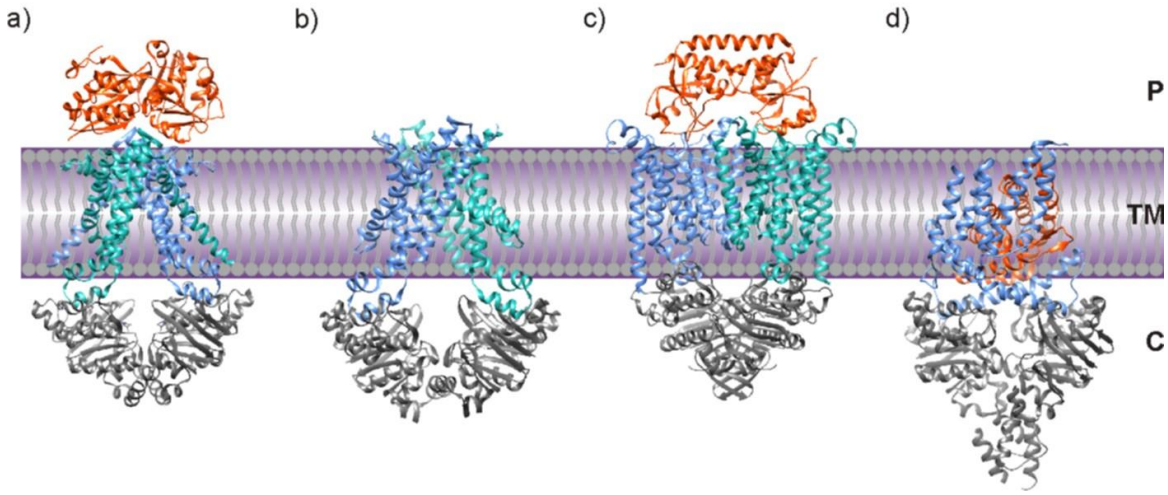

Figure 5.4: Crystal structures of three canonical ABC transporter systems and one ECF transporter. a) Importer type I molybdate/wolfram transporter Mod(BC)2-A from *Archeoglobus fulgidus* (PDB: 2ONK), with six helices per TMD and opened to the cytoplasmic side. b) Importer for positively charged amino acids (arginine, histidine) ArtQN from *Thermoanaerobacter tengcongensis* (PDB: 4YMU) with five helices per TMD and opened to the cytoplasmic side. c) Type II vitamine B12 importer Btu(CD)2-F from *E. coli* (PDB: 2QI9), with ten helices per TMD. TMDs are highlighted in blue and green. Cystosolic NBDs are highlighted in gray. Periplasmic SBPs are highlighted in orange. d) Crystal structure of the folate ECF transporter EcfAA´T + FolT (4huq.pdb). The EcfAA´T ECF module is highlighted in blue and gray. The FolT substrate binding S-unit is highlighted in orange. P: periplasm, TM: transmembrane regions, C: cytosol.

The so called alternating access model based on studies of $MalFGK_2$ describes the postulated transport mechanism of importer I type ABC transporters and is depicted in figure 5.5. It is theorized that the transport mechanism through the TMDs of importer II class complexes differs from the transport pathway of type I importers. For instance, the importer II class transporter from *E.coli*, $Btu(CD)_2F$, is in the periplasmic open conformation in the absence of nucleotides. TMDs of $Btu(CD)_2F$ are shown in figure 5.4 c. A tight packing of the structure results from the ten helices per TMD, forming a transport pore for the substrate vitamine B12 through the TMD´s interface [200].

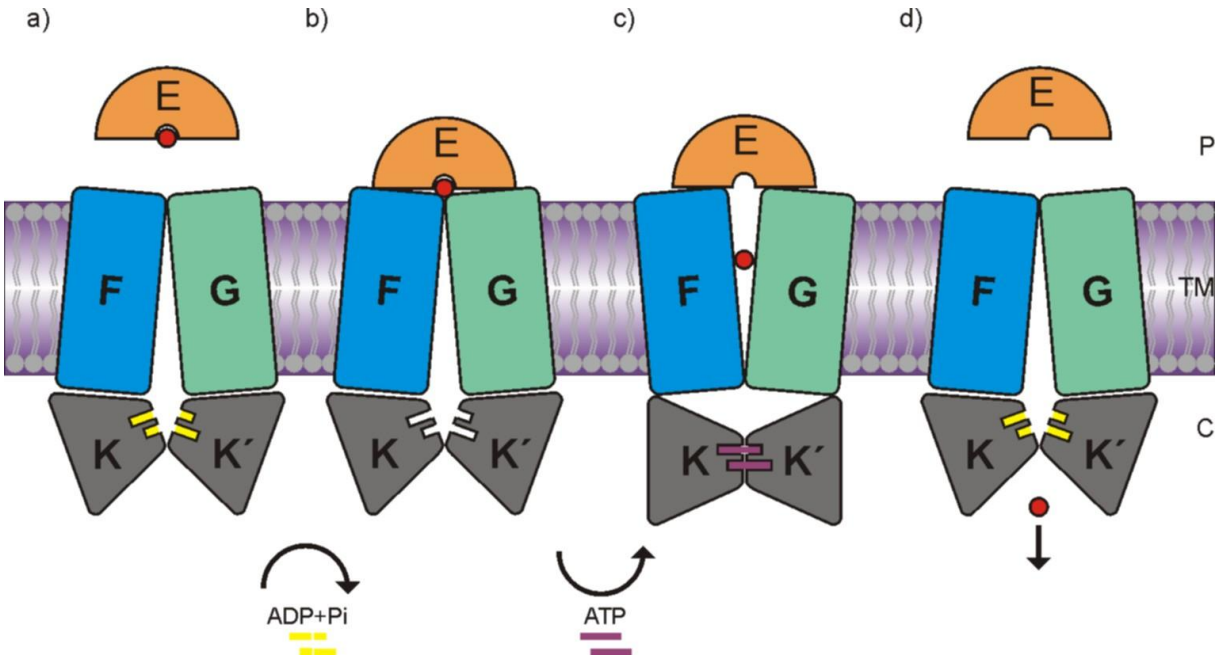

Figure 5.5: Mechanism of Type I ABC importers based on the maltose transporter MalFGK$_2$. The two TMD (MalFG) subunits are colored in blue and mint, the two NBD subunits (MalK$_2$) are colored in gray. The substrate binding protein (MalE) is colored in orange and the substrate is represented by a red sphere. ATP and ADP are shown as purple and yellow sticks, respectively. a) The substrate-loaded SBP binds to the inward-facing, periplasmic closed conformation of the TMDs. b) ADP+Pi dissociates from the NBDs. c) Binding of ATP triggers a conformational closure of the two NBDs, a conformational transition in the TMD subunits, and an opening of the SBP, resulting in release of substrate into the translocation pathway of the TMD subunits. d) The hydrolysis of ATP molecules releases the substrate into the cytoplasm and resets the transporter back to an inward resting state. P - periplasma; TM - transmembrane domain; C - cytosol. The figure was adapted from Rice et al. [169].

In contrast to canonical ABC transporter systems, ECF transporters exhibit functional and structural asymmetric TMDs, the T-unit and the S-unit. The S-unit, which is responsible for substrate binding, is described in a following paragraph, addressing substrate binding proteins in ABC and ECF systems. The T-unit comprises of four to eight transmembrane helices [48]. The completely solved crystal structure of the subclass II folate transporter EcfAA´T exhibits five helices in the T-unit, depicted in figure 5.4d [225]. Based on this crystal structure a transport mechanism for ECF transporters is postulated, that is characterized by a toppling over motion of the substrate binding unit, corresponding to a rotational movement of the domain between a periplasmic and cytoplasmic orientation. A schematic depiction of the transport mechanism is depicted in figure 5.6. [192, 218, 225, 231].

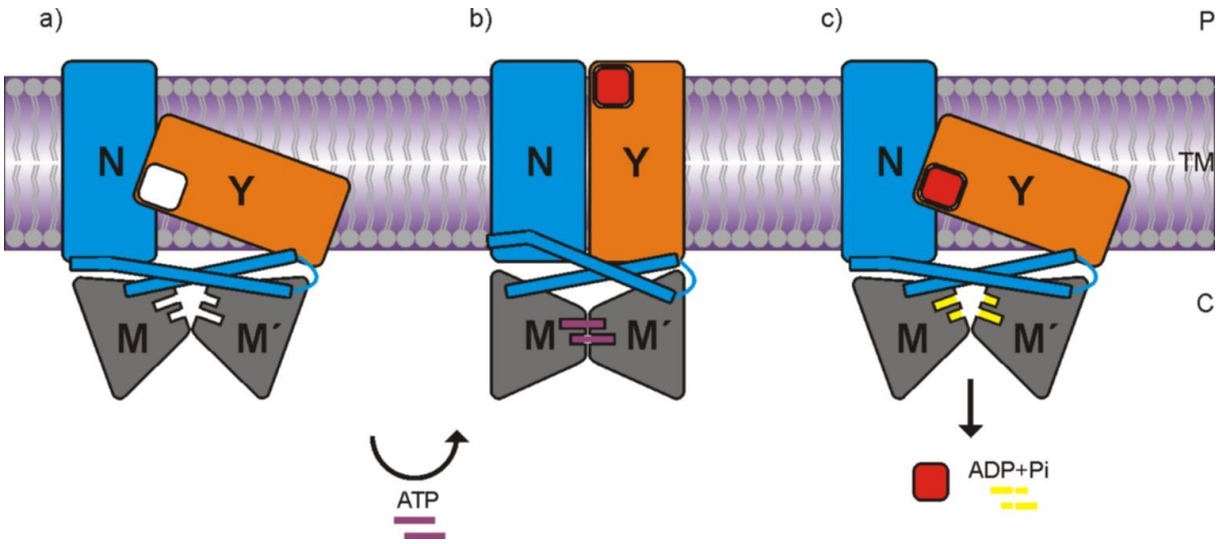

Figure 5.6: Model for BioMNY-catalyzed biotin transport. The ATP dependent transport cycle of BioMNY and a hypothetical toppling over mechanism is shown schematically [51]. BioN (transmembrane domain) - blue; BioY (substrate-binding domain) - orange; BioM/M´ (ATPase-domains) - gray; biotin - red; ATP - purple; ADP+Pi - yellow. The resting state, a), of the transporter resembles the toppled S-domain BioY and the open BioM-dimer. Binding of ATP to the transporter leads to an uplift of BioY, b). The physical contact of BioY to BioN remains during the conformational change. Biotin gets access to its specific binding site in BioY in the ATP-bound state. ATP hydrolysis, c), leads to a conformational change that rearranges BioY. The release of biotin and ADP+Pi induces the return to the nucleotide-free resting state. P - periplasma; TM - transmembrane domain; C – cytoplasma.

It is probable that the nucleotide hydrolysis cycle in the NBDs and the coupling to the TMDs is equally facilitated in all ABC and EFC transporters. A coupling helix that resides in the cytoplasmic part of the transmembrane domains of canonical ABC transporters and the T-unit of ECF-transporters interacts with the Q-loop in the NBDs. This distinct α-helix inserts in the interface between the RecA-like and the α-helical domain in the NBDs and transmits the conformational changes of the Q-loop onto the TMDs [221]. Importers of canonical ABC transporters harbor one coupling helix per TMD, while exporters possess two coupling helices in the cytoplasmic loops [200]. ECF transporter systems also feature two cytoplasmic helices that harbor two short sequences (XRX motif) that couple the T-unit to the ATPase A-units and are located in the C-terminus of T-unit [48]. These motifs are essential for signal transduction and complex stability, as was shown for subclass I (BioN) and subclass II (EcfT) transporters [139, 232]. Hints were found that the T-unit of EcfAA´T-RibU from *Streptococcus thermophilus* can feature an oligomerized state within the transporter

complex [102]. There is also indication that homo dimers and also hetero dimers of S-units can be associated to an ECF module [102]. The subclass I biotin transporter from *R. capsulates* also revealed oligomerized S- and T-units in *in vivo* experiments. Along with these results hetero-FRET experiments have shown oligomerized states of BioY alone as well as in association with its ECF module BioMN [50]. Cross-linking experiments on BioMNY revealed that its T-unit, BioN, can also exist as a homo-dimer within the complex [140].

These findings indicate that the stoichiometry of ECF transporter complexes is not as simple as for canonical ABC transporters, where the TMDs exist in a one to one ratio. Actually the stoichiometry of ECF type TMDs is a controversial debated issue. The stoichiometry of 1(A):1(A´):1(T):1(S) of the ATP- and substrate-free crystal structure of EcfAA´T-FolT, EcfAA´T-PdxU and EcfAA´T-PanT from *Lactobacillus brevis* [218, 225, 232] is opposed by a postulated stoichiometry of 2(A):2(T):2(S) [102]. Another indication for oligomerizing S-units are findings from X-ray crystallography in which RibU, ThiT and BioY were found as dimers and trimers [15, 49, 230]. Oligomerizing of BioY could be the prerequisite for the transport function that is facilitated by the S-unit alone in absence of the energy coupling factor. This notion is suggested by investigations on recombinant cells that only possessed single BioY and still could absorb biotin as a substrate [76].

5.1.5 Substrate binding in canonical ABC and ECF transporter types

The diversity of ABC transporter types is reflected by the various substrate specifities and the different mechanisms that mediate substrate uptake and transport. Canonical ABC import complexes utilize distinct substrate binding proteins (SBP). Additional substrate binding by the TMDs or the transition of the substrate from the SBP to the TMDs of the transport complexes is not well understood by now. Hitherto a substrate binding site was determined only for the maltose transporter from *E.coli* $MalFGK_2$ in the MalF TMD [181, 200]. In general SBPs are diffusing freely in the periplasm in the case of gram negative bacteria. In gram positive bacteria and archaea the SBPs are associated to the lipid membrane via an N-terminal hydrophobic α-helix or a lipid anchor. The SBP can also be N-terminally fused to the periplasmic side of the TMDs [48]. The size of SBPs varies from 25 to 70 kDa and their tertiary structural organization is very similar. SBPs consist of a N-terminal and a C-terminal globular

domain, that are connected by a hinge-region. The substrate binding site resides in the interface between the two globular domains and the hinge-region [165]. Upon substrate binding (K_D 0.01-1 µM) a closed conformation of the SBP is established which is described by a venus flytrap model. Without substrate the SBP exists mainly in its open conformation [60, 127]. SBPs are divided into six groups, depicted in figure 5.7, based on similarities and differences in their structural organization. Main characteristic for discrimination is the hinge region which can harbor a single α-helix, three random coil regions or two strands featuring either four to five amino acids or eight to ten amino acids [14]. The interaction of the substrate-bound SBP with the TMDs initiates the translocation process [42]. Each lobe-like domain of a SBP interacts with one TMD. This interaction drives a conformational transition through the TMDs which is linked to the NBDs by the coupling helices and triggers approximation of the ATPases. Dimerization of the NBDs upon ATP binding facilitates a conformational transition trough the TMDs again that enables substrate transfer from the SBP into the TMD substrate channel.

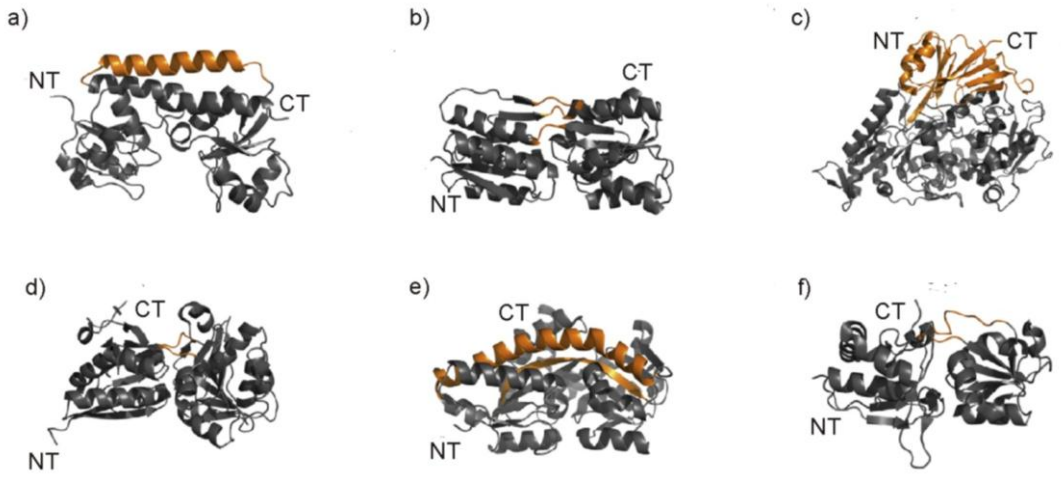

Figure 5.7: Various crystal structures of SPBs associated to six different SBP clusters. The structural feature of the hinge region that connects the two domains of the protein is colored in orange in all cases. a) SBPs of cluster A have a rigid helix connecting the two domains (BtuF, PDB: 1N2Z). b) SBPs of cluster B connects the two domains via three segments (RBP, PDB: 1DRJ). c) SBPs of cluster C have a higher molecular weight compare to other SBPs because of an additional domain (OppA, PDB: 3DRF). d) SBPs of cluster D contain two short interconnecting hinges (ModA, PDB: 1ONR). e) SBPs of cluster E are associated to TRAP-transporters containing a large helix as interconnecting hinge region. (UehA, PDB: 3FXB). f) SBPs of cluster F show large flexibility between the two domains because of a long single interconnecting segment (HisJ, PDB:1HSL). Clusters A, D

and F can be subdivided further depending on the according substrate. NT: N-terminus, CT: C-terminus. The figure was adapted from Berntsson et al. [14].

ECF transporters do not possess a periplasmic SBP but substrate binding is accomplished by the transmembrane S-units. S-units differ in size from 20 to 25 kDa and comprise of six transmembrane helices except S-units that bind metal ions specifically. Substrate affinity is high in general for S-units, as they exhibit dissociation constants in the nanomolar regime or below [15]. S-units have a common structural organization though they show only minor sequence similarity (10-20%). The S-units identified by now were assigned to 21 substrate specific families [192]. Subclass I transporters harbor five of these S-families specifically since their representatives interact exclusively with their distinct energy coupling factor. For instance, the S-units CbiM and NikM, binding cobalt and nickel, respectively, belong to those families. Most representatives of the remaining S-families belong to subclass II transporter types whose energizing modules share several S-units of different substrate specifity. The biotin specific BioY is in this case exceptional because it is assigned to subclass I or II or is encoded solitary depending on the origin organism [48]. Substrate transport is facilitated by the coupling between the transmembrane T-unit and the ATPases which triggers a conformational change in the S-unit. Therefore the T-unit works as a kind of mediator between the S-unit and the A-units. [218, 225]. It was proposed that the interaction between the T- and the S-unit could be accomplished by a conserved AXXXA motif (X: random amino acid) localized in the first transmembrane helix of the S-unit. Exchanging the motif´s alanine residues for tryptophane in ThiT from *Lactobacillus lactis* leads to the dissociation of the AA´T-/S-unit complex and therefore transport inactivity [49]. Metal specific ECF transporters, like the cobalt specific CbiMNQO or the nickel specific NikMNQO work somewhat different from other ECF transporter systems in respect of the S-unit. Both systems utilize an extra domain, CbiN and NikN, respectively, which is crucial for substrate uptake in the according S-units CbiM and NikM. NikM and NikN appear frequently in a fused form Nik(MN) while CbiM and CbiN are found only as two separate polypeptide chains with an exception of a fused form from *Geobacter sulfurreducens*. Theses extra domains are small, comprising two transmembrane helices only. Furthermore, the nickel transporter domain NikN can be substituted with the NikL domain which is additionally associated with NikK. However, the transport facilitating function of CbiN and NikN remains unsolved until now [106, 173, 185]. CbiM and

NikM also vary from vitamin specific S-units in the number of transmembrane helices. Seven transmembrane helices are predicted for CbiM and NikM therefore containing one additional N-terminal helix compared to S-units of vitamin specific transporters. The N-termini of both CbiM and NikM are highly conserved and contain a sequence that is essential for substrate binding as was attested for CbiM. Especially residues Met1 and His2 in CbiM seem to have a critical function and allow no amino acid exchange without loss of activity of the transporter. His2 for instance is a crucial residue that is partaking in the coordination of the substrate Co^{2+} [185].

5.1.6 Objective of this work

This section of this thesis deals with the investigation on different ABC transport systems, the canonical ABC transporter (importer class I) $HisQMP_2$ from *Salmonella enterica* serovar Typhimurium, the ECF transporter of subclass I BioMNY from *Rhodobacter capsulates,* and the S-unit CbiM of the cobalt specific ECF transporter from *Rhodobacter capsulates.*

The histidine transporter $HisQMP_2$ comprises the transmembrane domains HisQ and HisM, the ATPase dimer $HisP_2$ and the periplasmic substrate binding proteins HisJ and LAO, specific for histidine, arginine, lysine and ornithine. Conformational dynamics of the complex depending on the nucleotide hydrolysis cycle were investigated by DEER spectroscopy and compared to the alternating access model based on the well understood maltose/maltodextrin $MalFGK_2$ transporter. Further analysis was subjected to the interactions between HisJ and the TMDs HisQM studied by cw EPR and DEER. Additionally, conformational changes of the substrate binding protein HisJ upon substrate uptake were examined.

Another goal of this work was to explore the functional mechanisms of the biotin transporter BioMNY, which consists of the TMDs BioN (T-unit), BioY (S-unit) and a dimer of the nucleotide binding domain BioM (A-unit). DEER spectroscopy was utilized to trace conformational changes in the NBDs of BioMNY which are associated to the closure and reopening of the domains within the transport cycle. Furthermore, the toppling over mechanism of the S-unit was investigated by detecting changes of interspin distances between BioN and BioY by DEER spectroscopy.

The last part of this section considers substrate binding to the S-unit of the cobalt specific ECF transporter CbiMNQO analyzed by low temperature cw EPR.

5.2 Results of EPR studies on bacterial ABC- and ECF-type transporters

5.2.1 Investigations on the histidine ABC-transporter $HisQMP_2$ by cw EPR and DEER spectroscopy

5.2.1.1 Conformational dynamics of $HisQMP_2$ *

This section of the thesis covers the result on our study of the dynamics of the histidine transporter $HisQMP_2$ from *Salmonella enterica* serovar Typhimurium reconstituted into proteoliposomes. The transporter was studied in different states of the nucleotide-hydrolysis cycle, in the apo-state in the absence of nucleotides, in the ATP-bound and in the post-hydrolysis state using cw-EPR and DEER spectroscopy. All investigated samples were purified and prepared in the group of E. Schneider in accordance with published procedures and methods [189].

Figure 5.8 depicts the homology model of $HisQMP_2$,based on the crystal structure of the methionine transporter MetNI (PDB: 3DHW) from *E. coli*, together with the designated sites for site-directed spin labeling [189]. Different residue positions for spin labeling, which are depicted in figure 5.8 a, were chosen to detect and track conformational changes in the periplasmic NBDs, $HisP_2$, and the TMDs, HisQ and HisM, during the nucleotide-hydrolysis cycle. Positions D86 (HisQ) and D96 (HisM) are chosen to detect conformational dynamics at the putative perisplasmic gate. C197 (HisQ) and His C104 (HisM) are located at the periplasmic periphery of the complex. Near the cytoplasmic interface, residues A118 (HisQ) and G123 (HisM) are located, which span a distance vector across the cytoplasmic gate. To detect conformational changes in the NBDs, residues H153/H153´ were chosen for spin labeling. An additional pair of residues, H101/H101´, located in the Q-loops of the NBDs was designated for the same purpose according to the homologous site in the NBD MalK of the maltose transporter $MalFGK_2$ [71]. Chosen sites were pairwise modified by cysteine exchange and spin labeled with MTSSL. ATPase activity of modified $HisQMP_2$ variants in proteoliposomes was assayed. The cysteine-free control variant of $HisQMP_2$ had a reduced ATPase activity of 0.44 ± 0.04 µmol Pi min^{-1} mg^{-1} compared to the wild type of $HisQMP_2$ (0.68 ± 0.05 µmol Pi min^{-1} mg^{-1}) in the presence of the SBP HisJ and the substrate histidine. Compared to the intrinsic activity both the wildtype and the cysteine-free variant exhibited roughly threefold

* Part of this section was published prior to submission of this thesis [189].

stimulation, indicating functionality of ATP hydrolysis and substrate transport. Stimulation of $HisQMP_2$ complexes with introduced cysteine pairs ranged from 2-3.4-fold previous to spin labeling and 1.6-2.4-fold after labeling with MTSSL [189].

Figure 5.8 b depicts a visualization of the spin labeled complex including rotamer ensembles accomplished by introducing *in silico* spin-labeling at the described sites. Spatial rotamer populations and calculation of according interspin distance distributions were obtained by applying a rotamer library approach on the same model that is shown in figure 5.1 a. Predicted interspin distances between the implemented pairs of nitroxides are shown in figure 5.8 c. The spin pairs located in the NBDs exhibit distance maxima between 2.5-3.5 nm (H101R1-H101´R1) and 3.5-4.5 nm (H153R1-H153´R1). Interspin distances of spin pairs introduced into the TMDs of the complex range from 1.5 nm (A118R1-G123R1) to 3.2 nm (D86R1-A96R1). Upon these predictions DEER spectroscopy was deployed to investigate distances above 2 nm. Distances below 2 nm were subjected to low temperature cw EPR spectroscopy.

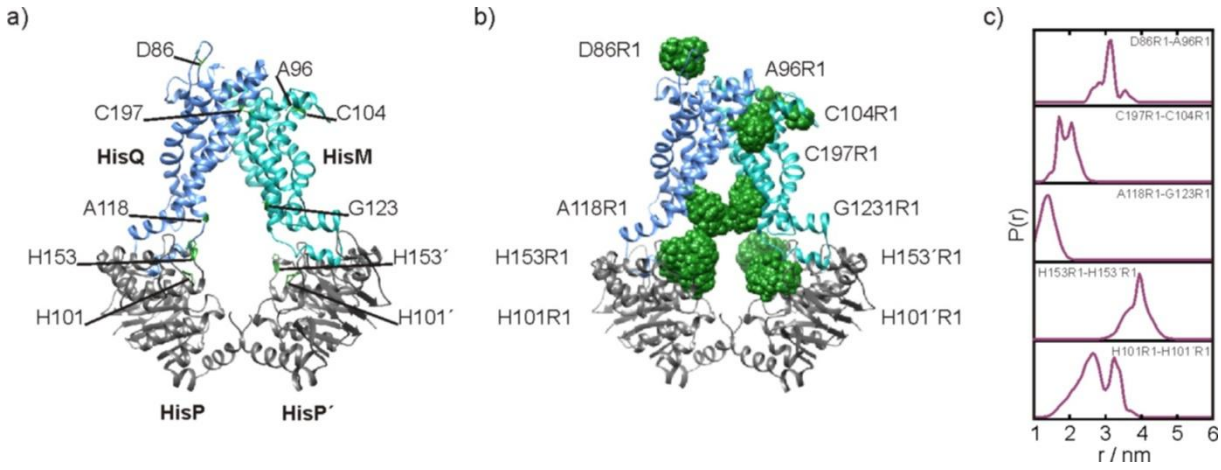

Figure 5.8: Homology model of $HisQMP_2$ based on the crystal structure of the methionine transporter MetNI (PDB: 3DHW). a) Amino acid residues designated for spin labeling are depicted in stick representation and highlighted green. b) Rotamer distributions of MTS-spin label are depicted in spheric representation and highlighted in green. c) Distance distributions between different pairs of spin labeled sites, calculated from the rotamer populations depicted in b) utilizing MMM2013 (MMM Version 2013 Y. Polyhach, St. Stoll, G. Jeschke ETH Zürich). The figure adapted from Sippach et al. [189].

Figure 5.9 depicts the obtained DEER data and associated distance distributions of the above described pairs of MTSSL residues in the reconstituted $HisQMP_2$ complex.

As stated, spin labeled $HisQMP_2$ complexes were reconstituted into liposomes and investigated in the presence of the substrate histidine and HisJ in three different states of the nucleotide hydrolysis cycle: in the apo-state (in the absence of nucleotides), in the nucleotide-bound state (in the presence of ATP and EDTA to inhibit hydrolysis) and in the posthydrolytic state. The latter state was induced by incubation with ATP and $MgCl_2$ for 30 min at 37 C for all samples. The spin pair H101R1-H101´R1 was investigated in terms of simulating a transition state during ATP hydrolysis by introducing the vanadate-trapped conformer. An exponential decay emerges in the raw DEER data,V(t), (appendix, figure 7.4) for all samples caused by a homogeneous multi-dimensional distribution of spins. Strongly damped oscillations arise in the first 0.5 µs of the DEER data for C197R1-C104R1, A118R1-G123R1 and H101R1-H101´R1. There is no evidence for damped oscillations in D86R1-A96R1 and H153R1-H153´R1. Such behavior is already described for reconstituted proteins. Assuming a three dimensional background of interacting spins for fitting the raw data of samples with obvious oscillations is therefore advisable and valid for D86R1-A96R1 and H153R1-H153´R1. Dividing the respective V(t) by the background B(t) and additional renormalizing at zero time results in the form factors, F(t), depicted in figure 5.9b.

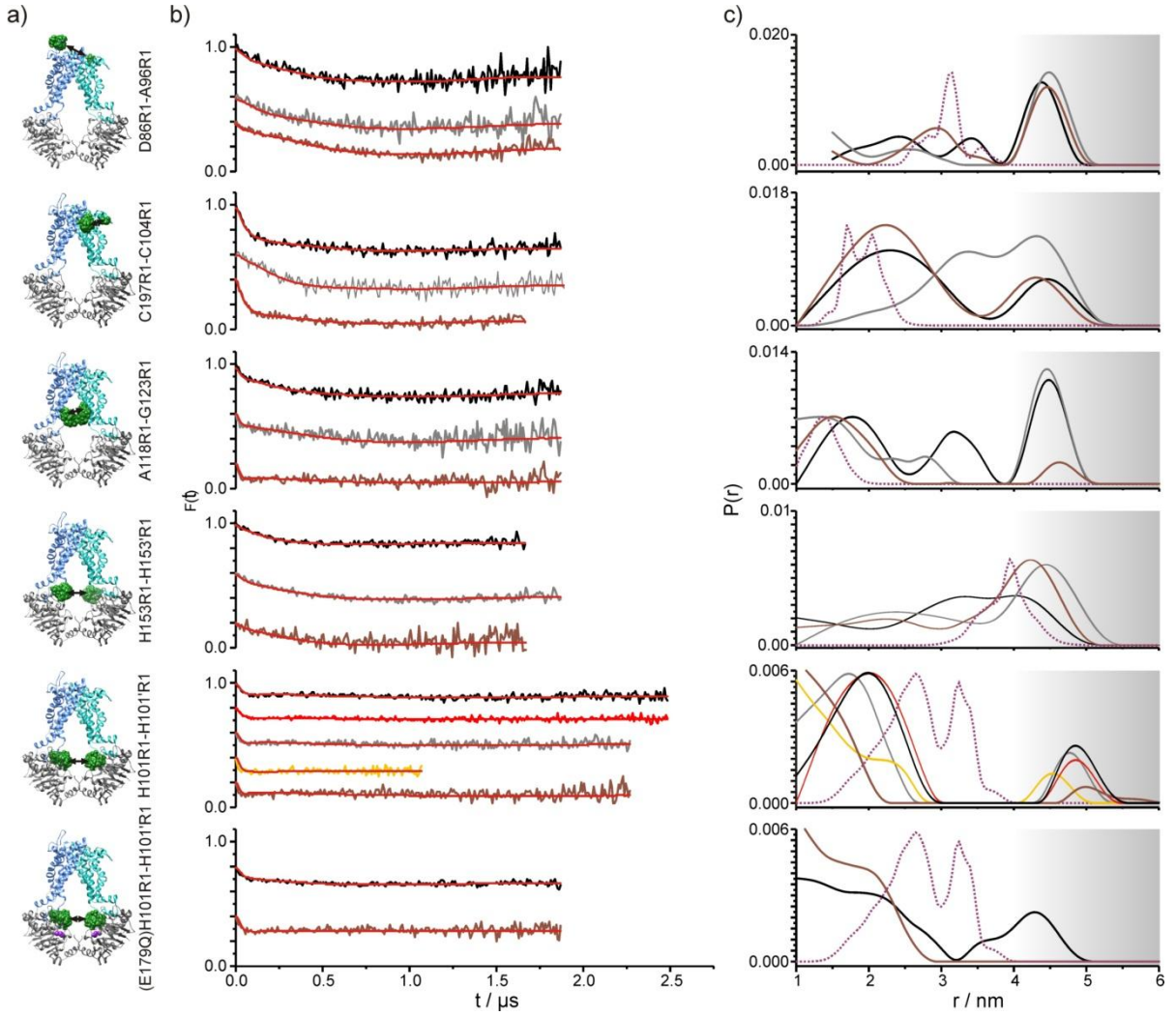

Figure 5.9: DEER traces and interspin distance distributions for three different states of the nucleotide hydrolysis cycle. a) Model of $HisQMP_2$ based on the structure of the methionine transporterMetNI (PDB ID: 3DHW). The nitroxide group spatial distributions are highlighted by green surfaces. b) Baseline corrected data, F(t), for the apo state (black), the ATP bound state (gray) and the post hydrolysis state (brown) in the presence of liganded HisJ. In addition, for positions 101/101′ the data for the vanadate-trapped state (yellow), for the state in the presence of ATP but in the absence of HisJ (red), and for the hydrolysis incompetent mutant E179Q in the absence of any substrate (black) and in the presence of HisJ, ATP and Mg^{2+} (brown) are shown. The noiseless lines in the plot of F(t) show the best fit according to the distance distributions depicted in c. c) Distance distributions calculated from the DEER traces shown in b. Tikhonov regularization is applied as implemented in DEERAnalysis2013. The gray shaded area above 4nm indicates limited certainty of the distance data (position and width of the distribution) based on the length of the shortest DEER time trace. In this region inter-complex spin–spin interaction also significantly contributes. The simulated distance distributions are superimposed (dotted lines) for comparison.

Position H101R1 is exhibiting very low modulation depths of 8-15% caused by the limited accessibility of the cysteine residue towards MTSSL in the progress of spin

labeling and interspin distances (<1,6 nm) that are located beyond the distance-range of DEER spectroscopy. The respective distance distributions, P(r), for H101R1-H101´R1 exhibit distance maxima at around 2 nm and below (figure 5.9 c), therefore making low temperature cw-EPR analysis favorable for this particular sample. Obtained cw spectra (figure 5.10) exhibited increased dipolar broadening only for the post-hydrolysis state. For the according state a distance of 1.4 nm obtained by line shape analysis utilizing the program DIPFIT [195]. In this array of experiments H101R1-H101´R1 get in closest proximity in the post-hydrolysis and in the vanadate-trapped states. In the absence of HisJ the apo state and the ATP-bound state of H101R1-H101´R1 are indistinguishable with respect to their distance maxima (2 nm). Upon addition of histidine-bound HisJ, the distance maximum of the ATP-bound state is shifted to 1.8 nm giving evidence of a coupling between the nucleotide-bound NBDs and the association of HisJ to the TMDs. The hydrolysis incompetent mutant HisQMP(E179Q)$_2$ shows broadening of the distance distribution of H101R1-H101´R1 in the range from 1-3 nm in the apo state. Additional contributions arise beyond 3 nm but vanish upon hydrolysis of ATP indicating that closure/dimerization of the NBDs is only possible in the nucleotide-bound state for this variant. Upon ATP-binding the distance distribution remains in the range between 1-3 nm with only marginal differences. Most importantly no shift below 2 nm occurs for the non-hydrolysable variant upon hydolysis in contrast to the non-mutated variants. This supports the notion that E179 is the catalytic trigger for the hydrolysis of nucleotides in HisP [91]. This finding is in agreement with the structures of MalFGK$_2$ which show coincidence of the nucleotide-bound wild type with the E159Q mutant [145, 146, 147].

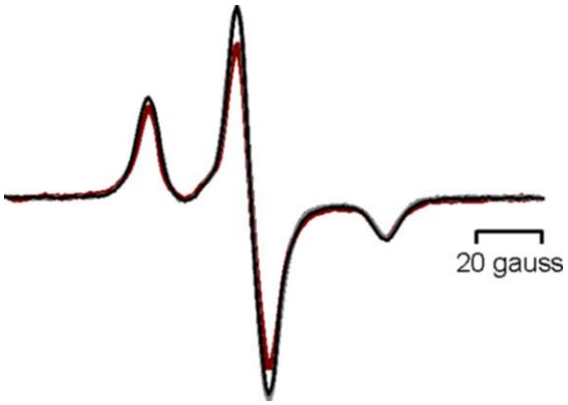

Figure 5.10: cw EPR spectra for three different states of the nucleotide hydrolysis cycle of H101R1-H101´R1. Superimposed continuous wave EPR spectra of 101R1–101′R1 for the apo state (black), the ATP bound state (gray), and the post-hydrolysis state (brown). The spectra are normalized to the same number of spins.

Deer data of variant H153R1-H153´R1 does not exhibit oscillations and does not show significant differences in the traces of all investigated states. Distance distributions reveal distance maxima between 3 nm and 5 nm which cannot be

designated definitely to spin-spin interactions between the NBDs of the same complex. Since in this scenario intra-molecular and possible inter-molecular contributions are undistinguishable H153R1-H153´R1 is excluded from further consideration.

Conformational transitions in the $HisP_2$ dimer during the different states of the nucleotide hydrolysis cycle also trigger conformational rearrangements in the TMDs HisQ and HisM. Different decays in the DEER traces were found for A118R1-G123R1 in the apo, ATP-bound and posthydrolysis states. Distance maxima emerged at 2 and 3.2 nm in the apo state of A118R1-G123R1 as depicted in figure 5.2 b. Both, the ATP-bound state and posthydrolysis state diminish the contributions to the distance distribution above 2.5 nm, while the major part of spin-spin interaction is associated to distances below 1.8 nm. This is supported by data originating from simulated distances of a rotamer library approach which sets the distance maxima at 1.5 nm in the apo state. Spin pair C197R1-C104R1 exhibits considerable differences in the distance distributions of the three states (figure 5.9 c). The apo state has a distance maximum at 2.2 nm which is shifted to 3.2 nm upon binding of ATP and re-shifts back to 2.1 nm in the posthydrolysis state. The maxima of the distance distributions of both the apo and posthydrolysis states are in agreement with the distance maximum, 1.8-2.1 nm, of the simulated distribution based on the model of $HisQMP_2$ supporting the validity of the model in regard to the periplasmic side of the complex. The DEER traces of D86R1-A96R1 exhibit the absence of oscillation and only minor alteration due to the different states (appendix, figure 7.4). Broad distance distributions were obtained for all investigated states which can probably be linked to the high motional freedom of the loop-region associated D86R1. The model-based simulated distance distribution, which is based on a solid protein-backbone, agrees with the obtained experimental data and yields distances between 2.5-3.5 nm. However, distinct changes in the distance distributions of the three states provide an indication for conformational transitions within the putative periplasmic gate within the ATP hydrolysis cycle.

In almost all cases the experimental data is in well agreement with the simulated data considering the fact that the rotamer library approach does not account backbone movement in its simulated distance distributions. The spin pair H101R1-H101´R1 is the only exception in this respect and shows shorter distances in all considered states for the experimental data than the ones presumed by simulations. This could

result from a discrepancy between the homology model and the structure of MetNI pointing out that the NBDs of the histidine transporter are in closer proximity than the NBDs of the methionine transporter.

5.2.1.2 Investigations on interactions between HisJ and $HisQMP_2$

Substrate transport through the membrane-bound complex is triggered by binding of the liganded SBP HisJ to the periplasmic side of the HisQM. The goal of the following experimental approach was to gain insight into the interactions between HisJ and $HisQMP_2$ and to follow possible conformational changes of HisJ by measuring distances and distance changes between single spin labeled positions of the SBP and positions of $HisQMP_2$ reconstituted into liposomes utilizing cw-EPR and DEER spectroscopy. Also, changes of the spin label mobility were assayed in different states of the nucleotide hydrolysis cycle of $HisQMP_2$ to trace if different loading-states of the NBDs cause conformational transitions that influence the interactions of HisJ with the periplasmic contact side of the complex. Different sites in HisJ and on the periplasmic side of HisQM were chosen for SDSL in order to establish the above explained approaches. In this work the measurements on spin pair G24R1(HisJ)-A96R1(HisM) are considered, depicted in the model in figure 5.11. All investigated samples were purified and prepared in the group of E. Schneider in accordance with published procedures and methods [189].
Cysteine substitution and spin labeling of both sites in HisJ and $HisQMP_2$ did not cause any loss of activity.

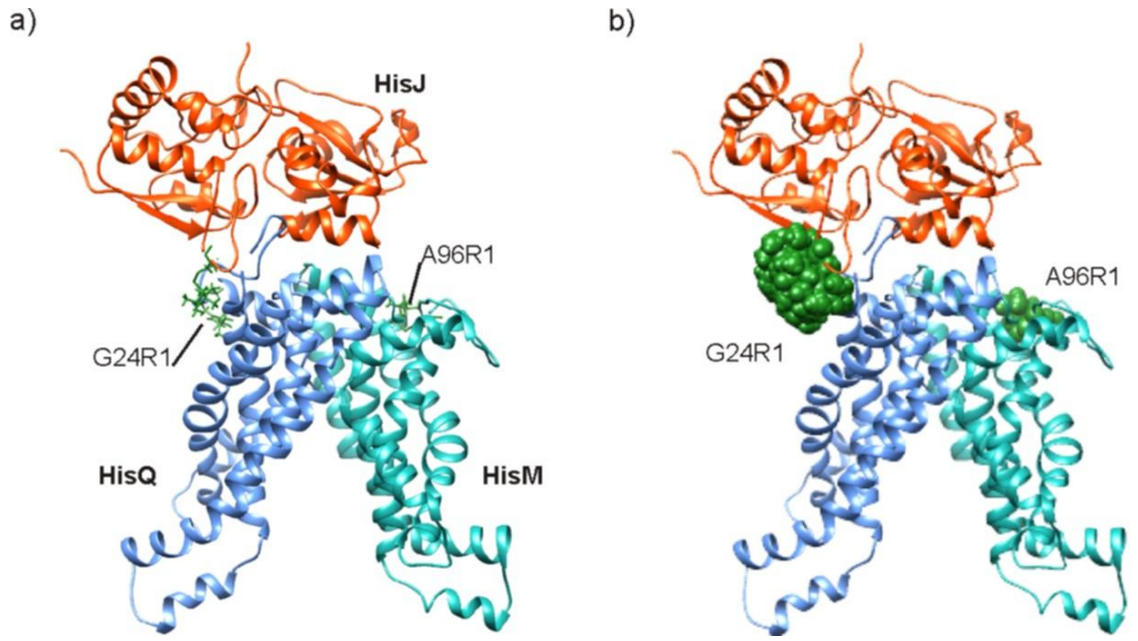

Figure 5.11: Model of HisJ in Interaction with HisQM. The model is based on the crystal structure of liganded HisJ (pdb: 1HPB) and the model of HisQM as depicted in figure 1. a) Single spin labels at positions G24R1 in HisJ and A96R1 in HisM are depicted in stick representation and highlighted in green. b) Rotamer spatial distributions of the R1 side chains are depicted in spheric representation and highlighted in green.

First experiments were accomplished utilizing a 1:1 molar ratio of HisJ to $HisQMP_2$. Since the affinity of the SBP for the ATP-bound transporter is quite low, the binding constant is about ~10 µM (independent of substrate) [82], and even lower for the ATP-free state, a fivefold molar excess of HisJ versus $HisQMP_2$ was established in the following DEER experiments to increase the presence of the coupled state.

Figure 5.12 depicts and compares cw EPR spectra of a 1:1 molar mixture of HisQM(A96R1)P_2 and HisJ G24R1 in the nucleotide-free and –bound states and in the absence or presence of the substrate histidine. To induce the nucleotide-bound state the non-hydrolyzable ATP analogue AMP-PNP was utilized. All spectra exhibit a two state equilibrium of an immobile and a major mobile nitroxide component. There is no visible spectral change upon inducing the nucleotide-bound state or upon addition of histidine in the apo state. However, minor changes occur upon the addition of the substrate while the transporter is locked in its nucleotide-bound state. Inset 2 in figure 5.12 shows an overlay of the low-field resonance lines of the apo state without substrate and the nucleotide-bound state in the presence of histidine. A marginal reduced mobility is revealed for the AMP-PNP-bound state in the presence of the substrate. However, in this experiment the cw EPR data is insufficient to prove

the coupling of HisJ to HisQM because of the low binding constant and therefore low amount of interacting molecules. In this context, DEER spectroscopy is a better means of investigating spin-spin interactions between the SBP and the TMDs of the transporter because only interacting molecules induce dipolar modulation.

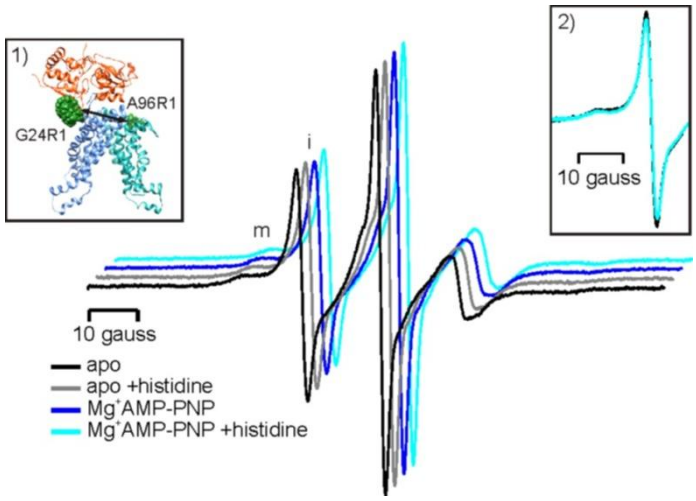

Figure 5.12: cw EPR spectra of HisJ interacting with $HisQMP_2$ in different states of the transporters nucleotide hydrolysis cycle. cw EPR spectra (normalized by maximum) recorded at room temperature of $HisQMP_2$, reconstituted into liposomes, and HisJ (1:1 molar ratio) in the apo and the AMP-PNP bound state of the transmembrane transporter and in the absence and presence of the substrate histidine. Inset 1: Model of the HisQM/HisJ Interface. The sturcture of HisQM is a homology model based on the crystal structure of MetNI combined with the crystal structure of HisJ (1HPB.pdb). The spatial nitroxide rotamer distributions at positions HisQ(A96)M and HisJ(G24), designated as R1, are highlighted (green). Arrows indicate interspin distances. Inset 2: overlay of the low-field resonance lines of the apo and Mg^+AMP-PNP + histidine spectra.

Figure 5.13 depicts the obtained DEER data and associated distance distribution of the above described HisJ(G24R1) and HisM(A96R1). Spin labeled $HisQMP_2$ complexes were reconstituted into liposomes and investigated in the presence of the liganded or non-liganded spin labeled HisJ in three different states of the nucleotide hydrolysis cycle: in the apo-state (in the absence of nucleotides), in the nucleotide-bound state (in the presence of AMP-PNP to inhibit nucleotide hydrolysis) and in the posthydrolytic state. All samples were incubated for 30 min at 37°C to ensure nucleotide binding and hydrolysis, respectively. One sample was also investigated by introducing the vanadate-trapped conformer of the NBDs trapping the transition state during ATP hydrolysis.

Strongly damped oscillations arise in the first 0.5 µs of the DEER data of all measurements similarly to observations made for $HisQMP_2$ as described above. The according form factors, F(t), are depicted in figure 5.13 b (the raw data are shown in the appendix, figure 7.5). The DEER data of the apo state as well as the posthydrolytic-state and the vanadate-trapped state of a 1:1 molar ratio HisQM(A96R1)P_2 and HisJ G24R1 with or without substrate exhibit almost no modulation depth (0-3%) which corresponds to 0-7.5% of interacting spins. The addition of the nucleotide analogue increases the modulation depth to 11% for a 1:1 ratio in the absence of histidine and to 23% for a molar ratio of 1:5 in the presence of histidine. These values correspond to 27.5% (1:1 ratio w/o substrate) and 57.5% (1:5 ratio w substrate) of interacting spins, respectively. These results show that the dimerization of the NBDs is necessary for binding of HisJ at the periplasmic side suggesting a conformational transition through the TMDs upon nucleotide binding. The form factors of HisQM(A96R1)P_2-HisJ G24R1 (1:1 ratio w/o substrate) and HisQM(A96R1)P_2-HisJ G24R1 (1:5 ratio w substrate) also show different progressions over time, which is furthermore reflected in the according distance distributions (figure 5.13 c). Due to the small modulation depths and small signal to noise ratio of most DEER traces only distance distributions of AMP-PNP-bound states are shown. Due to the very broad distance distribution of HisQM(A96R1)P_2-HisJ G24R1 (1:1 ratio w/o substrate) a Gaussian fit was applied instead of Thikonov regularization yielding a distance maximum at 4.3 nm which agrees with the simulated data from the rotamer library analysis approach applied on the model (distance maximum 4.7 nm). The broad distribution also reflects a high flexibility most probable attributed to the substrate-free HisJ. The distance distribution of HisQM(A96R1)P_2-HisJ G24R1 (1:5 ratio w substrate) yielded by Thikonov regularization is narrow in comparison with two distinct distance peaks at 3.4 nm and 5.1 nm. The two separated maxima could arise due to the high flexibility of the loop-region associated position G24 located in HisJ. This data is also in agreement with the simulated data giving validity to the suggested model of HisJ/$HisQMP_2$ interaction. Comparing the two distance distributions and the form factors also hints towards two differing conformations of the SBP in dependence of the substrate.

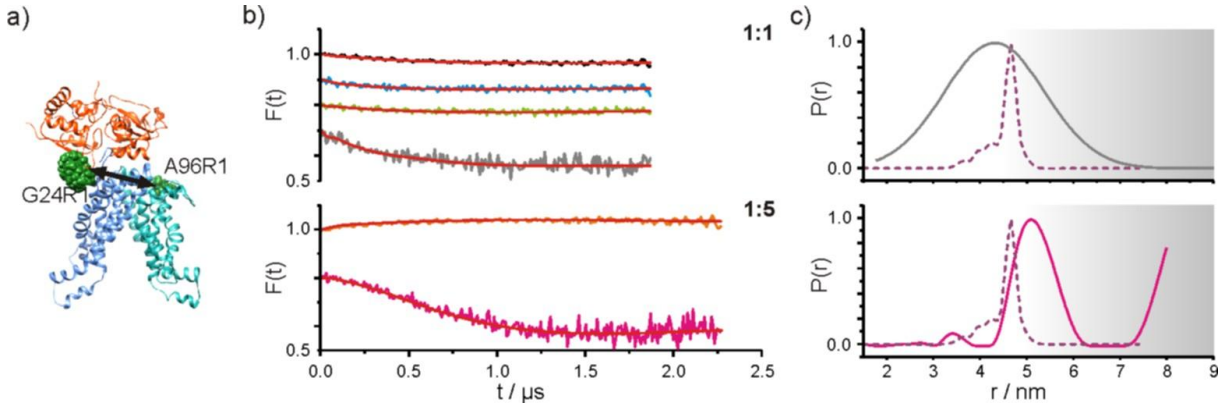

Figure 5.13: X-band DEER traces and interspin distance distributions detecting interaction between HisQMP$_2$ and HisJ in different states of the nucleotide hydrolysis cycle. a) Model of the HisQM/HisJ Interface. The sturcture of HisQM is an analogy model based on the crystal structure of MetNI combined with the crystal structure of HisJ (1HPB.pdb). The spatial nitroxide rotamer distributions at positions HisQ(A96)M and HisJ(G24), designated as R1, are highlighted (green). The arrow indicates the interspin distance. b) Baseline corrected data, F(t), of samples containing HisQM(A96R1)P$_2$ and HisJ(G42R1). Fits corresponding to the DEER traces are depicted as overlay (red line). Upper row (1:1 molar ratio of HisQMP$_2$:HisJ): The apo-state (black trace), the nucleotide-bound state of HisQMP$_2$ induced by Mg$^+$AMP-PNP (gray trace), the posthydrolysis-state (blue trace) and the vanadate-trapped state (green trace). Lower row (1:5 molar ratio HisQMP$_2$:HisJ and addition of 1 mM histidine): The apo-state (orange trace) and the nucleotide-bound state of HisQMP$_2$ induced by Mg$^+$AMP-PNP (pink trace). c) Distance distribution calculated from the DEER traces shown in b). Due to the small modulation depth of most DEER traces only distance distributions of AMP-PNP samples are shown. Tikhonov regularization and a Gaussian fit are applied by utilizing DEER Analysis 2013 [96]. Above 4.5 nm a gray shaded area indicates limited certainty of the distance data (position and width of the distribution) based on the length of the shortest DEER time trace. Simulated distance distributions based on the HisQM/HisJ interface model were calculated using MMM 2013 [159].

5.2.1.3 Conformational changes of HisJ upon substrate binding in dependence of the nucleotide hydrolysis cycle

The substrate binding protein HisJ works as a substrate delivery system for the membrane-bound transporter complex HisQMP$_2$, whereby its modus operandi works according to the venus flytrap principle [60]. The overall structure of the proteins is divided into two lobe domains connected by a hinge region. In this experimental approach the conformational transition occurring in HisJ upon substrate binding in dependence to the nucleotide hydrolysis cycle of the membrane-bound transporter complex was investigated. For this purpose spin labeled variants of HisJ were

studied by cw-EPR and DEER spectroscopy. Different sites in HisJ, G24 and C45 in lobe 1 and T151 in lobe 2 (depicted in figure 5.14 a) were chosen for SDSL with MTSSL in order to establish the described experimental approaches. The double mutant G24R1_T151R1 was introduced to observe distance changes between the two lobes of the protein upon substrate binding. In advance it was verified that cysteine substitutions and spin labeling at the according sites did not alter the functionality and activity of the protein.

Figure 5.14 b depicts the normalized cw spectra of HisJ G24R1, HisJ C45R1, T151R1 and of the double-mutant G24R1_T151R1. Position G24R1 shows the highest R1 dynamic according to its location in a surface exposed loop region. HisJ C45R1 exhibits spectral features that indicate a restricted degree of mobility the R1 orientation facing the protein interior. Site T151R1 is located in an α-helix exposed on the protein surface suggesting high motional freedom. However, the assumption of a highly mobile spin label is not reflected in the according EPR spectrum which exhibits motional restriction of R1. For the single mutants there is no observable effect emerging that binding of histidine alters the mobility of the attached nitroxides. The double mutant shows minor spectral changes in the substrate-bound state indicated by faint broadening and an increased amplitudes of the low field resonance line. This behavior can be interpreted as evidence of dipolar coupling due to approaching spins. A comparison of the spectra of the substrate-free HisJ G24R1_T151R1 with the superposition of the spectra of an equimolar mixture of the substrate-free HisJ G24R1 and HisJT151R (inset of figure 13b) shows the significant broadening of the spectrum of HisJ G24R1_T151R1 due to spin-spin interaction.

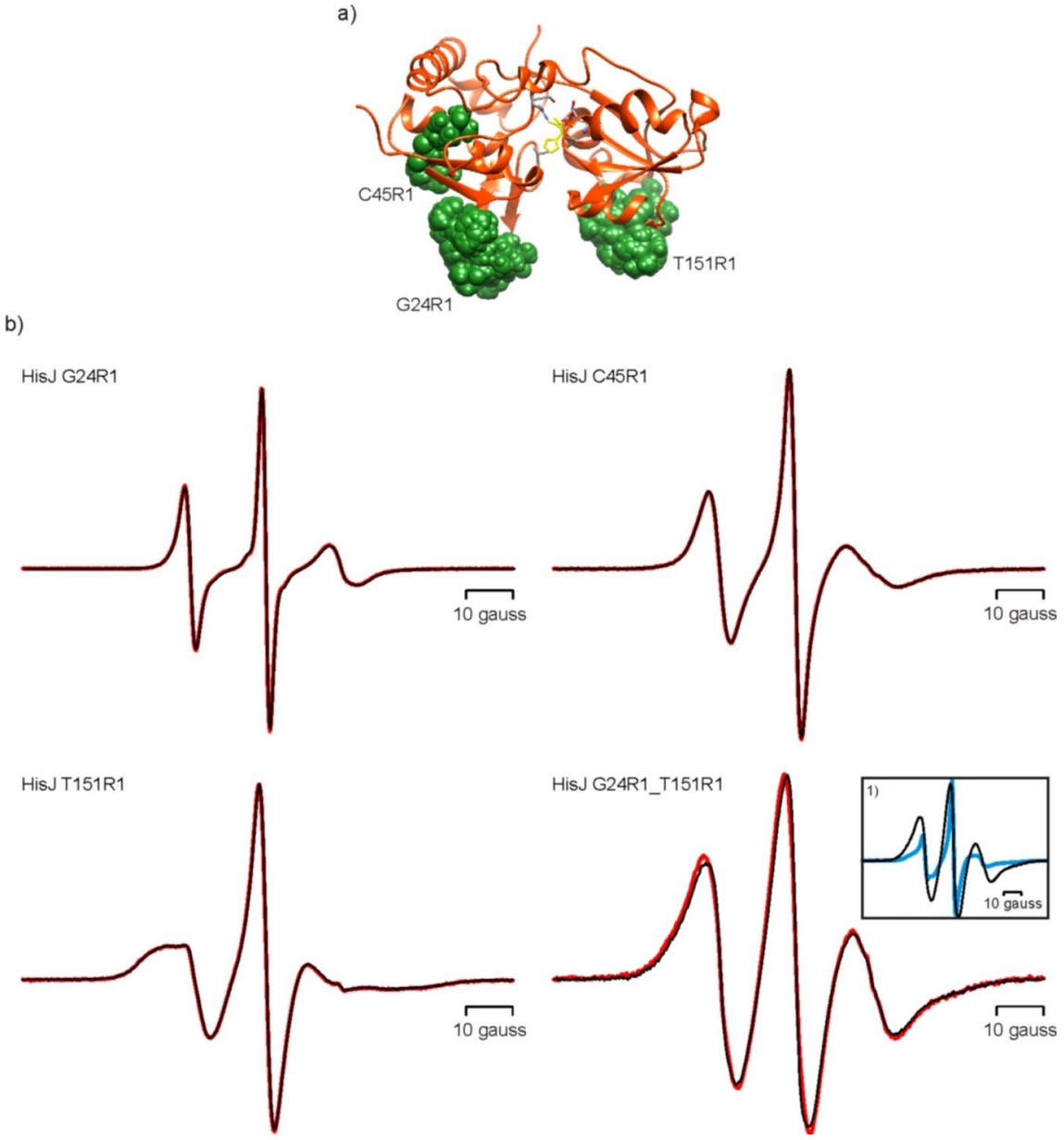

Figure 5.14: Cw EPR spectra of the substrate binding protein HisJ in presence and absence of substrate. a) Crystal structure of HisJ (1HPB.pdb) with bound histidine (yellow) and nitroxide rotamer distributions at positions G24, C45 and T151, designated as R1 (green). b) The cw EPR spectra of the spin labeled mutants of HisJ (recorded at room temperature) are normalized by their respective maximum. Each variant of the protein is examined in the absence of substrate (black lines) and in the presence of 1 mM histidine (red lines). Inset: Comparison of the spectrum of HisJ G24R1_T151R1 (no substrate) (black line) with the superposition of the spectra of an equimolar mixture of HisJ G24R1 (no substrate) and HisJT151R1 (no substrate) (blue line).

Figure 5.15 depicts the obtained DEER data and associated distance distributions of the double mutant HisJ G24R1_T151R1. The spin labeled HisJ was investigated with and without substrate in the absence and in the presence of the wild type $HisQMP_2$

(1:1 molar ratio of $HisQMP_2$:HisJ) reconstituted in liposmomes. For the transporter the different states of the nucleotide hydrolysis cycle where induced: the apo-state (in the absence of nucleotides), in the nucleotide-bound state (in the presence of AMP-PNP to inhibit nucleotide hydrolysis) and in the posthydrolytic state (in the presence of ADP). One sample was investigated in the presence of the vanadate-trapped conformer of the NBDs mimicking the transition state during ATP hydrolysis. Another sample was measured in the presence of the non-hydrolyzing variant of the transporter complex $HisQMP(E179Q)_2$. All samples were incubated for 30 min at 37°C to ensure nucleotide binding and hydrolysis, respectively. Figure 5.15 a depicts the structure of HisJ (PDB: 1HPB) together with the spatial rotamer ensembles of the attached spin labels obtained by *in silico* spin-labeling. The DEER data form factors, F(t), are depicted in figure 5.15 b (the raw data are given in the appendix, figure 7.6). The progress of F(t) is basically unaltered for all states of the nucleotide hydrolysis cycle with respect to the presence or absence of the substrate. This behavior is probably based again on the low binding affinity of HisJ to the periplasmic side of $HisQMP_2$, and contributions of the coupled HisJ molecules are too small to be detected. Therefore, the F(t) of HisJ G24R1_T151R1 in the absence of $HisQMP_2$ is in well agreement with the F(t) of HisJ G24R1_T151R1 in the presence of $HisQMP_2$ both in the substrate-bound and –free state. Further experiments investigating this context should therefore be executed with a molar excess of $HisQMP_2$ over HisJ. The resulting distance distributions, depicted in 5.15c) of the substrate-free form of HisJ G24R1_T151R1 vary only slightly with a prominent distance maximum between 3 nm and 3.1 nm for all investigated states. This find coincides with the simulated distance distribution obtained from the rotamer library analysis approach of the structure of HisJ G24R1_T151R1 (1HPB.pdb) (figure 5.15 b and c upper row).

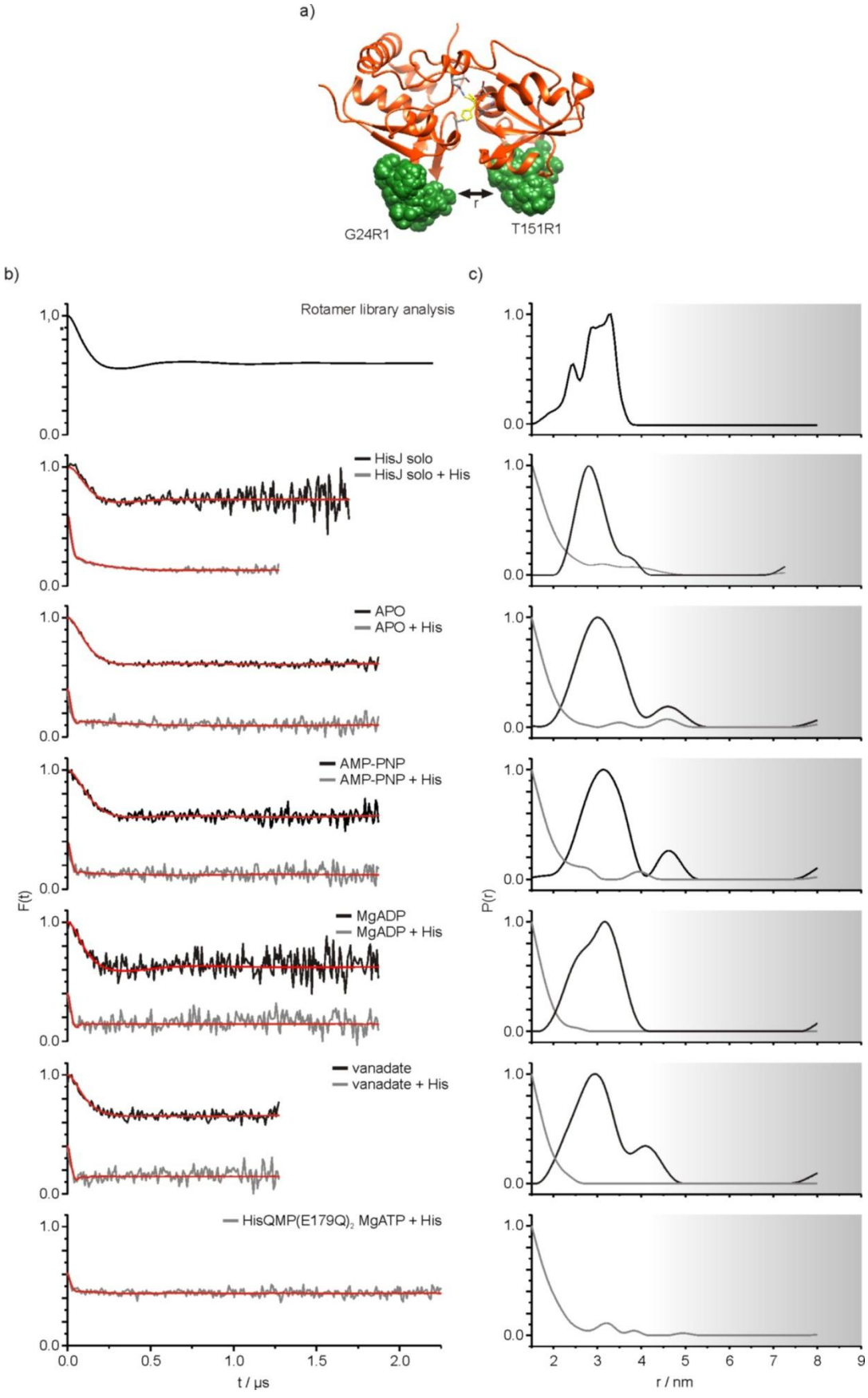

Figure 5.15: DEER traces and interspin distance distributions of HisJ G24R1_T151R1 in absence and presence of wt HisQMP$_2$ in different states of the nucleotide hydrolysis cycle. a)

Crystal structure of HisJ (1HPB.pdb) with bound histidine (yellow) and nitroxide rotamer distributions at positions G24 and T151, designated as R1 (green). b) DEER time traces of double labeled HisJ G24R1_T151R1 in absence and presence of reconstituted $HisQMP_2$ or $HisQMP(E179Q)_2$ (1:1 molar ratio of $HisQMP_2$:HisJ) (black traces) and in addition of the substrate histidine (gray traces). Fits corresponding to the DEER traces are depicted as overlay (red line). Nucleotide-bound states of $HisQMP_2$ are induced by Mg^+AMP-PNP, Mg^+ADP, Mg^+ATP or vanadate. c) Distance distribution calculated from the DEER traces shown in b). Tikhonov regularization is applied by utilization of DEER Analysis 2013 (DeerAnalysis2013 [96]). Above 4.2 nm a gray shaded area indicates limited certainty of the distance data (position and width of the distribution) based on the length of the shortest DEER time trace. Simulated distance distributions based on the HisJ crystal structure (1HPB.pdb) were calculated using MMM 2013 [159].

This find is of particular interest, since the utilized structure (PDB: 1HPB) [144] should reflect the histidine-bound form of HisJ but the data of this work suggests that it matches the substrate-free form. Binding of histidine induces shifts to very short distances with maxima located below 1.5 nm. This is reflected in the steep decay of F(t) within the first 50 ns. Small additional contributions that arise above 2 nm can be probably attributed to the flexible loop-region G24R1 resides in. This substrate-dependent shift to shorter distances in the distance distribution of HisJ G24R1_T151R1 reflects the protein´s transition into the closed conformation.

5.2.2 Investigations on the ECF-type biotin transporter BioMNY

5.2.2.1 Closure and reopening of the NBDs of BioMNY observed by DEER spectroscopy*

Within the substrate transport process of canonical ABC transporters the respective nucleotide binding domains experience a repetitive closing and reopening cycle [48, 71]. This is exemplified by the nucleotide hydrolysis cycle of the maltose ABC importer $MalFGK_2$. This notion is also supported by the findings of this work for the histidine transporter $HisQMP_2$ and its approaching Q-loops in the HisP dimer upon nucleotide binding. The following experimental approach covers investigations on the dimerization of the ATPases of the biotin specific ECF transporter BioMNY from *R. Capsulates* upon nucleotide binding and the opposed reorientation upon ATP hydrolysis. For this purpose the nucleotide hydrolysis cycle was simulated for in

* Part of this section was published prior to submission of this thesis [51].

nanodiscs reconstituted and spin labeled (MTSSL) BioMNY by inducing the apo-state in the absence of nucleotides, the nucleotide-bound and the post-hydrolysis states. To ensure nucleotide binding or ATP-hydrolysis all samples were incubated for 30 min at 37°C. Sufficient enzyme activity for the in nanodisc reconstituted and cysteine less BioMNY was verified by an ATPase assay and reached 70% of the wild types activity indicating the preserved functionality of the investigated variants. The according samples were subjected to DEER spectroscopy. All investigated samples were purified, prepared and tested for activity by the T. Eitinger group in accordance with procedures and methods given in the literature [51]. The bacterial ECF-type biotin transporter BioMNY from *Rhodobacter capsulates* consists of the transmembrane domains BioN (T-unit), BioY (S-unit) and the cytoplasmic ATPase dimer $BioM_2$ (A-unit) assuming a 1(T):1 (S):2 (A) stoichiometry. Measured spin-spin interactions cover the distance between the positions H87/H87´ which reside in the Q-helices in BioM, analogous to the Q-loop in canonical ABC transporters. A model with bound *in silico* generated spin labels (rotamer library analysis) at position H87/H87´ in $BioM_2$, spanning the observed distance vector, is depicted in figure 5.16. The amount of predicted sterically viable rotamers led to the assumption that the influence on the structural integrity at position H87 is uncritical.

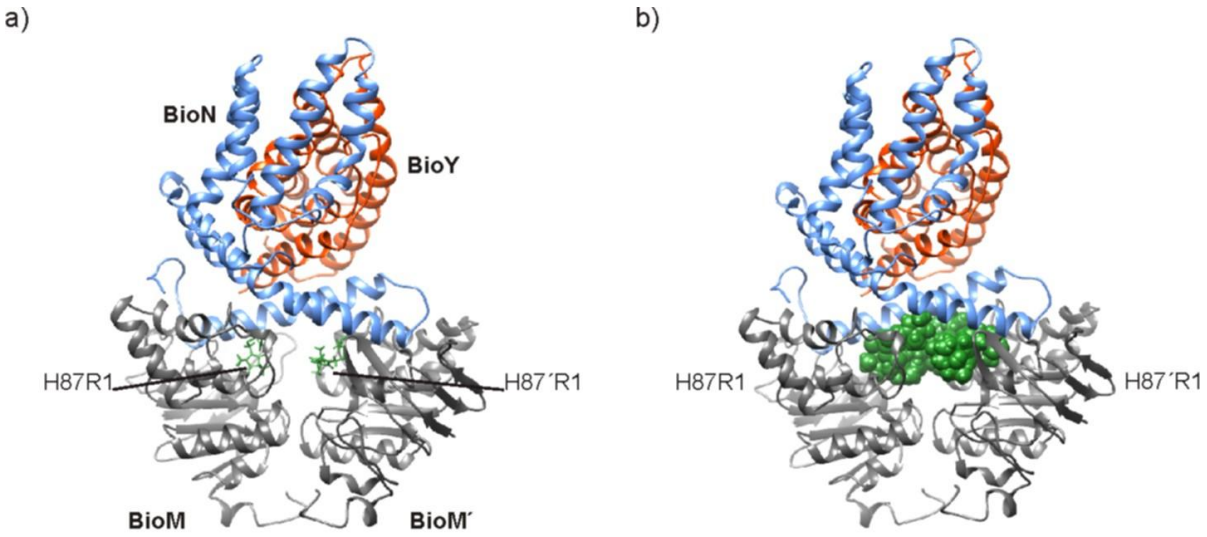

Figure 5.16: Model of BioMNY with bound R1 spin labels at position H87/H87´. The model is based on the NBDs and the T component of the folate transporter of *Lactobacillus brevis* and BioY of *Lactobacillus lactis* as described in the literature [51]. a) Single spin label side chains at positions H87 in BioM and BioM´ are depicted in stick representation and highlighted green. b) Rotamer spatial

distributions of spin labels are depicted in spheric representation and highlighted in green. Romaters were implemented *in silico* utilizing MMM2013 [159].

Figure 5.17 depicts the resulting DEER data and interspin distance distributions of the above described experimental approaches covering the different states of the transporter´s nucleotide hydrolysis cycle. DEER raw data (data shown in the appendix, figure 7.7) exhibited in all cases strongly damped oscillations due to spin-spin interaction and the background-contribution, the homogeneous multidimensional distribution of spins in the samples. The corresponding form factors, F(t), (figure 5.17 b) were determined after dividing the raw data by the background and renormalizing at zero time as described before. The form factors reveal in all cases low modulation depths (8-12%). This corresponds to a labeling efficiency of 0.35-0.5 spins per BioM molecule and is probably attributed to a restricted accessibility of positions H87/H87´ in the process of spin labeling. Gaussian distance distributions were obtained from fits to the form factors F(t) revealing state-dependent shifts of distance maxima, as depicted in figure 5.17 c. The distance maxima in the apo-state is located at 3.4 nm. Surprisingly, the interspin distances predicted by rotamer analysis, which reveal distances below 2 nm, do not correspond to the experimental data, indicating a more open conformation than suggested by the model. Upon nucleotide binding, in the presence of ATP or AMP-PNP, the distribution shifts to a shorter distance of 2.7 nm. However, the addition of the substrate biotin increases the distances maximum to 3.4 nm in the nucleotide-bound state. ATP-hydrolysis shifted the maxima of the respective samples (ATP $MgCl_2$ and ADP plus $MgCl_2$) to 3.9 nm. From the gathered DEER spectroscopy data the conclusion can be drawn that nucleotide binding and hydrolysis decreases and re-increase the distance between spin labeled positions H87R1/H87´R1, therefore resembling the closure and re-opening of the NBDs during the transport cycle of BioMNY.

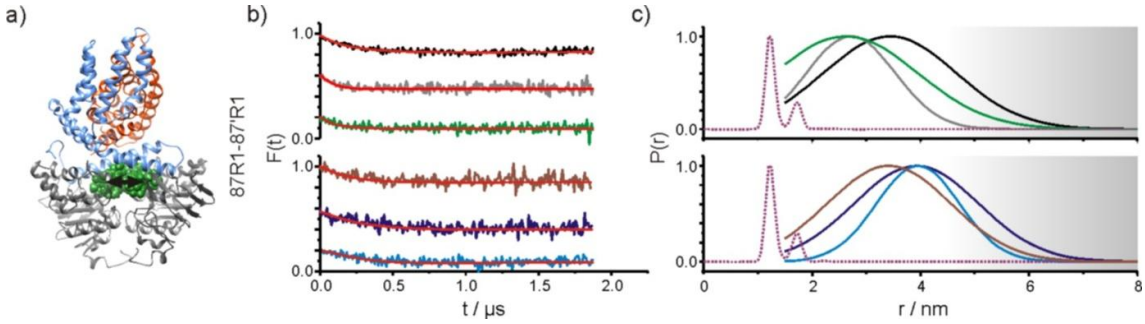

Figure 5.17: DEER traces and interspin distance distributions of BioM(H87R1)$_2$NY for three different states of the nucleotide hydrolysis cycle. a) Model of BioMNY with rotamer ensembles at position H87/H87`in BioM highlighted in green. b) Baseline corrected form factor, F(t) of In nanodiscs reconstituted BioM(H87R1)$_2$NY for the apo state (black line), the nucleotide-bound state (ATP plus EDTA, gray line; Mg^+AMP-PNP, green line), the nucleotide-bound state (ATP plus EDTA) plus biotin (brown line) and the posthydrolysis state (Mg^+ATP, dark blue line; Mg^+ADP, light blue line). Fits corresponding to the DEER traces are depicted as overlay (red line). c) Distance distribution calculated from the DEER traces shown in b). A Gaussion fit is applied by utilization of DEER Analysis 2013 [96]. Above 4.2 nm a gray shaded area indicates limited certainty of the distance data (position and width of the distribution) based on the length of the shortest DEER time trace. Simulated distance distributions based on the model of BioM$_2$NY were calculated using MMM 2013 [159].

5.2.2.2 Reorientation of the S-unit BioY in response to nucleotide binding in the NBDs

A proposed model for the substrate transport pathway of BioMNY and for ECF transporters in general suggests a reorientation of the transmembrane S-unit (BioY) by nearly 90° in response to the nucleotide binding in the NBDs, therefore facilitating substrate uptake at the extracellular side of the membrane [51]. Nucleotide hydrolysis would drive the opposite conformational transition and would enable substrate transport and release at the cytoplasmic side of the membrane. To investigate this so called toppling over mechanism by DEER spectroscopy spin labels were introduced at several sites in BioY and BioN to create spin pairs between the T- and S-unit. Chosen positions in BioY , K137 and A152, are located within the loop region connecting the transmembrane helices 5 and 6, which is assumed to be oriented to the extracellular side in the ATP-bound state of the NBDs. Positions in BioN, A166 and L82, are located in the loop region connecting the coupling helices 2 and 3 and the transmembrane helices 4 and 5, respectively. The according single- and double mutated cysteine variants BioM(A166C)NY, BioM(L82C)NY, BioMNY(K137C),

BioMNY(A152C), BioMN(A166C)N(A152C)Y and BioMN(L82C)Y(K137C) were modified with MTSSL and incorporated into nanodiscs after labeling. All investigated samples were purified and prepared in the group of T. Eitinger in accordance with procedures and methods given in the literature [51]. Figure 5.18 a and b depict the model of BioMNY and the described sites in BioY and BioN chosen for SDSL with MTSSL.

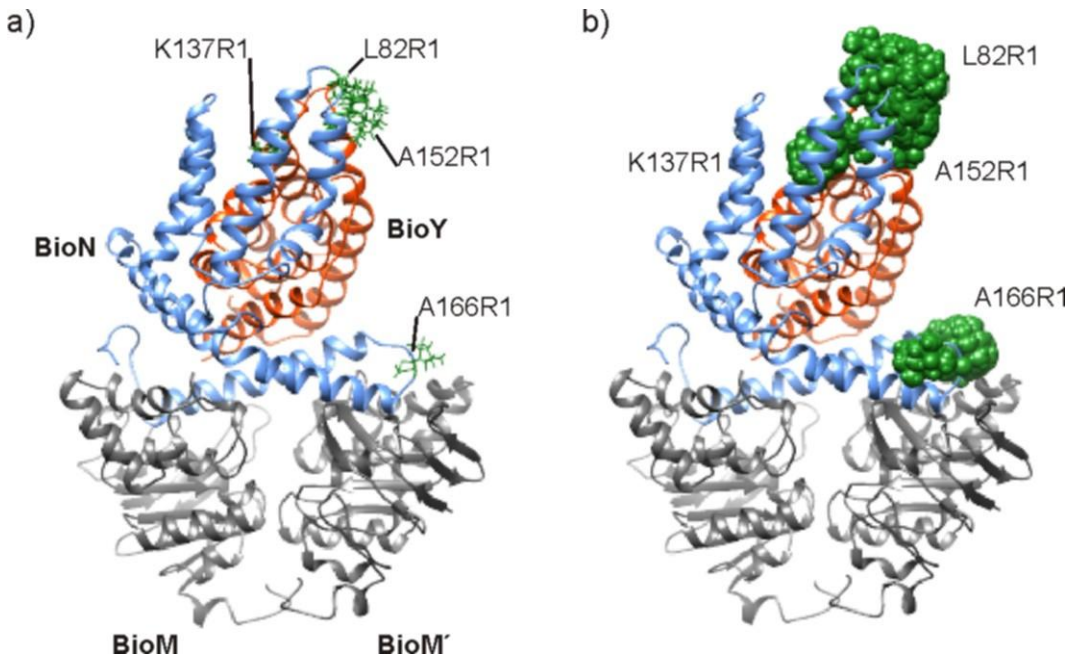

Figure 5.18: Model of BioMNY with spin labels bound to BioN and BioY. The model is based on the NBDs and the T component of the folate transporter of *Lactobacillus brevis* and BioY of *Lactobacillus lactis* as described in [51]. a) Single spin label residues at positions K137R1 and A152R1 in BioY and L82R1 and A166R1 in BioN are depicted in stick representation and highlighted green. b) Rotamer distributions of spin labels are depicted in spheric representation and highlighted in green. Romaters were implemented *in silico* utilizing MMM2013 [159].

Figure 5.19 shows the obtained DEER data for single labeled BioMN(A166R1)Y, BioMNY(A152R1) and the double mutant BioMN(A166R1)Y(A152R1) in the apo and the ATP-bound states. The rotamer ensembles of the respective analyzed sites in BioMNY, introduced by a rotamer library approach, and the schematic prediction of the resulting distance vector is depicted in figure 5.19 a. The DEER raw Q-band data of the single mutant samples (data shown in the appendix, figure 7.8) reveal strongly damped oscillations due to intermolecular spin-spin interactions. The form factors, F(t), derived after division of the raw data by the backgrounds contribution originating

from the homogeneous distribution of spins in the sample, of single and double mutants are depicted in figure 5.19 b. The modulation depths for the single mutants, especially for A152R1, which amounts to 10% corresponding to approximately 100% of interacting spin labels, reveal spin-spin interactions independent of the nucleotide, indicating inter-molecular interactions and accordingly the oligomerization of BioY. Smaller modulations depths are found for A166R1, 2.5% in the apo state and 4% in the ATP-bound state, which also pointing out that more than one BioN molecule is present in the nanodiscs. Thikonov regularization was applied to the form factors resulting in distance distributions depicted in figure 5.19 c. Single mutants in both the apo and nucleotide-bound states reveal broad distance distributions indicating oligomerization of BioY and BioN. The apo state of the double mutant exhibits two distance maxima at 2.1 nm and 4.3 nm. The ATP-bound state induces a partition of the maxima at 4.3 nm into distance peak at 4.7 nm and an additional emerging contribution between 2.5-3 nm. The emerging contribution at 2.5-3 nm could indicate the conformational transition of BioY and its reorientation in the membrane upon nucleotide binding. However, because of the inter-spin distance contributions from oligomerized S- and T-units drawing conclusions with respect to the reorientation of BioY is uncertain.

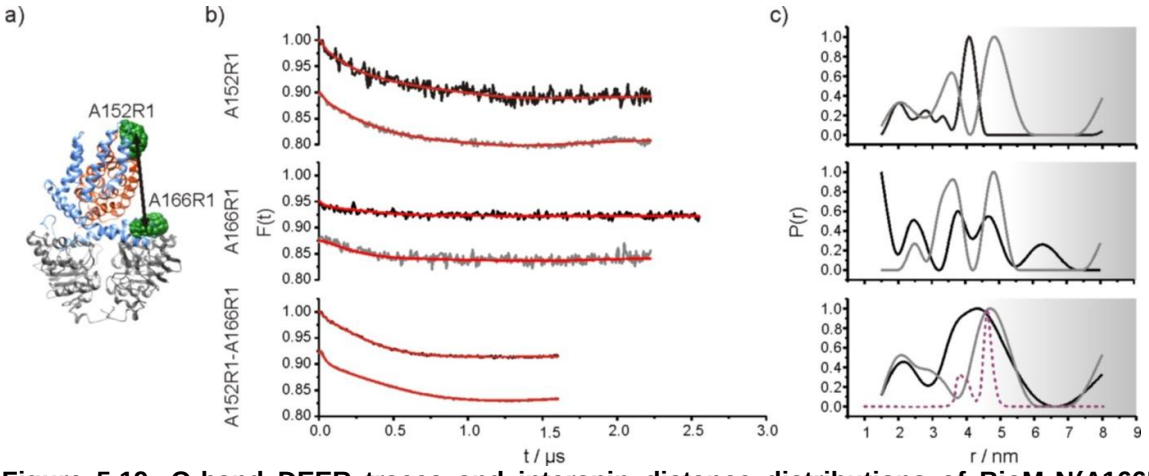

Figure 5.19: Q-band DEER traces and interspin distance distributions of BioM$_2$N(A166R1)Y, BioM$_2$NY(A152R1) and BioM$_2$N(A166R1)Y(A152R1) for the apo and nucleotide-bound states. a) Model of BioMNY with rotamer ensembles at positions A166 in BioN and A152 in BioY highlighted in green. b) Baseline corrected form factor, F(t) of in nanodiscs reconstituted BioM$_2$N(A166R1)Y, BioM$_2$NY(A152R1) and BioM$_2$N(A166R1)Y(A152R1) for the apo state (black line) and the nucleotide-bound state (ATP plus EDTA, gray line). Fits corresponding to the DEER traces are depicted as overlay (red line). c) Distance distribution calculated from the DEER traces shown in b. Thikonov regularisation is applied by utilization of DEER Analysis 2013 [96]. Gray shaded area indicates limited

certainty of the distance data (position and width of the distribution) based on the length of the shortest DEER time trace. Simulated distance distributions based on the model of $BioM_2NY$ were calculated using MMM 2013 [159].

Figure 5.20 depicts the DEER data of similarly executed experiments on single labeled BioMN(L82R1)Y, BioMNY(K137R1) and the double mutant BioMN(L82R1)Y(K137R1). The rotamer ensembles of the corresponding sites in the BioMNY model and the schematic distance vector are depicted in figure 5.20 a. As observed before the DEER raw data (data shown in the appendix, figure 7.9) reveal in all cases strongly damped oscillations. The form factors, F(t), of single and double mutants are depicted in figure 5.20 b. Again both single mutants BioMN(L82R1)Y and BioMNY(K137)R1 reveal inter-spin interactions in the apo-sate similar to BioMN(A166R1)Y and BioMNY(A152R1) due to intermolecular spin-spin interactions. ATP-bound BioMN(L82R1)Y(K137R1) reveals a steeper decay than the apo state within the first 100 ns. Resulting distance distributions of L82R1 and K137R1, depicted in figure 5.20 c, reveal similar widths with two almost equal maxima at 2.5 nm and 4.7 nm. Both the apo and ATP-bound state of BioMN(L82R1)Y(K137R1) yield broad distance distributions with multiple maxima. A shift of the distance maxima occurs upon nucleotide binding to the NBDs. However, due to the obvious intermolecular contributions a clear interpretation is difficult. Differences between the apo and the ATP-bound state could be interpreted as a shift to longer distances based on the distance maxima of the apo state at 2.9 nm and 4.6 nm.

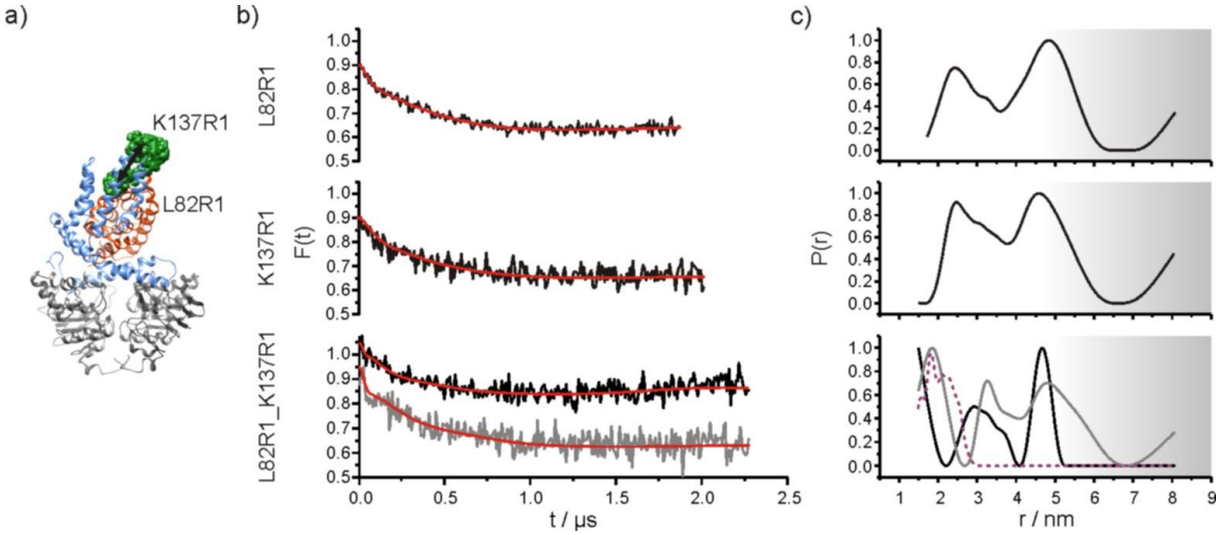

Figure 5.20: Q-band DEER traces and interspin distance distributions of BioMN(L82R1)Y, BioMNY(K137R1), BioMN(L82R1)Y(K137R1) for the apo and nucleotide-bound states. a) Model of BioMNY with rotamer ensembles at positions L82 in BioN and K137 in BioY highlighted in green. b) Baseline corrected form factor, F(t) of in nanodiscs reconstituted BioM_2N(L82R1)Y, BioM_2NY(K137R1) and BioM_2N(L82R1)Y(K137R1) for the apo state (black line), the nucleotide-bound state (ATP plus EDTA, gray line). Fits corresponding to the DEER traces are depicted as overlay (red line). c) Distance distribution calculated from the DEER traces shown in b. Thikonov regularisation is applied by utilization of DEER Analysis 2013 [96]. Gray shaded area indicates limited certainty of the distance data (position and width of the distribution) based on the length of the shortest DEER time trace. Simulated distance distributions based on the model of BioM_2NY were calculated using MMM 2013 [159].

5.2.3 Investigations on the S-unit CbiM of cobalt specific CbiMNQO

Substrate binding to vitamin-specific single S-units is independent of the complex assembly with the corresponding T-units and NBDs due to the high substrate affinity of the protein. This correlation is not verified for the purified metal ion specific S-unit CbiM of CbiMNQO. Here it is analyzed if Cbi(MN), the enzymatic inactive variant Cbi(M_{H2D}N) and CbiM are able to bind cobalt ions. Detection of paramagnetic Co^{2+} by EPR spectroscopy is challenging because of its very short longitudinal relaxation time T_1, which is responsible for vast line broadening. For this reason experiments must be accomplished at low temperature (10 K) and low microwave powers [86]. Detergent-solubilized samples of Cbi(MN), Cbi(M_{H2D}N) and CbiM, incubated with 25fold molar excess of $CoCl_2$ during purification, were analyzed with low temperature cw-EPR. All investigated samples were purified and prepared by the group of T. Eitinger in accordance with procedures and methods given in the literature [106].

Figure 5.21 depicts the cw EPR spectra and reveals a Co^{2+} signal only for the wild type Cbi(MN). It seems apparent that the presence of CbiN is necessary for the binding of the substrate to wild type CbiM. Cbi($M_{H2D}N$), which lacks the metal coordinating histidine at position 2, also does not show any signal. The small line width of the Cbi(MN) associated Co^{2+} allows the discrimination of the hyperfine interaction. Because of the nuclear spin I=7/2 eight hyperfine-lines emerge for the three g-tensor components. Due to the small g-anisotropy those hyperfine-lines overlap. The result indicates a rigid homogeneous structure of the ion ligandization. [12]. Simulation to the obtained spectra, utilizing the program EasySpin [196], yields a value of 6.76 for the sum of the three g-tensor components which is characteristic for low-spin Co-complexes with an electron spin of S=1/2 [86]. This condition is evident for quadratic planar or pseudo-tetrahedral spin systems [95]. The above findings correspond to the results obtained from in vivo experiments of bacterial uptake of the radioactive cobalt isotope $^{57}Co^{2+}$ which revealed functionality of Cbi(MN) but not of Cbi$M_{H2D}N$, Cbi($M_{H2D}N$) and CbiM [106, 173, 185] and verifies the essential relevance of CbiN in the process of substrate transport. However, the modus operandi of the CbiN unit within the transport cycle has not been solved until now.

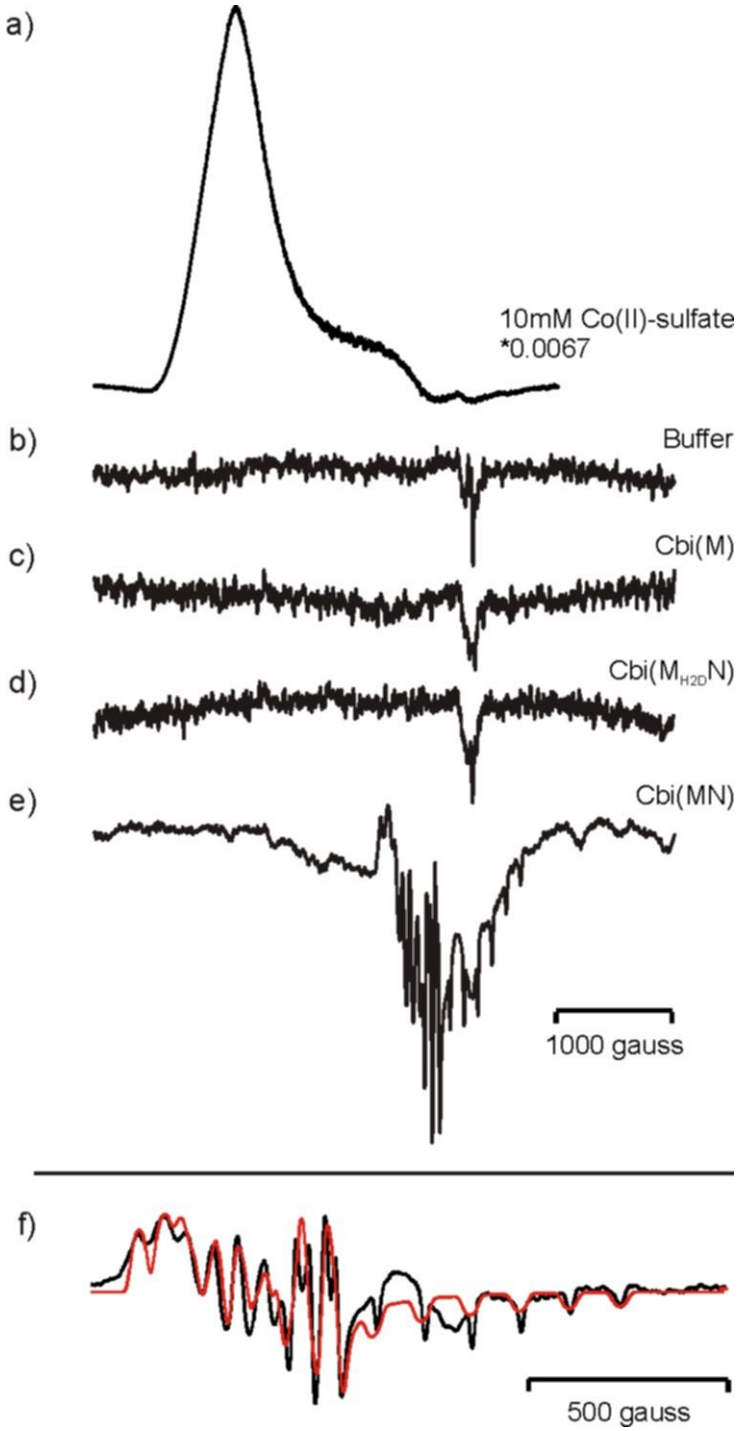

Figure 5.21: Cw-EPR spectra of free and CbiMN-bound cobalt.

a) $CoSO_4$, b) buffer without Co^{2+}, c) CbiM, d) $CbiM_{H2D}N$, e) CbiMN in buffer (100 mM Tris/HCl, pH8.0, 300 mM NaCl, 0.05% dodecyl-x, D-maltopyranoside, 20% glycerol) that were titrated with Co^{2+}. Experiments b) to e) were accomplished at a temperature of 10 K, at a microwave power of 7 µW. Experiment a) was accomplished at 10 K as well at 10 mW. Spectrum a) was multiplied by the factor of 0.0067. The signal at 3280 gauss in the buffer reference spectrum b), that is visible in the other spectra as well, is caused by the EPR capillary. f) Section of the baseline-corrected spectrum of CbiMN (black line) shown in e) with the superimposed computer simulation (red line) with the g-factors g_{xx}=2.38, g_{yy}=2.39, g_{zz}=1.99 and the hyperfine-splitting A_{xx}= 50 Gauss, A_{yy}=90 Gauss, A_{zz}= 120 Gauss.

First experiments to measure distances between a spin label and coordinated Co^{2+} in Cbi(MN) were accomplished with low temperature cw-EPR at 160 K. The presence of the fast relaxing paramagnetic Co^{2+} increases the spectral line width of the slowly relaxing nitroxide in dependence of the distance as predicted by Leigh theory [114]. Distances can then be determined by relating line widths of the interacting (with Co^{2+}) and non-interacting (without Co^{2+}) cw EPR spectrum. For this purpose MTSSL was incorporated into CbiM at position C67 which is the protein´s only native cysteine residue. Rotamer library analysis, based on the structure model of CbiM from *Rhodobacter capsulates* (PDB: 5X3X) (figure 5.22 a), predicted distances in the range from 0.8-1.4 nm between the *in silico* incorporated spin label at position C67 and the estimated position of a dummy Co-atom coordinated by four nitrogen ligands (amino group of Met1,the Nδ1-atom of the imidazol group and the backbone nitrogen of His2 and the Nε2-atom of the imidazol-group of His69). Figure 5.22 b depicts the superposition of low temperature cw-EPR spectra of Cbi(M(C67R1)N) and binding deficient Cbi(M_{H2D}(C67R1)N). Both protein variants were purified in the presence of $CoCl_2$ and were solubulized in detergent.

The resulting spectra both reveal distinct spectral line broadening but no differences in the overall spectral line shape. The line broadening could be caused by spin-spin interactions of adjacent spin labels which would indicate an oligomerization of CbiM. Therefore, an interaction between the nitroxide spin label and a possibly bound Co^{2+} ion is not detectable because it is superimposed by the much stronger nitroxide-nitroxide interaction. An oligomerization of CbiM could be due to the fact that the protein was solubilized in detergent. On the other hand it can also be theorized that the bound nitroxide at position C67 could prevent substrate uptake due to its close vicinity to the binding pocket and the Co^{2+}-coordinating residues.

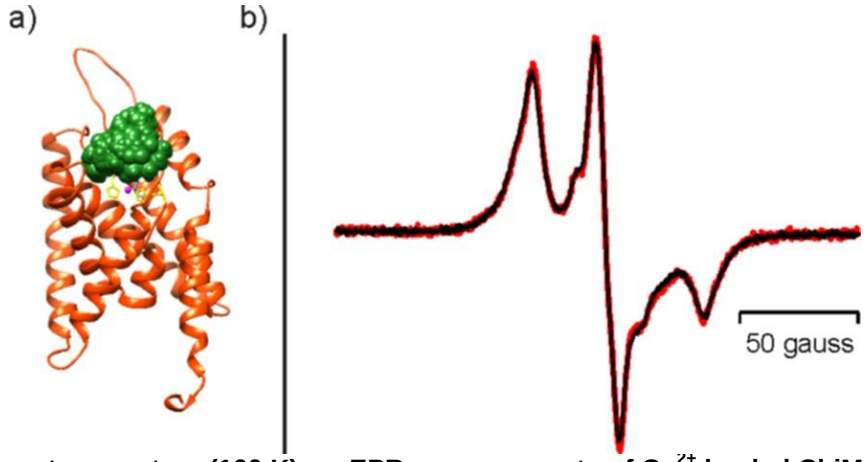

Figure 5.22: Low temperature (160 K) cw EPR measurements of Co^{2+} loaded CbiM(C67R1)N and Cbi(M_{H2D}(C67R1)N. a) Structure model of RcCbiM (PDB: 5X3X) modified *in silico* with MTSSL. The nitroxide group spatial distribution is highlighted in green. A dummy cobalt atom (purple sphere) is coordinated by four nitrogen-atoms located in residues Met1 (covered by structure), His2 and His69 (yellow). Romaters were implemented *in silico* utilizing MMM2013 [159]. b) cw EPR spectra (normalized by maximum) of Cbi(M(C67R1)N) (black line) and binding deficient variant Cbi(M_{H2D}(C67R1)N) (red line) normalized by the spin number.

5.3 Discussion

5.3.1 Transport cycle dependent conformational transitions in the histidine ABC-transporter system $HisQMP_2$ and interactions with its substrate binding protein HisJ

In order to gain insight into the conformational transitions that govern the substrate transport cycle of the bacterial histidine ATP-binding cassette transporter $HisQMP_2$, distance measurements between distinct sites in the cytoplasmic ATPase dimer $HisP_2$ and the transmembrane domains HisQM in dependence of the nucleotide hydrolysis cycle were executed. Additional experiments were accomplished to elucidate the binding mechanism of the substrate binding protein HisJ to the periplasmic side of the membrane-bound complex. Furthermore, this work covers the studies of the closing motion of HisJ upon ligandation.

A comparison of the conformational dynamics of $HisP_2$ observed in this work with experimental results made for the nucleotide binding domains of the maltose/maltodextrin transporter from *E.coli* $MalFGK_2$, illustrates its functional principle [189]. The different conformations of the transport cycle states (open/apo, semi-open/ADP-bound, closed/ATP-bound) of the MalK dimer, solved crystal structures of all states are available [28,143], exhibit different distance distributions between *in silico* spin labeled positions 83/83´ residing in the Q-loops of the NBDs. Positions 83/83´ in $MalK_2$ are homologous to positions 101/101´ in $HisP_2$. The apo-state of the maltose transporter complex (PDB: 3FH6) yields a distance distributions ranging from 1.5-2.8 nm with maxima between 2.2-2.6 nm. In the semi-open state (PDB: 3PV0, 3PUZ) the distance maximum decreases to 1.2 . Different crystal structures of the complex with closed NBDs (PDB: 3PUV, 3PUY, 3PUW, 2R6G, 3RLF) set the interspin distance maxima between the labeled positions in a range between 1.5-1.9 nm. The conformational transition into the closed state of the MalK dimer was also observed with EPR spectroscopy for the transporter complex solubulized in detergent and reconstituted in proteoliposomes [17, 71, 72, 150, 151]. Surprisingly the semi-open state reveals maxima at shorter distances than the closed state due to differing distributions of spin label rotamer populations indicating sterical restrictions for the spin label in the dimerized state of the NBDs. Interspin distance results acquired from EPR experiments [71] agree reasonably well with the data obtained from the rotamer library approach [189], assigning the largest distances to

the apo-state and the shortest distances to the posthydrolysis- or the semi-open state, respectively. However, interspin distance maxima in the apo state observed with DEER spectroscopy are somewhat shorter (2.0-2.2 nm) than the ones found from rotamer analysis indicating a closer proximity of the NBDs [71]. Simulation of the transition state during ATP-hydrolysis in the MalK dimer, by introducing the vanadate-trapped state, revealed interspin distances (1.6 nm) resembling those of the post hydrolysis state. The interspin distance distributions between positions 101/101´ of $HisP_2$, revealed in this work, are in close agreement with those of positions 83/83´ in $MalK_2$, therefore indicating a high similarity in the conformational dynamics within the transport cycles of the two systems.

Furthermore, the presence of the liganded substrate binding protein HisJ is necessary for the complete closure of $HisP_2$, which dimerized to only a small extend upon nucleotide binding alone, in the absence of HisJ. This gives evidence that the information of HisJ binding at the periplasmic side is transferred across the transmembrane domains upon and which stimulates ATP-hydrolysis, inducing the dimerization of ATP-bound $HisP_2$ at the cytoplasmic side. Limited proteolysis experiments support this notion of transmembrane signaling by substrate-bound SBP, as they demonstrated that specific cleavage sites in HisQ and HisP were made unresponsive for protease activity particularly in the presence of liganded HisJ and ATP [82]. In the results of this work the changes in the interspin distances between A118R1 and G123R1, located at the cytoplasmic gate (helix 3/3´), reflect the ATP-hydrolysis driven conformational changes in the NBDs which are transferred to the transmembrane domains. The ends of the cytoplasmic coupling helices 3/3´ of HisQ and HisM vary in their arrangement in the apo state from those in the closed and semi-open or posthydrolysis state. Distance distributions of these positions in the different states resemble those made for positions 101/101´in the Q-loops of HisJ in the according states. Normal mode analysis point to a concerted motion at the cytoplasmic gate, the Q-loops positions 101/101´and the center of mass of the nucleotide binding domains [189].

It was shown for the maltose transporter $MalFGK_2$, that the transition between the open and closed conformation of its substrate binding protein matches the shift from the semi-open to the closed state of $MalK_2$ [150]. Labeled sites at the periplasmic side of $HisQMP_2$, C197R1 and 104R1, exhibited a comparable relationship upon ATP-binding (closed state) and ATP-hydrolysis (semi-open state) in the NBDs, with

obvious changes in the correlating distance distributions, featuring conformational transition across the TMDs upon transitions (closed- to semi-open-state) in the NBDs. This particular transition is most probable not involving the helices 3/3´ at the cytoplasmic gate because the distance shifts for the observed positions A118 and G123 from the closed- to the semi-open state are rather small. It is more likely that the cytoplasmic coupling helices 3a and 3b are involved in this conformational transition from the cytoplasmic to the periplasmic side. EPR experiments on $MalK_2$ have shown that a shift from the closed to the semi-open state is connected via a reorientation of the NBD´s α-helical subdomain [151] thereby shifting the coupling helices 3a and 3b of the TMDs. Furthermore, coupling helix 3b is inflexibly coupled to transmembrane helix 4, in the case of the homology model of $HisQMP_2$ this connection is made by the conserved residues P144 in HisQ and P153 in HisM. Starting from the conformational transition in the NBDs a reorientation of coupling helix 3b could trigger a conformational transition across the TMDs by a coupled reorientation of helix 4 [189].

Additionally, the gathered experimental data also reveals two distinguishable conformations at the periplasmic side of the transmembrane domains. Upon ATP-hydrolysis in the NBDs a large shift from larger to shorter distances occurs measured between positions C197 and C104. This behavior could be related to the periplasmic gating process and be connected to the presumed interaction with HisJ. Moreover, measured distances between positions A86 and A96 exhibit differences in the apo and ATP-bound states although the yielded distance distributions are quit broad and make a convincing conclusion difficult. This could indicate a complex network of interactions at the periplasmic gate, which may also depend on the additional influence on the substrate binding protein HisJ.

As a result of this, experiments were accomplished to observe interactions between HisJ labeled at position G24 and the single labeled complex labeled at position A96 at the periplasmic side of HisM. The results reveal no interaction between HisJ and HisM in the apo-, the semi-open- or the transition-state trapped with vanadate. Interaction only occurred in the nucleotide bound closed state of $HisP_2$. Interestingly, two distinguishable distance distributions emerged in the nucleotide-bound state dependent of the ligandation state of HisJ revealing a mean distance at 4.3 nm when HisJ is without substrate and a distance of 5.1 nm in the case of the substrate-bound

HisJ. The broader distance distribution of the interaction between the substrate free HisJ and $HisQMP_2$ is most likely attributable to the high flexibility of position G24R1 in HisJ. This reveals two substrate-dependent interactions of HisJ with $HisQMP_2$. This notion is also supported by cross-linking experiments between HisJ and HisQ [8]. Further experiments by analyzing additional spin pairs that span the interface of HisJ and the periplasmic side of HisQM in addition to molecular dynamics simulations introducing the respective distance constrains gained from DEER spectroscopy could solve the orientation of the SBP with respect to the transmembrane domains.

DEER analysis of a double spin labeled His J variant spin labeled in both of its lobe-like domains at positions G24 and T151 shows two substrate-dependent conformations which differ clearly in their distance distributions. In the absence of histidine the average distance amounts to 3 nm, which resembles the open conformation of HisJ. In the presence of histidine a conformational transition occurs, which results in a shorter interspin distance below 1.5 nm between the observed positions, resembling the closed conformation, therefore trapping the substrate in its binding pocket in between the proteins two lobe-like domains. Surprisingly the according crystal structure of HisJ (PDB: 1HPB), which was solved in the presence of histidine [144] is not in accordance with these results. Interspin distance measurements between the investigated sites accomplished by rotamer library analysis revealed an average distance between 2.5-3.3 nm that resembles the open, histidine-free conformation according to the experimental data of this thesis. It was not possible to provide data that would allow discrimination between different conformational states of HisJ in dependence of the different states of $HisQMP_2$. This is most likely due to the low affinity of HisJ for the membrane-bound complex. Thus, the large signal of the non-interacting HisJ population dominates over, the small signal of the His J population that interacts with $HisQMP_2$. A similar closing mechanism and two distinct conformational states, resembling the open and closed conformation, were observed by DEER spectroscopy for the substrate binding protein VcSiaP of the sialic acid TRAP transporter [66].

5.3.2 Closure and reopening of the NBDs of the ECF-type transporter system BioMNY and investigations on the toppling over mechanism of the S-unit

One investigational focus applied to the biotin ECF-type transporter of subclass I BioMNY was on the closure and reopening dynamics of the NBD dimer $BioM_2$ upon nucleotide binding and nucleotide hydrolysis. It is generally accepted that the ATPases of ABC transporter systems get in close proximity upon binding nucleotides, as was already verified in this work for the histidine transporter $HisQMP_2$ or for the maltose/maltodextrin specific transporter $MalFGK_2$ [71]. In this context the Walker A motif of one monomer is brought in close vicinity to the LSGGQ sequence of the other monomer [43]. With respect to the homology model of BioMNY it was assumed that the Q-helices in the NBDs, ECF-transporter specific motifs that comprise of six residues (XP(D/E)XQϕ, with ϕ as a hydrophobic amino acid [102], would also get into close proximity upon ATP binding. The Q-helix is homologous to the Q-loop motif in the NBDs of ABC transporters. For the acquired interspin distance measurements between the BioM molecules, position H87, residing in the Q-helix, was chosen because a variety of sterical viable spin label rotamers was predicted by rotamer analysis for this site. *In silico* inter spin distance measurements of positions H87R1/H87´R1 on the model of BioMNY yielded distances below 2 nm. Since the model of the BioMNY and the BioM dimer was compiled with the heterodimer EcfA1A2 of *Lactobacillus brevis* as template, the distances calculated by rotamer analysis can deviate from the experimentally obtained data. Distances between C_β atoms of H87/H87´ amount to 1.3 nm. Considering the distance between C_β and the nitroxide group of an attached MTSSL side chain (0.4-0.8 nm) [6, 108] a theoretical interspin distance maximum of 2.9 nm is possible. Distances observed with DEER analysis agree reasonably with this predicted distance, revealing distances of 3.4 nm in the apo state, 2.7 nm in the ATP-bound state and 3.9 nm in the posthydrolytic state. Surprisingly, the posthydrolysis state seems to represent the fully open state of the $BioM_2$ dimer. Interestingly, the addition of biotin to the transporter´s nucleotide-bound state did not cause any shift to shorter distances and its distance distribution resembles that of the apo-state with an average distance maximum of 3.4 nm. This leads to the speculation that biotin uptake prevents ATP-binding in case of the modified H87R1/H87´R1 variant. The broad distance distributions reveal that positions H87/H87´ and the respective Q-helix motifs are very flexible. For the canonical ABC transporter $MalFGK_2$ as well as for the $HisQMP_2$ the apo, the

posthydolysis and the ATP-bound states correspond to the open, the semi-open and the closed conformations of the NBD dimer, respectively [71, 189]. In contrast the experiments presented in this work designate the open conformation of the $BioM_2$ dimer to the posthydrolytic state of $BioM_2$. Cross-linking experiments with mono cysteine variants of BioM support these findings [51]. Corresponding experiments were performed on positions D86/D86´, H87/H87´and Q88/Q88´ locate in the Q-helices. Especially results for Q88/Q88´ have shown increased cross-linking, utilizing EBS- (0.5 nm) and HBS-linkers (1 nm), upon the addition of ATP, indicating a dimerization of the NBDs. The high flexibility of the Q-helix motif is also reflected in those experiments, exhibiting cross-linking via the PBS-linker (2.5 nm) as well.

The substrate-translocation mechanism of ECF-transportes remains unsolved until today. It was therefore a goal of this work to shed light on the conformational transitions of the asymmetric S- and T-units of ECF transporters, in this case BioMNY, during the transport cycle.

A direct transport through the interior of the substrate binding S-unit is unlikely, as was shown for the structures of ThiT and BioY [15, 49]. Transloction through an interface built by the T- and S-units is likewise improbable. In subgroup II ECF transporters the module comprising the ATPase dimer EcfA1A2 and the T-unit EcfT can facilitate the transport of chemically different ligands by interacting with different substrate-specific S-units. Considering a transport trough an interface of the T- and S-units would therefore require that the T-unit would feature the transport of substrates of different chemical composition.

The elucidation of the crystal structures of three ECF holotransporters from *Lactobacillus brevis* [218, 225, 232] gave rise to a notion for a mechanism of substrate-transport across the membrane. It was found that the S-units of the complex had a parallel orientation to the lipid bilayer plane and that the substrate binding pocket was localized near the cytoplasmic face of the transmembrane T-unit. The so called toppling over mechanism suggests a reorientation of the substrate-binding S-unit within the membrane by nearly 90° depending on the binding of ATP or dimerization of the NBDs. This uplift would facilitate the uptake of substrate at the extracellular side of the membrane. ATP hydrolysis would trigger the opposite rotational motion of the S-unit and the substrate release in the cytoplasm. Experimental indication for the validity of this notion was given by fluorescence spectroscopy on MIANS-labeled BioMNY complexes in detergent and incorporated in

nanodiscs. Labeled positions on the cytoplasmic side of BioY and in the coupling helices of BioN revealed ATP-induced shifts of their fluorescence maxima that indicated the uplift motion of BioY upon nucleotide-binding [51]. Spin labeled double mutants of BioMNY reconstituted in nanodiscs were studied by DEER spectroscopy to measure spin-spin distances between positions A152(BioY)/A166(BioN) and K137(BioY)/L82(BioN) in dependence of the binding and hydrolysis of ATP. Considering $BioM_2NY$(A166R1)Y(A152R1), an emerging distance contribution between 2.5-3 nm upon nucleotide binding could indicate a shift to smaller distances between the labeled sites. This shift could further be interpreted as a reorientation of the S-unit in the membrane according to the toppling over mechanism. Emerging shifts to longer distances in the distance distributions of $BioM_2N$(L82R1)Y(K137R1) could support this interpretation. However, in both cases the broad distance distribution render an interpretation difficult. Moreover, DEER spectroscopy revealed interspin interaction in all single labeled variants, A152R1 and K137R1 in BioY and A166R1 and L82R1 in BioN, pointing towards oligomerization of S- and T-units in nanodiscs. As a consequence of the arising inter-molecular contributions from oligomers, distinguishing conformational states associated to the apo or ATP-bound states of the NBDs from distance distributions was not possible, rendering an interpretation uncertain. This correlates with findings of *in vivo* oligomerized BioY observed with FRET spectroscopy [50] and *in vitro* dimerized BioY [52, 76]. Specific investigations on the stoichiometry of BioY proteins of the ECF transporter subclass I exhibited that dimerization, and even higher multimeric compounds (dimers of dimers) could be a general feature of BioY but does not affect substrate transport [107]. Cross-linking experiments and pull-down assays indicated that the T-unit, BioN, can also adopt a dimeric state [102, 140]. Further analysis verified that BioN can exist as dimers in the whole transporter complex and in complex with the ATPase dimer only [107]. Considering these findings renders further investigations of the interactions between the T- and the S-unit of BioMNY with DEER spectroscopy challenging. Additional inter-molecular interactions by oligomerized T- and S-units cannot be excluded, as shown.

5.3.3 Substrate uptake by the S-unit of the bacterial cobalt importer CbiMNQO

The metal ECF transporter system, specific for Co^{2+}, consists of the cytosolic ATPase (CbiO) in association with the transmembrane T-unit (CbiQ) and the substrate-binding S-unit (CbiM). Additionally, another transmembrane protein, CbiN, is associated with CbiM. CbiN is a small protein comprising two transmembrane helices which are separated by an extracytosolic domain. This extra domain is crucial for substrate transport and the same relation is also given for other metal specific systems like the Ni^{2+} transporter NikMNQO and NikN [106, 173, 185]. However, the transport facilitating function of CbiN remains unsolved until now. Herein the substrate uptake of the artificially merged Cbi(MN) [106, 185], along with the substrate-binding deficient variant Cbi(M_{H2D}N) and single CbiM in detergent were investigated. It was shown that only Cbi(MN) was able to bind Co^{2+} ions and that the coordination of the ion corresponds to a pseudo-tetrahedral or square planar geometry which matches the proposed planar binding site. Furthermore, the inability of Cbi(M_{H2D}N) for substrate uptake confirms the importance of the N-terminal histidine residue at position 2 in coordinating the metal ion and as part of the binding pocket [185, 228]. The importance of CbiN in substrate binding was also verified by the results, since single CbiM was not able to bind the substrate. These results are in agreement with in vivo experiments of bacterial uptake of the radioactive cobalt isotope $^{57}Co^{2+}$ which revealed functionality of Cbi(MN) but not of CbiM$_{H2D}$N, Cbi(M_{H2D}N) and single CbiM [106, 173, 185]. Further experiments heading in this direction should be accomplished by investigating substrate binding of Cbi(MN), Cbi(M_{H2D}N) and CbiM incorporated in nanodiscs and also of the full transporter complex of CbiMQO with and without CbiN.

Experiments to quantify the interactions and to measure interspin distances between an incorporated spin label at position 67, the only native cysteine in CbiM, and the bound Co^{2+} were not successful. However, the experimental data reveals interaction with an adjacent paramagnetic entity. This could point towards oligomerization of CbiM similarly to the emerging oligomerized S-units of BioMNY. Such an oligomerization could be due to the fact that the protein was solubilized in detergent. This issue could be solved by reconstituting the transporter into nanodiscs or liposomes. Since in this case it cannot be ascertained whether Co^{2+} was bound to CbiM it cannot be excluded that the spin label prevents substrate binding. It can be theorized that the close proximity of the spin label to the substrate coordinating

residues Met1, His2 and His69, might interfere sterically with the process of substrate binding. To overcome this barrier positions in CbiM must be detected that do not interfere with substrate-binding after spin labeling, and which are in close proximity to the putative binding site, for instance in the N-terminus, so that spin-spin interaction is detectable. One possible position would be M4 which is not involved in coordination of Co^{2+} and whose amino acid exchange does not cause a substrate-binding deficiency [185]. Still position M4 is located close enough to the binding pocket (~1.5- nm) to allow detection of spin-spin interactions by low temperature EPR.

6. Summary

In this work two overall subjects were addressed.

1. In recent years high pressure perturbance has become a tool to investigate the folding energy landscape, the volumetric properties and the conformational equilibria of proteins. Conformational states which are not populated at ambient conditions thus become accessible to spectroscopic characterization. In this work a high pressure application was combined with EPR spectroscopy to investigate three spin labeled proteins, BSA from *Bos taurus*, HisJ from *Salmonella enterica* serovar Typhimurium and α-synuclein from *Homo sapiens*. The goal of these studies was to comprehend the influence of pressure on the respective EPR spectra and to identify changes in conformational equilibria and volumetric properties of the investigated proteins.

   Studies on BSA revealed a negative activation volume for rotational diffusion of the spin labeled site. Moreover, a rotameric equilibrium was derived from the pressure-dependent side chain dynamics and a correlating negative partial molar volume was observed, indicating a shift of the rotameric equilibrium to lesser order. In this regard it was also shown that a chaotropic medium (guanidine hydrochloride) supports the pressure-dependent effect.

   Spin labeled sites in the substrate binding protein HisJ revealed to be highly influenceable by low pressures between ambient conditions and 200 bar. Pressurization induced oligomerization and precipitation of the protein. Substrate binding revealed differences in pressure-dependence with regard to a decreased precipitation effect but not in relation to oligomerization.

   The natively unfolded protein α-synuclein plays a key role in Parkinson´s disease and is known for forming β-sheet rich aggregates, so called amyloid fibrils. The experimental data of this work revealed that hydrostatic pressure can induce a non-amyloid aggregation of monomeric α-synuclein which produces an unspecific oligomer. Furthermore, it was shown that α-synuclein

amyloid fibrils can be dissolved by hydrostatic pressure. From the pressure dependent conformational equilibrium between the monomer and the fibril form the change of the partial molar volume of the investigated site was determined.

2. The second subject of this work was focused on different import systems, ATP-binding cassette (ABC) transporters and Energy-Coupling-Factor (ECF) transporters, for amino acids, vitamins and metal ions in prokaryotes. Studies on one bacterial ABC and two ECF transporter systems from two different organisms, the histidine ABC-type transporter $HisQMP_2$ from *Salmonella enterica* serovar Typhimurium, the biotin ECF-type importer BioMNY from *Rhodobacter capsulatus* and the cobalt-specific ECF-type transporter CbiMNQO from *Rhodobacter capsulatus*, were performed using DEER and cw EPR spectroscopy. The goal of the studies on $HisQMP_2$ and BioMNY was to shed light on conformations and dynamics connected to their transporter function. Studies on CbiMNQO aimed at the detection of the substrate in the transporter´s substrate binding unit.

   For $HisQMP_2$ transport cycle dependent conformational changes and interactions with the substrate binding protein HisJ were revealed. Three different distance values between sites H101R1 and H101'R1 in the transporter´s nucleotide binding domains were assigned to the apo-, the ATP-bound and the posthydrolysis state. It was shown that the closed conformation of the nucleotide binding domains is achieved only in the presence of the ligand-bound HisJ which indicates a transmembrane communication of the association of HisJ to the transporter. Furthermore, interspin distances were determined between sites D86R1-A96R1, C197R1-C104R1 and A118R1-G123R1 in the transmembrane domains HisQ and HisM revealing distinguishable conformational states which correlate to the different states of the nucleotide binding sites during the hydrolysis cycle. Measured interspin distances between HisJ and HisM in the $HisQMP_2$ complex showed that interaction only occurred in the closed state of the $HisP_2$ dimer, the nucleotide bound state. Two different, substrate-dependent interactions between site G24R1 in HisJ and site A96R1 in $HisQMP_2$ were observed, revealing that the

substrate-free and substrate-bound form of HisJ both associate with $HisQMP_2$. Distance measurements between sites G24R1 and T151R1 in HisJ in the presence and absence of its substrate revealed interspin distance changes that correlate with the proteins open and closed conformation.

Investigations on the ECF transporter BioMNY, reconstituted into nanodiscs, revealed a closure and reopening of the nucleotide binding domains between sites H87R1 and H87'R1 using DEER spectroscopy which delivered interspin distance values that correlate with the apo-, the ATP-bound and the posthydrolysis state of the transporter. Further experiments were aimed to shed light on the transporters substrate-translocation mechanism with regard to the so called toppling over mechanism. Unfortunately, the experiments of this work were not able to give a distinct answer with respect to the proposed model because of the transmembrane domains tendency to oligomerize when reconstituted into nanodiscs.

In this work we showed that substrate uptake by the substrate binding unit CbiM of the cobalt-specific ECF transporter CbiMNQO depends on the presence of the small transmembrane protein CbiN. Measurements of spin labeled CbiMN in detergent showed oligomerization of CbiM.

7. Appendix

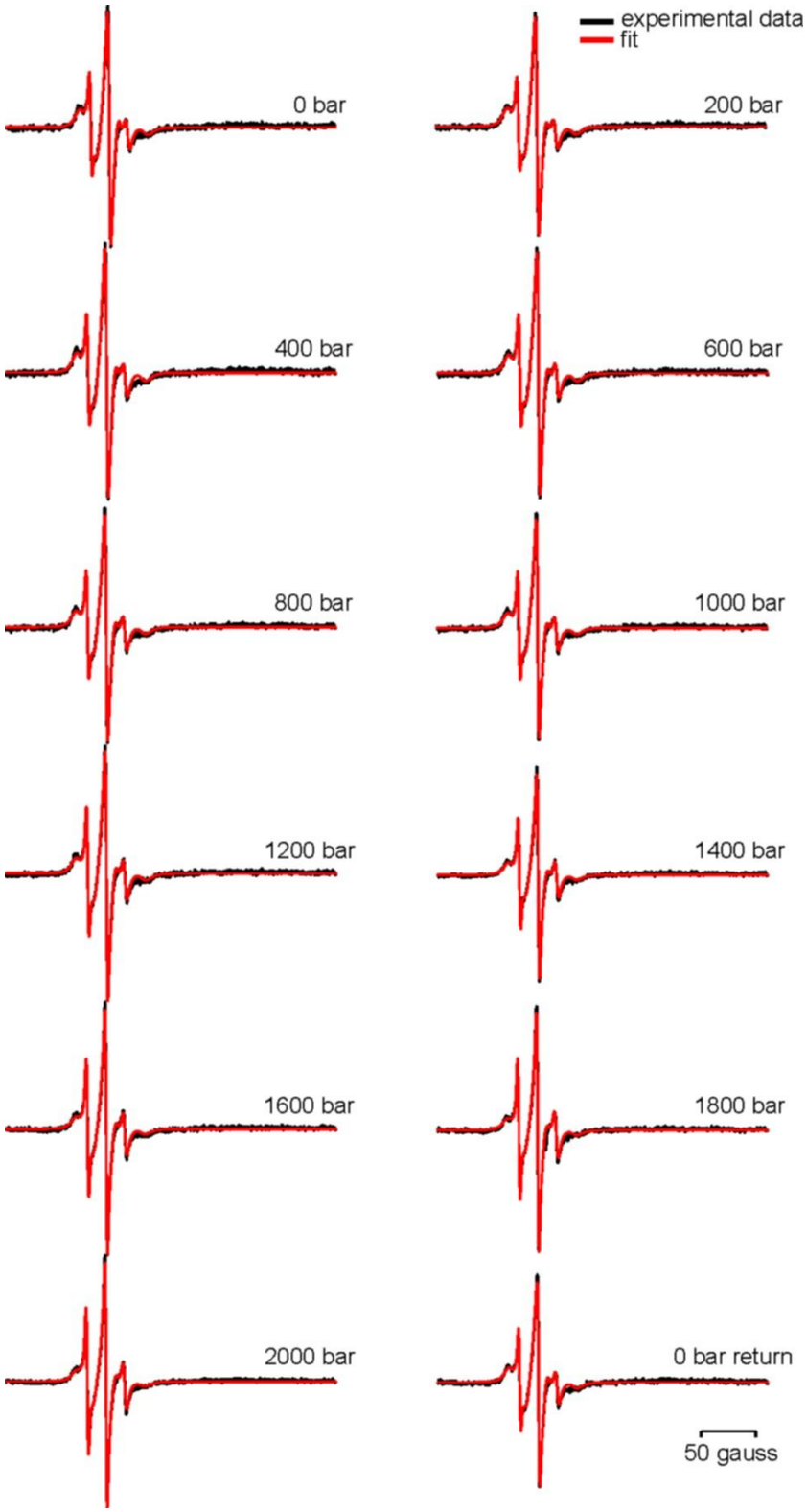

Figure 7.1: Experimental and simulated HP-EPR data of BSA. High pressure measurements of BSA (154µM) (black line) were accomplished in steps of 200 bar starting at atmospheric pressure (1 bar) rising up to 2000 bar in total.Fits (red line) were accomplished with the EPR analysis program MultiComponent.

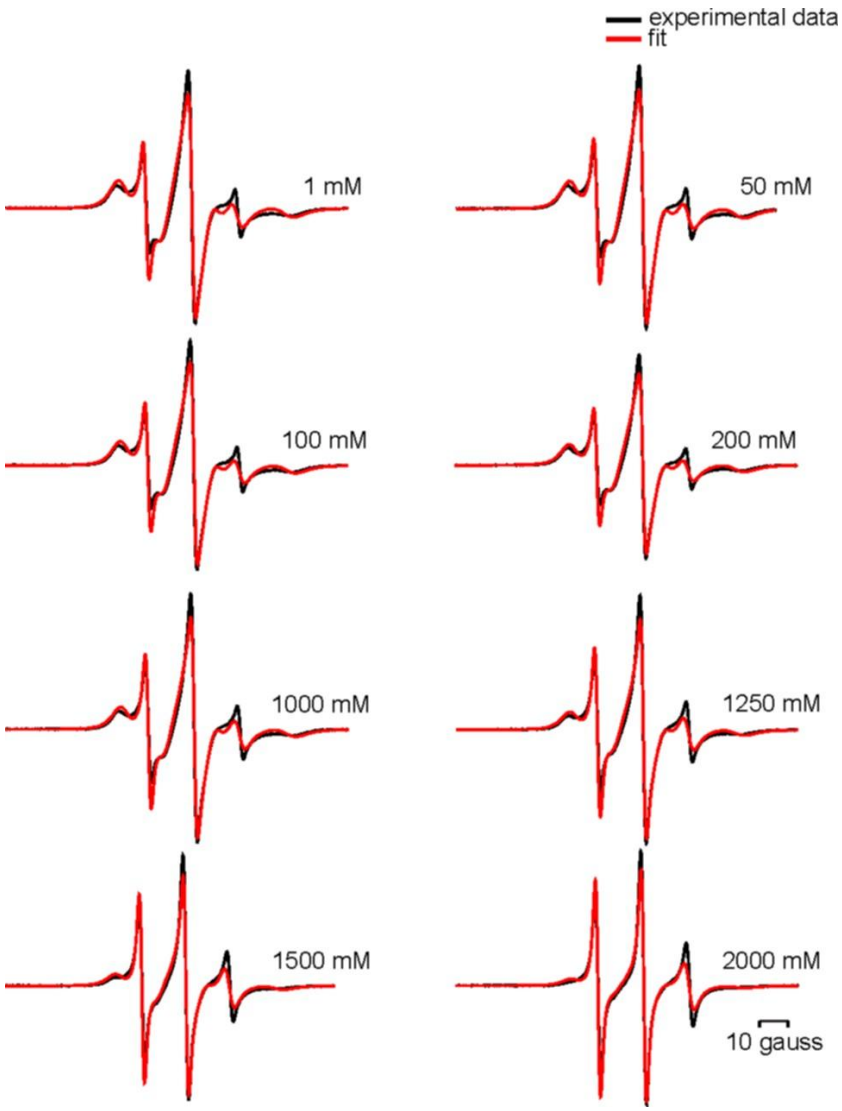

Figure 7.2: Experimental and simulated EPR data of BSA in addition to guandidine hydrochloride. Cw EPR measurements of BSA (154µM) in addition to 1-2000mM GdnHCl (black line). Fits (red line) were accomplished with the EPR analysis program MultiComponent.

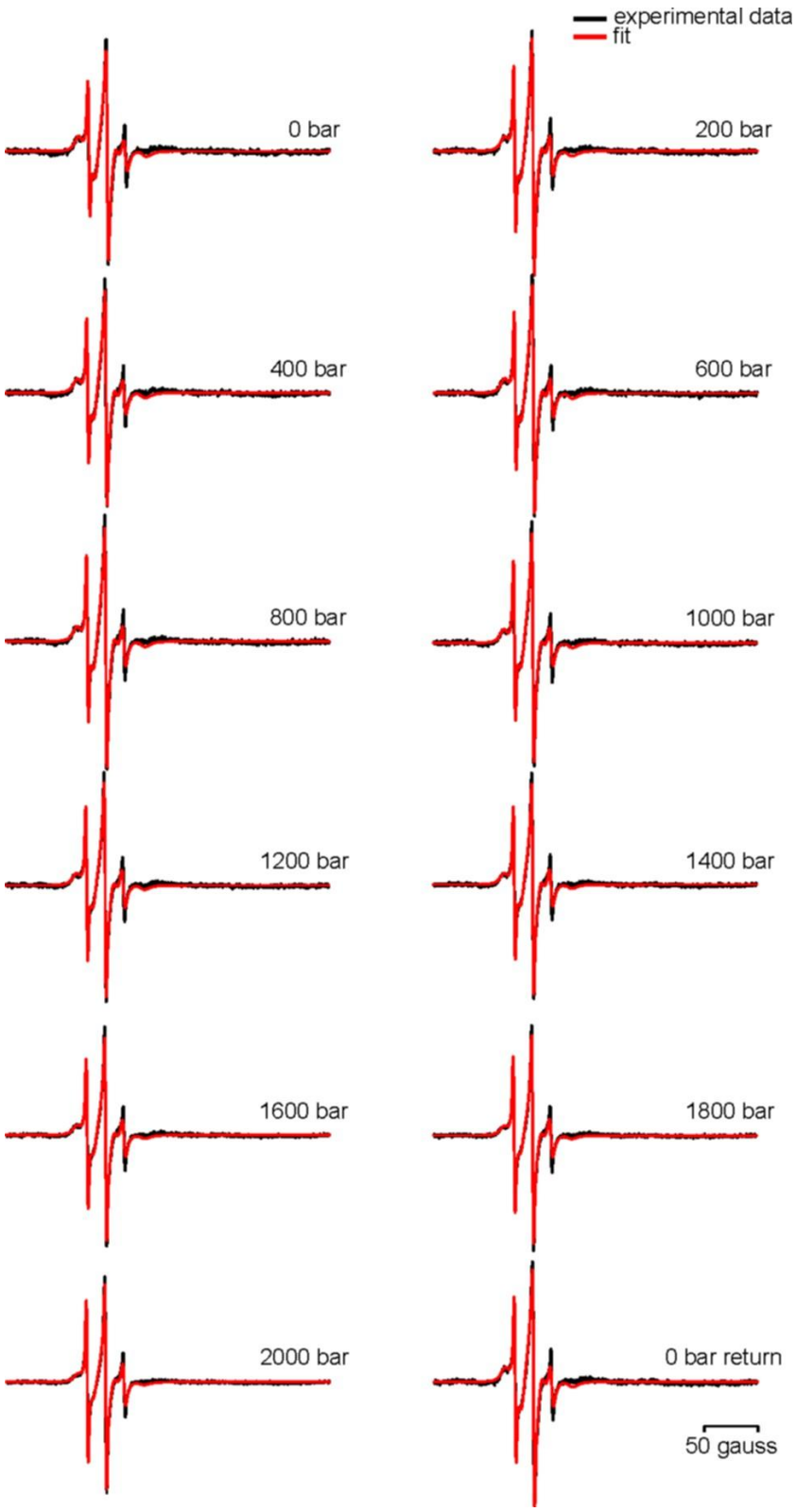

Figure 7.3: Experimental and simulated HP-EPR data of BSA in addition to guandidine hydrochloride. High pressure measurements of BSA (154µM) in addition to 200mM GdnHCl (black line) were accomplished in steps of 200 bar starting at atmospheric pressure (1 bar) rising up to 2000 bar in total. Fits (red line) were accomplished with the EPR analysis program MultiComponent.

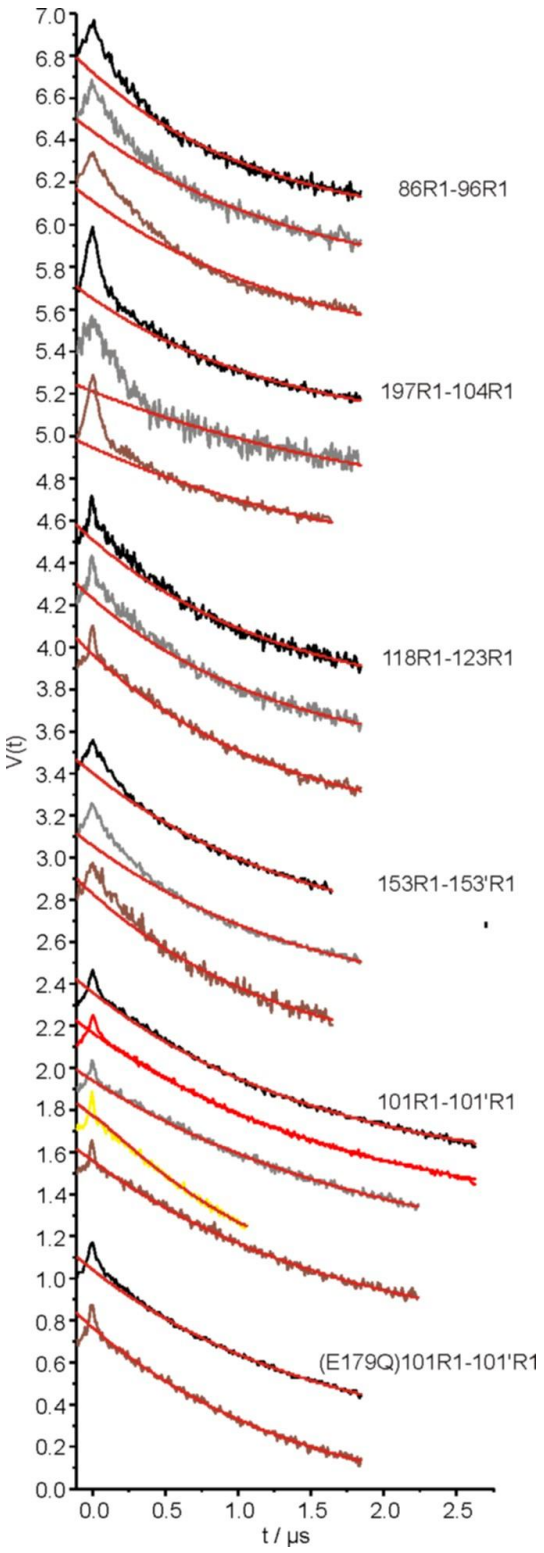

Figure 7.2: DEER traces for three different states of the nucleotide hydrolysis cycle. DEER data, V(t), for the apo state (black), the ATP bound state (gray) and the post hydrolysis state (brown) in the presence of liganded HisJ. In addition, for positions 101/101′ the data for the vanadate-trapped state (yellow), for the state in the presence of ATP but in the absence of HisJ (red), and for the hydrolysis incompetent mutant E179Q in the absence of any substrate (black) and in the presence of HisJ, ATP and Mg2+ (brown) are shown. Fits corresponding to the DEER traces are depicted as overlay (red line).

D

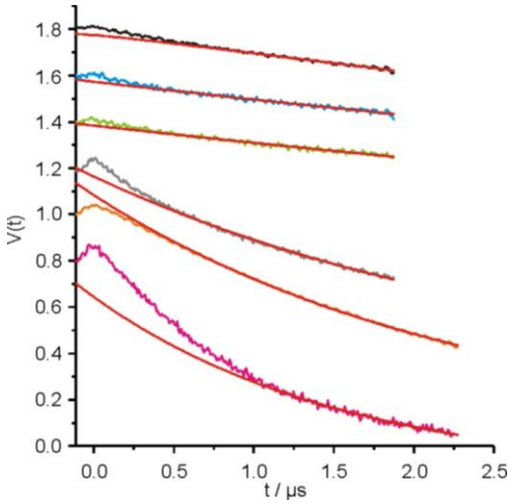

Figure 7.3: DEER traces detecting interaction between HisQMP2 and HisJ in different states of the nucleotide hydrolysis cycle. DEER traces, V(t), of labeled positions HisQM(A96R1)P2 and HisJ(G42R1) (1:1 ratio). Fits corresponding to the DEER traces are depicted as overlay (red line). The apo-state (black trace - 1:1 molar ratio of HisQMP2:HisJ). Nucleotide-bound states of HisQMP2 is induced by AMP-PnP (gray traces - 1:1 molar ratio of HisQMP2:HisJ). The posthydrolysis-state (blue traces - 1:1 molar ratio of HisQMP2:HisJ) and the vanadate-trapped state (green traces - 1:1 molar ratio of HisQMP2:HisJ). HisQM(A96R1)P2 and HisJ(G42R1) (1:5 ratio) in addition to 1 mM histidine. The apo-state (orange trace - 1:5 molar ratio of HisQMP2:HisJ). Nucleotide-bound states of HisQMP2 is induced by AMP-PnP (pink traces - 1:5 molar ratio of HisQMP2:HisJ).

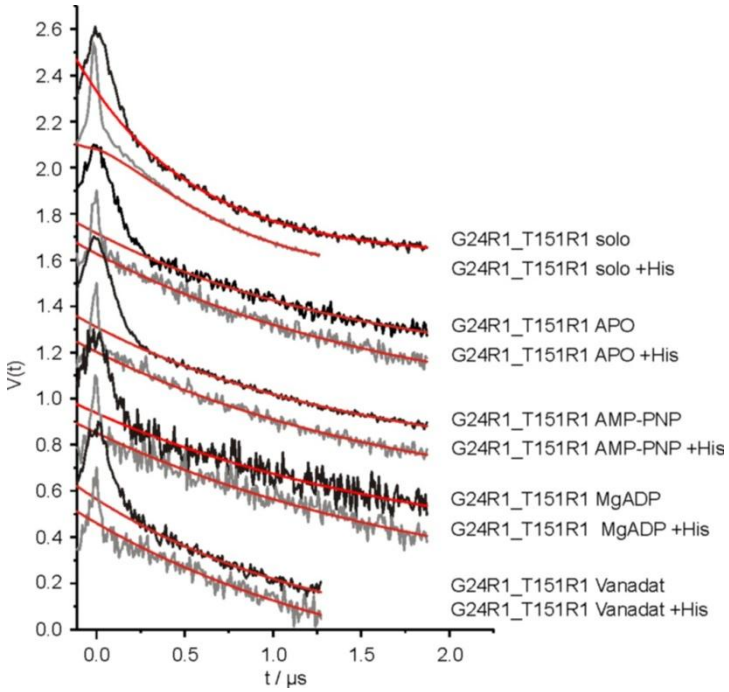

Figure 7.4: DEER traces of HisJ G24R1_T151R1 in absence and in presence of HisQMP2 in different states of the nucleotide hydrolysis cycle. DEER time traces of double labeled HisJ G24R1_T151R1 in absence (solo) and in presence of reconstituted HisQMP2 or HisQMP2 (E179Q)

(black traces) and in addition of the substrate histidine (gray traces). Fits corresponding to the DEER traces are depicted as overlay (red line). Nucleotide-bound states of HisQMP2 are induced by AMP-PnP, Mg+ADP, Mg+ATP or Vanadat.

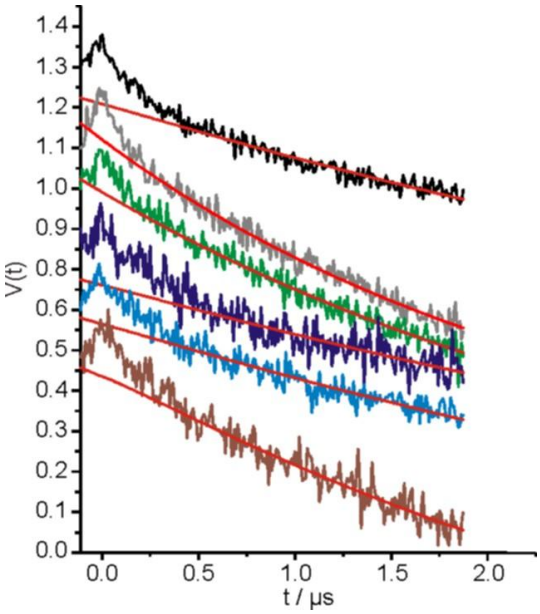

Figure 7.5: DEER traces of BioM(H87R1)$_2$NY for three different states of the nucleotide hydrolysis cycle. DEER data, V(t) of in nanodiscs reconstituted BioM(H87R1)$_2$NY for the apo state (black line), the nucleotide-bound state (ATP plus EDTA, gray line; Mg^+AMP-PNP, green line), the nucleotide-bound state (ATP plus EDTA) plus biotin (brown line) and the posthydrolysis state (Mg^+ATP, dark blue line; Mg^+ADP, light blue line). Fits corresponding to the DEER traces are depicted as overlay (red line).

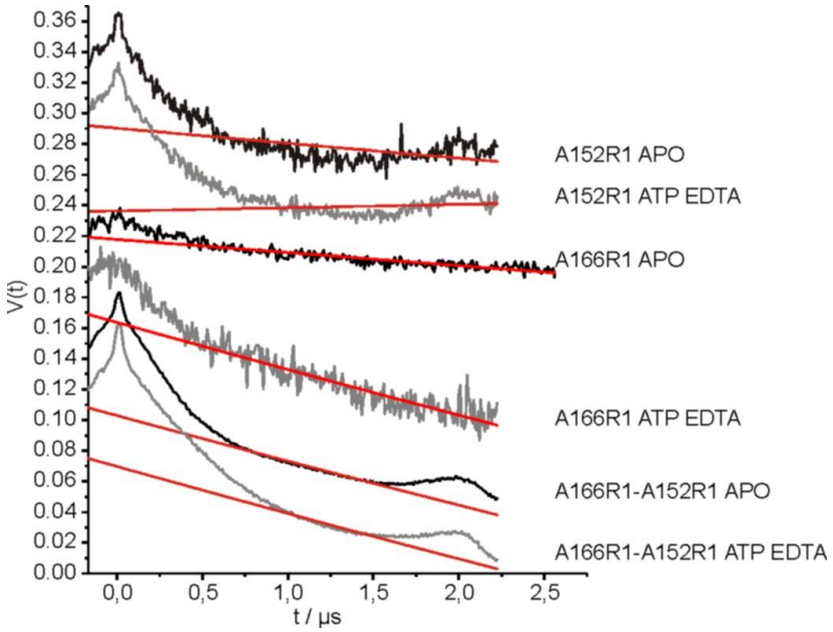

Figure 7.6: DEER traces of BioM$_2$N(A166R1)Y, BioM$_2$NY(A152R1) and BioM$_2$N(A166R1)Y(A152R1) for the apo and nucleotide-bound state of the nucleotide hydrolysis cycle. DEER data, V(t) of in nanodiscs reconstituted BioM$_2$N(A166R1)Y, BioM$_2$NY(A152R1) and BioM$_2$N(A166R1)Y(A152R1) for the apo state (black line) and the nucleotide-bound state (ATP plus EDTA, gray line). Fits corresponding to the DEER traces are depicted as overlay (red line).

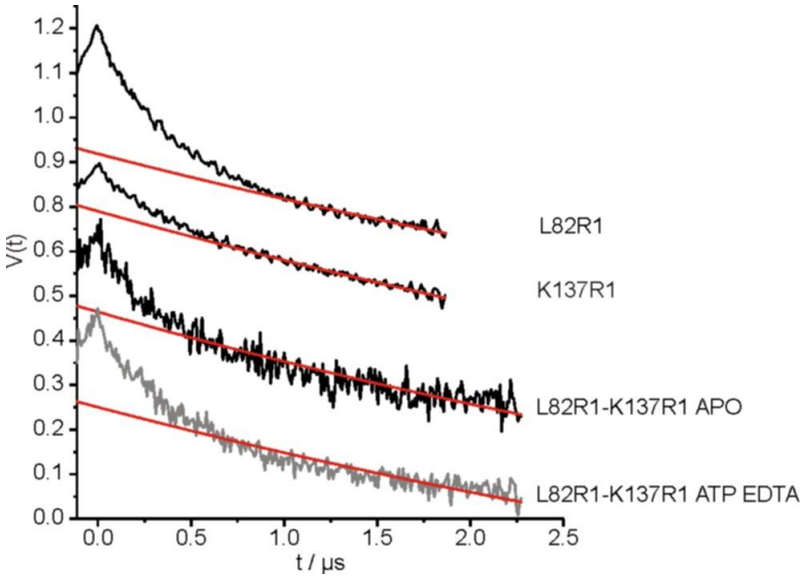

Figure 7.7: DEER traces of BioMN(L82R1)Y, BioMNY(K137R1), BioMN(L82R1)Y(K137R1) for the apo and nucleotide-bound state of the nucleotide hydrolysis cycle. DEER data, V(t) of in nanodiscs reconstituted BioM$_2$N(L82R1)Y, BioM$_2$NY(K137R1) and BioM$_2$N(L82R1)Y(K137R1) for the apo state (black line), the nucleotide-bound state (ATP plus EDTA, gray line) Fits corresponding to the DEER traces are depicted as overlay (red line).

8. References

[1] Ahn B. H., Rhim H., Kim S. Y., Sung Y. M., Lee M. Y., Choi J. Y. (2002). Alpha-synuclein interacts with phospholipase D isozymes and inhibits pervanadate-induced phospholipase D activation in human embryonic kidney-293 cells. J. Biol. Chem., 277, 12334-42.

[2] Akasaka K., Tezuka T., Yamada H. (1997). Pressure-induced changes in the folded structure of lysozyme. J. Mol. Biol., 5, 271(5), 671-8.

[3] Akasaka K., Li H. (2001). Low-lying excited states of proteins revealed from nonlinear pressure shifts in 1H and 15N NMR. Biochemistry, 40(30), 8665-71.

[4] Akasaka K. (2003). Highly fluctuating protein structures revealed by variable-pressure nuclear magnetic resonance. American Chem. Society., 42(37).

[5] Akasaka K., Kitahara R., Kamatari Y.O. (2013). Exploring the folding energy landscape with pressure. Archives of Biochemistry and Biophysics, 531, 110–115.

[6] Altenbach C., Flitsch S. L., Khorana H. G., Hubbell W. L. (1989). Structural studies on transmembrane proteins. 2. Spin labeling of bacteriorhodopsin mutants at unique cysteines. Biochemistry, 28, 7806–7812.

[7] Alonso A., dos Santos W. P., Leonor S. J., dos Santos J. G., Tabak M. (2001). Stratum corneum protein dynamics as evaluated by a spin-label maleimide derivative: effect of urea. Biophysical journal, 81(6), 3566-3576.

[8] Ames G. F., Liu C. E., Joshi A. K., Nikaido K. (1996). Liganded and unliganded receptors interact with equal affinity with the membrane complex of periplasmic permeases, a subfamily of traffic ATPases. J. Biol. Chem., 271, 14264-14270.

[9] Anjos J. L. V., Santiago P. S., Tabak M., Alonso A. (2011). On the interaction of bovine serum albumin with ionic surfactants: Temperature induced EPR changes of a maleimide nitroxide reflect local protein dynamics and probe solvent accessibility. Colloids and Surfaces B: Biointerfaces, 88(1), 463-470.

[10] Anfinsen, C. (1973). Principles that govern the folding of protein chains. Science, 181(4096), 223–230.

[11] Antony T., Hoyer W., Cherny D., Heim G., Jovin T. M., Subramaniam V. (2003). Cellular Polyamines Promote the Aggregation of Alpha-Synuclein. J. Biol. Chem., 278, 3235-3240.

[12] Bennett B. (2010). EPR OF COBALT-SUBSTITUTED ZINC ENZYMES *in:* Metals in Biology, Applications of High-Resolution EPR to Metalloenzymes, edited by Graeme Hanson, Lawrence Berliner, Springer.

[13] Berliner J. (1976). Spin Labeling – Theory and Applications. Academic Press, New York.

[14] Berntsson R. P., Smits S. H., Schmitt L., Slotboom D. J., Poolman B. (2010). A structural classification of substrate-binding proteins. FEBS Lett., 584(12), 2606-17.

[15] Berntsson R. P. A., ter Beek J., Majsnerowska M., Duurkens R. H., Puri P., Poolman B., Slotboom D. J. (2012). Structural divergence of paralogous S components from ECF-type ABC transporters. Proc. Natl. Acad. Sci. USA.,109, 13990-13995.

[16] Bett K. E., Cappi J. B. (1965). Effect of pressure on the viscosity of water. Nature, 207, 620–621.

[17] Böhm S., Licht A., Wuttge S., Schneider E., Bordignon E. (2013). Conformational plasticity of the type I maltose ABC importer. Proc. Natl. Acad. Sci., 110, 5492–5497.

[18] Bordignon E., Steinhoff H.-J. (2007). Membrane protein structure and dynamics studied by site-directed spin-labeling ESR. In: Hemminga MA, Berliner LJ, ESR spectroscopy in membrane biophysics. Springer Science and Business Media, 129–164.

[19] Bordignon E., Grote M., Schneider E. (2010). The maltose ATP-binding cassette transporter in the 21st century--towards a structural dynamic perspective on its mode of action. Mol. Microbiol., 77(6),1354-66.

[20] Bridges M. D., Hideg K., Hubbell W. L. (2010). Resolving conformational and rotameric exchange in spin-labeled proteins using saturation recovery EPR. Appl. Magn. Reson., 37, 363–390.

[21] Bryngelson J.D, Onuchic J.N, Socci N.D, Wolynes P.G. (1995). Funnels, Pathways, and the energy landscape of protein folding: A synthesis. Proteins: Structure, Function and Genetics, 21, 167-195.

[22] Buell A. K., Galvagnion C., Gaspar R., Sparr E., Vendruscolo M., Knowles T. P. J., Linse S., Dobson C. M. (2014). Solution conditions determine the relative importance of nucleation and growth processes in α-synuclein aggregation. PNAS, 111(21), 7671-7676.

[23] Burré J., Sharma M., Tsetsenis T., Buchman V., Etherton M. R., Südhof T. C. (2010). Alpha-synuclein promotes SNARE-complex assembly *in vivo* and *in vitro*. Science, 329, 1663-7.

[24] Burré J., Sharma M., Südhof T. C. (2014). α-synuclein assembles into higher-order multimers upon membrane binding to promote SNARE complex formation. Proc. Natl. Acad. Sci., USA, 111, 4274-83.

[25] Caughey B., Lansbury P. T. (2003). Protofibrils, pores, fibrils, and neurodegeneration: Separating the responsible protein aggregates from the innocent bystanders. AnnuRev. Neurosci., 26, 267–298.

[26] Chandra S., Gallardo G., Fernández-Chacón R., Schlüter O. M., Südhof T. C. (2005) Alpha-synuclein cooperates with CSPalpha in preventing neurodegeneration. Cell, 123, 383-96.

[27] Chen C. T., Fine R. A., Millero F. J. (1977). The equation of state of pure water determined from sound speeds. The Journal of Chemical Physics, 66(5), 2142–2144.

[28] Chen J., Lu G., Lin J., Davidson A. L., Quiocho F. A. (2003B). A tweezers-like motion of the ATP-binding cassette dimer in an ABC transport cycle. Mol. Cell, 12, 651–661.

[29] Chen M., Margittai M., Chen J., Langen R. (2007). Investigation of alpha-synuclein fibril structure by site-directed spin labeling. J. Biol. Chem., 282, 24970–24979.

[30] Choi B. K., Choi M. G., Kim J. Y., Yang Y., Lai Y., Kweon D. H. (2013). Large α-synuclein oligomers inhibit neuronal SNARE-mediated vesicle docking. Proc. Natl. Acad. Sci. USA,110, 4087-92.

[31] Cohlberg J. A., Li J., Uversky V. N., Fink A. L. (2002). Heparin and Other Glycosaminoglycans Stimulate the Formation of Amyloid Fibrils From R-Synuclein in Vitro. Biochemistry, 41, 1502-1511.

[32] Collins S. R., Douglass A., Vale R. D., Weissman J. S. (2004). Mechanism of prion propagation: Amyloid growth occurs by monomer addition. PLoS Biol., 2(10), 321.

[33] Columbus L., Hubbell W. L. (2004). Mapping backbone dynamics in solution with sitedirected spin labeling: GCN4–58 bZip free and bound to DNA. Biochemistry, 43(23), 7273–7287.

[34] Comellas G., Lemkau L. R., Nieuwkoop A. J., Kloepper K. D., Ladror D. T., Ebisu R., Woods W. S., Lipton A. S.,George J. M., Rienstra C. M. (2011). Structured regions of α-synuclein fibrils include the early-onset Parkinson´s disease mutation sites. J. Mol. Biol., 411, 881–895.

[35] Conway K. A., Harper J. D., Lansbury P. T. (1998). Accelerated *in vitro* fibril formation by a mutant α-synuclein linked to early-onset Parkinson disease. Nature Medicine, 4, 11.

[36] Conway K. A., Lee S. J., Rochet J. C., Ding T. T., Williamson R. E., Lansbury P. T. Jr. (2000). Acceleration of oligomerization, not fibrillization, is a shared property of both alpha-synuclein mutations linked to early-onset Parkinson's disease: Implications for pathogenesis and therapy. Proc. Natl. Acad. Sci. USA, 97, 571–576.

[37] Conway K. A., Harper J. D., Lansbury P. T. Jr. (2000). Fibrils formed in vitro from alpha-synuclein and two mutant forms linked to Parkinson´s disease are typical amyloid. Biochemistry, 39, 2552–2563.

[38] Cooper A. (1984). Protein fluctuations and the thermodynamic uncertainty principle. Progress in Biophysics and Molecular Biology, 44(3), 181–214.

[39] Cordeiro Y., Foguel D., Silva J. L. (2013). Pressure-temperature folding landscape in proteins involved in neurodegenerative diseases and cancer. Biophys. Chem., 183, 9–18.

[40] Cornell C. N., Chang R., Kaplan, L. J. (1981). The environment of the sulfhydryl group in human plasma albumin as determined by spin labeling. Archives of biochemistry and biophysics, 209(1), 1-6.

[41] Dadali A. A., Barashkova I. I., Lastenko I. P., Wasserman A. M. (1991). Effect of pressure on the rotational mobility of spin label in polymer. Eur. Polym. J., 27, 1097–1100.

[42] Davidson A. L., Chen J. (2004). ATP-binding cassette transporters in bacteria. Annu. Rev. Biochem., 73, 241–268.

[43] Davidson A. L., Dassa E., Orelle C., Chen J. (2008). Structure, Function, and Evolution of Bacterial ATP Binding Cassette Systems. Microbiol. Mol. Biol. Rev., 72, 317–364.

[44] Dawson T., Mandir A., Lee M. (2002). Animal models of PD: Pieces of the same puzzle? Neuron, 35, 219–222.

[45] Der-Sarkissian A., Jao C C., Chen J., Langen R. (2003) Structural organization of alphasynuclein fibrils studied by site-directed spin labeling. J. Biol. Chem., 278, 37530–37535.

[46] Doige C. A., Ames G. F. L. (1993). ATP-dependent transport systems in bacteria and humans: relevance to cystic fibrosis and multidrug resistance. Annu. Rev. Microbiol., 47, 291-319.

[47] Dusa A., Kaylor J., Edridge S., Bodner N., Fink A. L. (2006). Characterization of Oligomers during α-Synuclein Aggregation Using Intrinsic Tryptophan Fluorescence. Biochemistry, 45, 2752-2760.

[48] Eitinger T., Rodionov D.A., Grote M., Schneider E. (2011). Canonical and ECF-type ATP binding cassette importers in prokaryotes: diversity in modular organisation and cellular functions, FEMS Microbiol. Rev., 35, 3-67.

[49] Erkens G. B., Berntsson R. P., Fulyani F., Majsnerowska M., Vujičić-Žagar A., Ter Beek J., Poolman B., Slotboom D. J. (2011). The structural basis of modularity in ECF-type ABC transporters. Nat. Struct. Mol. Biol., 18(7), 755-60.

[50] Finkenwirth F., Neubauer O., Gunzenhäuser J., Schoknecht J., Scolari S., Stöckl M., Korte T., Herrmann A., Eitinger T. (2010). Subunit composition of an energy-coupling-factor-type biotin transporter analysed in living bacteria. Biochem. J., 431(3), 373-80.

[51] Finkenwirth F., Sippach M., Landmesser H., Kirsch F., Ogienko A., Grunzel M., Kiesler C., Steinhoff H.-J., Schneider E., Eitinger T. (2015). ATP-dependent Conformational Changes Trigger Substrate Capture and Release by an ECF-type Biotin Transporter. J. Biol. Chem., 290(27),16929-42.

[52] Fisher D. J., Fernandes R. E., Adams N. E., Maurelli A. T. (2012). Uptake of biotin by Chlamydia spp. Through the use of a bacterial transporter (BioY) and a host cell transporter (SMVT). PLoS One, 7, e46052.

[53] Foguel D., Silva J.L. (1994). Cold denaturation of a repressor–operator complex: the role of entropy in protein–DNA recognition. Proc. Natl. Acad. Sci. USA. 91, 8244–8247.

[54] Foguel D., Suarez M. C., Ferrao-Gonzales A. D., Porto T. C. R., Palmieri L., Einsiedler C. M., Andrade L. R., Lashuel H. A., Lansbury P. T., Kelly J. W., Silva J. L. (2003) Dissociation of amyloid fibrils of α-synuclein and transthyretin by pressure reveals their reversible nature and the formation of water-excluded cavities. PNAS 19, 100(17), 9831–9836.

[55] Foguel D., Silva J.L. (2004) New insights into the mechanisms of protein misfolding and aggregation in amyloidogenic diseases derived from pressure studies. Biochemistry, 43, 11361–11370.

[56] Freed J.H., Bruno G.V., Polnasze C.F. (1971). Electron spin resonance line shapes and saturation in slow motional region. *Journal of Physical Chemistry*, 75, 3385–3399.

[57] Fredenburg R. A., Rospigliosi C., Meray R. K., Kessler J. C., Lashuel H. A., Eliezer D. (2007). The impact of the E46K mutation on the properties of alpha-synuclein in its monomeric and oligomeric states. Biochemistry, 46, 7107-18.

[58] Fu H., Subramanian R. R., Masters S. C. (2000). 14-3-3 proteins: Structure, function, and regulation. Annu. Rev. Pharmacol. Toxicol., 40, 617-47.

[59] Fuentes E. J., Wand A. J. (1998). Local Stability and Dynamics of Apocytochrome b562 Examined by the Dependence of Hydrogen Exchange on Hydrostatic Pressure. Biochemistry, 37, 9877-9883.

[60] Fulyani F., Schuurman-Wolters G. K., Zagar A. V., Guskov A., Slotboom D. J., Poolman B. (2013). Functional diversity of tandem substrate-binding domains in ABC transporters from pathogenic bacteria. Structure, 21(10), 1879-88.

[61] Gath J., Habenstein B., Bousset L., Melki R., Meier B. H., Böckmann A. (2012). Solid-state NMR sequential assignments of α-synuclein. Biomol. NMR Assign. 2012, 6, 51–55.

[62] Ghosh D., Sahay S., Ranjan P., Salot S., Mohite G. M., Singh P. K. (2014). The newly discovered Parkinson's disease associated Finnish mutation (A53E) attenuates α-synuclein aggregation and membrane binding. Biochemistry, 53, 6419-21.

[63] Giasson B. I., Uryu K., Trojanowski J. Q., Lee V. M. (1999). Mutant and wild type human alpha-synucleins assemble into elongated filaments with distinct morphologies in vitro. J. Biol. Chem., 274, 7619–7622.

[64] Giehm L., Svergun D. I., Otzen D. E., Vestergaard B. (2011). Low-resolution structure of a vesicle disrupting α-synuclein oligomer that accumulates during fibrillation. Proc. Natl. Acad. Sci. USA, 108(8), 3246–3251.

[65] Glaser C. B., Yamin G., Uversky V. N., Fink A. L. (2005). Methionine Oxidation, Alpha-Synuclein and Parkinson's Disease. Biochim. Biophys. Acta, 1703, 157-169.

[66] Glaenzer J.,Peter M. F., Thomas G. H., Hagelueken G. (2017). PELDOR Spectroscopy Reveals Two Defined States of a Sialic Acid TRAP Transporter SBP in Solution. Biophysical Journal, 112, 109–120.

[67] Goers J., Uversky V. N., Fink A. L. (2003). Polycation-Induced Oligomerization and Accelerated Fibrillation of Human Alpha-Synuclein *in Vitro*. Protein Sci., 12, 702-707.

[68] Goldberg M.S., Lansbury P. T. Jr. (2000). Is there a causeand- effect relationship between alpha-synuclein fibrillization and Parkinson's disease? Nat. Cell Biol., 2,115–119.

[69] Golebiewska U., Scarlat S.(2015). High pressure promotes alpha-synuclein aggregation in cultured neuronal cells. FEBS Letters, 589, 3309-3312.

[70] Govindarajan S., Goldstein R. A.. (1998). On the thermodynamic hypothesis of protein folding. Proc. Natl. Acad. Sci. USA., Vol. 95, 5545-5549.

[71] Grote M., Bordignon E., Polyhach Y., Jeschke G., Steinhoff H. J., Schneider E.. (2008). A comparative EPR study of the nucleotide-binding domains' catalytic cycle in the assembled maltose ABC-importer, Biophys. J., 95, 2924–2938.

[72] Grote M., Polyhach Y., Jeschke G., Steinhoff H. J., Schneider E., Bordignon E. (2009). Transmembrane signaling in the maltose ABC transporter MalFGK2-E: periplasmic MalF-P2 loop communicates substrate availability to the ATP-bound MalK dimer, J. Biol. Chem., 284, 17521–17526.

[73] Hagen W. C. (2009). Biomolecular EPR Spectroscopy. CRC Press.

[74] Hanson P., Millhauser G., Formaggio F., Crisma M., Toniolo C., Vita C. (1999). ESR characterization of hexameric, helical peptides using double TOAC spin-labeling. J. Am. Chem. Soc., 118, 7618-7625.

[75] Harpaz Y. (1994) Volume changes on protein folding. Structure, 2, 641–649.

[76] Hebbeln P., Rodionov D.A., Alfandega A., Eitinger T. (2007). Biotin uptake in prokaryotes by solute transporters with an optional ATP-binding cassette-containing module. Proc. Natl. Acad. Sci. USA, 104(8), 2909-14.

[77] Heise H., Hoyer W., Becker S., Andronesi O. C., Riedel D., Baldus M. (2005). Molecular-level secondary structure, polymorphism, and dynamics of full-length α-synuclein fibrils studied by solid-state NMR. PNAS, 102(44), 15871-15876.

[78] Henderson G.B., Zevely E.M., Huennekens FM. (1976). Folate transport in *Lactobacillus casei*: solubilization and general properties of the binding protein. Biochem Biophys Res Commun. 68(3), 712-7.

[79] Henderson G.B., Zevely E.M., Huennekens F.M. (1977). Purification and properties of a membrane-associated, folate-binding protein from Lactobacillus casei. J Biol Chem., 252(11), 3760-5.

[80] Henderson G.B., Zevely E.M., Huennekens F.M. (1979). Coupling of energy to folate transport in Lactobacillus casei. J Bacteriol., 139(2), 552-9.

[81] Henderson G.B., Zevely E.M., Huennekens F.M. (1979). Mechanism of folate transport in Lactobacillus casei: evidence for a component shared with the thiamine and biotin transport systems. J Bacteriol., 137(3), 1308-14.

[82] Heuveling J., Frochaux V., Ziomkowska J., Wawrzinek R., Wessig P., Herrmann A., and Schneider E. (2014). Conformational changes of the bacterial type I ATP-binding cassette importer HisQMP2 at distinct steps of the catalytic cycle. Biochim. Biophys. Acta, 1838, 106-116.

[83] Heremans K., Jonas J., Winter R. (1999). The phase diagram and the pressure-temperature behavior of proteins. In *High Pressure Molecular Science*, Kluwer Academic Publishers, 437–472.

[84] Higgins, C. F., Haag P. D., Nikaido K.; Ardehir F.; Garcia G. Ames, G. F. (1982). Complete nucleotide sequence and identification of membrane components of the histidine transport operon of S. Typhimurium. Nature 298, 723–727.

[85] Higgins C. F. (2001). ABC transporters: physiology, structure and mechanism--an overview. Res. Microbiol. 152, 205–210.

[86] Hoffmann S.K., Goslar J., Lijewski S. (2013). Electron paramagnetic resonance and electron spin echo studies of Co^{2+} coordination by nicotinamide adenine dinucleotide (NAD^{+}) in water solution. Appl. Magn. Reson., 44, 817-826.

[87] Hoyer W., Antony T., Cherny D., Heim G., Jovin T. M., Subramaniam V. (2002). Dependence of alpha-synuclein aggregate morphology on solution conditions. J. Mol. Biol., 322,383-93.

[88] Hoyer W., Cherny D., Subramaniam V., Jovin T. M. (2004). Impact of the Acidic C-Terminal Region Comprising Amino Acids 109-140 on alpha-Synuclein Aggregation *in Vitro*. Biochemistry, 43, 16233-16242.

[89] Hsu L.J., Sagara Y., Arroyo A., Rockenstein E., Sisk A., Mallory M., Wong J., Takenouchi T., Hashimoto M., Masliah E. (2000). Alpha-Synuclein promotes mitochondrial deficit and oxidative stress. Am. J. Pathol., 157, 401–410.

[90] Hubbell W.L., Altenbach C. (1994). Investigation of structure and dynamics in membrane proteins using site-directed spin labeling. Curr. Opin. Struct. Biol., 4, 566-573.

[91] Hung L. W., Wang I. X., Nikaido K., Liu P. Q., Ames G. F. L., Kim S. H. (1998). Crystal structure of the ATP-binding subunit of an ABC transporter, Nature, 396, 703–707.

[92] Iwai A., Masliah E., Yoshimoto M., Ge N., Flanagan L., de Silva H.A., Kiteel A., Saitoh T. (1995). The precursor protein of non-A beta component of Alzheimer´s disease amyloid is a presynaptic protein of the central nervous system. Neuron. 14(2), 467-75.

[93] Jakes R., Spillantini M. G., Goedert M. (1994). Identification of two distinct synucleins from human brain. FEBS Lett., 345, 27-32.

[94] James T. L., Matson G. B., Kuntz I. D. (1978). Protein Rotational Correlation Times Determined in Aqueous Solution by Carbon- 13 Rotating Frame Spin-Lattice Relaxation in the Presence of an Off-Resonance Radiofrequency Field. Journal of the American Chemical Society, 100, 11.

[95] Jenkins D. M., Di Bilio A. J. , Allen M. J., Betley T. A., Peters J. C. (2002). Elucidation of a Low Spin Cobalt(II) System in a Distorted Tetrahedral Geometry. JACS, 124, 15336-15350.

[96] Jeschke G. (2006). Deer analysis 2006 - a comprehensive software package for analyzing pulsed eldor data. *Appl. Magn. Reson.*, 30, 473.

[97] Jeschke G., Polyhach Y. (2007). Distance measurements on spin-labeled biomacromolecules by pulsed electron paramagnetic resonance. PCCP,9 , 1895-1910.

[98] Jeschke G., Sajid M., Schulte M., Godt A. (2009) Three-spin correlationsin double electron-electron resonance. Physical chemistry chemical physics, 11, 6580–6591.

[99] Jin H., Kanthasamy A., Ghosh A., Yang Y., Anantharam V., Kanthasamy A. G. (2011) α-synuclein negatively regulates protein kinase Cδ expression to suppress apoptosis in dopaminergic neurons by reducing p300 histone acetyltransferase activity. J. Neurosci., 31, 2035-51.

[100] Jones P. M., George A. M. (2012). Role of the D-Loops in Allosteric Control of ATP Hydrolysis in an ABC Transporter. *J. Phys. Chem. A,* 116, 3004–3013.

[101] Kang J., Park J., Choi H., Burla B. Kretschmar T., Lee Y; Matinoia E. (2011). Plant ABC Transporters. *Arabidopsis Book* 9, pp. e0153.

[102] Karpowich N. K, Wang D. N. (2013). Assembly and mechanism of a group II ECF transporter. Proc. Natl. Acad. Sci. USA., 110(7), 2534-9.

[103] Kaylor J., Bodner N., Edridge S., Yamin G., Hong D. P., Fink A. L. (2005). Characterization of Oligomeric Intermediates in α-Synuclein Fibrillation: FRET Studies of Y125W/Y133F/Y136F R-Synuclein. J. Mol. Biol. 353, 357-372.

[104] Khurana R., Coleman C., Ionescu-Zanetti C., Carter S. A., Krishna V., Grover R. K., Roy R., Singh S. (2005). Mechanism of thioflavin T binding to amyloid fibrils. Journal of Structural Biology, 151, 229–238.

[105] Kirsch F., Frielingsdorf S., Pohlmann A., Ziomkowska J., Herrmann A., Eitinger T. (2012). Essential Amino Acid Residues of BioY Reveal That Dimers are the Functional S Unit of the Rhodobacter capsulatus Biotin Transporter. J. Bacteriol., 194, 4505–4512.

[106] Kirsch F., Eitinger T. (2014). Transport of nickel and cobalt ions into bacterial cells by S components of ECF transporters. BioMetals, 27, 653-660.

[107] Kirsch F. (2015). Analyse der Substratbindestelle, der Stöchiometrie und der TRansportfunktion von S-Einheiten bakterieller ECF-Transporter. Dissertation. Humboldt-Universität zu Berlin.

[108] Klose D., Klare J. P., Grohmann D., Kay C. W. M., Werner F., Steinhoff, H. J. (2012). Simulation vs. reality: a comparison of *in silico* distance predictions with DEER and FRET measurements. PLoS One, 7, e39492.

[109] Kühn M. (2003). Orientierung von Helix 9 in membrangebundenemColicin A untersucht mit ESR Spektroskopie und SDSL. Dissertation,Ruhr-Universität Bochum.

[110] Kuipers B.J., Gruppen H. (2007). Prediction of molar extinction coefficients of proteins and peptides using UV absorption of the constituent amino acids at 214 nm to enable quantitative reverse phase high-performance liquid chromatography-mass spectroscopy analysis. J.Agric. Food Chem., 55, 5445-5451.

[111] Lashuel H. A., Petre B. M., Wall J., Simon M., Nowak R. J., Walz T., Lansbury P. T. Jr. (2002). Alpha-synuclein, especially the Parkinson's disease-associated mutants, forms pore-like annular and tubular protofibrils. J. Mol. Biol., 322, 1089–1102.

[112] Lee H.J., Lee S.J. (2002). Characterization of cytoplasmic alpha-synuclein aggregates. Fibril formation is tightly linked to the inclusion-forming process in cells. J. Biol. Chem., 277, 48976–48983, 10.

[113] Lee S., Heerklotz H., Chalikian T. V. (2010). Effects of buffer ionization in protein transition volumes. Biophysical Chemistry, 148(1–3), 144–147.

[114] Leigh J. S. (1970). ESR rigid-lattice line shape in a system of two interacting spins. J. Chem. Phys., 52, 2608-2612.

[115] Leopold P.E., Montal M., Onuchic J. N. (1992). Protein folding funnels: A kinetic approach to the sequence-structure relationship. Proc. Natl. Acad. Sci. USA., 89, 8721-8725.

[116] Lerch M. T., Horwitz J., McCoy J., & Hubbell W. L. (2013). Circular dichroism and sitedirected spin labeling reveal structural and dynamical features of high-pressure states of myoglobin. Proceedings of the National Academy of Sciences of the United States of America, 110(49), 4714–4722.

[117] Lerch M. T., Yang Z., Altenbach C., Hubbell W. L. (2015) High-Pressure EPR and Site-Directed Spin Labeling for Mapping Molecular Flexibility in Proteins. METHODS IN ENZYMOLOGY Electron Paramagnetic Resonance Investigations of Biological Systems by Using Spin Labels, Spin Probes, and Intrinsic Metal Ions, Part B.

[118] Levinthal C., Debrunner P., Tsibris J. C. M., Munck E. (1969). Mossbauer Spectroscopy in Biological Systems, eds. Univ. of Illinois Press, Urbana, 22–24.

[119] Li T. M., Hook III J. W., Drickamer H. G., Weber G. (1976). Plurality of pressure-denatured forms in chymotrypsinogen and lysozyme. Biochemisty, 15(25), 5571.

[120] Li J., Uversky V. N., Fink A. L. (2002). Conformational Behavior of Human Alpha-Synuclein Is Modulated by Familial Parkinson's Disease Point Mutations A30P and A53T. Neurotoxicology, 23, 553-567.

[121] Li J., Zhu M., Rajamani S., Uversky V. N., Fink A. L. (2004). Rifampicin Inhibits Alpha-Synuclein Fibrillation and Disaggregates Fibrils. Chem. Biol., 11, 1513-1521.

[122] Licht, Schneider E. (2011). ATP Binding cassette systems: structures, mechanisms, and functions. Cent. Eur. J. Biol., 6(5), 785-801.

[123] Lopez C. J., Oga S., Hubbell W. L. (2012). Mapping molecular flexibility of proteins with site directed spin labeling: A case study of myoglobin. Biochemistry, 51(33), 6568–6583.

[124] Luckhurst G. R. (1966). Alternating linewidths. A novel relaxation processin the electron resonance of biradicals. Mol. Phys., 10, 543–550.

[125] Ly T., Julian R. R. (2008). Protein-metal interactions of calmodulin and Alpha-synuclein monitored by selective noncovalent adduct protein probing mass spectrometry. J. Am. Soc. Mass Spectrom., 19, 1663-72.

[126] Ma B., Shatsky M., Wolfson H.J., Nussinov R. (2002) Multiple diverse ligands binding at a single protein site: A matter of pre-existing populations. Protein Sci. 1,184–197.

[127] Mao B., Pear M. R., McCammon J. A., Quiocho F. A. (1982). Hinge-bending in L-arabinose-binding protein. The "Venus's-flytrap" model. J. Biol. Chem., 257(3), 1131-3.

[128] Majorek K. A., Porebski P.J., Dayal A., Zimmerman M. D., Jablonska K., Stewart A. J., Chruszcz M., Minor W. (2012) Structural and immunologic characterization of bovine, horse, and rabbit serum albumins .Mol.Immunol., 52, 174-182.

[129] Margraf D., Bode B.E., Marko A., Schiemann O., Prisner T.F. (2007) Conformational flexibility of nitroxide biradicals determined by x-band peldor experiments. Molecular Physics, 105, 2153–2160.

[130] Martin R. E., Pannier M., Diederich F., Gramlich V., Hubrich M., Spiess H.W. (1998). Determination of end-to-end distances in a series of TEMPO diradicals of up to 2.8 nm length with a new four-pulse double electron electron resonance experiment. Angew. Chem. Int. Ed., 37(20), 2834-2837.

[131] Martinez J., Moeller I., Erdjument-Bromage H., Tempst P., Lauring B. (2003). Parkinson's disease-associated alpha-synuclein is a calmodulin substrate. J. Biol. Chem. 278, 17379-87.

[132] Matsuo S., Makita T. (1989). Viscosities of Six 1-Alkanols at Temperatures in the Range 298-348 K and Pressures up to 200 MPa. International Journal of Thermophysics, 10(4).

[133] McCoy J., Hubbell W. L. (2011). High-pressure EPR reveals conformational equilibria and volumetric properties of spin-labeled proteins. Proceedings of the National Academy of Sciences of the United States of America, 108(4), 1331–1336.

[134] Mchaourab H. S., Lietzow M. A., Hideg K., Hubbell W. L.. (1996). Motion of spin-labeled side chains in t4 lysozyme. Correlation with protein structure and dynamics. *Biochemistry*, 35, 7692–7704.

[135] Milov, A.D., Ponomarev, A.B., Tsvetkov, Yu.D. (1984). Electron-electron double resonance in electron spin echo: Model biradical systems and the sensitized photolysis of decalin. Chemical Physics Letters, 110, 67-72.

[136] Moussatova A., Kandt C., O'Mara M.L., Tieleman D.P. (2008). ATP binding cassette transporters in Escherichia coli, Biochim. Biophys. Acta, 1778, 1757-1771.

[137] Munishkina L. A., Phelan C., Uversky V. N., Fink A. L. (2003). Conformational Behavior and Aggregation of Alpha-Synuclein in Organic Solvents: Modeling the Effects of Membranes. Biochemistry, 42, 2720-2730.

[138] Munishkina L. A., Henriques J., Uversky V. N., Fink A. L. (2004). Role of Protein-Water Interactions and Electrostatics in Alpha-Synuclein Fibril Formation. Biochemistry, 43, 3289-3300.

[139] Neubauer O., Alfandega A., Schoknecht J., Sternberg U., Pohlmann A., Eitinger T. (2009). Two essential arginine residues in the T components of energy-coupling factor transporters. J Bacteriol., 191(21), 6482-8.

[140] Neubauer O., Reiffler C., Behrendt L., Eitinger T. (2011). Interactions among the A and T units of an ECF-type biotin transporter analyzed by site-specific crosslinking. PLoS One., 6(12), e29087.

[141] Niraula T. N., Konno T., Li H., Yamada H., Akasaka K., Tachibana H. (2004). Pressure-dissociable reversible assembly of intrinsically denatured lysozyme is a precursor for amyloid fibrils. Proceedings of the National Academy of Sciences of the United States of America, 101, 4089–4093.

[142] Oblak M., Prezelj A., Pecar S., Solmajer T. (2004). Thiol-reactive clenbuterol analogues conjugated to bovine serum albumin. Z. Naturforsch., C: J. Biosci, 59, 880-886.

[143] Oh B. H., Ames G. F. L., Kim S. H. (1994) Structural basis for multiple ligand specificity of the periplasmic lysine-, arginine-, ornithine-binding protein, J. Biol. Chem., 269, 26323–26330.

[144] Oh B. H., Kang C. H., De Bondt H., Kim S. H., Nikaido K., Joshi A. K., Ames G. F. (1994). The bacterial periplasmic histidine-binding protein. Structure/function analysis of the ligand-binding site and comparison with related proteins. J. Biol. Chem., 269(6), 4135-43.

[145] Oldham M. L., Khare D., Quiocho F. A., Davidson A. L., Chen J. (2007). Crystal structure of a catalytic intermediate of the maltose transporter. Nature, 450, 515–521.

[146] Oldham M. L., Chen J. (2011). Snapshots of the maltose transporter during ATP hydrolysis. Proc. Natl. Acad. Sci., 108, 15152–15156.

[147] Oldham M. L., Chen J. (2011). Crystal structure of the maltose transporter in a pretranslocation intermediate state. Science, 332, 1202–1205.

[148] Oliveira A.C. (1994). Arc repressor will not denature under pressure in the absence of water. J. Mol. Biol., 240, 184–187.

[149] Onuchic J. N., Luthey-Schulten Z., Wolynes P. G. (1997). THEORY OF PROTEIN FOLDING: The Energy Landscape Perspective. Annu. Rev. Phys. Chem., 48, 545–600.

[150] Orelle C., Ayvaz T., Everly R. M., Klug C. S., Davidson A. L. (2008) Both maltose-binding protein and ATP are required for nucleotide-binding domain closure in the intact maltose ABC transporter. Proc. Natl. Acad. Sci. USA, 105, 12837–12842.

[151] Orelle C., Alvarez F. J., Oldham M. L., Orelle A., Wiley T. E., Chen J., Davidson A. L. (2010). Dynamics of α-helical subdomain rotation in the intact maltose ATP-binding cassette transporter. Proc. Natl. Acad. Sci., 107, 20293–20298.

[152] Oswald C., Holland B. I., Schmitt L. (2006). The motor domains of ABC-transporters. Naunyn-Schmiedebergs Arch. Pharmacol., 372, 385–399.

[153] Pannier M., Veit S., Godt A., Jeschke G., Spiess H.W. (2000). Dead-time free measurement of dipole-dipole interactions between electron spins. Journal of Magnetic Resonance, 142, 331–340.

[154] Park S. M., Jung H. Y., Kim T. D., Park J. H., Yang C. H., Kim J. (2002). Distinct Roles of the N-terminal-binding Domain and the C-terminalsolubilizing Domain of α - Synuclein, a Molecular Chaperone. Biological Chemistry, 277, 28512-20.

[155] Peng X., Tehranian R., Dietrich P., Stefanis L., Perez R. G. (2005). Alpha-synuclein activation of protein phosphatase 2A reduces tyrosine hydroxylase phosphorylation in dopaminergic cells. J. Cell. Sci., 118, 3523-30.

[156] Peters Jr. T. (1995). *All about albumin: biochemistry, genetics, and medical applications*. Academic press.

[157] Pfund D.M., Zemanian T.S., Linehan J.C., Fulton J.L., Yonker C. R. (1994) Fluid Structure in Supercritical Xenon by Nuclear Magnetic Resonance Spectroscopy and Small Angle X-ray Scattering. J. Phys. Chem., 1994, 98, 11 846-11 857.

[158] Plato M., Steinhoff H.-J., Wegener C., Torring J., Savitsky A., Moebius K.. (2002). Molecular orbital study of polarity and hydrogen bonding effects on the g and hyperfine tensors of site directed no spin labelled bacteriorhodopsin. Frontiers in Bioscience, 100, 3711–3721.

[159] Polyhach Y., Bordignon E., Jeschke G. (2011). Rotamer libraries of spin labelled cysteines for protein studies, Phys. Chem. Chem. Phys., 13, 2356–2366.

[160] Polyhach Y., Bordignon E., Tschaggelar R., Gandra S., Godt A., Jeschke G. (2012). High sensitivity and versatility of the DEER experiment on nitroxide redical pairs at Q-band frequencies. Phys. Chem. Phys., 14, 10762-10773.

[161] Poole C. P. (1983). *Electron Spin Resonance*: A comprehensive treatise on experimental techniques. Dover Publications, Inc., Mineola, New York.

[162] Pornsuwan S., Giller K., Riedel D., Becker S., Griesinger C., Bennati M. (2013). Long-Range Distances in Amyloid Fibrils of a-Synuclein from PELDOR Spectroscopy. Angew. Chem. Int. Ed., 52, 10290-10294.

[163] Pranke I. M., Morello V., Bigay J., Gibson K., Verbavatz J. M., Antonny B. (2011) α-synuclein and ALPS motifs are membrane curvature sensors whose contrasting chemistry mediates selective vesicle binding. J. Cell. Biol.,194, 89-103.

[164] Qin Z., Hu D. M., Han S., Reaney S. H., Di Monte D. A, Fink A. L. (2006). Effect of 4-Hydroxy-2-Nonenal Modification on R-Synuclein Aggregation. J. Biol. Chem.

[165] Quiocho F. A., Ledvina P. S. (1996). Atomic structure and specificity of bacterial periplasmic receptors for active transport and chemotaxis: variation of common themes. Mol. Microbiol., 20(1), 17-25.

[166] Rabenstein M. D., Shin Y.-K. (1995). Determination of the distance between two spin labels attached to a macromolecule. *Proc. Natl.Acad. Sci. USA*, 92, 8239–8344.

[167] Radzwill, N. (2001). Bestimmung der Strukturänderungen der lichtgetriebenen Protonenpumpe Bakteriorhodopsin mittels zweifacher Spinmarkierung und ESR-Spektroskopie. Dissertation. Ruhr-Universität Bochum, Germany.

[168] Rea P.A. (2007). Plant ATP-binding cassette transporters, Annu. Rev. Plant Biol., 58, 347–375.

[169] Rice A. J., Park A., Pinkett H.W. (2014). Diversity in ABC transporters: Type I, II and III importers. Crit. Rev. Biochem. Mol. Biol., 49(5), 426–437.

[170] Ritter C., Maddelein M. L., Siemer A. B., Lührs T., Ernst M., Meier B. H., Saupe S. J., Riek R. Correlation of structural elements and infectivity of the HET-s prion. Nature, 435, 844-848.

[171] Roche J., Caro J. A., Norberto D. R., Barthe P., Roumestand C., Schlessman J. L. (2012). Cavities determine the pressure unfolding of proteins. Proceedings of the National Academy of Sciences of the United States of America, 109(18), 6945–6950.

[172] Rochet J. C., Conway K. A., Lansbury P. T. Jr. (2000). Inhibition of Fibrillization and Accumulation of Prefibrillar Oligomers in Mixtures of Human and Mouse Alpha-Synuclein. Biochemistry, 39, 10619-10626.

[173] Rodionov D.A., Hebbeln P., Gelfand M.S., Eitinger T. (2006). Comparative and functional genomic analysis of prokaryotic nickel and cobalt uptake transporters: evidence for a novel group of ATP-binding cassette transporters. J Bacteriol., 188(1), 317-27.

[174] Rodionov D. A., Hebbeln P., Eudes A.; ter Beek J., Rodionove I. A., Erkens G. B., Slotboom D. J., Gelfand M. G., Osterman A. L., Hanson A.D., Eitinger T. (2009): A novel class of modular transporters for vitamins in prokaryotes. J. Bacteriol., 191, 42–51.

[175] Rodriguez J. A., Ivanova M. I., Sawaya M. R., Cascio D., Reyes F. E., Shi D. (2015). Structure of the toxic core of α-synuclein from invisible crystals. Nature, 525, 486-90.

[176] Royer C.A. (2002). Revisiting volume changes in pressure-induced protein unfolding. Biochemica et Biophysica Acta 1595, 201-209.

[177] Samaranayake C. P., Sastry S. K. (2010). In situ measurement of pH under high pressure. The Journal of Physical Chemistry B, 114(42), 13326–13332.

[178] Schmelzer J. W., Zanotto E. D., Fokin V. M. (2005). Pressure dependence of viscosity. J. Chem. Phys. 15, 122(7), 074511.

[179] Schneider E., Hunke S. (1998). ATP-binding-cassette (ABC) transport systems: functional and structural aspects of the ATP-hydrolyzing subunits/domains. FEMS Microbiol Rev., 22(1), 1-20.

[180] Schneider, E. (2008). A comparative electron paramagnetic resonance study of the nucleotide-binding domains' catalytic cycle in the assembled maltose ATP-binding cassette importer. Biophys. J., 95, 2924–2938.

[181] Schneider E., Eckey V., Weidlich D., Wiesemann N., Vahedi-Faridi A., Thaben P., Saenger W. (2012). Receptor-transporter interactions of canonical ATP-binding cassette import systems in prokaryotes. Eur. J. Cell Biol., 91(4), 311-7.

[182] Scott D., Roy S. (2012) α-synuclein inhibits intersynaptic vesicle mobility and maintains recycling-pool homeostasis. J. Neurosci. 32, 10129-35.

[183] Serio T.R. (2000). Nucleated conformational conversion and the replication of conformational information by a prion determinant. Science, 289(5483):1317–1321.

[184] Serpell L. C., Berriman J., Jakes R., Goedert M., Crowther R. A. (2000). Fiber diffraction of synthetic alpha-synuclein filaments shows amyloid-like cross-beta conformation. *Proc. Natl. Acad. Sci. USA,* 97, 4897–4902.

[185] Siche S., Neubauer O., Hebbeln P., Eitinger T. 2010. A bipartite S unit of an ECF-type cobalt transporter. Res. Microbiol., 161, 824-829.

[186] Silva, J.L. (1996). The use of hydrostatic pressure as a tool to study viruses and other macromolecular assemblages. *Curr. Opin. Struct. Biol.* 6, 166–175.

[187] Silva J.L., Foguel D., Royer C. A. (2001). Pressure provides new insights into protein folding, dynamics and structure. TRENDS in Biochemical Sciences, 26(10).

[188] Silva J. L., Vieira T. C., Gomes M. P., Ano Bom A. P., Lima L. M., Freitas M. S., Ishimaru D., Cordeiro Y., Foguel D. (2010). Ligand binding and hydration in protein misfolding: insights from studies of prion and p53 tumor suppressor proteins. Accounts of Chemical Research, 43, 271–279.

[189] Sippach M., Weidlich D., Klose D., Abé C., Klare J., Schneider E., Steinhoff H.-J. (2014). Conformational changes of the histidine ATP-binding cassette transporter studied by double electron–electron resonance spectroscopy. Biochimica et Biophysica Acta 1838, 1760–1768.

[190] Slichter C.P. (1996). Principles of Magnetic Resonance. Springer-Verlag, 3 edition.

[191] Slipenyuk A. M., Glinchuk M. D., Bykov I. P., Ragulya A. V., Klimenko V. P., Konstantinova T. E. (2004). ESR investigation of Yttria stabilized Zirconia powders with nanosize particles. Ferroelectrics, 298(1), 289–296.

[192] Slotboom D.J. (2014). Structural and mechanistic insights into prokaryotic energy-coupling factor transporters. Nat. Rev. Microbiol., 12(2), 79-87.

[193] Smith W. W., Jiang H., Pei Z., Tanaka Y., Morita H., Sawa A., Dawson V. L., Dawson T. M., and Ross C. A. (2005). Endoplasmic reticulum stress and mitochondrial cell death pathways mediate A53T mutant alpha-synuclein-induced toxicity. Hum. Mol. Genet. 14, 3801–3811.

[194] Sode K., Ochiai S., Kobayashi N., Usuzaka E. (2007). Effect of reparation of repeat sequences in the human α-synuclein on fibrillation ability. Biol. Sci. 3, 1-7.

[195] Steinhoff H.-J., Radzwill N., Thevis W., Lenz V., Brandenburg D., Antson A., Dodson G.G., Wollmer A. (1997). Determination of interspin distances between spin labels attached to insulin: comparison of electron paramagnetic resonance data with the X-ray structure, Biophys. J. 73, 3287–3298.

[196] Stoll S., Schweiger A. (2006). EasySpin, a comprehensive software package for spectral simulation and analysis in EPR *J. Magn. Reson.* 178(1), 42-55.

[197] Tang L., Lucas A. H., Eaton J. W. (1993). Inflammatory responses to implanted polymeric biomaterials: role of surface-adsorbed immunoglobulin G. Journal of Laboratory and Clinical Medicine, 122(3), 292-300.

[198] Tang, L., & Eaton, J. W. (1995). Inflammatory responses to biomaterials. American journal of clinical pathology, 103(4), 466-471.

[199] Ter Beek J., Duurkens R.H., Erkens G.B., Slotboom D.J. (2011). Quaternary structure and functional unit of energy coupling factor (ECF)-type transporters. J. Biol. Chem., 286(7), 5471-5.

[200] Ter Beek J., Guskov A., Slotboom D.J. (2014). Structural diversity of ABC transporters. J. Gen. Physiol., 143(4), 419-35.

[201] Torrent J., Alvarez-Martinez M. T., Heitz F., Liautard J. P., Balny C., Lange R. (2003). Alternative Prion Structural Changes Revealed by High Pressure. Biochemistry, 42, 1318-1325.

[202] Uéda K., Fukushima H., Masliah E., Xia Y., Iwai A., Yoshimoto M. (1993). Molecular cloning of cDNA encoding an unrecognized component of amyloid in Alzheimer disease. Proc. Natl. Acad. Sci. USA, 90, 11282-6.

[203] Ulmer T. S., Bax A., Cole N. B., Nussbaum R. L. (2005). Structur and dynamics of micelle-bound human alpha-synuclein. J. Biol. Chem., 280, 9595-9603.

[204] Uversky V. N., Li J., Fink A. L. (2001). Pesticides Directly Accelerate the Rate of Alpha-Synuclein Fibril Formation: a Possible Factor in Parkinson's Disease. FEBS Lett., 500, 105-108.

[205] Uversky V. N., Li J., Fink A. L. (2001). Evidence for a Partially Folded Intermediate in Alpha-Synuclein Fibril Formation. J. Biol. Chem., 276, 10737-10744.

[206] Uversky V. N., Li J., Fink A. L. (2001). Metal-Triggered Structural Transformations, Aggregation, and Fibrillation of Human Alpha-Synuclein. A Possible Molecular Link Between Parkinson's Disease and Heavy Metal Exposure. J. Biol. Chem., 276, 44284-44296.

[207] Uversky V. N., Li J., Zhu M., Bower K., Fink A. L. (2002). Synergistic Effects of Pesticides and Metals on the Fibrillation of Alpha- Synuclein: Implications for Parkinson's Disease. Neurotoxicology, 23, 527-536.

[208] Uversky V. N., Li J., Souillac P. O., Millett I. S., Doniach S., Jakes R., Goedert M., Fink A. L. (2002). Biophysical properties of the synucleins and their propensities to fibrillate: inhibition of alpha-synuclein assembly by beta- and gamma-synucleins. J. Biol. Chem., 277, 11970-11978.

[209] Uversky V. N., Yamin G., Souillac P. O., Goers J., Glaser C. B., Fink A. L. (2002). Methionine Oxidation Inhibits Fibrillation of Human Alpha-Synuclein in Vitro. FEBS Lett., 517, 239-244.

[210] Uversky V. N., Fink A. L. (2004). Conformational Constraints for Amyloid Fibrillation: the Importance of Being Unfolded.Biochim. Biophys. Acta, 1698, 131-153.

[211] Uversky V. N. (2007). Neuropathology, biochemistry, and biophysics of alpha-synuclein aggregation. J. Neurochem., 103, 17–37.

[212] Van Gastel M. (2009). Pulsed epr spectroscopy. *Photosynth Res*,102, 367–373.

[213] Varkey J., Isas J. M., Mizuno N., Jensen M. B., Bhatia V. K., Jao C. C., (2010). Membrane curvature induction and tubulation are common features of synucleins and apolipoproteins. J. Biol. Chem., 285, 32486-93.

[214] Vasiliou V., Konstandinos Vasiliou K., Nebert D.W. (2009). Human ATP-binding cassette (ABC) transporter family. Hum. Genomics, 3, 281-290.

[215] Venda L.L., Cragg S.J., Buchman V.L., Wade-Martins R. (2010). α-synuclein and dopamine at the crossroads of Parkinson's disease. Trends in Neuroscience, 33, 559-68.

[216] Vilar M., Chou H. T., Lührs T., Maji S. K., Riek-Loher D., Verel R., Manning G., Stahlberg H., Riek R. (2008). The fold of alpha-synuclein fibrils. Proc. Natl. Acad. Sci. USA, 105, 8637–8642.

[217] Wang G. F., Li C., Pielak G. J. (2010). 19F NMR studies of α-synuclein-membrane interactions. Protein Sci.,19, 1686-91.

[218] Wang T., Fu G., Pan X., Wu J., Gong X., Wang J., Shi Y. (2013). Structure of a bacterial energy-coupling factor transporter. Nature, 497(7448), 272-6.

[219] Weil J. A., Bolton J. R, Wertz J. E. (1994). Electron Paramagnetic Resonance Elementary Theory and Practical Applications. John Wiley & Sons, Inc.

[220] Weber G. (1992). Effects of temperature andpressure on molecular associations and on single peptide chain proteins. In *Protein Interactions*, Chapman and Hall, 199–215.

[221] Wen P.C., Tajkhorshid E. (2011). Conformational coupling of the nucleotide-binding and the transmembrane domains in ABC transporters. Biophys. J., 101(3), 680-90.

[222] Wilfred Raymond Hagen (2009). Biomolecular EPR Spectroscopy. CRC Press.

[223] Witt S. N. (2013). Molecularchaperones, α-synuclein, and neurodegeneration. Mol. Neurobiol., 47, 552-60.

[224] Wood S. J., Wypych J., Steavenson S., Louis J. C., Citron M., Biere A.L. (1999). Alpha-synuclein fibrillogenesis is nucleationdependent. Implications for the pathogenesis of Parkinson's disease. J. Biol. Chem., 274, 19509–19512.

[225] Xu K., Zhang M., Zhao Q., Yu F., Guo H., Wang C., He F., Ding J., Zhang P. (2013) Crystal structure of a folate energy-coupling factor transporter from Lactobacillus brevis. Nature., 497(7448), 268-71.

[226] Yamin G., Glaser C. B., Uversky V. N., Fink A. L. (2003). Certain Metals Trigger Fibrillation of Methionine-Oxidized R-Synuclein. J. Biol. Chem., 278, 27630-27635.

[227] Yamin G., Uversky V. N., Fink A. L. (2003). Nitration Inhibits Fibrillation of Human Alpha-Synuclein in Vitro by Formation of Soluble Oligomers. FEBS Lett., 542, 147-152.

[228] Yu Y., Zhou M., Kirsch F., Xu C., Zhang L., Wang Y., Jiang Z., Wang N., Li J., Eitinger T., Yang M. (2014). Planar substrate binding site dictates the specificity of ECF-type nickel/cobalt transporters. Cell Res., 24, 267-277.

[229] Zaitseva J., Jenewein S., Jumpertz T., Holland I. B., Schmitt L. (2005). H662 is the linchpin of ATP hydrolysis in the nucleotide-binding domain of the ABC transporter HlyB. EMBO J., 24(11), 1901-10.

[230] Zhang P., Wang J., Shi Y.(2010). Structure and mechanism of the S component of a bacterial ECF transporter. Nature., 468(7324), 717-20.

[231] Zhang P. (2013). Structure and mechanism of energy-coupling factor transporters. Trends Microbiol., 21(12), 652-9.

[232] Zhang M., Bao Z., Zhao Q., Guo H., Xu K., Wang C., Zhang. (2014). Structure of a pantothenate transporter and implications for ECF module sharing and energy coupling of group II ECF transporters. Proc Natl Acad Sci U S A., 111(52), 18560-18565.

[233] Zhu M., Fink A. L. (2003). Lipid Binding Inhibits Alpha-Synuclein Fibril Formation. J. Biol. Chem., 278, 16873-16877

[234] Zhu M., Rajamani S., Kaylor J., Han S., Zhou F., Fink A. L. (2004). The Flavonoid Baicalein Inhibits Fibrillation of Alpha-Synuclein and Disaggregates Existing Fibrils. J. Biol. Chem., 279, 26846-26857.

[235] Zoghbi M.E., Altenberg G.A. (2013). Hydrolysis at one of the two nucleotide-binding sites drives the dissociation of ATP-binding cassette nucleotide-binding domain dimers. J Biol Chem., 288(47), 34259-65.

[236] Zoghbi M. E., Altenberg G.A. (2014). ATP binding to two sites is necessary for dimerization of nucleotide-binding domains of ABC proteins. ATP binding to two sites is necessary for dimerization of nucleotide-binding domains of ABC proteins. Biochem. Biophys. Res. Commun., 443(1), 97-102.

[237] Oliveira G. A. P., Marques M. A., Cruzeiro-Silva C., Cordeiro Y., Chuabb C., Moares A.H., Winter R., Oschkinat H., Foguel D., Freitas M.S., Silva J.L. (2016). Structural basis for the dissociation of α-synuclein fibrils triggered by pressure perturbation of the hydrophobic core. Sci. Rep., 30, 6:37990.

Acknowledgement

I would like to thank all those who have supported me during my studies.

First and foremost, I would like to thank my supervisor Prof. Dr. Heinz Steinhoff for his guidance and support during the preparation of this work and beyond. I would also like to thank him for the opportunity to work in his working group and in a fascinating field of work.

My sincere thanks to Prof. Dr. Eitinger for the willingness to act as second reviewer of this work.

I also want to acknowledge the exceptional collaboration with Prof. Dr. Eitinger, Prof. Dr. Schneider, Dr. Friedrich Finkenwirth, Dr. Johanna Heuveling and Dr. Daniela Weidlich from the Humboldt University of Berlin. I gratefully thank not only for a vast amount of provided samples but for a lot of helpful and fruitful discussions as well.

I would like to thank all the other members of the working group Professor Dr. Steinhoff for my friendly reception in their midst, the constant willingness to help and the great atmosphere in the lab and office.

My deep and sincere thanks to my girlfriend Jaqueline for her love and support as well as for her well placed motivational punches when writing this thesis became a real annoyance.

Finally, I would like to express my deepest thanks to my family, and especially to my parents. Their long-standing and loving support, patience and care is my greatest thanks.

Declaration

I hereby declare that the submitted work has been created by myself the signatory.
To the best of my knowledge I have not used any other than permitted reference sources or materials. All utilized contents and references originating from other sources have been appropriately acknowledged in this work. Furthermore, I declare that this work has not been submitted for the purpose of academic examination anywhere else.

Osnabrueck, Germany

December, 2017